THE UNIVERSITY *of* EDINBURGH

This thesis has been submitted in fulfilment of the requirements for a postgraduate degree (e.g. PhD, MPhil, DClinPsychol) at the University of Edinburgh. Please note the following terms and conditions of use:

This work is protected by copyright and other intellectual property rights, which are retained by the thesis author, unless otherwise stated.
A copy can be downloaded for personal non-commercial research or study, without prior permission or charge.
This thesis cannot be reproduced or quoted extensively from without first obtaining permission in writing from the author.
The content must not be changed in any way or sold commercially in any format or medium without the formal permission of the author.
When referring to this work, full bibliographic details including the author, title, awarding institution and date of the thesis must be given.

Hall Resistivity and Torque Magnetometry Studies of the Ferromagnetic Superconductors UGe_2 and URhGe

Calum T. Lithgow

Doctor of Philosophy
The University of Edinburgh
March 2016

Abstract

Ferromagnetism (FM) and superconductivity (SC) are traditionally thought of as competing states of matter, since the opposite-spin electron pairing mechanism required for conventional SC is rendered impossible by FM spin alignment. However, recently discovered heavy-fermion compounds UGe_2 and URhGe are examples where SC and FM are cooperative, and rather than antagonistic the presence of FM is actually necessary for the occurrence of the SC phase.

A cooperative state of FM and SC is a topic of interest because it presents a possible solution to one of the two main problems with present superconductors: technology inhibiting limits on the highest temperature and highest magnetic field to which the SC phase can exist. Although both UGe_2 and URhGe cease to be superconductors before even reaching 1 K, unlike the various 'high temperature' superconductors currently known that easily surpass 100 K, it is their magnetic properties that are interesting, the inherent FM ordering allowing them to exceed conventional limits on the maximum magnetic field that SC can withstand. For example, URhGe remains superconducting above 35 T and the upper limit is so high that it is still experimentally undetermined.

How exactly the FM SC phase arises in these compounds is as yet unknown. The necessary opposite-spin pairing mechanism is theoretically provided by magnetic fluctuations in an easily polarizable system right on the edge of a magnetic phase transition, and indeed SC emerges in UGe_2 and URhGe around a first-order quantum critical point (QCP) where the temperature of the transition to an FM phase is reduced to absolute zero, by application of pressure in the case of UGe_2 and by application of a magnetic field for URhGe.

The aim of the research detailed in this thesis is to probe the FM phase transition and the associated QCP related to the emergence of SC in these compounds, to gather more information about the precise nature of the phases

either side of the transition and exactly what changes occur in the system crossing the QCP. Specifically, the main objective is to characterise the magnetic fluctuations at the phase boundary and determine whether, by current FM SC theory, these fluctuations could be responsible for SC or if instead other, modified, unconventional theories are required to explain the unconventional electron pairing.

The probes of choice for this PhD were Hall effect and magnetoresistance measurements of UGe_2, and capacitive torque magnetometry and simultaneous magnetoresistance measurements of URhGe.

The main result of the UGe_2 project is an observed order-of-magnitude change in the Hall coefficient crossing the FM transition as a function of temperature and a dramatic change, similar in magnitude but also accompanied by a sign reversal, crossing the QCP as a function of pressure. Furthermore, the sign reversal at the critical pressure persists up to roughly 12 K, far beyond the 7 K critical end point of the phase transition, suggesting that in fact three different phases converge at the QCP where fluctuations between them presumably lead to the emergence of SC. Further investigation of the Fermi surface, either by deeper analysis of the Hall effect results or by other experimental methods, will be required to complete the main objective and determine exactly what the differences are between these newly identified phases.

The main result of the URhGe project is actually the successful development of the capacitive torque magnetometry technique itself and the proof of operation for simultaneous measurement of all the individual components of both the magnetization and differential susceptibility tensors in a high magnetic field, which is currently not possible by any other technique. Completing the main objective was hampered by the extremely high susceptibility components encountered in the vicinity of the QCP, which in itself could be considered evidence for the theoretical relationship between strong FM fluctuations and the emergence of SC in URhGe.

A number of results incidental to the main aim of the URhGe project are also summarised in this thesis, including the characterisation of quantum oscillations frequencies not previously reported in scientific literature and a variety of subtle features in resistivity measurements, which could, in conjunction with evidence from the susceptibility measurements, suggest the presence of another superconducting state such as surface or domain wall SC.

Lay Summary

Superconductors have amazing potential to dramatically improve a huge range of electric and magnetic devices and make possible the invention of countless new technologies. These materials conduct electricity perfectly, without resistance, without losing energy as heat, and can either expel magnetic fields entirely or fix them in place in a way that allows superconductors to levitate above a magnet or hang below it unsupported.

Currently their most common use is for powerful electromagnets, with the electric current circulating forever even when the power source is removed. These magnets are often used in scientific research, in a variety of cryostat systems or in particle accelerators like the Large Hadron Collider (LHC) at CERN, and in diagnostic medicine for Magnetic Resonance Imaging (MRI), and occasionally in motors and power generators, such as those in wind turbines.

The stable levitation of superconductors can be used to build virtually frictionless trains, while the ability to carry current without loss makes superconducting wire perfect for power cables, connecting cities to power plants. A significant advancement would be the use of superconductors in electronics, where the absence of any heat produced during operation would solve one of the major limitations on the growth of computing power: overheating and catastrophically melting the silicon chips.

Unfortunately the superconducting state is particularly fragile, easily destroyed by high electric currents, high magnetic fields and high temperatures. Even the lowest naturally occurring temperature on Earth is too high for our currently known superconductors and liquid nitrogen must be used to cool them, making them pragmatically and economically useless for the vast majority of conceivable technologies. Thus before the fantastic potential of superconductivity can be realised this exotic and confounding state of matter must be understood well

enough that new, more robust superconductors can be created.

The materials under study in this thesis are uranium compounds that stop being superconductors and become normal metals at about -272°C, a long way from room temperature and far from useful for any practical application. Instead they are of scientific interest because of their magnetic properties. Both are strong magnets, even when superconducting, and the magnetism appears to help in the emergence of superconductivity rather than hinder it as it does in conventional superconductors. This allows them to far surpass the conventional upper limit on the magnetic field they can withstand.

The theoretical description of how magnetism and superconductivity exist cooperatively rather than antagonistically in these compounds is as yet unverified, and the fundamental mechanisms responsible for the emergence of superconductivity not exactly known, but the aim is that by studying these materials, by investigating their electrical and magnetic properties at very low temperature, enough information can be gathered about their nature that this type of superconductivity can eventually be entirely explained.

This thesis covers two experimental studies. Firstly the electrical properties of the compound UGe_2 are measured at very low temperature and very high pressure, investigating a sudden change in the type of magnetism at conditions close to those under which the material becomes superconducting. The change in magnetism and emergence of superconductivity are seemingly related, and understanding the former is expected to be key to understanding the latter.

Secondly the electrical and magnetic properties of the compound URhGe are measured at extremely low temperature and very high magnetic field, the conditions under which there is also a sudden change in the magnetic state apparently associated with the occurrence of superconductivity.

A greater comprehension of how and why the magnetism in UGe_2 and URhGe abruptly alters at these critical combinations of extreme conditions, and how and why those variations give rise to superconductivity, is ultimately one small step toward a complete theory of magnetic superconductivity and a better understanding of the superconducting state in general. Hopefully such understanding will then aid in unlocking the full potential of future superconductors that operate at technologically viable temperatures and magnetic fields, with the research outlined in this thesis mostly contributing to the latter.

Declaration

I declare that this thesis was composed by myself, that the work contained herein is my own except where explicitly stated otherwise in the text, and that this work has not been submitted for any other degree or professional qualification except as specified.

Some parts of this work began during a preceeding MPhys project at The University of Edinburgh, specifically the preparation work for the Hall resistivity study of UGe_2, as detailed in my MPhys Project Report "Hall resistivity crossing a ferromagnetic quantum critical point in UGe_2" submitted for assessment in 2011. However, all experimental results and analysis presented within this thesis were obtained and performed during the PhD project and no content from the MPhys project report is included herein.

(*Calum T. Lithgow, March 2016*)

Acknowledgements

I would firstly like to thank my supervisors Andrew Huxley and Ed Yelland for their great ideas, tutelage, guidance and support over the years. I would also like to thank the rest of the St Andrews group, Jack Barraclough and Jean-Philippe Reid, for their invaluable laboratory assistance and instruction, and for innumerable helium transfers.

Jack Barraclough should also be credited with the design and construction of the sample platform rotator used in the St Andrews dilution refrigerator, and Ed Yelland credited with the general development of the fridge measurement systems, including those for the torque magnetometry project.

Full credit for the design and construction of the piston-cylinder cell utilised for the high pressure study of UGe_2 goes to Weiwei Wang and his PhD supervisor Konstantin Kamanev, who also assisted me with the operation of the cell for the duration of the project.

Full credit for crystal growth goes to Dmitry Sokolov and Andrew Huxley; I had absolutely no involvement in the process other than to inherit the products of their excellent work.

I would also like to thank the mechanical and electronic workshops of the St Andrews physics department for their regular help and expertise, and the cryogenics department for meeting the research group's incessant demand for liquid helium.

Finally I would like to thank my wife, Holly, for supporting me in every possible way for the entirety of my postgraduate studies.

Contents

Abstract i

Lay Summary iii

Declaration v

Acknowledgements vii

Contents ix

List of Figures xv

1 Introduction 1

1.1 UGe_2 Essential Facts 9

1.2 UGe_2 Literature Review 10

1.3 URhGe Essential Facts 19

1.4 URhGe Literature Review 21

2 Background Theory 29

2.1 Introduction to Electronic Transport 29

2.1.1 Fermi Surfaces and the Hall Coefficient 33

2.1.2 Kohler's Law 36

2.1.3 Fermi Liquid Theory and Lifshitz Transitions 37

2.2 Ferromagnetism 41

2.2.1 Localised Magnetism 43

2.2.2 Itinerant Magnetism 46

2.2.3 Kondo Screening and the Doniach Diagram 48

2.2.4 Domains and Hysteresis 52

2.3 The Hall Effect 54

2.3.1 The Anomalous Hall Effect 62

2.4 Quantum Oscillations 73

2.4.1 Landau Quantization 73

2.4.2 The de Haas-van Alphen Effect 75

2.5 Capacitive Torque Magnetometry 79

2.5.1 Introduction to the Method 81

2.5.2 Two-Component Magnetometry 86

2.5.3 Simultaneous Torque and Force Magnetometry 88

2.6 Ferromagnetic Superconductivity 94

3 Hall Resistivity Experimental Methods 101

3.1 Introduction 101

3.2 Sample Preparation 102

3.3 Motivation for the Van der Pauw Method 104

3.4 The Van der Pauw Method in Detail 107

3.4.1 Placement of Contacts 107

3.4.2 The Sign of the Hall Voltage 110

3.4.3 Experiment Details 110

3.5 Measuring Pressure 112

3.5.1 Advatages of the Manganin Pressure Sensor..... 113

3.5.2 Pressure Sensor Calibration 114

4 Torque Magnetometry Experimental Methods 119

4.1 Introduction 119

4.2 Sample Preparation 120

4.3 Field Modulations and Gradients..... 126

4.3.1 Transverse Field Coils..... 129

4.4 Magnetometer Calibration 134

4.4.1 From Torque to Magnetization..... 136

4.5 Lock-In Amplifiers and Tandem Demodulation 138

4.6 Experiment Details..... 142

5 UGe_2 Hall Resistivity Results and Discussion 147

5.1 Determining Curie Temperature 149

5.1.1 Method 1..... 149

5.1.2 Method 2..... 151

5.1.3 Method 3..... 155

5.2 Determining T_X and H_X 157

5.2.1 Method A 157

5.2.2 Method B 160

5.2.3 Method C 163

5.3 UGe_2 Phase Diagram 164

5.4 Separating the Ordinary and Anomalous Hall Effects ... 168

5.4.1 A Case Study at 2 K ... 169

5.4.2 Fitting the Data ... 172

5.4.3 Extensions to Higher Temperature ... 177

5.5 Data Analysis Summary ... 181

5.6 Base Temperature Hall Coefficients ... 182

5.6.1 Higher Temperatures ... 185

5.7 The Ordinary Hall Coefficient ... 187

5.8 The Anomalous Hall Coefficients ... 208

6 URhGe Torque Magnetometry Results and Discussion 219

6.1 Zero-Field Resistance ... 219

6.2 Finding The $\phi = 0$ Position ... 221

6.3 Resistivity Measurements ... 227

6.4 Non-Ohmic Behaviour ... 232

6.5 Quantum Oscillations ... 235

6.6 Capacitance Measurements ... 245

6.6.1 Field Gradient Magnetometry ... 248

6.6.2 Measurements at $\phi \simeq 0°$ ... 252

6.6.3 Measurements up to $\phi \sim 10°$ ... 257

6.6.4 Corresponding Resistance Measurements ... 264

6.7 Decomposed Magnetization ... 268

7 Conclusions 273

7.1 Detailed UGe_2 Hall Resistivity Conclusions 276

7.2 Detailed URhGe Torque Magnetometry Conclusions 280

7.2.1 Extensions and Improvements 285

A UGe_2 Critical Points 289

B The Force on a Magnetized Material 291

C Unsuccessful Magnetoresistance Fitting 297

Bibliography 299

List of Figures

(1.1) A figure from Ref. [1]. The original caption reads: "Cartoon of the pairing interaction due to magnetic fluctuations. The magnetization (green line) has a small nonzero average (the red line) plus a large fluctuating part. Two conduction electrons induce local polarization clouds. If the two electrons are separate (top panel) their energy is higher than if they share the same polarization cloud (bottom panel), thus it can be energetically favorable for them to be paired." 4

(1.2) The pressure-temperature phase diagram of UGe_2 showing the transitions from paramagnetism (PM) to ferromagnetism (FM) and the lower temperature transition within the ferromagnetic state between the strongly polarised FM2 phase and the weakly polarised FM1 phase. The FM1-FM2 transition is only a true phase transition up to a critical end point (CEP) at 7 K beyond which it becomes a broad crossover. The PM-FM transition is second order at low pressure but becomes first order at a tricritical point (TCP). The superconducting transition temperature peaks at 0.8 K around the critical pressure at which the FM1-FM2 transition occurs at absolute zero. Source: Ref. [2] 11

(1.3) A sketch of the calculated Fermi surface of UGe_2. Note that only a half-length of the Brillouin zone is shown for the c-axis direction in order to show a cross-section through the centre of the main, roughly cylindrical Fermi surface, which has its axis parallel to b. Source: Ref. [3] 13

(1.4) The quantum oscillation frequencies found from a.c. susceptibility measurements and the de Haas-van Alphen effect for magnetic field applied parallel to the a-axis in UGe_2, the easy axis of magnetization, for a number of different pressures passing both P_X at 12.5 kbar and P_C at 16 kbar. Source: Ref. [4] 14

(1.5) Sketches of calculated Fermi surfaces in the ferromagnetic state of UGe_2, highlighting in particular the extremal orbit related to the β frequency found in quantum oscillation measurements, related to the roughly cylindrical Fermi surface sheet with axis parallel to the crystallographic b-axis. Source: Ref. [5] 15

(1.6) The pressure-temperature-field phase diagram of UGe_2 showing one side of the wing structure that extends from the CEP and the TCP, with the latter decreasing in height until reaching zero at a quantum critical end point (QCEP). By contrast the CEPs for the wing associated with the FM1-FM2 transition seem to remain relatively constant at 7 K. At very, very high field this wing may also reach a QCEP, though such a point has yet to be measured. Source: Ref. [6] 17

(1.7) The field-temperature phase diagram of URhGe for field applied parallel to the crystallographic b-axis, showing the low and high field regions of superconductivity, as measured by a zero resistance state. The high field superconductivity is peaked at 12 T, the position of a magnetic moment rotation transition, above which there is also a peak in the normal state resistance, as shown in the inset. Source: Ref. [7] 21

(1.8) Sketches of the the unit cells of UGe_2 and URhGe. Each cell contains 4 formula units. Source: Ref. [8] 22

(1.9) The magnetization as a function of field applied parallel to the b-axis at 2 K, measured by neutron scattering, showing the moment rotation transition at 12 T where the easy axis changes from c to b. Source: Ref. [7] 23

(1.10) The schematic field-temperature phase diagram of URhGe for magnetic fields in the b-c plane.The magnetization changes discontinuously on crossing the first-order transition surface shaded green, which is bounded by the Curie temperature line. The tricritical point and wing structure typical to the ferromagnetic superconductors occurs at high field just before the quantum critical point, the Curie temperature then reaching zero at a pair of QCEPs. Superconductivity at 50 mK is shown by the red shading, corresponding to the zero resistance state. Source: Ref. [9] 24

(1.11) A figure from Ref. [9]. The original caption reads: "The quantity plotted is proportional to the inverse-square coherence length, $\phi_0/2\pi\xi^2$, given in units of magnetic field where $\xi = (\xi_a\xi_b\xi_c)^{1/3}$ is the geometric mean of the coherence lengths along the different axes, calculated assuming a constant anisotropy. The vertical line marks the magnetic field at which the rotation transition occurs. The other straight line gives the value of $\phi_0/2\pi\xi^2$ below which the critical field for superconductivity for $H \parallel b$ is less than the applied field along the b axis; superconductivity cannot occur when $\phi_0/2\pi\xi^2$ falls below this line. The coherence length, ξ, changes from 143 Å for the data point closest to the origin to 44 Å for the data point with the highest value of $\phi_0/2\pi\xi^2$. The line through the data points is to guide the eye." 25

(1.12) The phase diagram of URhGe for components of the field parallel to the b and a-axes, showing the superconductivity probed by the zero-resistance state at 45 mK. The upper critical field in the a-axis direction is sharply peaked at $\mu_0 H_R \simeq 12$ T applied parallel to the b-axis, the position of the moment rotation transition. Directly at H_R the upper critical field is beyond the measurement range. Source: Ref. [9] 26

(2.1) A few pictorial examples of the complex Fermi surfaces found in real metals (the exact nature of the corresponding materials is unimportant to the discussion here). Only a single Brillouin zone is shown. These surfaces demonstrate the topological feature of a 'neck' though to the next Brillouin zone, which looks like a hole in this single-zone representation. Source: Ref. [10]. 39

(2.2) A graphic from the original Lifshitz publication[11] on the topic, illustrating the two types of Fermi surface reconstruction referred to as Lifshitz transitions. 40

(2.3) The generic Doniach diagram with the ambient pressure positions of several heavy fermion compounds. The characteristic asymmetric curve is the result of two competing magnetic interactions. Source: Ref. [12] 50

(2.4) Diagram of the Hall effect. Field B produces a Hall voltage V_H transverse to current I due to the Lorentz force $\vec{F_L}$. Source: Ref. [13] 54

(2.5) Demonstration of anholonomy for the case of vectors on a spherical surface. Starting with the red path, parallel transport to the pole then down along the blue path back to the starting point results in a rotation between the orientation of the initial red arrow and the final blue arrow. 69

(2.6) Depictions of the three main mechanisms for the anomalous Hall effect with short descriptions of each. Adapted from Ref. [14]. . . 72

(2.7) Landau quantization of electron orbits in k-space for a vertical magnetic field. Landau levels for free electrons are a series of concentric cylinder surfaces. Only the occupied portions of the Landau levels, contained within the Fermi surface, are shown. Source: Ref. [15]. 76

(2.8) Illustration of a hypothetical Fermi surface with variety of extremal orbits highlighted for two different directions of magnetic field. Orbits 1, 2 and 3 (in red) are present for field H_1 whereas only orbit 4 (in blue) is present for field H_2. Adapted from Ref. [16]. 77

(2.9) Several different oscillation periods superimposed in a single measurement, from different extremal orbits present simultaneously for a particular direction of applied field. Source: Ref. [16]. 78

(2.10) The field modulation strength as a function of position, relative to the field centre, for small distances surrounding the centre point. The magnet system is in 'gradient mode' in these calculations, and the field strength plotted is per ampere of current supplied to the magnet coils. **Top:** The field strength in the axial $\hat{z}$ direction. **Bottom:** The field strength in the radial $\hat{x}$ direction. 92

(3.1) **Top Left:** Photograph and sketch of the UGe_2 sample used for the Hall effect study. In the photograph four spot-welded gold wires can be seen. The approximate contact positions of these wires are indicated by gold spots in the sketch, along with the sample dimensions and crystallographic orientation. **Top Right:** The Laue diffraction pattern for the sample, for a backscattered x-ray beam parallel to the crystallographic a-axis, matched to show the c-axis vertical and the b-axis horizontal. **Bottom Left:** Diagram of the piston-cylinder pressure cell showing the sample space within the 4 mm diameter bore. **Bottom Centre:** Labelled photograph of the pressure cell mounted on the cryostat probe stage, showing initial testing at low pressure. **Bottom Right:** Photograph of an actual measurement run at high pressure, showing well secured, twisted-pair wiring. 103

(3.2) Several examples of possible placement of electrical contacts on a sample for Hall effect measurements. **a)** The ideal case of well-aligned and perpendicularly-oriented contacts, placed on the edge of the sample as per the van der Pauw method. **b)** An exaggeration of mis-aligned contacts, where both voltage and current contacts are skewed from ideal alignment with the crystallographic axes and their relative orientations are far from perpendicular. **c)** For a non-ideal sample shape, with rough edges, the orientation of the voltage and current contacts are still perpendicular, however alignment to the crystallographic axes has been lost. **d)** One possible method of quantitatively determining the longitudinal resistivity while also optimising the Hall effect measurement by using six contacts. . . . 107

(3.3) **Main:** The measured voltage as a function of field at 2 K and 10.3 kbar. At positive field the reduced magnitude, relative to negative field, suggests that the Hall voltage has opposite sign to the current. From the physical direction of the field, this implies that the Hall voltage is negative. **Inset:** A sample diagram showing the positions of the electrical contacts, where the voltage contact mis-alignment has been exaggerated. 111

(3.4) A plot of α, the change in Manganin resistance with change in pressure, relative to the ambient pressure resistance, as a function of temperature, according to the approximation to experimental data determined in Ref. [17]. It is worth reiterating that this is a plot of two temperature regions characterised by different linear equations, developed for generic use with Manganin pressure sensors, which are only approximations to the real behavior. . . . 115

(3.5) The pressure determined by the Manganin pressure sensor, plotted as a function of temperature for every high-pressure experimental run. Note that the E run has been fitted with a smoothing interpolation because of excessive noise that obsured the other plots on the graph. The increase in pressure from room temperature down to 2 K becomes greater as the runs progress from B to M. 116

(3.6) The pressure determined by the Manganin pressure sensor, plotted over the low-temperature measurement range for the main Hall effect dataset, for every high-pressure experimental run. Note that the E run has been fitted with a smoothing interpolation because of excessive noise that obscured the other plots on the graph. Compared to the variation in pressure observed at higher temperature, seen in figure 3.5, there is relatively little change in pressure at low temperature. The value at the centre of this graph is the pressure used to label the whole experimental run for subsequent Hall effect analysis. 117

(4.1) The Laue diffraction pattern for the primary sample of URhGe, shown on the tip of a wooden cocktail stick in the photograph in the bottom right corner. The coordinate system for the Laue pattern is shown in the bottom left corner; the x-ray beam direction was parallel to the x-axis. The sample was positioned 5 cm from the backscatter image plate. The a-axis of the sample is almost parallel to the vertical z-axis. The b and c axes have no particular alignment. 121

(4.2) Diagrams and a photograph of the torque magnetometer. **Top:** A labelled, side elevation diagram showing the small gap between the cantilever and base plate and also the loose nature of the gold wires. **Bottom Left:** Labelled, plan view diagram of the magnetometer showing the screws used to clamp the cantilever between the quartz blocks that comprised the fulcrum. **Bottom Right:** Plan view photograph for comparison. 123

(4.3) Labelled photograph of the rotator platform and gearing; the axis of rotation is the horizontal in this image. The magnetometer is positioned such that the sample, located near the screw that secured the box to the platform, is close to the rotation axis and as such will change position relatively little when the platform rotates. 125

(4.4) A diagram of the six magnet coils surrounding the sample space. Coils 1 & 3 are wired in series, as are coils 2 & 4. When current is supplied to both circuits in-phase the direction of the field generated by each coil is indicated by the arrows marked 'mod'. This is the 'modulation mode', providing a uniform field across the sample space. When the direction of current supplied to coils 1 & 3 is reversed, such that it becomes 180° out of phase with that supplied to coils 2 & 4, the field directions are those marked by 'grad'. This is the 'gradient mode', where the field in the centre is approximately zero but has opposite sign immediately above and below the sample space, creating a strong gradient. The two transverse coils are also wired in series and always provide horizontal field modulation. In this diagram the rotator platform is oriented such that the crystallographic b-axis of the sample is vertical and the c axis is horizontal, which occurs at $\theta \simeq 35°$. The pick-up coils labelled α and β are angled to probe the vertical and horizontal field modulation at this orientation, while the pick-up coils labelled γ and δ are angled to primarily probe the orientation of the rotator platform. 128

(4.5) An illustration of the space surrounding the rotator platform, not-to-scale, with the separation between the inner vacuum can (IVC) and the radiation shield exaggerated. A photograph of the rotator has been inserted instead of a diagram, showing the connection to the dilution fridge mixing chamber at the top of the figure. 132

(4.6) **Top Left:** The phosphor bronze coil holder, designed to be sprung against the inside wall of the dilution refrigerator IVC. The ends of the vertical slits close up as the holder is squeezed into the tail of the IVC. **Bottom Left:** The coil winding equipment used to make the transverse field coils. The white plastic washers are a tight fit to the metal former but are free to slide. The gap between them in this photograph is approximately 0.5 mm, the intended height of the coils. **Top Right:** The resulting coil, 200 turns of 50 μm diameter enamelled copper wire, weakly held together by diluted GE varnish. **Bottom Right:** The coils mounted onto the holder (a second coil is mounted on the other side). The holder has been covered by electrical insulation and the coils have been covered by a substantial layer of full-strength GE varnish. The two coils are wired in series, with the arrows indicating the relative direction of current flow, such that the generated magnetic fields are parallel rather than anti-parallel. 133

(4.7) An example of the phase rotation applied to the lock-in amplifier measurements of the sample transport voltage. The phase angle was found empirically, by ensuring that the X component was constantly zero within the superconducting regions. The data before and after the phase rotation is shown, for both up and down field ramps. 140

(5.1) The positions of critical points T_C, T_X and H_X as determined by magnetization measurements in Ref. [18], which is also the source of the figure. 148

(5.2) **Top:** The first derivative of the resistivity with respect to temperature, plotted over the low temperature range, showing the features associated with the Curie temperature, T_C, and the metamagnetic transition at T_X, for the experimental H run at 12.0 kbar, just below P_X. **Bottom:** The second derivative of the same dataset, indicating that T_C and T_X correspond to the positions of a negative troughs. 150

(5.3) The Hall resistivity as a function of temperature for a number of different applied fields. The peak is a result of the anomalous Hall effect, proportional to both the longitudinal resistivity and the magnetization. The dramatic decrease in the Hall resistivity at the Curie temperature, $\sim$34 K, at the lowest fields is due to the sudden drop in magnetization at the transition from ferromagnetism to paramagnetism. 152

(5.4) The temperature of the trough in the first derivative of the Hall resistivity with respect to temperature, indicative of the Curie temperature, as a function of field using the dataset shown in figure 5.3. A linear fit provides a y-axis intercept that is therefore related to the Curie temperature in the limit of zero field. 153

(5.5) **Main:** The Hall resistivity as a function of temperature. Each data point is the result of an extrapolation to zero field of a number of measurements in field, using the data set shown in figure 5.3. **Inset:**The derivative of the curve in the main figure with respect to temperature. The position of the negative trough is related to the Curie temperature in the limit of zero field. 154

(5.6) **Left:** The first derivative of the magnetoresistivity with respect to temperature, for a small selection of different applied fields, as a function of temperature. Application of field suppresses the feature related to the Curie temperature. **Right** A close-up of the 0.5 T data around the Curie temperature demonstrating how the complicated feature observed at zero field has simplified into a single hump. 155

(5.7) Raw experimental data for measurements at 12.0 kbar, before separation into Hall resistivity and magnetoresistivity, for a number of different field strengths applied in both directions, plotted as a function of temperature. The extrapolation to a zero-field curve is also shown, lying between the datasets for opposite field directions as expected. 156

(5.8) **Top Left:** The measured resistance as a function of field for a few low temperatures at 12.0 kbar, below P_X. **Top Right:** The resistance as a function of field for a few low temperatures at 14.3 kbar. The influence of crossing H_X is obvious in comparison to the 12.0 kbar data. **Bottom Left:** The magnetoresistivity (ρ_{xx}) as a function of field for a few low temperatures at 14.3 kbar. **Bottom Right:** The Hall resistivity (ρ_{xy}) as a function of field for a few low temperatures at 14.3 kbar. 158

(5.9) The magneto- and Hall resistivity as a function of applied field at 3.5 kbar at 14.3 kbar, along with first and second derivatives (with respect to field) respectively. The troughs in the derivatives may aid in determining the exact position of the critical field H_X, which appears to be around 4 to 4.5 T. 159

(5.10) The derivative of the magnetoresistivity with respect to temperature, at 14.3 kbar, as a function of temperature for a range of field strengths. Above 4 T a low temperature peak can be seen, a feature associated with T_X, first emerging around 7 K before moving to higher temperature with higher fields. There is also a notable difference between the y-axis intercept of the plots above and below H_X. The data below H_X has been plotted with broken lines in order to make the graph clearer. 160

(5.11) The critical temperature T_X plotted as a function of field for every experimental run. For high pressure runs J, K, L and M, above P_X, the field corresponding to 0 K is referred to as H_X. For the I run the extrapolated 0 K value of H_X may lie below 0 T, which is unphysical and would indicate that the pressure is below P_X. The positions of the critical end points drawn on this graph are crude estimates, based on drawing a straight line from H_X at 0 K to the first finite-temperature data point for each high pressure plot. . . 162

(5.12) The resistivity as a function of field at 12.0 kbar for a few low temperatures. The line of the arrow roughly indicates the feature associated with H_X, which refers to a broad crossover at this pressure, and points toward a zero field extrapolation, an estimate of T_X, of between 6 and 8 K. A more accurate extrapolation, defining the position of H_X as the point of maximum curvature, using the second derivative, provides the result $T_X \sim 6.2$ K. . . . 163

(5.13) The gradient of the Hall resistivity with temperature, $\partial\rho_{xy}/\partial T$, for the 12 pressures measured between 7.8 and 14.3 kbar. The high temperature arrows, ranging from 25 to 42 K, indicate the position of the Curie temperature. The low temperature arrows indicate the position of T_X at pressures where it is observable. The letters used to label each experimental run are also shown, alongside the pressure at 30 K. 165

(5.14) The experimentally determined pressure-temperature-field phase diagram for UGe_2. The differences between the determined values for T_X and H_X and the literature values are likely due to the literature value marking the begining of the transition and the value determined by the resistance indicating the midpoint of the transition. The error bars included here are not true errors (the uncertainties in the data points have been omitted from this graph); instead the 'error bars' provide an estimate of the width of the critical region of the crossover. The solid lines are rough guides for the eye. 166

(5.15) The magnetization data presented in Ref. [18], which is also the source of the figures. **Left:** Magnetization as a function of field for the following pressures: 0, 6.5, 9.0, 11.1, 12.8, 13.8, 15.3, 15.5, 16.0, 16.7, 17.3 and 18.2 kbar. **Right:** Magnetization as a function of temperature at several pressures ranging from 0 to 15 kbar. . . 168

(5.16) The magneto- and Hall resistivity as a function of field at 10.3 kbar and 2 K. Both appear approximately linear at high field, with a negative gradient to the Hall resistivity. The linear fit gives the gradient as $-328\times10^{-12}\,\mathrm{m^3C^{-1}}$. The departure from linearity, in both plots, at very low field is primarily due to changes in the domain structure. 171

(5.17) The variables α_1 and α_2 as a function of field at 10.3 kbar and 2 K. The field range begins at 1 T instead of zero partly because the data at very low field is not included in the fitting procedure for finding the Hall coefficients and partly because the exponential rise due to dividing by H as $H \to 0$ obscures the behaviour of the rest of the plot. 173

(5.18) The Hall resistivity divided by field, the variable Γ, as a function of magnetoresistivity at 10.3 kbar and approximately 2.7 T. Although the data from 2 to 13 K is shown, only the range 3 to 12 K was fitted, though the line of best fit is plotted across the whole x-axis range. 175

(5.19) The Hall resistivity divided by field, the variable Γ, as a function of field at 10.3 kbar and 2 K. The line shows the fit to equation 5.2, which fits the data reasonably well, although it should be noted that the data scatter is quite large with generally large uncertainties. 176

(5.20) The three terms seen in equation 5.2 plotted as a function of field, at 10.3 kbar and 2 K, in order to compare magnitudes. The ordinary Hall coefficient is a constant. The second anomalous Hall coefficient is larger than the first across the whole field range, though both are similar in magnitude and neither dominates over the other. None of the three terms are negligible. 178

(5.21) **Left:** The magnetoresistivity as a function of field for several low temperatures at 14.3 kbar, directly measured by experimentally sweeping the field. **Right:** The same data set but constructed from temperature sweep measurements at various fixed field strengths, as indicated by the symbols. 179

(5.22) **Left:** The Hall resistivity as a function of field for several pressures, two below P_X and two above, around 3 K, showing a change in slope at H_X in the high pressure data but generally negative, constant gradient within a particular phase. **Right:** The longitudinal resistivity for the same dataset, also showing features around H_X but with generally positive gradient away from the transition. 182

(5.23) **Left:** The ordinary Hall coefficient for several pressures, two below P_X and two above, around 3 K. There is little difference between the FM2 state at low pressure and the induced FM2 state at high pressure, whereas the FM1 values are significantly different at an order of magnitude smaller. The estimated values are reasonably similar to the exact data. **Right:** The anomalous Hall coefficients for the same dataset, showing FM1 values that are not too dissimilar to the FM2 ones. The FM1 data at 13.3 kbar has uncertainty too large to claim significance in any difference from the FM2 values. 184

(5.24) Colour plot of the first derivative of the magnetoresistivity with respect to temperature, at 12.0 kbar, plotted as a function of temperature and field. The peak in the derivative, associated with T_X, is coloured blue. The exact peak positions at each measured field are indicated by markers. The value of T_X corresponding to the centre of the crossover region lies slightly above this line. . . . 186

(5.25) The gradient of the Hall resistivity with field, $\tilde{R}_0 = \partial\rho_{xy}/\partial\mu_0 H$, as a function of temperature up to T_C for a variety of pressures, three below P_X and three above. At low pressure, above T_X the field induced FM2 phase is shown in addition to the low field FM1 data. 188

(5.26) The gradient of the Hall resistivity with field, $\tilde{R}_0 = \partial\rho_{xy}/\partial\mu_0 H$, as a function of temperature up to and beyond T_C. The highest pressure data has been used as an example, where FM1 data can be shown from 2 K up to a relatively low Curie temperature at 25 K, beyond which the paramagnetic phase is shown up to the end of the measurement range at 60 K. On this scale the Hall coefficient at low temperature, below 10 K, appears to be about zero. 189

(5.27) Colour plot of the gradient of the Hall resistivity with field, $\tilde{R_0} = \partial\rho_{xy}/\partial\mu_0 H$, as a function of temperature and pressure, created by linear interpolation between discrete pressure values. The T_X and P_X phase lines from figure 5.14 have been overlaid. White triangles have been used to blank areas of unreliable data. At low temperature there is a clear change in $\tilde{R_0}$ crossing the P_X line, from around $-300\times10^{-12}\,\mathrm{m^3C^{-1}}$ at low pressure to around zero, if not slightly positive, at high pressure. Surprisingly this change is evident at temperatures up to about 13 K, well above the T_X values just below P_X. 190

(5.28) The gradient of the Hall resistivity with field, $\tilde{R_0} = \partial\rho_{xy}/\partial\mu_0 H$, as a function of pressure, plotted for a number of low temperatures. Above P_X the field induced FM2 data is shown in addition to the low field FM1 phase. Error bars have been omitted to avoid obscuring the plots, but typical uncertainties can be gauged from figure 5.25. There is a clear change in $\tilde{R_0}$ crossing P_X, as highlighted by the dividing line at $-210\times10^{-12}\,\mathrm{m^3C^{-1}}$. 192

(5.29) The ordinary Hall coefficient, R_0, as a function of temperature up to T_C for a variety of pressures, three below P_X and three above. At low pressure, above T_X the field induced FM2 phase is shown in addition to the low field FM1 data. 194

(5.30) Colour plot of the ordinary Hall coefficient R_0 as a function of temperature and pressure, created by linear interpolation between discrete pressure values. The T_X and P_X phase lines from figure 5.14 have been overlaid. White triangles have been used to blank areas of unreliable data. There is a clear change in R_0 from the relatively constant FM2 value of about $-300\times10^{-12}\,\mathrm{m^3C^{-1}}$, coloured yellow, to much larger negative values of R_0 in the high temperature FM1 phase, coloured blue. In contrast, at low temperature above P_X, the FM1 phase is characterised by small and positive values of R_0, coloured red, particularly in the region immediately above the critical pressure. 195

(5.31) The ordinary Hall coefficient, R_0, as a function of pressure, plotted for a number of low temperatures. Above P_X the low-field FM1 phase is shown. Error bars have been omitted to avoid obscuring the plots, but typical uncertainties can be gauged from figure 5.29. There is a significant change at P_X, although the somewhat erratic scatter of data points makes detailed analysis difficult. 197

(5.32) The inverse of the ordinary Hall coefficient, and the corresponding carrier concentration for a one-band model, as a function of temperature up to T_C for a variety of pressures, three below P_X and three above. Above T_X or P_X only the FM1 data is shown, for clarity. In general there is a change from $n \sim 1$ per uranium in the FM2 phase to $|n| < 0.2$ per uranium in the FM1 phase, except at the highest pressure where it reaches about 0.3 per uranium. . 198

(5.33) Colour plot of the one-band model carrier concentration, essentially the inverse of R_0, as a function of temperature and pressure, created by linear interpolation between discrete pressure values. The T_X and P_X phase lines from figure 5.14 have been overlaid. White triangles have been used to blank areas of unreliable data. There is a clear change from the FM2 value of about 1 electron per uranium to generally much lower values in the FM1 phase, around 0.1 to 0.2 electrons per uranium, with some small regions above P_X at low temperature indicating 0.1 to 0.2 holes per uranium. . . 199

(5.34) The one-band model carrier concentration, n, as a function of pressure, plotted for a number of low temperatures. Above P_X the low-field FM1 phase is shown. Error bars have been omitted to avoid obscuring the plots, but typical uncertainties can be gauged from figure 5.32. There is a significant change at P_X, although the somewhat erratic scatter of data points makes detailed analysis difficult. 200

(5.35) The relative increase in resistivity as a function of field, fitted by equation 2.27. **Left:** Just below P_X and in the FM2 phase at 3 K, fitting reveals a hole concentration roughly twice that of the electron concentration, though both are very small, of the order 0.01 charge carriers per formula unit of UGe_2. **Right:** Well above P_X at 2 K the data up to 4 T lies within the FM1 phase. Fitting reveals similar hole and electron concentrations as in the FM2 phase, though the hole concentration has increased by almost 50%. 201

(5.36) The magnetoresistance as a function of field for a range of temperatures at 7.8 kbar where T_X is relatively high at around 20 K. At low temperature the relative increase in resistivity with field can be fitted by equation 2.27 but beyond about 8 K the fitting procedure fails. 204

(5.37) The hole and electron concentrations, and the corresponding conductivities, resulting from fits to equation 2.27 for a two-band model, for ambient pressure and two other pressures below P_X. The hole concentration and conductivity are consistently greater than those of the electron band for all pressures. The conductivity generally falls as temperature increases, as expected for a metal. The electron concentration appears approximately constant while the hole concentration seems to increase with temperature. 205

(5.38) The hole and electron concentration, and the corresponding conductivities, resulting from low field (FM1 phase) fits to equation 2.27 for a two-band model, for 14.3 kbar, well above P_X. As for the FM2 data, the hole concentration and conductivity is consistently greater than the electron band values. 207

(5.39) The anomalous Hall coefficient R_{a_1} as a function of temperature up to T_C for a variety of pressures, three below P_X and three above. At low pressure, above T_X the field induced FM2 phase is shown in addition to the low field FM1 data. 209

(5.40) Colour plot of the anomalous Hall coefficient R_{a_1} as a function of temperature and pressure, created by linear interpolation between discrete pressure values. The T_X and P_X phase lines from figure 5.14 have been overlaid. White triangles have been used to blank areas of unreliable data. 210

(5.41) The anomalous Hall coefficient R_{a_2} as a function of temperature up to T_C for a variety of pressures, three below P_X and three above. At low pressure, above T_X the field induced FM2 phase is shown in addition to the low field FM1 data. 211

(5.42) Colour plot of the anomalous Hall coefficient R_{a_2} as a function of temperature and pressure, created by linear interpolation between discrete pressure values. The T_X and P_X phase lines from figure 5.14 have been overlaid. White triangles have been used to blank areas of unreliable data. 212

(5.43) Colour plot of the anomalous Hall coefficient R_{a_1} multiplied by the zero-field resistance, a quantity called 'term 1', as a function of temperature and pressure, created by linear interpolation between discrete pressure values. The T_X and P_X phase lines from figure 5.14 have been overlaid. White triangles have been used to blank areas of unreliable data. 214

(5.44) Colour plot of the anomalous Hall coefficient R_{a_2} multiplied by the zero-field resistance squared, a quantity called 'term 2', as a function of temperature and pressure, created by linear interpolation between discrete pressure values. The T_X and P_X phase lines from figure 5.14 have been overlaid. White triangles have been used to blank areas of unreliable data. 215

(5.45) Colour plot of the difference between 'term 1' and 'term 2' of the anomalous Hall resistivity, as a function of temperature and pressure, created by linear interpolation between discrete pressure values. Since term 2 is negative, the difference is given by term 1 + term 2. The T_X and P_X phase lines from figure 5.14 have been overlaid. White triangles have been used to blank areas of unreliable data. 216

(5.46) Colour plot of the the ratio of the two terms of the anomalous Hall resistivity, i.e.term 1 / |term 2|, as a function of temperature and pressure, created by linear interpolation between discrete pressure values. The T_X and P_X phase lines from figure 5.14 have been overlaid. White triangles have been used to blank areas of unreliable data. The colour scale was chosen such that if term 2 is greater in magnitude than term 1, the region is coloured blue. At higher temperatures, term 1 is mostly about twice the size of term 2, coloured green. 217

(6.1) **Left:** URhGe resistance as a function of temperature in the absence of field, demonstrating a change in slope around 9.8 K, the Curie temperature, and superconductivity below 255 mK. **Right:** Low temperature close-up showing the superconducting transition in more detail and a small step in resistance around 350 mK. The T^2 fit works well at low temperature but noticeably poorly above about 1.5 K. 220

(6.2) **Left:** The base temperature capacitance measured by the digital AH bridge instrument as a function of field, relative to the zero-field value, at a sample platform rotation of roughly 34° from vertical. There is a sudden fall to zero around 12 T due to the magnetic moment rotation transition. **Right:** The resistance measured simultaneously with the capacitance, showing the two regions of superconductivity, with critical fields 2, 8 and 13 T. . . 222

(6.3) The gradient of the capacitance against field over the first 1 T, allowing the zero-crossing point to be determined, which gives the sample platform rotation angle at which $B \perp c$-axis and effectively $B \parallel b$-axis. The angle that ϕ refers to is indicated in the sketch in the upper left corner; variations in ϕ are the result of rotating the cantilever relative to the field, which is always vertical. 223

(6.4) The capacitance, relative to the zero-field value, as a function of field for a few small rotation angles around the $B \| b$-axis position, as measured by the AH bridge. Even for the smallest angle the capacitance is not zero across the entire field range, as would be the case for a perfectly balanced domain structure, but instead crosses zero in several places. This is due to a small a-axis misalignment. 224

(6.5) **Left:** The capacitance, relative to the zero-field value, as function of field for $\phi \sim 0.1°$. **Right:** The same for $\phi \sim 0.01°$. In both cases there is significant hysteresis below the metamagnetic transition field, and a sign change above. Note that the magnitude of ΔC decreases roughly linearly with ϕ at these tiny angles. 225

(6.6) The URhGe sample resistance as a function of field, at the fridge base temperature, for a range of rotation angles from 0 to 90°. At small angles superconductivity re-emerges at high field. The high field superconductivity disappears around $\phi \sim 5°$. Quantum oscillations are clearly visable at 13.5° where the magnetoresistance also reaches a maximum, before falling to a minimum at $B \| c$-axis at $\phi \simeq 90°$. 228

(6.7) The URhGe sample resistance as a function of field, at the fridge base temperature, for a range of rotation angles from 0 to 5.5°. The initial superconducting transition field is weakly anisotropic, showing little variation from just under 2 T, but the re-entrant superconductivity at high field is highly angle dependent. There is additional structure to the data while entering and exiting the high field superconductivity. 229

(6.8) The resistance at low field at around 120 mK, showing mostly data from the 'negative' rotation direction, which as expected demonstrates similar behaviour to the usual 'positive' rotation angles. Of particular interest are the −63.5° and −83.5° rotations, which show a two-step exit from superconductivity similar to that observed in the temperature ramp. The same feature is also present at smaller angles, such as in the 26.5° data, though is more difficult to see due to the greater gradient of the resistance with field. Note that the y-axis of this graph has a split range in order to show both the superconducting state and the fine detail in the normal state. 230

(6.9) The resistance as a function of field at the $\phi = 0°$ position, at a variety of temperatures, showing the evolution of the data from the superconducting to the normal state as temperature is increased. Of specific interest are the number of features in addition to the simple transitions in and out of superconductivity, most notably the peak in the resistance at the moment rotation transition. . . . 231

(6.10) The 3F signal measured by the lock-in amplifier as a function of temperature for a variety of fields from 0 to 14 T. For a normal, Ohmic metal the 3F signal should be zero. Non-zero measurements are to be expected at a superconducting transition temperature. . 232

(6.11) The 3F signal measured by the lock-in amplifier as a function of temperature for a variety of fields from 3.5 and 8 T, between the low and high field regions of bulk superconductivity. For a normal, Ohmic metal the 3F signal should be zero. Non-zero measurements are to be expected at a superconducting transition temperature. . 234

(6.12) The resistance as a function of field, from 8 to 15 T, at the base temperature of the dilution refrigerator ($\sim$50 mK), for a number of rotation angles between 8° and 22°. The quantum oscillations have been extracted from the raw data, fitted by a smoothing average, multiplied by 10, and then superimposed onto the smooth background curve fitted to the original data. The plots have been vertically spaced for clarity but not rescaled. 236

(6.13) Shubnikov-de Haas oscillations between 14 and 17 T at the base temperature of the dilution refrigerator ($\sim$50 mK), for a number of rotation angles between 10° and 28°. A single frequency can be seen, unchanging with angle, which (after plotting against B^{-1}) corresponds to a frequency of 555 T. 237

(6.14) The Fourier transform of quantum oscillation data from 10 to 15 T, plotted against B^{-1}, for a number of rotation angles from 6° to 22°. The graph is focused on the frequency 555 T but there are no other oscillation frequencies with significant amplitude over the range 0 to 10,000 T. 238

(6.15) **Main:** The resistance as a function of field, for several low temperatures, for the high field range 13 to 17 T. The field is applied parallel to the c-axis. There are two obvious frequencies, one low, one high. The high frequency is very temperature dependent and is barely evident at the highest temperature. **Inset:** The Fourier transform of the same data, plotted against B^{-1}, showing three frequencies, around 100, 700 and 1200 T. The amplitudes of the lower two are relatively unaffected by the temperature over this range, but the amplitude of the higher frequency oscillation decreases dramatically as temperature increases, as expected from the main plot. 239

(6.16) **Main:** The capacitance divided by the field, a quantity proportional to the magnetization, plotted as a function of field at roughly 50 mK and a rotation angle of 10°. A substantially slower field ramp rate, ensuring a high data density, was employed from 10 to 17 T. For this graph the residual data, after subtraction of a smooth background curve, has been multiplied by 500 and then superimposed onto the background, which is the plotted curve. **Inset:** The residual data, fitted by a smoothing average and plotted against B^{-1}. There appears to be no periodic variation, suggesting that this may merely be a plot of random experimental noise. 240

(6.17) **Main:** The transport voltage as a function of field at roughly 50 mK and a rotation angle of 10°. A substantially slower field ramp rate, ensuring a high data density, was employed from 10 to 17 T. For this graph the residual data, after subtraction of a smooth background curve, has been multiplied by 30 and then superimposed onto the background, which is the plotted curve. **Inset:** The residual data, fitted by a smoothing average and plotted against B^{-1}. Clear oscillations are observed below about 0.11 T^{-1}. 241

(6.18) The Fourier transform of the magnetization and resistivity data presented in the insets of figures 6.16 and 6.17. The expected frequency of 555 T is marked. The Fourier transform amplitudes of both measurements are peaked at this frequency. 242

(6.19) **Left:** The resistance as a function of field, from 8 to 17 T, at $\phi \simeq 12°$ and ~ 50 mK. For this graph the residual data, after subtraction of a smooth background curve, has been multiplied by 20 and then superimposed onto the background, which is the plotted curve. **Right:** The Fourier transform of the quantum oscillation data plotted in the inset as a function of B^{-1}. The peak amplitude is at 555 T as expected. Analysing only the data above 10 T results in very little change to the FFT, but analysing the data below 10 T results in a decease of the peak amplitude to almost zero, suggesting that quantum oscillations are not detected in this field range. 243

(6.20) The capacitance as a function of field, measured with the AH bridge instrument, for a wide range of rotation angles, at dilution fridge base temperature. The stated angles are correct to within 0.5°, except for the lowest two, which are $0.1° \pm 0.05°$ and $-0.01° \pm 0.01°$. 245

(6.21) The capacitance as a function of field, measured with the AH bridge, for a range of different temperatures at $\phi \simeq -0.01°$. Measurements for both increasing and decreasing field are shown, with the up ramps in 'warm' colours and the down ramps in 'cool' colours to highlight the difference. The temperature variation is much smaller than the magnetic hysteresis. 247

(6.22) The first demodulation signal from the lock-in amplifier, measuring capacitance using the GR bridge instrument, as a function of field for several rotation angles, at 120 and 620 mK. Only the decreasing field measurements are shown, for clarity. There are two 'zoom bubbles' on the graph, showing in greater detail the oscillations due to the a.c. field modulation, which become much larger in amplitude approaching $\phi \sim 0°$. 250

(6.23) The second demodulation signal from the lock-in amplifier, measuring capacitance using the GR bridge instrument, resulting from the gradient mode modulation field, plotted as a function of rotation angle at 7 T and 620 mK, demonstrating the dramatic increase in oscillation amplitude approaching 0°. 251

(6.24) The first demodulation signal from the lock-in amplifier, measuring capacitance using the GR bridge instrument, at $\phi \simeq 0°$. Both X and Y components of the low and high temperature measurements, for both increasing and decreasing field, are plotted as a function of field. The Y signal is generally small and constant. The X signal shows the expected moment rotation transition at 12 T, and unexpected hysteresis is observed below 4 T. 252

(6.25) The second demodulation signal from the lock-in amplifier, measuring oscillations in capacitance using the GR bridge instrument, at $\phi \simeq 0°$. Both X and Y components of the low and high temperature measurements, for both increasing and decreasing field, are plotted as a function of field. At high temperature the X signal shows the expected moment rotation transition at 12 T and the large magnetic susceptibility below it. At low temperature the diamagnetic response is also present in the superconducting region. The Y signal behavior is complicated, neither small nor constant as might be expected. 253

(6.26) The second demodulation signal from the lock-in amplifier, measuring oscillations in capacitance using the GR bridge instrument, at $\phi \simeq 0°$. Both X and Y components of the 620 mK measurement are plotted as a function of field, for decreasing field only. The corresponding phase angle, θ, and total signal amplitude, R, are also plotted. The X and R signals are mostly the same, except around 10 T where the Y signal reaches a maximum. The phase angle varies greatly over the field range. 255

(6.27) The second demodulation signal from the lock-in amplifier, measuring oscillations in capacitance using the GR bridge instrument, at $\phi \simeq 1.8°$. Both X and Y components of the low and high temperature measurements, for both increasing and decreasing field, are plotted as a function of field. There is a sharp peak in the X signal at $B_R \simeq 13$ T, preceded by a large trough at low temperature due to the diamagnetic response of the superconducting state. There is also an unexpected oscillatory nature to the X component at low field, shown in more detail in the 'zoom bubble'. 257

(6.28) The second demodulation signal from the lock-in amplifier, measuring oscillations in capacitance using the GR bridge instrument, at $\phi \simeq 3.4°$. Both X and Y components of the low and high temperature measurements, for both increasing and decreasing field, are plotted as a function of field. There is a clear peak in the X signal at $B_R \simeq 14$ T. Measurements at lower field contain unexpected, large-period oscillations. The only indication of superconductivity is in the low temperature Y component. . . . 259

(6.29) The second demodulation signal from the lock-in amplifier, measuring oscillations in capacitance using the GR bridge instrument, at $\phi \simeq 4.6°$. Both X and Y components of the low and high temperature measurements, for both increasing and decreasing field, are plotted as a function of field. Similar to the graphs at other rotation angles, there is a peak at B_R, positive in contrast to the negative X signal at lower fields, and the Y signal appears to be consistently of opposite sign to the X component, except just below B_R at low temperature where there is some indication of the superconducting state. 260

(6.30) The second demodulation signal from the lock-in amplifier, measuring oscillations in capacitance using the GR bridge instrument, at $\phi \simeq 6.0°$. Both X and Y components of the low and high temperature measurements, for both increasing and decreasing field, are plotted as a function of field. Similar to the graphs at other rotation angles, there is a peak at B_R, positive in contrast to the negative X signal at lower fields, and the Y signal appears to be consistently of opposite sign to the X component. There in no evidence of superconductivity at this rotation angle. 261

(6.31) The second demodulation signal from the lock-in amplifier, measuring oscillations in capacitance using the GR bridge instrument, at $\phi \simeq 9.5°$. Both X and Y components of the low and high temperature measurements, for both increasing and decreasing field, are plotted as a function of field. The high temperature X signal is large and positive across most of the field range, dropping at high field, possibly due to the influence of the moment rotation crossover expected to be around 16.5 T. The low temperature X signal, by contrast, is negative across most of the field range. . . . 262

(6.32) The critical field for the magnetic moment rotation transition, B_R, as a function of rotation angle ϕ for the angles encountered in the main torque magnetometry dataset, with the exception of $\phi \simeq 9.5°$ for which there is no obvious indication of a transition or crossover. The position of the transition was taken as the position of the peak in the second demodulation signal for the 620 mK decreasing field measurements. A linear fit, extrapolated to 17 T, the maximum field available in this project, would suggest a crossover around 16.5 T at $\phi \simeq 9.5°$. 263

(6.33) The resistance as a function of field for the rotation angles comprising the main dataset of the torque magnetometry project, for decreasing field measurements at 120 mK and 620 mK. The low temperature data is particularly useful since it indicates the extent of the zero-resistance state of the high-field superconductivity. . . 264

(6.34) The sample resistance, and the second demodulation signal from the capacitance bridge, as a function of temperature at $\phi \sim 0.1°$ and 12 T. The oscillations in capacitance are caused by a transverse field modulation of about 6 G. The transition to a zero-resistance state occurs roughly 100 mK higher than the temperature at which the oscillations in capacitance become out-of-phase with the field modulation, i.e. a diamagnetic response, indicative of bulk superconductivity. Diamagnetism is then strengthened as temperature is decreased further. 265

(6.35) The superconducting transition temperatures, determined by the zero-resistance state and the presence of diamagnetism, plotted as a function of field at $\phi \sim 0.1°$. The position of the transition in resistance was taken as the temperature at which the resistance reaches 50% of the normal state value. There is a consistent and significant difference between the two, with the departure from the diamagnetic state generally occurring ~ 100 mK before the departure from the zero-resistance state. 267

(6.36) The second demodulation signal as a function of field at 620 mK. **Main:** Measurements in modulation and gradient mode, where both have the same transverse field modulation applied. In field gradient mode an apparently unsuccessful attempt has been made to eliminate any field modulation at the sample, resulting in a peak at the moment rotation transition at approximately 15 T. **Inset:** The modulation mode data has been halved such that the peak high is roughly the same as in the gradient mode data. The difference between the curves is possibly entirely due to the effects of the field gradient. 269

(6.37) The second demodulation signal as a function of field from 9 to 15 T for various different ratios of the current supplied to the field modulation magnet coils operating in gradient mode. The current in coils 1 & 3 was fixed at 52 mV $\rightarrow$ 0.62 A and the current in coils 2 & 4 was as indicated by the legend (1 V $\rightarrow$ 12 A). Zero field modulation was picked up by the angle sensors at 23 mV input to the coils 2 & 4 power supply. The rotation angle was $\phi \sim 2°$. The expected signal at 15 T for a pure field gradient was around 8 μV. The temperature was roughly 600 mK, ensuring that the sample was in the normal (rather than superconducting) state. 270

(6.38) **Top:** The component of magnetization perpendicular to the field, as a function of field, for various rotation angles, showing the sudden decrease expected at the moment rotation transition, which moves to higher field as the rotation angle increases. **Bottom:** The derivative of the plots above, thus showing the transverse susceptibility $\partial B_x/\partial B_z$, which peaks at the moment rotation transition. 272

(A.1)Estimates of the Curie temperature as determined by the various methods outlined in section 5.1, for each experimental run. The weighted average taken as the final result is highlighted in red. . . 289

(A.2)Estimated values of T_X and H_X as determined by the various methods outlined in section 5.2, for each experimental run. The literature values corresponding to the calculated Curie temperatures shown in red in figure A.1, sourced from [18], are also listed. The T_X values plotted on the phase diagram shown in figure 5.14 are highlighted in red. 290

(C.1) An example of attmpting to fit the magnetoresistance to the two-band model described by equation 2.28. The $\omega_c\tau = 1$ point implied by the fit, which is obviously invalid, occurs mid-way though the field range, transitioning from the low field limit, where 2.28 is defined and the magnetoresistace is supposedly quadratic, to the high field limit, where the magneotresistance supposedly begins to saturate. The actual data appears to be simply linear, however, with neither quadratic field dependence at low field nor saturation of the magnetoresistance at high field. The conclusion therefore is that the model is incorrect and cannot accurately describe the experimental evidence. More sophisticated models that can give rise to linear magnetoresistance will be required. 298

Chapter 1

Introduction

Superconductivity was first discovered over a century ago but the phenomenon is yet to make a truly significant contribution to modern technology, hampered by the major restraint of requiring very low temperatures for its existence. Indeed the standard theory for conventional superconductors, the BCS theory, places an upper limit of about 30 K on the phenomenon, a temperature not even high enough to reach using common cryogens like liquid nitrogen.

The discovery in the 1980s of so-called unconventional superconductors, materials for which the BCS theory fails to properly explain the emergence of superconductivity, abolished this upper limit and superconductors with critical temperatures beyond 100 K were soon synthesized, comfortably above the 77 K boiling point of liquid nitrogen.

Unfortunately the trend to higher temperatures stalled well short of ambient conditions and the goal of a room-temperature superconductor remains the ultimate prize for the field (at present the record is around 140 K at ambient pressure). However, superconductivity is useful enough that even burdened with the complications of using liquid nitrogen the newly discovered superconductors swiftly found a home in a number of technological applications, by far the most common being extremely powerful and efficient electromagnets.

Superconductors are metals with zero resistance. Not just very low resistance, not even extremely low resistance, but exactly zero. This means that they can carry electric currents without dissipation, a bit like a perpetual motion machine for electrons, allowing the current to move through the wire without losing energy.

An electric current established in a coil of superconducting wire will circulate forever, without producing any heat, generating a steady magnetic field without the need for a power supply.

Conventional electromagnets, made from copper wire, are limited in the strength of magnetic field they can produce by resistive heating: if the current gets too high the copper will overheat and melt. This is also a major limitation in modern computing, where resistive heating holds back computing power by the necessity to avoid catastrophically melting silicon chips.

Unfortunately, despite being free of the heating constraint, superconductors still have a limit on the current that can be used and therefore on the magnetic field that can be produced. In fact it is a major and inescapable (and arguably somewhat amusing) problem within the realm of superconductivity research that, while the main technological use of superconductors is to make powerful magnets, strong magnetic fields destroy superconductivity.

The material almost always used in commercial superconducting wire is commonly called YBCO, and its popularity is essentially due to a combination of being superconducting at liquid nitrogen temperature but also having a high critical current and a correspondingly high magnetic field at which it ceases to be a superconductor and becomes a normal metal. There are materials that are superconducting to much higher temperatures, and materials that can be manufactured more easily, but the importance of having a high critical current cannot be overlooked.

Following this brief introduction it should be clear that although reaching a room-temperature superconductor is perhaps the supreme goal of the field another major avenue of research is into extending the maximum achievable magnetic field, and it is the latter pursuit that this PhD thesis describes.

Specifically this PhD research contributes to the exploration of one particular idea for solving the problem of the restrictive limit on the magnetic field. The idea is to create a superconductor from a magnetic material, the logic being that if magnetism is inherent to the material and superconductivity coexists harmoniously with it then that type of superconductivity will be immune to the destructive effects of high magnetic fields.

The compounds UGe_2 and URhGe were the first two such materials discovered, at the very beginning of the 21st century, compounds where superconductivity

and magnetism are cooperative phenomena, rather than antagonistic, and the presence of magnetism in the material is actually necessary for the occurrence of the superconducting state. How superconductivity arises in these compounds is still poorly understood however, since conventional theory strictly forbids the electronic state found in the magnetic phases of UGe_2 and URhGe.

The experimental investigation into UGe_2 described in this thesis involves the use of Hall effect measurements to probe the electronic structure of the material around the region of the pressure-temperature phase diagram where superconductivity emerges, while the investigation into URhGe aims to probe the magnetic properties of the material around the superconducting regions of its magnetic field-temperature phase diagram.

This introduction will henceforth shift to a higher level of scientific language and any reader unfamiliar with the physics of magnetism and superconductivity is referred to chapter 2 for the background theory, and the references listed at the start of section 2.6 in particular.

The theory for conventional superconductivity involves pairing electrons with opposite spin, creating composite quasi-particles called Cooper pairs. In high magnetic fields it becomes energetically favourable for electron spins to align with the field and so the electron in the Cooper pair oriented anti-parallel to the field will eventually, as the field strength increases, flip to align parallel to the field and enter the same spin state as the other Cooper pair electron, thus breaking the opposite-spin pairing mechanism and destroying superconductivity. This is called the Pauli limit of the magnetic field.

In an itinerant ferromagnet the conduction electron spins are all already aligned parallel to one another and creating a Cooper pair from these electrons, an equal-spin pairing, will therefore avoid the Pauli limit, allowing superconductivity to persist to much higher fields. Such equal-spin Cooper pairing is not covered by the conventional BSC theory however, and the usual mechanism for electron pairing, mediated by phonons and the positive ions of the lattice, is no longer expected to be applicable.

Thus although ferromagnetic superconductivity is observed to exist empirically, the electron pairing mechanism is still not known for sure. A good review of the topic is provided in Ref. [1] and the key figure from the article is reproduced here in figure 1.1. The essential point is that equal-spin paring can be mediated by spatial fluctuations in the magnetization of the material, much the same as

phonon mediated superconductivity relies on spatial fluctuations in the density of positive change. In both cases the requirement is that a single electron can affect the background conditions of the material in such a way that it attracts a second electron, coupling the momentum states of the two.

Materials right on the edge of a ferromagnetic phase transition are the perfect candidates for this type of electron pairing, where the system is very easily polarized by the spin of an itinerant electron. It is energetically favourable for a conduction electron to be in a region of high polarization, and will essentially feel an attractive force to the space polarized by the presence of another conduction electron, leading to what is effectively an attractive interaction between the two itinerant, negative charges (which would otherwise repel each other due to the Coulomb interaction).

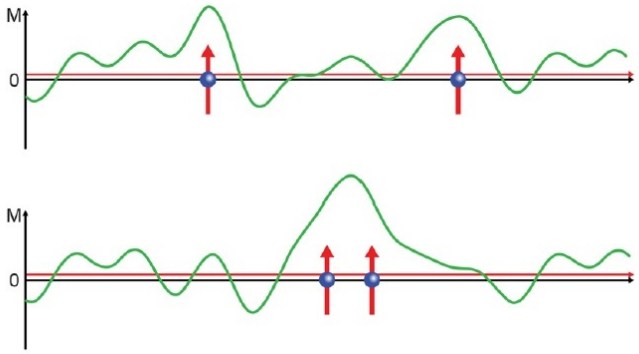

Figure 1.1 A figure from Ref. [1]. The original caption reads: "Cartoon of the pairing interaction due to magnetic fluctuations. The magnetization (green line) has a small nonzero average (the red line) plus a large fluctuating part. Two conduction electrons induce local polarization clouds. If the two electrons are separate (top panel) their energy is higher than if they share the same polarization cloud (bottom panel), thus it can be energetically favorable for them to be paired."

In Ref. [1] the author refers to a "shared polarization cloud" that results in it being energetically favourable for the equal-spin electrons to be paired, and also points out that ferromagnetic superconductivity may be expected close to a quantum critical point (QCP), where magnetic fluctuations are maximised but the temperature at the border to the ferromagnetic phase is very low (theoretically at absolute zero), ideal for the emergence of superconductivity.

Both UGe_2 and URhGe have a ferromagnetic transition at low temperature and in both the transition temperature can be driven even lower, toward absolute zero, by applying either pressure or magnetic field in the case of UGe_2 or URhGe respectively. Hence these materials would appear to be ideal ferromagnetic

superconductor candidates and indeed superconductivity is found to exist for both in the region of their phase diagram surrounding a QCP.

The superconducting state in UGe_2 emerges below 700 mK at high pressure, around the QCP at about 12.5 kbar, the point at which the temperature of a metamagnetic transition between two different ferromagnetic states (called FM1 and FM2) is reduced to absolute zero. The exact nature of the FM1 and FM2 states and the fundamental differences between them is as yet unknown. The transition is characterised by a sudden and substantial change in magnetization, with the low pressure phase being the more strongly polarized, and it is presumably the magnetic fluctuations between these polarization states that provides a foundation for the electron pairing mechanism.

UGe_2 is an itinerant ferromagnet (though there is also a local character to the magnetism, as discussed in sections 2.2 and 2.6) where the same $5f$ conduction electrons responsible for magnetism are also those involved in superconductivity and bound together in Cooper pairs. Thus to understand the nature of the FM1 and FM2 states it is necessary to understand the nature of the conduction bands of the material, or in other words the Fermi surfaces of the charge carriers. By understanding how the Fermi surfaces change crossing the phase transition between FM1 and FM2 it should elucidate the nature of the magnetic fluctuations responsible for superconductivity and provide more information about how the electrons are paired.

Hall effect measurements probe, somewhat indirectly (see section 2.1), the Fermi surfaces of a metal, though for gathering information across a large region of the pressure-temperature phase diagram the combination of Hall effect and magnetoresistance measurements is actually the most effective probe available.

The key findings of this PhD research are that there is a order-of-magnitude jump in the ordinary Hall coefficient crossing the FM1-FM2 transition as a function of temperature on the low pressure side of the QCP, but a very different change in the Hall coefficient crossing the QCP as a function of pressure, with a change in sign and magnitude crossing from FM1 to FM2. Furthermore, the same sign change is seen crossing the critical pressure at higher temperature, up to about 12 K, between what was previously expected to be the same FM1 phase.

Such dramatic changes in the Hall coefficient (both in magnitude and sign) are associated with significant Fermi surface reconstruction, though there is as yet insufficient information available to settle on a specific theory. As discussed

in chapters 2 and 7, a Lifshitz transition or a substantial alteration in the Kondo coupling strength are the likely causes of the observed changes in the Hall coefficient around the QCP. Regardless of the cause, such changes indicate major differences in the electronic structures in three regions of the phase diagram that converge at the point where superconductivity emerges, clearly suggesting that fluctuations between them are responsible for the electron pairing mechanism in UGe_2.

The superconducting state in URhGe emerges below 450 mK at high field, applied in the *b*-axis direction, around the 12 T critical point where the ferromagnetic transition temperature is reduced to absolute zero and also where the easy axis of magnetization suddenly switches from *c* to *b*. Fluctuations associated with this easy axis rotation transition are expected to be responsible for the electron pairing mechanism in this case.

Probing the rotation of the easy axis requires measuring the magnetization parallel to both the *b* and *c* axes while sweeping the field past the quantum critical point and additionally probing the fluctuations, i.e. how easy the system is to polarize, which requires measuring the magnetic susceptibility for both directions too.

There are several methods routinely used to measure the magnetic properties of a material at low temperature and high field: neutron scattering, SQUID magnetometry (both a.c. and d.c.), vibrating sample magnetometry, a.c. induction methods, or torque magnetometry. All of these can be discounted as unsuitable for the conditions required to investigate URhGe. Firstly a.c. susceptibility cannot provide vectorial components of the magnetization, or indeed provide magnetization in addition to susceptibility, which can be very different quantities in a ferromagnetic superconductor. SQUID magnetometry *can* provide vectorial components with the required precision but is very difficult to use at dilution refrigerator temperatures and simply does not work up to fields such as the 17 T maximum utilized in this PhD research. Vibrating sample magnetometry has similar difficulties operating at dilution fridge temperatures and in any case lacks the high precision required. Neutron scattering similarly cannot meet the requirements for vectorial decomposition of the magnetization and susceptibility to high precision at ultra low temperatures and high fields.

The only suitable technique remaining from the list is torque magnetometry, although achieving the aforementioned vectorial decomposition of both the

magnetization and the susceptibility is still a challenge. In fact the technique for determining all those quantities simultaneously while also applying a field like 17 T is yet to be described in scientific literature and the main achievement of the PhD project on URhGe described in this thesis was to develop such a technique.

The chosen methodology was capacitive torque magnetometry, using a passive capacitance bridge and lock-in amplifier double demodulation techniques in combination with three pairs of modulating magnets in addition to the main field, as detailed in section 2.5 and chapter 4. Simultaneous magnetoresistance measurements were performed on the sample, which could also be rotated with respect to the field to 0.01° precision.

A range of successful measurements demonstrate proof-of-concept of this technique and the constructed capacitive torque magnetometer but unfortunately the main objective, to probe the magnetic fluctuations in URhGe at the quantum critical point, was not achievable in the timeframe of the project, predominantly because the magnetization becomes difficult to measure by such methodology in the presence of divergent susceptibility, precisely as encountered around the QCP in URhGe.

However, the presence of such large susceptibility could be taken as a conclusion in itself, as providing evidence that there are indeed large magnetic fluctuations at the critical point at which superconductivity emerges. Furthermore, over the course of the many experimental iterations that provided the necessary incremental improvements to the newly developed technique, a great number of measurements incidental to the main objective were performed and initial data analysis reveals some interesting observations.

These observations are summarised in chapter 7, the main conclusions, but one that stands out is a disparity between the zero-resistive state and the bulk superconducting state as probed by the susceptibility, a disparity that in conjunction with a number of other observations suggests the presence of domain wall superconductivity, although significantly more work would need to be done to advance that suggestion into a firm conclusion. Nevertheless, such observations point toward potentially fruitful avenues for future research into URhGe and chapter 7 also lists a number of improvements to the developed torque magnetometry technique that should provide results for the main objective of the project too.

The remainder of this chapter is split into four sections consisting of brief

literature reviews for UGe_2 and URhGe, each preceded by a quick-reference list of "essential facts" about the materials.

In chapter 2 the background theory of ferromagnetic superconductivity is covered as well as the necessary background for the two main experimental projects, i.e. an introduction to electronic transport theory with a specific focus on the Hall effect and magneotresistance and a full mathematical description of modulated, two-component capacitive torque magnetometry. The specific experimental methodology employed in the UGe_2 and URhGe projects is then detailed in chapters 3 and 4 respectively, and the results and accompanying discussion for each are presented in chapters 5 and 6 respectively.

Finally a general conclusion of the thesis is provided in chapter 7, followed by more technical, detailed conclusions for each project.

1.1 UGe_2 Essential Facts

- UGe_2 has an orthorhombic crystal structure with space group *Cmmm* and lattice parameters $a = 4.0089$ Å, $b = 15.0889$ Å, $c = 4.0950$ Å.[19]
- The material is paramagnetic (PM) at room temperature and ferromagnetic (FM) below 53 K at ambient pressure, with the Curie temperature T_C driven to zero by application of critical pressure $P_C \approx 16$ kbar.
- At high pressure two different FM ground states emerge: a higher temperature 'weakly polarised' FM1 phase and a lower temperature 'strongly polarised' FM2 phase, where the FM1-FM2 transition temperature T_X is driven to zero at critical pressure $P_X \approx 12.5$ kbar. At pressures lower than the critical end point (CEP) at $P_{CEP} \approx 11.6$ kbar the phase transition becomes a broad crossover.
- Both FM1 and FM2 phases have spontaneous magnetization along the *a*-axis, with ordered moments 0.9 μ_B/U and 1.4 μ_B/U respectively.[20] The *b* and *c*-axes are relatively hard, with anisotropy field $\sim$100 T.
- The FM1-FM2 transition is first order, as is the FM-PM transition at pressures close to P_C, however the FM-PM transition becomes second order at pressures below the tricritical point (TCP) at $P_{TCP} \approx 14$ kbar.[6]
- Application of magnetic field shifts the first order transitions to higher pressures, resulting in the so-called 'wing structure' seen in the pressure-temperature-field phase diagram in figure 1.6. These wings terminate at quantum critical end points (QCEP), where the critical end points of the transitions are driven to zero kelvin by application of field.
- Superconductivity (SC) is found to exist within the ferromagnetic state at pressures around 12 kbar. The transition temperature is greatest very close to P_X, where $T_{SC} \approx 0.8$ K, and decreases either side of the critical pressure, thus suggesting a strong link between the FM1-FM2 transition and the emergence of SC. The superconducting region terminates at P_C, suggesting the co-operative existence of FM and SC and that ferromagnetism is likely an essential requirement for this type of superconductivity.[21]
- The SC pairing is of *p*-wave, spin triplet type, likely mediated by magnetic fluctuations around the unconventional quantum critical point at P_X, though the exact nature of the pairing mechanism is as yet unknown.

1.2 UGe_2 Literature Review

Recent interest in UGe_2 begins around the turn of the millennium. In 1998 Oomi *et al* sketched out a pressure-temperature phase diagram by plotting two features in the temperature derivative of the resistivity, one at the Curie temperature and one characterised by a broad peak in $\partial\rho/\partial T$ at a lower temperature later referred to in the literature as T_X.[22] Both critical points seem as though they can be driven to zero kelvin by the application of pressure.

Thorough investigation of these potential quantum critical points led to the discovery, announced in 2000 in Ref. [23], of the coexistence of ferromagnetism and superconductivity in UGe_2 just below the critical pressure at which the Curie temperature reaches zero kelvin, providing "a new, and apparently unique, example of superconductivity in the field of magnetism." It was proposed that a p-wave, spin-triplet electron pairing mechanism was responsible for the presumably magnetically mediated superconductivity, though the exact nature of the mechanism was (and arguably still remains) unclear.

A "more extensive and substantial account of some of the experimental data reported or referred to" in Ref. [23] was subsequently published in Ref. [21], providing evidence to confirm that ferromagnetism and superconductivity were both bulk properties of the material and so did indeed physically coexist. It was proposed that the metamagnetic transition defined by T_X was intimately related to the emergence of superconductivity in UGe_2 and may be associated with the appearance of coupled charge and spin density wave (CSDW) order, although no evidence of a CSDW transition was observed in neutron scattering experiments.

In 2001 bulk superconductivity was independently confirmed in Ref. [19] by specific heat measurements, and Ref. [24] announced the occurrence of the SC state in polycrystalline materials with mean free path smaller than the coherence length, suggesting that high-purity specimens are not strictly necessary in order to observe superconductivity in UGe_2.

Also in 2001, Tateiwa *et al* searched for a CSDW state in UGe_2 around T_X but found no experimental evidence of such ordering.[25] A good discussion of charge density and spin density waves in UGe_2 can be found in Ref. [26], taking band structure calculations by Shick and Pickett published in Ref. [3] as a starting point. These calculations suggest that the main Fermi surface is a roughly

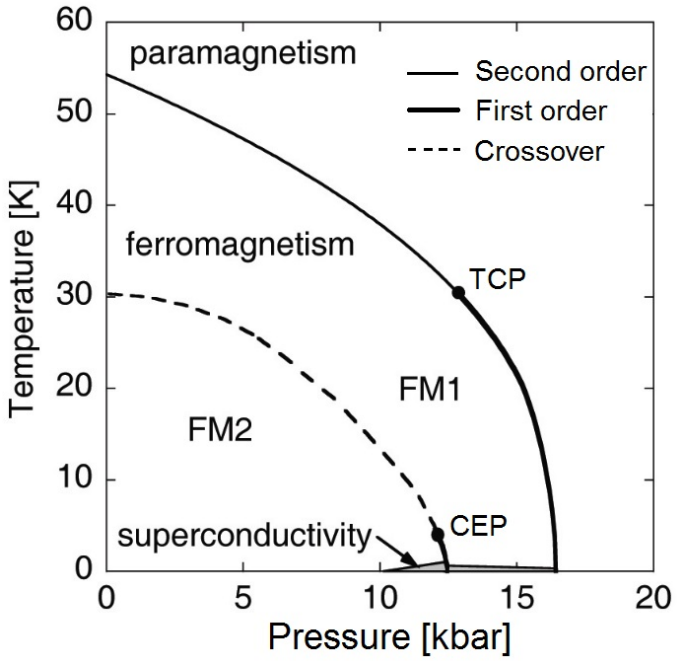

Figure 1.2 The pressure-temperature phase diagram of UGe_2 showing the transitions from paramagnetism (PM) to ferromagnetism (FM) and the lower temperature transition within the ferromagnetic state between the strongly polarised FM2 phase and the weakly polarised FM1 phase. The FM1-FM2 transition is only a true phase transition up to a critical end point (CEP) at 7 K beyond which it becomes a broad crossover. The PM-FM transition is second order at low pressure but becomes first order at a tricritical point (TCP). The superconducting transition temperature peaks at 0.8 K around the critical pressure at which the FM1-FM2 transition occurs at absolute zero. Source: Ref. [2]

cylindrical sheet with axis parallel to the crystallographic b-axis (see figure 1.3).

As stated in Ref. [26], this means that the majority spin band Fermi surfaces are nearly nested in the a and c axis directions. In general, parallel section of Fermi surface look quasi-1d in the nesting vector direction, where the nesting vector is thus similar to the momentum-space vector of the well-known Peierls distortion, which results in a new periodicity for any 1d chain of atoms. The distortion is energetically favorable: the nesting vector joins Fermi surface points such that a gap opens at the Fermi surface and lowers the occupied states in energy. For parallel sections of 2d surfaces, many points on the surface can be joined by the same nesting vector, and a charge density wave can form at that momentum-space vector. If there are spins on the lattice points as well as charge, then a coupled CSDW state can arise.

Ref. [26] looks at the lattice entropy observed by specific heat measurements and at temperatures around T_X there seems to be some extra entropy that could be

ascribed to CSDW formation, though it may possibly be some other degree of freedom. The presence of a CDW in α-uranium, which zig-zag chains of uranium atoms similar to UGe_2 (see figure 1.8), suggests that CDW formation in UGe_2 is likely however. Also, the disappearance of CSDW order at the transition from FM1 to FM2 would remove a source of conduction electron scattering, thus lowering the resistivity, as indeed characterises the transition at T_X.

The possibility of CSDW order is relevant for ferromagnetic superconductivity because of the magnetic fluctuations present in a system on the border of a potential CSDW state. As Shick and Pickett put it in Ref. [3], the "roughly nesting portions of quasi-2D surfaces should promote strong magnetic interactions between spin majority carriers" and they conclude that this potential for longitudinal magnetic fluctuations, with reference to the theory by Fay and Appel[27] discussed in section 2.6, "supports the likelihood of magnetically mediated p-wave triplet pairing."

An interesting point regarding magnetoresistance studies on UGe_2 is that the required sharp turns in the the Fermi surface resulting from the nesting conditions necessary for CDW formation should lead to linear-in-field magnetoresistance, as discussed by Pippard in Ref. [28] for the model of a square Fermi surface, and such behaviour is indeed observed in the resistivity measurements presented in this thesis in chapter 5.

The first pictures of the Fermi surface of UGe_2 were actually published in 1993,[29] though at that time there was much confusion in the literature over the space group, the crystallographic axes and the lattice parameters, and so the results are not particularly useful. Specifically, in many early publications in the field (those from the 1990s mostly) the a and c axes are swapped, such that the easy magnetization axis is stated as the c-axis instead of the correct a-axis. Nevertheless, an interesting statement from Ref. [29] with reference to earlier de Haas-van Alphen (dHvA) measurements by Onuki *et al*[30] is that these initial results find UGe_2 to be a compensated metal, as expected.

The aforementioned study by Shick and Pickett, published 8 years later in Ref. [3], aimed to repeat the calculations of Ref. [29] using the updated crystal structure and the correct lattice parameters, and also attempted to include the effects of the interplay between magnetism and spin orbit coupling (SOC) in UGe_2. The authors state that it is "crucial" to use the correct easy axis orientation because of the big differences in the calculated Fermi surface structure after inclusion of

the the magnetocrystalline anisotropy, due to the anisotropy in the interplay of strong SOC and the large exchange splitting.

The strong magnetocrystalline anisotropy in UGe_2, 2∼3 orders of magnitude larger than typical for 3d ferromagnets, reflects the strong SOC for $5f$ electron states. The calculated Fermi surface is complex and consists of three sheets. The largest and "most interesting" sheet is shown in figure 1.3, and is quasi-2d as mentioned earlier in relation to CSDW formation.

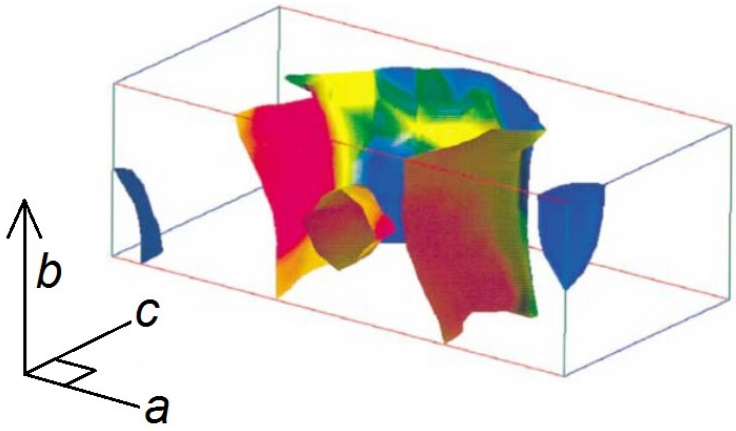

Figure 1.3 A sketch of the calculated Fermi surface of UGe_2. Note that only a half-length of the Brillouin zone is shown for the c-axis direction in order to show a cross-section through the centre of the main, roughly cylindrical Fermi surface, which has its axis parallel to b. Source: Ref. [3]

Measurements of dHvA oscillations in a.c. susceptibility by Terashima *et al* are presented for field parallel to the b-axis in Ref. [31] and for field parallel to the a-axis in Ref. [4]. For the former, three main frequencies are found (at ambient pressure) and labelled α, β and γ, with frequencies $F_\alpha = 6800$ T, $F_\beta = 7710$ T and $F_\gamma = 9130$ T. The strongest frequency is β with an estimated 29% of the cross-sectional area of the Brillouin zone, and this is attributed to the extremal orbit (see section 2.4 for a description of the dHvA effect) of the majority-spin, cylindrical sheet found by band structure calculations.

The oscillation amplitude of the β frequency is reduced as pressure is increased beyond 11 kbar, and at 13 kbar there is a measured enhancement of the effective mass, both of which could be related to passing the FM1-FM2 quantum critical point, although the pressure increments of this study are too large, and thus the data-point density in the critical region of the phase diagram too low, to attribute the observed changes to the QCP with certainty. It is worth noting, however, that Tateiwa *et al* also reported an enhancement of the effective mass

near P_X, as determined by a peak in the T^2 coefficient of the resistivity around the critical pressure.[19]

The other study by Terashima *et al*, for field parallel to the easy magnetization axis, the *a*-axis, found a number of different frequencies all below 1600 T.[4] These are shown in figure 1.4. The authors state that they are awaiting reliable band structure calculations for high pressure that can match these frequencies to a model of the Fermi surfaces. In contrast to the other results (those for field parallel to the *b*-axis) the amplitudes of these oscillations seem to vary continuously with pressure across P_X and beyond, up to 17.7 kbar, past even the transition to paramagnetism where there is a dramatic change in the dHvA spectrum for the *b*-axis results.

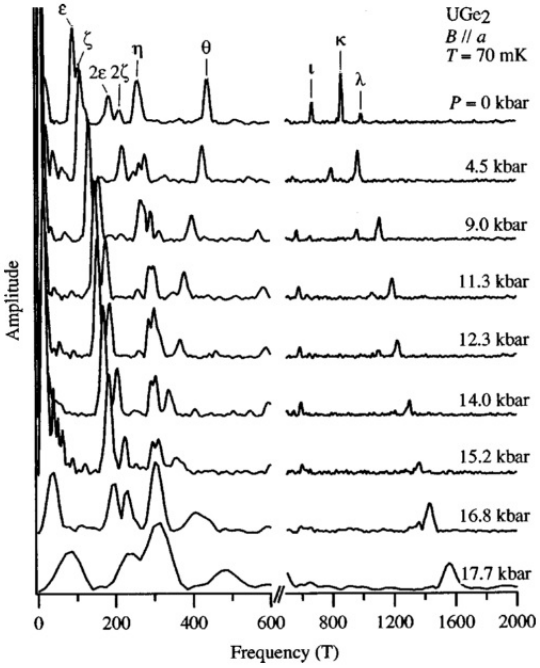

Figure 1.4 The quantum oscillation frequencies found from a.c. susceptibility measurements and the de Haas-van Alphen effect for magnetic field applied parallel to the *a*-axis in UGe_2, the easy axis of magnetization, for a number of different pressures passing both P_X at 12.5 kbar and P_C at 16 kbar. Source: Ref. [4]

A different dHvA study, by Settai *et al* published in 2002,[5] provides the Fermi surface pictures shown in figure 1.5. Similar to the results from Terashima *et al*, for field applied parallel to the *b*-axis, three main frequencies were identified from the measurements and labelled α, β and γ. Adding information from the band structure calculations detailed in Ref. [32] to these measurements allowed the authors to sketch out the Fermi surfaces for the ferromagnetic state, as presented in figure 1.5.

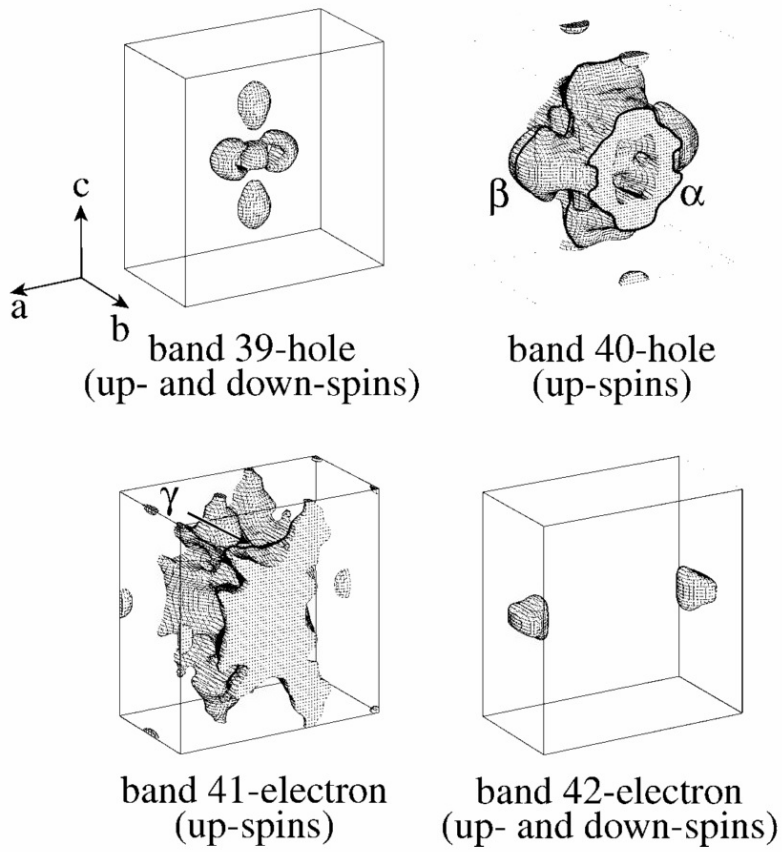

Figure 1.5 Sketches of calculated Fermi surfaces in the ferromagnetic state of UGe_2, highlighting in particular the extremal orbit related to the β frequency found in quantum oscillation measurements, related to the roughly cylindrical Fermi surface sheet with axis parallel to the crystallographic b-axis. Source: Ref. [5]

At present these are probably the most complete models of the Fermi surface of UGe_2 available but they still contain insufficient information to make a reasonable estimate of the Hall coefficient for comparison with the experimental results obtained in this PhD research (as discussed in section 2.3), especially as the low frequency dHvA oscillations measured by Terashima *et al* for field parallel to the a-axis are yet to be incorporated into any sketches such as these. A fair statement would thus be that the complete Fermi surface of UGe_2, and in particular the details of how it changes between the FM1 and FM2 phases, is as yet undetermined.

Moving on from studies of the Fermi surface and returning to a review of the literature in general, the two metamagnetic transitions in UGe_2 were investigated in 2002 by resistivity measurements in Ref. [33] and the determined values of H_X are found to be related to the values of the upper critical field

for superconductivity, prompting the conclusion that "these results support the notion that critical fluctuation due to the disappearance of T_X causes superconductivity".

A comprehensive study of the magnetization at various pressures and temperatures is presented in Ref. [18], which notes that the transition at P_X is of first-order and thus lacks the characteristics of a conventional QCP. The FM1-FM2 transition at H_X is observed to occur at a constant, pressure-independent value of magnetization, suggesting "a particular spin splitting between the majority and minority spin bands as would occur when the Fermi-energy passes through a sharp maximum in the electronic density of states for one spin direction," and that the SC pairing could also be associated with such a spike in the density of states.

The possibility that the emergence of SC may be related to the FM domain size and structure is raised in Ref. [34], measuring jumps in magnetization attributed to very small domains. The presence of a domain structure can favor the coexistence of FM and SC since "if the domains are adversely oriented then internal molecular fields due to the FM can be canceled out in the scale of the coherence length." Moving into 2003, neutron scattering experiments probing the magnetic excitation spectrum are presented in Ref. [2], providing further support for the scenario of magnetically mediated superconductivity.

In 2004 a Hall effect study on UGe_2 was published,[35] basically carrying out the investigations of this PhD project but only at ambient pressure and for field applied parallel to the c-axis rather than the easy axis. Nevertheless, the measured behaviour of the Hall coefficient mostly agrees with the results presented in this thesis, essentially showing the same increase in the single-band carrier concentration when decreasing temperature through T_X.

The conclusions of Ref. [35] are that this result suggests a sudden delocalisation of some part of the uranium $5f$ electrons below the critical temperature, and that the behavior of the anomalous Hall coefficient suggests that both the side-jump and skew scattering mechanisms are present, as in itinerant-electron ferromagnets, implying that the Fermi surface above T_X contains fewer itinerant $5f$ electrons due to hybridisation of local moments and conduction electrons but that in the lower temperature phase this hybridisation is destroyed or suppressed.

The next flurry of publications relevant to this thesis begins in 2010 with Ref. [36], which presents precise resistivity measurements outlining the wing structure in

the pressure-temperature-field phase diagram defined by the CEP lines extending from the TCP to the QCEPs. An interesting observation is the change in the anomaly in $\partial\rho/\partial T$ at the Curie temperature, which morphs from a peak at low pressure to a trough at pressures just above the TCP, indicating the switch from a second order to a first order transition. Similar results are presented in this thesis in figure 5.13.

The phase diagram presented in Ref. [36] also gives a useful indication of the width of the crossover associated with T_X by comparing results from thermal expansion measurements and resistivity measurements, where the two converge approaching P_X in a similar manner to the phase diagram constructed in this thesis, shown in figure 5.14. By the same author, Ref. [6] outlines the wing structure for the FM1-FM2 transition too and presents the phase diagram reproduced here in figure 1.6.

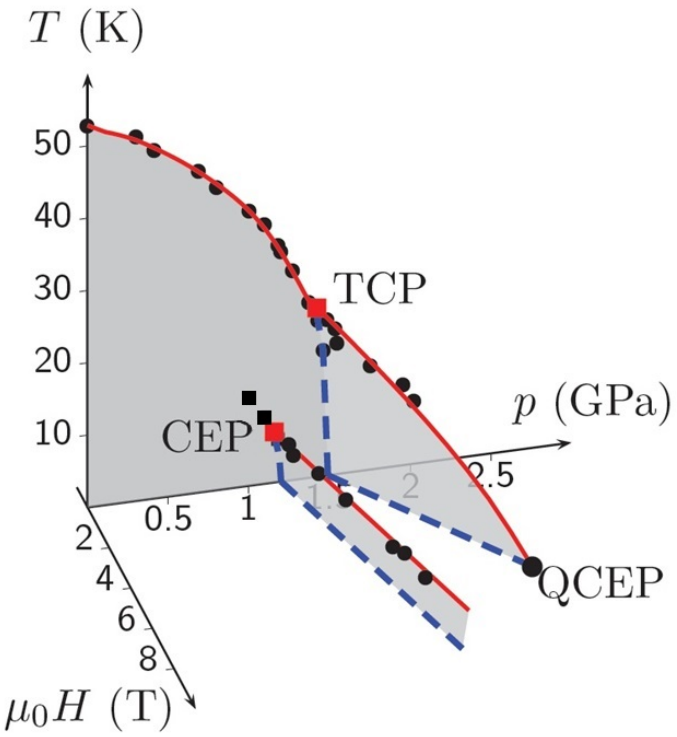

Figure 1.6 The pressure-temperature-field phase diagram of UGe_2 showing one side of the wing structure that extends from the CEP and the TCP, with the latter decreasing in height until reaching zero at a quantum critical end point (QCEP). By contrast the CEPs for the wing associated with the FM1-FM2 transition seem to remain relatively constant at 7 K. At very, very high field this wing may also reach a QCEP, though such a point has yet to be measured. Source: Ref. [6]

In 2011 Ref. [20] reported on further resistivity measurements detailing the wing structure, specifically aiming to reach the QCEP of the first order FM-PM

transition. The authors note that "the QCEP is clearly distinguished, by the lack of spontaneous symmetry breaking, from a conventional quantum critical point, which is a second order phase transition at 0 K." They also study the Hall resistivity but note that "quantitative analysis is difficult due to the lack of absolute magnetization data", which is a common problem encountered while measuring measuring ferromagnets where a large anomalous Hall effect is present. The main conclusion is that the QCEP is expected to be located around 36 kbar and 18 T.

A 2012 publication on the dualism of the $5f$ electrons in UGe_2 presents various experimental evidence to support the idea that the $5f$ electrons have simultaneously both a local and itinerant nature.[37] The broad, negative minimum in the transverse resistivity is also taken as a signature of CSDW fluctuations around T_X, however the authors note that "a SDW phase has not been detected so far in UGe_2, e.g. by neutron scattering."

Finally, an inelastic neutron scattering study, reported in 2014,[38] attempts to verify whether longitudinal magnetic fluctuations at the FM1-FM2 transition could be responsible for the SC electron pairing but, as in all previous literature, concludes that neutron scattering "does not reveal ferromagnetic spin fluctuations at T_X" and points out that muon spin rotation and relaxation measurements[39] published in 2010 suggest that the FM1-FM2 transition is likely due to the behaviour of the conduction electrons (which are not detected by the neutron scattering experiment).

1.3 URhGe Essential Facts

- URhGe has an orthorhombic crystal structure with space group *Pnma* and lattice parameters $a = 6.8752$ Å, $b = 4.3310$ Å, $c = 7.5076$ Å.[40]

- The material becomes ferromagnetic below an ambient pressure Curie temperature of 9.5 K, with spontaneous moment 0.42 μ_B/U, and then becomes superconducting below 0.25 K, with bulk coexistence of both states.

- Like UGe_2, URhGe is a heavy fermion compound and the uranium $5f$ electrons, simultaneously local and itinerant in nature, are responsible for both magnetism and superconductivity, likely with p-wave, spin-triplet electron pairing.

- Unlike UGe_2 however, application of pressure increases T_C and the SC transition temperature falls to zero at around 30 kbar.[41]

- Instead application of magnetic field in the b-axis direction reduces the Curie temperature at ambient pressure, driving T_C to zero around 12 T. Although the superconductivity is weakened by the field and disappears at 2 T, it re-emerges between 8 and 13 T, with the transition temperature peaked at 450 mK around 12 T, the point at which $T_C \to 0$ K.

- In the absence of field the c-axis is the easy axis of magnetization. The a-axis is magnetically hard by comparison but applying field in the b-axis direction leads to a gradual rotation of the magnetic moment away from c and towards b. At the critical point at 12 T the easy axis switches from c to b, leading to a sudden shift in magnetization referred to as the 'moment rotation transition'.

- This transition, at critical field B_R, appears to be intimately associated with the emergence of the high-field superconductivity, as well as related to suppression of the Curie temperature to absolute zero.

- Similar to UGe_2, the FM-PM transition, second order under ambient conditions, becomes first order at a tricritical point before T_C reaches zero, resulting in a familiar wing structure in the phase diagram, and superconductivity extends out towards the two QCEPs.[9]

- With rotation of the tuning field in the b-c plane, by some angle ϕ away from b-axis alignment, B_R is shifted to higher fields faster than simply $12/\cos(\phi)$ tesla but the transition becomes a crossover once the QCEP is passed at about $\phi \sim 5°$.

- Longitudinal (or possibly transverse) magnetic fluctuations surrounding B_R are hypothetically responsible for electron pairing and the emergence of superconductivity, though as in UGe_2 this is yet to be confirmed and the exact nature of the pairing mechanism is still unknown.

- One of the remarkable qualities of the high-field superconductivity in URhGe is its robustness to field applied in the a-axis direction. The superconducting state has been measured in magnetic fields up to 35 T and likely persists to even higher, with the upper critical field sharply peaked at the moment rotation transition.[9]

1.4 URhGe Literature Review

The discovery of superconductivity at ambient pressure in URhGe was announced in 2001,[42] just one year after UGe_2 (and to complete the current family, ferromagnetic superconductivity in UCoGe was announced[43] in 2007). The superconducting transition temperature was reported as 250 mK, which is much the same as for modern, high purity samples even though Ref. [42] used polycrystals for their measurements due to an inability at the time to synthesize single crystals with a high RRR. This meant that the reported upper critical field, of just 0.7 T, was substantially lower (due to the magnetocrystalline anisotropy) than the maximum 2 T observed later, as in figure 1.7 for example. Specific heat measurements presented in Ref. [42] verified that the superconducting transition was a bulk phase transition and consistent with spin-triplet electron pairing, as expected.

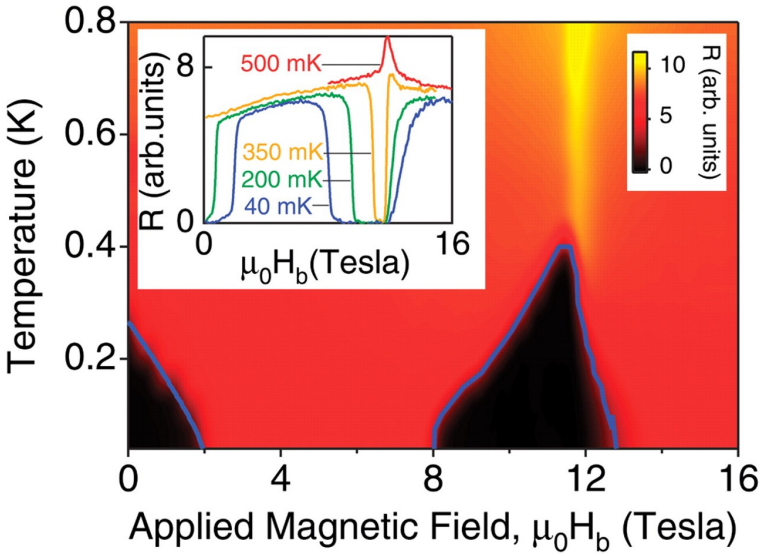

Figure 1.7 The field-temperature phase diagram of URhGe for field applied parallel to the crystallographic *b*-axis, showing the low and high field regions of superconductivity, as measured by a zero resistance state. The high field superconductivity is peaked at 12 T, the position of a magnetic moment rotation transition, above which there is also a peak in the normal state resistance, as shown in the inset. Source: Ref. [7]

A comparison of UGe_2 and URhGe followed in 2002 in Ref. [8], pointing out the similarities: "The physical properties of URhGe at zero pressure closely resemble those of UGe_2 at around 15 kbar." A helpful comparison of the unit cells was also included, reproduced here in figure 1.8.

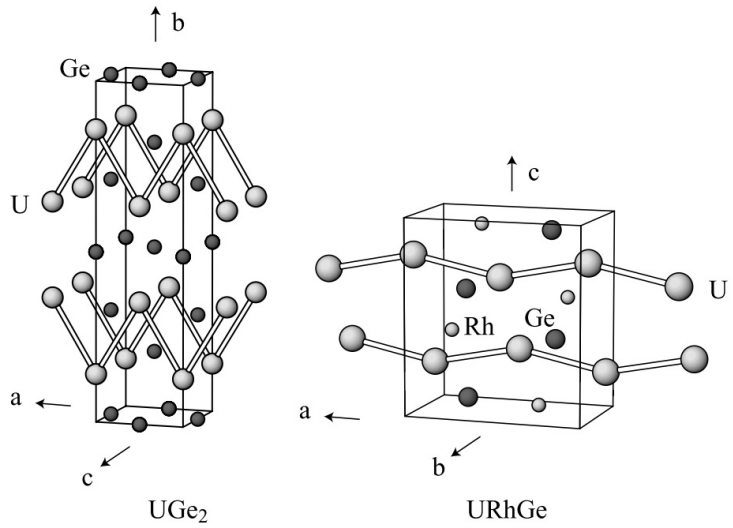

Figure 1.8 Sketches of the the unit cells of UGe_2 and URhGe. Each cell contains 4 formula units. Source: Ref. [8]

A 2005 publication reported the first measurements on a superconducting single crystal (RRR $\sim$ 21) of URhGe, detailing the anisotropy in the upper critical field, found to be roughly 2, 1.3 and 0.6 T at 0 K for the a, b, and c-axes respectively.[44] These values exceed the Pauli paramagnetic limit for URhGe, for all three axes, which is taken as further evidence of p-wave, spin-triplet pairing, with the anisotropic order parameter (the superconducting gap) at maximum parallel to the a-axis.

The discovery of a high field region of re-entrant superconductivity was announced slightly later in 2005,[7] relating the occurrence of the new SC state to a phase transition at $B_b \sim 12$ T also reported for the first time. Torque magnetometry was used to probe the component of the magnetic moment in the c-axis direction while field was applied parallel the b-axis in order to tune the system through the transition, at which point the c-axis moment abruptly drops to zero. The component of the moment in the b-axis direction was measured by neutron scattering and shows a sudden step up at the critical point at approximately 12 T, as plotted in figure 1.9.

The conclusion from Ref. [7] is therefore that the magnetic moment, of roughly fixed magnitude, suddenly rotates at the critical point, discontinuously enough to suggest a first order transition. Resistivity measurements then show the superconducting region existing between 8 and 12.5 T, with the transition temperature peaked at the critical point at 12 T, suggesting that the two

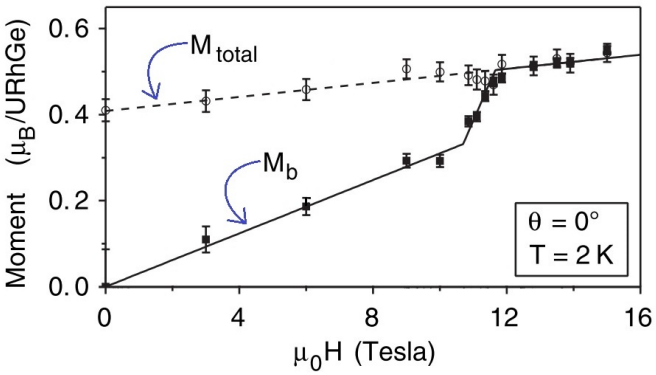

Figure 1.9 The magnetization as a function of field applied parallel to the b-axis at 2 K, measured by neutron scattering, showing the moment rotation transition at 12 T where the easy axis changes from c to b. Source: Ref. [7]

phenomena are probably linked and magnetic fluctuations associated with the moment rotation transition are likely beneficial to SC electron pairing. A relevant quotation from Ref. [7] is:

> "It appears that the high field superconductivity in URhGe, like the superconductivity in UGe_2, is not directly driven by fluctuations associated with a quantum critical point or QCEP separating ferromagnetism from paramagnetism. In both materials superconductivity is instead associated with a magnetic transition between two strongly polarized states [...] The apparent relationship of high field superconductivity to a field-induced quantum critical point in URhGe [...] reinforces the general notion that new strongly correlated electron ground states emerge close to quantum critical transitions between apparently simpler magnetic phases."

A two-component expansion of the free energy is also provided in Ref. [7], setting the stage for the torque magnetometry project described in this thesis. For directions x and y, which could be assigned to the crystallographic b and c axes of URhGe, the free energy can be written as the Ginzburg-Landau type expression $F = a_x m_x^2 + a_y m_y^2 + (b_x m_x^2 + b_y m_y^2)^2 + b_{xy} m_x^2 m_y^2 - \vec{m} \cdot \vec{B}$.

If the magnetization components m_x and m_y can be measured individually in the presence of field B then the various a and b coefficients can be determined by minimising the free energy (i.e. by finding the solutions of $\partial F/\partial m_x = 0$ and $\partial F/\partial m_y = 0$). Arguably the most interesting parameter is the cross term, b_{xy}, but information about how all the coefficients vary when crossing the magnetic

moment rotation transition would be very useful in understanding exactly which changes in the magnetic state of the system are driving the emergence of superconductivity.

This type of free energy analysis is discussed further in Ref. [45] and readers of this thesis are referred to that publication for more details.

The quantum critical point at 12 T was studied further in Ref. [9] in 2007, showing that this is also the point at which the FM-PM transition is driven towards absolute zero, though as in UGe_2 a tricitical point is reached before that happens and the transition splits into a wing structure, reaching 0 K at the QCEPs at a higher field directed a few degrees away from *b*-axis alignment. The superconducting region follows the wing structure and also terminates at the QCEP, demonstrated in this thesis by figure 1.10. A more detailed look at the bounds of the SC state surrounding the QCEP is provided in Ref. [46].

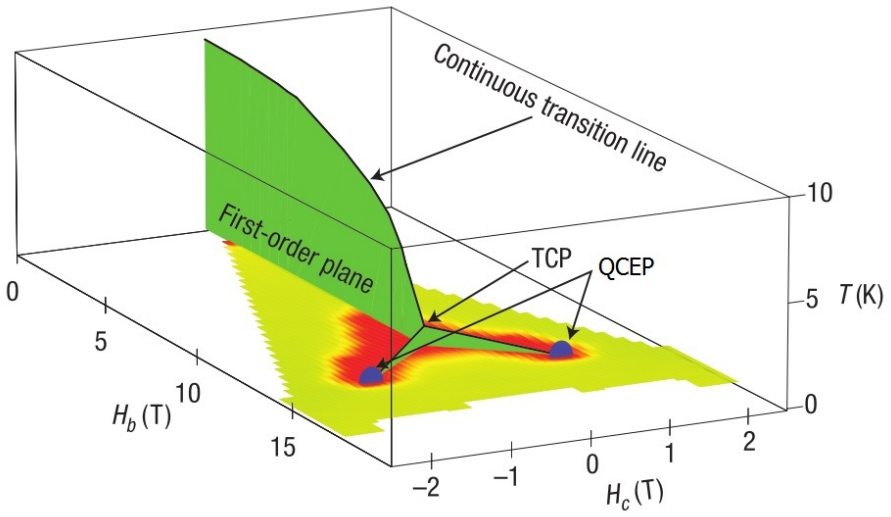

Figure 1.10 The schematic field-temperature phase diagram of URhGe for magnetic fields in the *b*-*c* plane.The magnetization changes discontinuously on crossing the first-order transition surface shaded green, which is bounded by the Curie temperature line. The tricritical point and wing structure typical to the ferromagnetic superconductors occurs at high field just before the quantum critical point, the Curie temperature then reaching zero at a pair of QCEPs. Superconductivity at 50 mK is shown by the red shading, corresponding to the zero resistance state. Source: Ref. [9]

In Ref. [9] the high-field superconductivity is proposed to be the same state as that observed at low field; the SC state is suppressed in-between the two regions because the upper critical field temporarily dips below the level of the applied field before peaking at the moment rotation transition, rising above the level of

the applied field for the brief range 8 to 13 T. The caption for figure 1.11, the original figure and caption from Ref. [9], explains this concept more clearly.

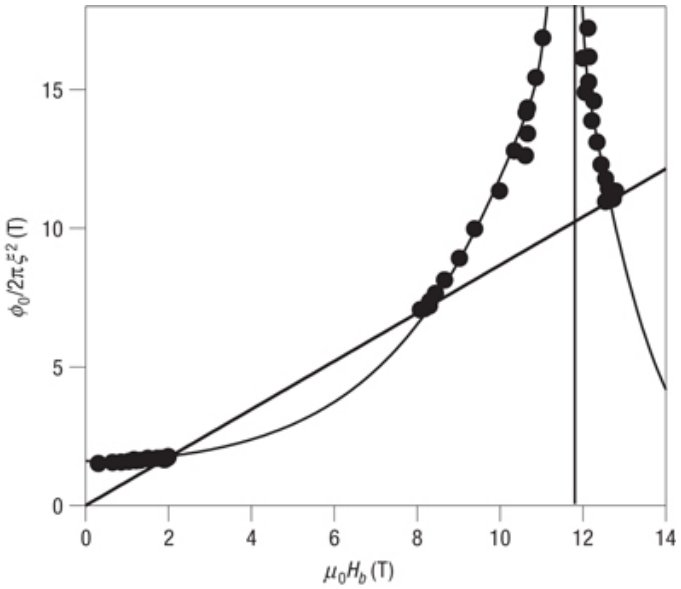

Figure 1.11 A figure from Ref. [9]. The original caption reads: "The quantity plotted is proportional to the inverse-square coherence length, $\phi_0/2\pi\xi^2$, given in units of magnetic field where $\xi = (\xi_a\xi_b\xi_c)^{1/3}$ is the geometric mean of the coherence lengths along the different axes, calculated assuming a constant anisotropy. The vertical line marks the magnetic field at which the rotation transition occurs. The other straight line gives the value of $\phi_0/2\pi\xi^2$ below which the critical field for superconductivity for $H \parallel b$ is less than the applied field along the b axis; superconductivity cannot occur when $\phi_0/2\pi\xi^2$ falls below this line. The coherence length, ξ, changes from 143 Å for the data point closest to the origin to 44 Å for the data point with the highest value of $\phi_0/2\pi\xi^2$. The line through the data points is to guide the eye."

Measurements of the upper critical field for external field applied in the a-axis direction, while traversing the phase diagram with tuning field parallel to the b-axis, are shown in this thesis in figure 1.12. Remarkably the SC state persists to >25 T, with the upper critical field so sharply peaked at the moment rotation transition that it exceeded the capabilities of the Grenoble High Magnetic Field Laboratory.

A 2011 publication on the the electronic specific heat,[47] probed by temperature-dependent magnetization measurements, reported a large enhancement of the effective mass at the moment rotation transition.[1] Previous direct measurements

[1]The magnetization can be linked to the electronic specific heat via a thermodynamic Maxwell relation, and the temperature coefficient of the specific heat, γ, the so-called Sommerfeld coefficient, is related to the effective mass by $\gamma \propto m^*$. Although the effective mass can also be found from the resistivity through the T^2 coefficient A, which is proportional

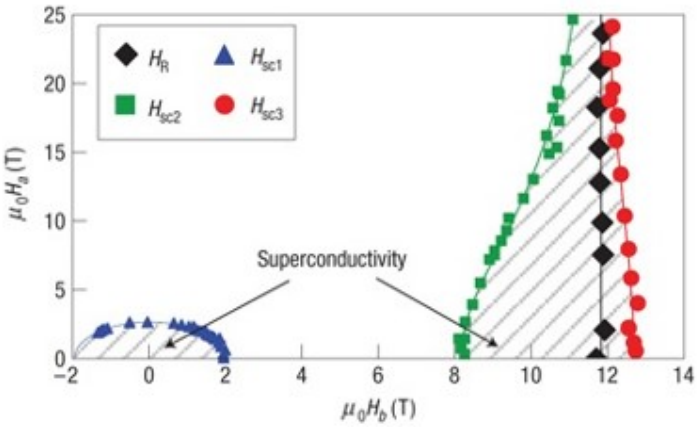

Figure 1.12 The phase diagram of URhGe for components of the field parallel to the b and a-axes, showing the superconductivity probed by the zero-resistance state at 45 mK. The upper critical field in the a-axis direction is sharply peaked at $\mu_0 H_R \simeq 12$ T applied parallel to the b-axis, the position of the moment rotation transition. Directly at H_R the upper critical field is beyond the measurement range. Source: Ref. [9]

of the specific heat had failed to detect any increase in γ around the transition, hence the somewhat roundabout method of measuring magnetization and calculating the Sommerfeld coefficient instead. The authors conclude: "We find roughly a 40% enhancement of $\gamma(H)$ at the field-induced FM instability, which must be related to a proliferation of magnetic fluctuations."

Also in 2011 a quantum oscillation (Shubnikov-de Haas) study reported the disappearance of the main oscillation frequency (555 T) at around 15.5 T for a field applied 10° off alignment with the b-axis, and so in the vicinity of a quantum critical end point.[48] From the temperature dependence of the oscillation amplitude it was found that under these conditions the effective mass remains finite across the transition and, rather than being enhanced, m^* actually decreases as field increases.

This implies that the superconducting pairing mechanism need not be related to an enhancement of magnetic fluctuations around the quantum critical point, but could instead be related to the disappearance of the quantum oscillation frequency, likely due to the disappearance of a tiny pocket of the Fermi surface, i.e. a Lifshitz transition, as described in this thesis in section 2.1. In this case it is the field-tuning of the Fermi surface, and the resulting Lifshitz transition at the

to $(m^*)^2$ according to Fermi liquid theory, thus linking γ and A by what is known as the Kadowaki-Woods relation ($A \propto \gamma^2$) for heavy fermion compounds, Ref. [47] notes that this relation may not be obeyed in the vicinity of a ferromagnetic instability.

moment rotation transition, that is potentially responsible for the emergence of superconductivity, rather than quantum criticality alone.

A few years later, a 2014 publication takes this conclusion on board and examines Fermi surface instabilities in URhGe by performing Hall effect measurements.[49] A large change in the Hall resistivity is observed crossing the moment rotation transition, "most likely explained by the Lifshitz-type transition," and magnetic hysteresis in the measurements provides further confirmation of the first-order nature of the transition.

A recent review, from 2015,[50] provides a good quote regarding superconductivity in URhGe to end this chapter:

> "The presence of a Lifshitz transition due to a vanishing Fermi-surface pocket could be responsible for the short coherence length needed to achieve superconductivity in such a high field. With regard to the superconductivity, the elephant in the room for the standard theory of magnetically mediated superconductivity is that for URhGe it appears to be driven by a rotation transition. Theoretically for equal spin pairing only longitudinal fluctuations are pair forming while transverse moment fluctuations that might be expected at a moment rotation are pair breaking. The pairing mechanism is therefore an open question."

Chapter 2

Background Theory

2.1 Introduction to Electronic Transport

UGe_2 and URhGe could be referred to as quasi-itinerant 3d ferromagnets with unusually strong magnetocrystalline anisotropy, or as novel p-wave, spin-triplet superconductors, or possibly as heavy-fermion compounds with unconventional quantum criticality, but perhaps most simply these two materials could be called metals.

The metallic state is characterised by the existence of a Fermi surface, i.e. by partially-filled energy bands that cross the Fermi level. It is only the electrons close to this constant-energy surface in momentum space that determine the electronic response of a material to external fields, and so the precise nature of the Fermi surface is an essential piece of knowledge for understanding electronic transport phenomena such as superconductivity.

For the transport experiments described within this thesis a constant current, I, is applied by way of an external electric field, E, and the resulting potential difference, the voltage V, is the measured variable. The important information is contained within the constant of proportionality expressed by Ohm's law, $V = IR$, and studies of how resistance, R, changes as a function of temperature and magnetic field (i.e. the magnetoresistance) comprises the majority of the results presented in chapters 5 and 6.

Resistance in metals is often described in terms of scattering, which in the

standard semi-classical picture, the Drude-Sommerfeld model for free electrons, refers to instantaneous collisions between conduction band electrons and the ionic lattice. In this model the conduction electrons are classical particles, non-interacting except for the instantaneous collisions, which scatter them isotropically into momentum states governed by the Fermi-Dirac distribution. The average time between collisions is the so-called relaxation time, τ, a parameter that seems beguilingly simple to define in this simple description of electrons in metals.

In real materials the picture is more complicated. Bloch's theorem removes the scattering of conduction electrons by the ionic lattice directly and replaces it with the scattering of electron wavefunctions by quantized excitations of the lattice from a stationary ground state. These quantized lattice vibrations are called phonons and, via wave-particle duality, can be thought of as particles moving at the speed of sound. Electron-phonon collisions are the dominant source of resistance in metals at room temperature.

At much lower temperatures, when these phonon modes begin to freeze out of the system, electron-electron scattering also becomes significant and in magnetic materials electrons can also be scattered by collective, quantized magnetic excitations called magnons (as described in section 2.1.3). Finally there is impurity scattering, chemical impurities and/or lattice imperfections that disrupt the perfectly periodic lattice potential required by Bloch's theorem. The resistivity due to impurity scattering is referred to as the residual resistivity, since it exists even at absolute zero when all other sources of electron scattering have been frozen out.

Resistivity measurements can provide information about all of these scattering sources and also give some hints about the nature of the Fermi surface, which is responsible for a wide range of behaviour, including superconductivity. The scattering rate, τ^{-1}, is related to the resistivity–or more precisely the inverse, the conductivity–by the well-established formula:[16]

$$\sigma = \frac{J}{E} = \frac{ne^2\tau}{m^*} \tag{2.1}$$

In general, the current density, J, and electric field, E, are both vectors and the conductivity, σ, is a tensor, not simply a scalar constant, which is an important distinction for materials like UGe_2 that have a high degree of electronic and

magnetocrystalline anisotropy.

From the formula above (equation 2.1) it can immediately be seen that changes in the scattering rate, due to phase transitions between different magnetic states for example, will be reflected by changes in the conductivity, making it a useful probe even at the level of this rather crude treatment of the phenomena.

Although equation 2.1 is an expression for a system of non-interacting electrons, interactions do enter obliquely via the effective mass, m^*, which can be greatly enhanced from the fundamental electron mass, as in heavy fermion compounds (see section 2.2.3). It should be pointed out however that an increased effective mass, which is essentially related to the curvature of the bands near the Fermi surface (i.e. $(m^*)^{-1} \propto \partial^2\varepsilon/\partial k^2$ for energy ε and momentum k), effectively slows down the conduction electrons, lengthening τ by a factor equal to the mass enhancement, thus resulting in no measurable change in conductivity.

As well as changes in τ being being reflected in σ it is clear that the charge carrier number density, n, also enters equation 2.1, raising the possibly that it could be measured directly...for this isotropic, single Fermi surface, free-electron model at least. The measured quantity is the parameter $R_H = 1/ne$, known as the Hall coefficient, and is the focus of the UGe_2 investigation covered in this thesis.

Once again sticking to a very basic treatment for now, classically the Hall effect arises from a magnetic field, B, applied in addition to the electric field responsible for the current, producing the combined force $\vec{F} = \Delta\vec{p}/\tau = e(\vec{E} + \vec{v} \times \vec{B})$. Instead of traveling in straight lines between collisions the electrons will thus travel in helical paths according to the Lorentz force, the cross product $e\vec{v} \times \vec{B}$.

The angular velocity of an electron about the helix axis is given by the cyclotron frequency $\omega_c = eB/m^*$ and magnetoresistance effects only become truly significant when $\omega_c\tau > 1$. This criterion essentially states that the mean free path between scattering events must be large enough that electrons cover a significant angular distance.

As discussed by Hurd in the opening chapter of Ref. [51], both large magnetic fields and large relaxation times are required in order to meet the "high field" condition $\omega_c\tau \gg 1$, for which a fully developed theoretical treatment exists. Similarly, for pure samples at low temperatures (as is the case for the investigations described in this this thesis, on low-temperature UGe_2 and URhGe), only for very small fields will the "low field" condition $\omega_c\tau \ll 1$ be

encountered.

For the "intermediate field" condition $\omega_c\tau \sim 1$, Hurd states quite clearly that "there is no theory for the intermediate region. This is unfortunate...many of the experiments at low and intermediate temperatures made upon pure metals are, in fact, carried out in the intermediate condition."

Substituting the conductivity from equation 2.1 into the expression above for the cyclotron frequency gives $\omega_c\tau = B\sigma/en = R_H B\sigma$, where the Hall coefficient defined earlier has been introduced. Hence R_H can be a useful measure of $\omega_c\tau$, a point that will be returned to later (in discussion of Kohler's law, section 2.1.2).

The Hall effect is not the only cause of magnetoresistance, a quantity that moving beyond an isotropic treatment should be expressed as a conductivity tensor, σ_{ij}. Usually only two directions are relevant, parallel and perpendicular to the magnetic field, specified as x and y respectively. The parallel-to-field conductivity is thus σ_{xx} and the off-diagonal term of the tensor is σ_{xy}.

As Pippard states as a section heading in chapter 1 of Ref. [28], "The free-electron gas shows no magnetoresistance", and strong interactions, or scattering rate anisotropy, or multiple Fermi surfaces, both hole and electron or open sheets, are required to bring about the complications that necessitate an entire textbook on the topic. Since this thesis does not aim to be such a textbook the reader is referred to the excellent opening chapters of the aforementioned books by Pippard (Ref. [28]) and Hurd (Ref. [51]).

A more realistic formula for electronic transport than equation 2.1 is the Boltzmann transport equation, which essentially involves three terms, a diffusion term for the drift of conduction electrons, a force term for the influence of external fields, and a scattering term. An excellent introduction to Boltzmann transport theory can be found in chapter 7 of Ref. [52].

On the other hand, some of the content from the textbooks mentioned above–namely how the Hall effect, and the conductivity in general, is related to the Fermi surface–is particularly important for later discussion in section 2.3 and is therefore worth briefly summarising here.

2.1.1 Fermi Surfaces and the Hall Coefficient

Defining the crystal momentum as $\hbar\vec{k}$, the force on charge e from an external electric field applied for an infinitesimal time δt is $\vec{F} = e\vec{E} = \hbar\delta\vec{k}/\delta t$. Each electron in the system experiences this impulse, such that the distribution of filled momentum states (a Fermi sphere for a free-electron gas) is shifted bodily in k-space. Rearranging, the change in momentum is:

$$\delta\vec{k} = \frac{e\vec{E}\delta t}{\hbar} \tag{2.2}$$

Only states within $\sim k_B T$ of the Fermi surface, for temperature T, have their occupation affected. Pippard takes the approach that the impulse due to the E field leads to the creation of new electrons on one side of the Fermi surface and the destruction of an equal number on the opposite side. For an infinitesimal Fermi surface element $\delta\vec{S}$, the created volume of occupied states is $\delta\vec{S}\cdot\delta\vec{k}$ and thus contains $\delta\vec{S}\cdot\delta\vec{k}/4\pi^3$ electrons per unit volume of material. The number density of states created in time δt is therefore:

$$\delta^2 n = \frac{e\vec{E}\cdot\vec{S}\delta t}{4\pi^3\hbar} \tag{2.3}$$

The charge density is en and so the current density can be defined $\vec{J} = en\vec{v_F}$, where $\vec{v_F}$ is the Fermi velocity. However, after the inital impulse scattering will slow the average velocity of a group of newly created electrons, from the initial $\vec{v_F}$ to an eventual mean of zero. Substituting the time-dependent $v(t)$ for v_F and integrating over time to infinity provides the expression:

$$\delta\vec{J} = \frac{e^2\vec{E}\cdot\delta\vec{S}}{4\pi^3\hbar}\int_0^\infty \vec{v(t)}dt = \frac{e^2\vec{E}\cdot\delta\vec{S}}{4\pi^3\hbar}\vec{L} \tag{2.4}$$

where $\vec{L}$ is the mean distance travelled by each electron from creation until scattering scattering brings the mean velocity (the average of all created electrons) to zero.

Integrating over the whole Fermi surface (FS) then provides an expression for the current density:

$$\vec{J} = \frac{e^2}{4\pi^3\hbar}\int_{FS}\vec{L}(\vec{E}\cdot d\vec{S}) \tag{2.5}$$

Finally, recalling that $J_i = \sigma_{ij} E_j$ and so $\vec{L}(\vec{E} \cdot d\vec{S}) = L_i(E_j dS_j)$, an expression relating the conductivity to the Fermi surface is:

$$\sigma_{ij} = \frac{e^2}{4\pi^3 \hbar} \int_{FS} L_i dS_j \tag{2.6}$$

Hence the conductivity is essentially given by the integral of the mean free path over the Fermi surface, for that interpretation of the quantity L, which is defined more rigorously by the formulae above. A short discussion of the subtleties arising in the physical interpretation of L can be found on page 21 of Ref. [28].

Applying a magnetic field then allows the conductivity to function as a probe of Fermi surface size, using the Hall effect to extract some limited information about the value of L across the surface. The aforementioned Lorentz force ($e\vec{v} \times \vec{B}$) results in momentum change $\hbar k_y$ for electron velocity v_x and field B_z. Defining L_x as the distance travelled due to v_x over the time period of that momentum change, the Lorentz force can be written:

$$\hbar k_y = e L_x B z \tag{2.7}$$

which then allows the substitution of k_y for L_x in equation 2.6, using the off-diagonal component of the conductivity tensor, σ_{xy}, known as the Hall conductivity.

$$\sigma_{xy} = \frac{e^2}{4\pi^3 \hbar} \int_{FS} L_x dS_y = \frac{e}{4\pi^3 B_z} \int_{FS} k_y dS_y \tag{2.8}$$

Since $\delta\vec{S}$ has direction normal to the surface, the surface element δS_y could be written $\delta k_x \delta k_z$, and the Fermi surface integral $\int k_y dk_x$ could then be denoted by A_k, the area defined by the k-space orbit perpendicular to the magnetic field (this is the same cross-sectional area discussed in section 2.4 regarding the Onsager relation for quantum oscillations). Using this notation, the conductivity becomes:

$$\sigma_{xy} = \frac{e}{4\pi^3 B_z} \int_{FS} A_k dk_z \tag{2.9}$$

In other words, the Hall conductivity is related to the integral, over all momentum states parallel to the field, of the cross-sectional area of the volume bounded by the Fermi surface.

The Hall coefficient defined earlier, during the discussion of the more simple

Drude-Sommerfeld expression for the conductivity (equation 2.1), can be introduced by considering the number density of the charges. The quantity $A_k \delta k_z$ defines a volume element, and $A_k \delta k_z / 4\pi^3$ is the number of electrons per unit volume for $\vec{k}$ within infinitesimal interval δk_z.

Integrating this volume element over the range of k_z bounded by the Fermi surface gives n, the number per unit volume, the charge carrier density. Mathematically:

$$n = \int_{FS} \frac{A_k}{4\pi^3} dk_z \tag{2.10}$$

and $\sigma_{xy} = ne/B = 1/R_H B$ where $R_H = 1/ne$ as before. This basic expression for the Hall conductivity is the starting point for section 2.3, written in terms of the resistivity in equation 2.3.

In general, from complete knowledge of the Fermi surface and the direction of the magnetic field, a summation of infinitesimally thick volume elements, each with a particular cross-sectional area perpendicular to the field, would yield the charge carrier density, and the inverse of that quantity essentially yields the Hall coefficient, the constant of proportionality between the off-diagonal component of the resistivity tensor and the applied field strength. In this way the calculated value from a theoretical Fermi surface can be compared to the measured Hall coefficient obtained from electronic transport experiments.

The converse, however, is not possible, i.e. constructing a complete picture of the Fermi surface from measurements of the Hall coefficient. Obviously the result of an integral can never contain information about every infinitesimal element that went into the calculation, but interpretation of the Hall coefficient is also made difficult by a number of complications. Firstly the measured R_H is a combined result of all the Fermi surfaces present, both electron and hole, and untangling the different contributions can prove impossible from electronic transport measurements alone.

Further complications are anisotropic scattering rates, anisotropic effective mass (which only affects the magnetoresistance if τ is also anisotropic), open orbits across open Fermi sheets, and any possible field dependence to τ such that $\omega_c \tau$ is not directly proportional to B (i.e. in violation of Kohler's law). All of these can make extracting information about the Fermi surfaces from the Hall coefficient extremely difficult, as discussed later in section 2.3.

2.1.2 Kohler's Law

The magnetic field dependence of the conductivity defined in equation 2.6 enters via the parameter $\vec{L}$, essentially because $\vec{v}(t)$ is no longer parallel to $\vec{v_F}$ in the presence of a magnetic field. If B is increased then the charge carrier scattering rate increases (the extra component to the electron velocity results in a greater distance covered per unit time, making collisions more probable) and, in the language used in the previous section for a single, infinitesimal impulse from the electric field, the electrons newly created with the Fermi velocity reach the zero mean velocity condition faster, thus reducing $\vec{L}$ and hence reducing σ_{ij}.

The reduction in σ due to the increase in B is what defines magnetoresistance, and by this definition it is implied that the relative change in resistance should be directly proportional to the applied field. More specifically it implies that any temperature dependence of the magnetoresistance should be entirely related to the temperature dependence of the scattering rate, empirically encapsulated by measurements of the zero-field resistivity $\rho(B = 0) \equiv \rho_0$.

As Pippard puts it on page 23 of Ref. [28]: "It follows that keeping the ratio B/ρ_0 constant ensures that in different samples the probability of being scattered in the course of one cycle of the orbit remains constant, and the relative effect of B on the resistivity should be the same for all." The field dependence of the resistivity is essentially contained within the parameter $\omega_c\tau$ mentioned many times before. Mathematically, for some function F or f:

$$\frac{\rho(B) - \rho_0}{\rho_0} = \frac{\Delta\rho}{\rho_0} = F(\omega_c\tau) = f\left(\frac{B}{\rho_0}\right) \tag{2.11}$$

This is Kohler's law, and generally holds for a single species of charge carrier and an isotropic scattering rate, regardless of the topology or geometry of the Fermi surface. The final step in equation 2.11 arises from application of equation 2.1, viz. $\omega_c\tau = \sigma_0 B/ne = R_H B/\rho_0$.

When Kohler's law is applicable, so-called Kohler plots of $\Delta\rho/\rho_0$ vs. B/ρ_0, or $\Delta\rho/\rho_0$ vs. calculated values of $\omega_c\tau$, should all lie on top of each other for various different temperatures or samples.

When Kohler's law holds it can be taken as a good indication that other results routed in semi-classical transport theory, based on the Boltzmann equation, such

as all those discussed throughout this chapter, are also likely to hold, making it a useful relation to check the validity of a particular approach to data analysis.

Unfortunately Kohler's law can be violated by a number of circumstances: if the electronic structure varies with temperature (i.e. close to a phase transition), if there is more than one type of charge carrier and their mobilities have different temperature dependencies, if the temperature dependence of the scattering rate varies significantly at different points on the Fermi surface, or if the scattering rate itself has a field dependence.[53]

2.1.3 Fermi Liquid Theory and Lifshitz Transitions

The absolute value of resistivity of a sample provides very little information compared to the trends in measured resistance as a function of temperature or magnetic field.

At high temperature electron-phonon scattering is the main cause of resistivity in metals, and the magnitude theoretically (by the Debye model; see Ref. [54]) scales as $\sim T^5$ while cooling to intermediate temperatures (around a tenth of the Debye temperature), decreasing very steeply with decreasing temperature. In other words, the number of phonons rapidly diminishes as the lattice cools and the thermal energy available for vibrations is reduced.

At low temperature electron-electron scattering then becomes the dominant mechanism for resistivity in metals, in a system known as the Fermi liquid. A comprehensive overview of the Fermi liquid state is provided by Ref. [16] and Ref. [55], with the latter covering Fermi liquid theory in conjunction with superconductivity and quantum criticality (see section 2.6), and also the RKKY interaction and Kondo breakdown (see section 2.2).

Fermi liquid theory essentially attempts to preserve the independent electron approximation, and the simplified physics that follows from it, even when electrons are strongly interacting. This is achieved by the concept of quasiparticles. Interactions are considered as excitations of the ground state, taken to be the non-interacting electron gas, and the excitation energy treated as a system of quasiparticles, each with one-to-one correspondence to the non-interacting electrons, which works as long as the wavefunctions change adiabatically as the interaction strength is increased continuously from zero to the full strength of

the Fermi liquid state. The quasiparticles obey the Pauli exclusion principle and only weakly interact, and characteristics of the system such as sample resistivity are governed by the quasiparticle behaviour.

The resistivity derived from Fermi liquid theory has the characteristic temperature dependence $\rho = \rho_0 + AT^2$, where ρ_0 is the resistivity due to imperfections in the atomic lattice, or chemical impurities, or any other defects affecting the Bloch states in general, and is called the residual resistivity. At very, very low temperatures, approaching absolute zero, the residual resistivity will dominate the resistance of even the purest metals.

At temperatures between this regime and the higher temperature regime dominated by electron-phonon scattering, the sample resistance will have the distinctive temperature-squared dependence of the Fermi liquid state, where the coefficient A is proportional to the square of the effective mass. Thus measurements of the T^2 coefficient, A, can be used as an indicator of heavy fermion behavior.

Electrons can also be scattered from magnons, which like phonons are a particle representation of a quantized excitation energy. In the case of magnons it is the spin structure of the system that is excited from the ground state, which for a ferromagnet is a state of perfect spin co-alignment (see section 2.2). A low-energy excitation of a ferromagnet is a slowly evolving deviation in the direction of spins about the ground state orientation, a gradual and long-range variation called a spin wave, which like all standing waves can be considered quantized.

Whereas the differing influence of various scattering mechanisms must be considered in order to interpret the resistivity, and the magnetoresistance of a material can be incredibly difficult to understand, the Hall effect is more directly related to a single parameter: as detailed earlier, the Hall effect is a measure of the volume bounded by the Fermi surface size, albeit with all the caveats discussed above.

In a simple free electron model, where the Fermi surface is a sphere, determining the size of the Fermi surface may seem trivial (the Fermi momentum is the radius), but adding complexity to the model (a band structure, crystalline anisotropy, electron interactions, etc.) adds complexity to the shape and number of Fermi surfaces in the system. Several examples of complex Fermi surfaces found in real metals are shown in figure 2.1.

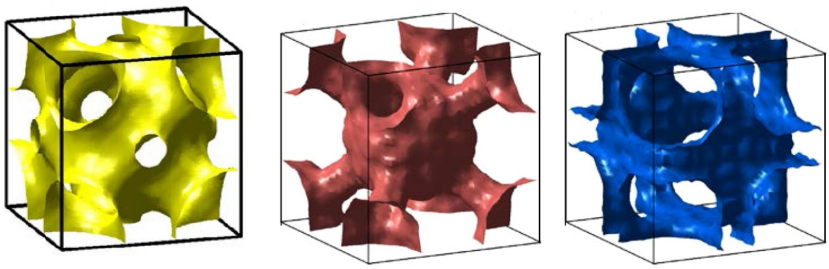

Figure 2.1 A few pictorial examples of the complex Fermi surfaces found in real metals (the exact nature of the corresponding materials is unimportant to the discussion here). Only a single Brillouin zone is shown. These surfaces demonstrate the topological feature of a 'neck' though to the next Brillouin zone, which looks like a hole in this single-zone representation. Source: Ref. [10].

In addition to complicated shapes, both electron and hole Fermi surfaces can be present, and both can be closed (self-contained within the Brillouin zone) or open (an infinite sheet in an repeated-zone representation). The topology of the Fermi surface is therefore variable as well as the geometry, and both are instrumental in determining the electronic behavior of the material.

In general, there are often multiple bands at the Fermi level and the Hall coefficient is dependent on all of them, as well as the mobility of the charge carriers for each band, as discussed in section 2.3. Hence in real metals the Hall effect is a rather complicated phenomena to interpret, and although with some hard work it may be possible to calculate the Hall coefficient from a collection of known Fermi surfaces, the reverse, extracting any information about the Fermi surfaces from Hall effect measurements, can prove almost impossible.

The real strength of Hall effect measurements therefore lies not in probing the precise, minute details of Fermi surfaces but instead in indicating major changes in geometry or topology, either through gradual trends or sudden variations in the Hall coefficient, as the result of physical phase changes or crucial shifts in the strengths of various competing interactions.

One example is the shifting dominance between the RKKY interaction and Kondo screening in itinerant ferromagnets, as discussed in section 2.2, which can abruptly alter the size of the Fermi surface. Another abrupt alteration indicated by the behaviour of the Hall coefficient is the sudden change in Fermi surface topology referred to as a Lifshitz transition.[56]

A Lifshitz transition can refer to either of two similar processes, illustrated by figure 2.2. One type is when a section of the Fermi surface that bridges adjacent

Brillouin zones, sometimes referred to as a 'neck', is created or destroyed by opening or closing the neck. Fermi surface necks can be seen in figure 2.1 if a repeated zone image is imagined. In a single zone representation the the necks appear as holes in cross-section, so it is easy to understand why closing them, producing a surface self-contained within the zone, is a topological transition.

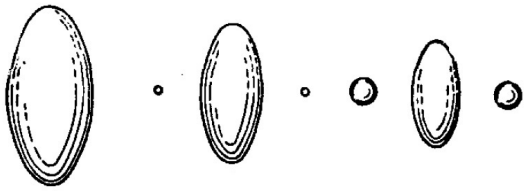

FIG. 3. Appearance of a new sheet of the constant-energy surface. Surface a corresponds to the critical energy ϵ_k.

FIG. 4. Breakup of a "bridge" on the constant-energy surface. Surface a corresponds to the critical energy ϵ_k. It contains a conical point.

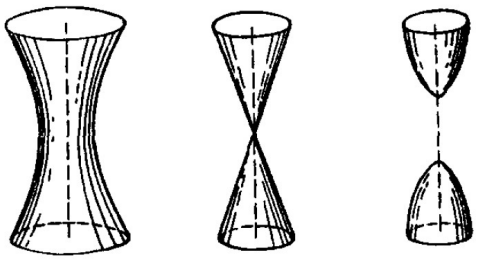

Figure 2.2 A graphic from the original Lifshitz publication[11] on the topic, illustrating the two types of Fermi surface reconstruction referred to as Lifshitz transitions.

The other type of Lifshitz transition also results in a topological change in Fermi surface, through the creation or destruction of an individual closed Fermi surface within the Brillouin zone, the volume bounded by the surface either shrinking to nothing or expanding to finite size from nothing. These small Fermi surfaces can have a disproportionately large effect on the electronic properties of the system, particularly the Hall effect, depending on the type and mobility of the charges associated with the band. For instance it may be the case that, although small in number, these charges are responsible for the majority of the sample resistivity and so at the Lifshitz transition there is a dramatic change in both the measured resistance and the Hall coefficient.

Lifshitz transitions are of particular interest to investigations of UGe_2 since a change in Fermi surface topology is often linked to metamagnetism in heavy-fermion compounds[57], and Ref. [58], as an example, makes the observation that the emergence of superconductivity has been seen to coincide with substantial Fermi surface reconstruction at a quantum critical point (see section 2.6).

In conclusion, a reasonable proposal could be that the superconductivity in UGe_2 is driven by a Lifshitz transition at the critical pressure, an occurrence potentially measurable by the Hall effect.

2.2 Ferromagnetism

Both UGe_2 and URhGe are paramagnetic under ambient conditions and become ferromagnets upon cooling, and for both research projects outlined in this thesis it is principally the exact nature of the ferromagnetic state that is under investigation. Before proceeding with a discussion on ferromagnetism, however, it seems pertinent to highlight the differences between magnetic fields B and H and justify the frequent use of B in this section, and section 2.4, while H is more commonly used in sections 2.3 and 2.5.

The response of magnetization to external field, the magnetic susceptibility, can be written in differential form as:

$$\chi = \frac{\partial M}{\partial H} \tag{2.12}$$

where, for a single vector component, $M = |\vec{M}|$ is magnetization and $H = |\vec{H}|$ is the applied field. Both quantities have units (in the S.I. system) Am^{-1}. The total magnetic field, $B = |\vec{B}|$, can be related to the H field by:

$$B = \mu_0 (M + H) \approx \mu_0 (M + (H_{\text{ext.}} - \gamma M_0)) \tag{2.13}$$

where $H_{\text{ext.}}$ is the external field applied to the region and γ is the demagnetization factor. The word 'demagnetization' arises from the minus sign in equation 2.13, which results in a decrease in H from the strength of $H_{\text{ext.}}$ and thus, for a positive susceptibility, a decrease in magnetization. Often H is called the 'internal' field to avoid confusion with $H_{\text{ext.}}$ when referring to the field applied to a magnetic material. At low field, below saturation of the magnetization, the susceptibility is related to the demagnetization factor by $\chi \simeq 1/\gamma$.[59]

The approximation symbol appears in equation 2.13 since characterization of the demagnetizing field in terms of a single factor, γ, is a simplification only correct for a uniformly magnetized sample of an ellipsoidal geometry and a single-component

treatment of $\vec{M}$, $\vec{H}$ and $\vec{B}$. In a 3d treatment the demagnetization factor is replaced by the demagnetization tensor, usually denoted $N = \text{diag.}(n_x, n_y, n_z)$, where the demagnetizing field is $\vec{H}_{\text{demag.}} = -N\vec{M}$. In this case the susceptibility is also a tensor.

The demagnetizing factor is reduced by a sample geometry where the major length is parallel to the field direction, such as a thin needle mounted vertically in a vertical field, while it is enhanced by samples where the majority of material lies in a plane perpendicular to the field. Hence the UGe_2 sample geometry optimised for Hall effect measurements, of a thin plate lying horizontal in a vertical field, necessarily exacerbates the modification of H by the demagnetizing field. Creating real samples as perfect ellipsoids is usually not possible in practice and the demagnetization factor is generally difficult to calculate exactly (see Ref. [60–62] for example) but by approximation of the UGe_2 sample to a very flat oblate ellipsoid Ref. [63] and Ref. [64] can be used to estimate a demagnetization factor of ~ 0.74 for the dimensions listed in figure 3.1.

This comparatively high value (for example $\gamma = 1/3$ for a uniformly magnetized sphere) then combines with relatively high magnetization and low fields of interest to make the demagnetizing field highly significant for UGe_2. The typical value of magnetization in the FM2 state is around $1.4\,\mu_B$ per formula unit,[21] which for the primary UGe_2 sample can be converted (including a factor of μ_0) to 0.27 T. This is 3 % of a 9 T applied field and almost 30 % of a 1 T field. Hence, even when multiplied by $\gamma \simeq 0.74$, the demagnetizing field necessitates a significant correction of H_{ext} to give the true H value, with the correction generally being larger at lower field. Therefore, wherever possible, the actual H field is determined and used for plots and calculations in the Hall effect investigation of UGe_2.

By contrast, the primary sample of URhGe used in this project is roughly spherical and so has a much smaller demagnetizing factor ($\gamma \sim 0.4$). Coupled with the fact that the magnetization for URhGe is typically a third of that of UGe_2, at around $0.4\,\mu_B$ per formula unit[48] (roughly $\mu_0 M \simeq 0.084$ T), while the H fields encountered in the URhGe investigation are typically larger (the important data is all above 10 T), the approximation that $H \simeq H_{\text{ext}}$ is fairly safe.

Furthermore, if the approximation $B \simeq H$ is also made following the same reasoning (that magnetization is small compared to the applied field) equation 2.12 could be re-written as $\chi \simeq \partial M/\partial B$, which is the form most commonly used in this section.

Magnetism in UGe_2 and URhGe arises from unpaired electrons within the material, specifically the uranium $5f$ orbital electrons, and chiefly from their individual, intrinsic magnetic moment known as spin. These electrons have an indefinite character in regard to either being localised to atomic sites as valence electrons, or being delocalised as itinerant conduction band electrons. Like most heavy fermion materials, UGe_2 and URhGe can be called intermediate valence compounds (IVC), by which it is meant that the $5f$ electrons are neither localised nor itinerant but are instead a combination of the two, a mix lying somewhere between these extremes.

2.2.1 Localised Magnetism

Localised magnetism is easy to picture: a lattice of uranium atoms each with a number of unpaired electrons in the $5f$ valence shell, resulting in a magnetic moment on each lattice site. The moment associated with each electron spin is (as a slight oversimplification) approximately 1 μ_B, the Bohr magneton. At high temperature the large thermal energy of the system results in a ground state where the magnetic moments are randomly oriented according to a Boltzmann distribution of highly degenerate orientation states. This is the paramagnetic state and the magnetization, the net moment per unit volume, averages to zero.

Now consider application of an external field, $\vec{B}$, which breaks the degeneracy. There is an energy cost $\Delta E = +\mu_B B$ for moments oriented anti-parallel to the field, or conversely an energy saving of $\Delta E = -\mu_B B$ for moments aligned parallel to the field. The thermodynamic drive to lower the energy of the system thus tends to align the moments with the field, producing a finite magnetization. In a classical formulation, this tendency for the moments to align with the field can be thought of as a magnetic torque generated by the interaction between them, a force that causes rotation of the moment in the direction of alignment with the field. The concept of magnetic torque is explored further in section 2.5.

Although it is energetically favourable for moments to align with the field, energy-entropy competition makes such alignment only probabilistically more likely. Consider a two state Boltzmann equation where the number of moments in each state, N_1 or N_2, is governed by the factor e^x for $x = \mu_B B/k_B T$. The total net

moment, m, is given by:

$$m = (N_1 - N_2)\mu_B = N\left(\frac{e^x - e^{-x}}{e^x + e^{-x}}\right)\mu_B \tag{2.14}$$

The term in brackets is $\tanh(x)$, which increases with increasing x. Interestingly, $\tanh(x) \to 1$ as $T \to 0$, and the number of field aligned moments $N_1 \to N$ with the net moment $m \to N\mu_B$, i.e. every moment is aligned to the field in an ordered state of minimum entropy, producing a saturated maximum magnetization, regardless of the field strength.

Inspection of equation 2.14 reveals a simplification for small x, specifically for $x \ll 1$ when the thermal energy is much greater than the magnetic interaction energy. In that case $\tanh(x) \approx x$ and the net moment can be calculated by:

$$m = Nx\mu_B = \frac{N\mu_B^2}{k_B}\frac{B}{T} \tag{2.15}$$

From this it can be seen that the susceptibility is inversely proportional to temperature, a result known as Curie's law where the constant of proportionality is C, the material-specific Curie constant. At absolute zero there is no thermal disorder and any small field can break the degeneracy and fully polarise the system in to a state of complete magnetic ordering. This is an interesting idea because the moments themselves produce a small field, which although weak over large length scales is strong enough to influence nearest neighbour sites.

Thus, merely by internal magnetic interactions, a finite field is generated that coaligns neighbouring moments, which in turn generates a stronger field, which then influences more sites over greater length scales. Eventually this process will spontaneously coalign every local moment and produce a fully magnetized material. This is a 'mean field' effect, where each moment interacts with the average field generated by every other moment.

This is basically the description of a ferromagnet in the localised moment picture: magnetic interactions between sites produces a spontaneous magnetization in the absence of any externally applied field. And the criteria for the formation of this state is not strictly $T = 0$ but simply that the magnetic interaction energy must be greater than the disordering thermal energy, i.e. roughly that $\mu_B B_E > k_B T$, where B_E is the internal magnetic field generated by the interaction between the moments, the so-called exchange field. The temperature at which the inequality

becomes true is known as the Curie temperature, T_C, and leads to a modification of Curie's law to the Curie-Weiss law:

$$M = \frac{C}{T - T_C} B \tag{2.16}$$

which describes the susceptibility in the paramagnetic regime above the Curie temperature.

Note that according to equation 2.16 the susceptibility diverges at $T = T_C$, where at a point just above the Curie temperature a small external field will produce a huge magnetic response as it triggers the formation of the spontaneous magnetization state. However, the Curie-Weiss law is only strictly correct for $T \gg T_C$ as mentioned above when the criteria $x \ll 1$ was invoked. Near and below T_C equation 2.16 no longer holds and unfortunately there is no simple law that describes the susceptibility of a ferromagnet.

The exchange field responsible for localised moment ferromagnetism at finite temperature (more accurately described by the Heisenberg model as detailed in Ref. [16]) is a consequence of the fact that electrons follow the Pauli exclusion principle and as an interacting, many-body system must have an overall anti-symmetric wavefunction. Electrons localised to neighbouring atomic sites will be subject to electrostatic repulsion due to the Coulomb interaction and the energy of the system will be lowered by smaller spatial overlap of electron orbitals.

This overlap can be reduced by neighbouring electrons sharing the same spin state. The Pauli principle demands that for a symmetric spin state the the spatial part of the wavefunction be antisymmetric, which necessarily introduces a wavefunction node in the space between sites and so reduces the spatial overlap of the individual electron wavefunctions, reducing the Coulomb repulsion. This interaction between neighbouring electrons, which favours a symmetric spin state, is called the direct exchange interaction and the effective field it generates called the exchange field.

The direct exchange interaction clearly becomes stronger as atomic sites become closer, resulting in greater potential for orbital overlap, and because of its short range the effects of the exchange field become significantly more influential. Thus it might be expected that pushing uranium atoms closer together in UGe_2 would produce a more magnetic ground state, that application of hydrostatic pressure would decrease the separation between lattice sites and result in increased

magnetization, if localised magnetism and the direct exchange interaction were the only relevant physics. The experimental observation, however, is that higher pressure actually reduces the strength of magnetic ordering in UGe_2 and so additional effects must play a significant role. One such addition is the RKKY interaction, as described below, and another is the Kondo effect, described in the next section.

The direct exchange interaction is typically short-ranged and in metals with large separation between lattice sites the effects of the exchange field may be vanishingly small. In metals with a high density of conduction electrons, however, the effects of *indirect* exchange can play a key role in the establishment of ferromagnetic order. Indirect exchange refers to the effective long-range magnetic interaction of local spin moments via their coupling to the conduction band electrons, a mechanism named the RKKY interaction (after Ruderman-Kittel-Kasuya-Yosida), which can be described (by classical analogy in a Drude-model-like manner) as follows. A local moment interacts with a nearby conduction electron, the interaction tending to align the electron spin to the local moment. The itinerant electron then moves on to interact with another local moment some distance away, tending to align the local moment to the electron spin. In this way the two local moments have an effective long-range magnetic interaction, tending to coalign their spins, mediated by the conduction electron, despite being too far apart to influence each other directly.

2.2.2 Itinerant Magnetism

In order to understand the Kondo effect, and how it and the RKKY interaction vary with pressure, the concept of itinerant electron magnetism must be introduced. Instead of magnetic moments localised to atomic sites, generated by the spin of unpaired valence electrons, consider now an electron gas populated from the conduction band. As before it is easier to start with the paramagnetic state and extend those concepts to low temperatures to reach ferromagnetism.

There are two competing energy costs associated with creating a magnetized system from electrons around the Fermi surface. There is the familiar energy cost $\Delta E = +\mu_B B$ for being anti-aligned to the field, leading to a number, n, of electrons transferring from anti-aligned states to aligned ones, creating a net total moment $m = 2n\mu_B$. The limit on n is the other energy cost, which is of transferring electrons from one spin state to the other, essentially shifting

electrons across the spin-split Fermi surface to higher momentum states and thus states of higher energy, according to the Pauli exclusion principle.

This is called Pauli paramagnetism. Unlike localised magnetism, where thermal disorder limits the magnetisation and keeps susceptibility small at high temperature, Pauli paramagnetism is governed by the temperature of the electron gas, the Fermi temperature, T_F, which does not change as sample temperature is varied. Therefore Curie's law is not observed and there is very little temperature dependence to the Pauli susceptibility; or rather Curie's law is indeed observed but for temperature T_F rather than sample temperature T. Since $T_F \gg T$ Pauli susceptibility is generally much smaller than the local moments case.

The dependence of Pauli paramagnetism on the Fermi energy, $E_F = k_B T_F$, can be approximated by realising that the electrons involved can only be those within the range $k_B T$ above or below the Fermi energy. Thus the fraction able to participate is $k_B T / E_F$, which when multiplied by the expression found for the net paramagnetic moment in equation 2.15, gives:

$$m = \frac{N\mu_B^2}{k_B}\frac{B}{T} \cdot \frac{k_B T}{E_F} = \frac{N\mu_B^2 B}{E_F} \tag{2.17}$$

A more accurate expression can be found by proper consideration of the density of states, though for the free electron gas, with its usual parabolic dispersion relation, the difference from the result in equation 2.17 is only a factor of $\frac{3}{2}$ and the general concept of a small, temperature invariant susceptibility remains robust.

Despite the paramagnetic effect associated with itinerant moments being relatively small, below the Curie temperature the system becomes ferromagnetic and the contribution from itinerant moments becomes significant. The reason for this lies, once again, in the exchange interaction, but also in the band structure and specifically in the density of states at the Fermi surface.

To estimate the magnitude of the exchange field it is useful to consider the average density of conduction electrons at any particular point, and so work with a neighbouring lattice site model as before, a local spin density approximation (LSDA) to the true delocalised nature of the electrons. Since the total net moment per site is now simply a sample average divided by the number of sites it is no longer reasonable to expect an integer number of μ_B as associated with an integer number of electrons. Instead the LSDA allows for fractional values of spontaneous

magnetization, such as the observed $M = 1.4\,\mu_B$ per uranium atom for UGe_2 or $M = 0.42\,\mu_B$ per uranium for URhGe.[1]

If a further approximation is made, that the exchange interaction strength is fairly constant in space (an approximation that underlies the Stoner model), then the so-called Stoner criterion for ferromagnetism becomes $IN(E_F) > 1$, where $N(E_F)$ is the density of states at the Fermi level and I is the Stoner parameter, which contains information about the strength of the exchange interaction. Thus for itinerant moments to order ferromagnetically a strong exchange interaction is required, which is perhaps obvious, and also a large number of electrons to participate in that interaction, a high density of states at the Fermi level. It is historically observed from experiment that very few metals have high enough $N(E_F)$ in combination with a strong exchange interaction to become fully itinerant ferromagnets, and it is of particular interest to the study on UGe_2 to note that application of pressure can vary $N(E_F)$, thus strengthening or weakening the ferromagnetic order.

It is also worth pointing out here that although an itinerant ferromagnet meets the Stoner criterion and thus the exchange field is strong enough to spontaneously coalign spins, the spontaneous moment is limited, as for Pauli paramagnetism, by the energy cost of increasing the population of the spin-alignment band and moving electrons to higher momentum states. Hence the spontaneous magnetization increases from zero to a maximum as temperature is lowered from the Curie temperature to absolute zero.

2.2.3 Kondo Screening and the Doniach Diagram

The Kondo effect is similar to the RKKY interaction in that it involves the coupling of local moments to conduction electron spins. The coupling in this case is antiferromagnetic and in the language of Kondo screening it is said that the local moment is screened by the itinerant conduction electrons to produce a non-magnetic entity. The local moment and conduction electron are effectively bound together like a pair of valence electrons, mutually cancelling each other's magnetic moment. The two are described as hybridised.

[1] Fractional values of the magnetic moment per atomic site can also arise due to the screening of the local moment by the conduction electrons, which reduces the moment by a variable amount. Changes in the screening strength can thus result in significant changes to the magnetization, even with no change in the strength of the local moments. See section 2.2.3 for more discussion on this type of screening.

This hybridisation with localised electrons dramatically slows the otherwise itinerant conduction electrons, which manifests as a greatly enhanced effective mass, as strong electron interactions were described to do in section 2.1 where the term heavy fermion was first introduced. Conversely, the hybridisation essentially incorporates valence electrons into the Fermi surface, resulting in a dramatic increase in the k-space density of the charges that carry the current, an increase in n possibly detectable by the Hall effect.

For instance, if the Kondo effect were to suddenly break down entirely, in the aptly named 'Kondo breakdown' scenario, there would be an accompanying jump in the Hall coefficient as the hybridised quasi-particles disintegrate and the Fermi surface shrinks. On the other hand, very strong Kondo screening can also lead to a decrease in charge carrier density and Fermi surface size, or conversely a weakening of the Kondo coupling strength can free conduction electrons from screening, making them more itinerant and increasing the charge carrier density while also increasing the magnetization.

If the coupling is strong enough, and there is a sufficient density of conduction electrons, then the system is said to be fully screened: every localised moment is hybridised with conduction electron spins to produce an entirely non-magnetic ground state and the sample magnetization will be zero. With weaker coupling, or insufficient numbers of conduction electrons compared to the number of localised moments, the system is under-screened (or partially-screened) and although the magnetization will be reduced compared to the complete absence of the Kondo effect the ferromagnetic ordering generated via the exchange interaction will still produce a finite magnetization.

The strength of both the RKKY interaction, responsible for long-range ferromagnetic order, and Kondo screening, responsible for a non-magnetic ground state, increases as temperature decreases, with the critical temperatures T_{RKKY} and T_K denoting the point at which each dominates the magnetic behaviour of the system. If $T_K > T_{RKKY}$ then at low temperature the system will be generally non-magnetic (or suffer from a heavily reduced magnetization in the partially-screened case). If $T_{RKKY} > T_K$ then at low temperature the system will be be more strongly ferromagnetic. These two critical points, indicating the relative strengths of the interactions, have significantly different dependence on the coupling strength, J, as shown by what is known as the Doniach diagram, seen in figure 2.3.

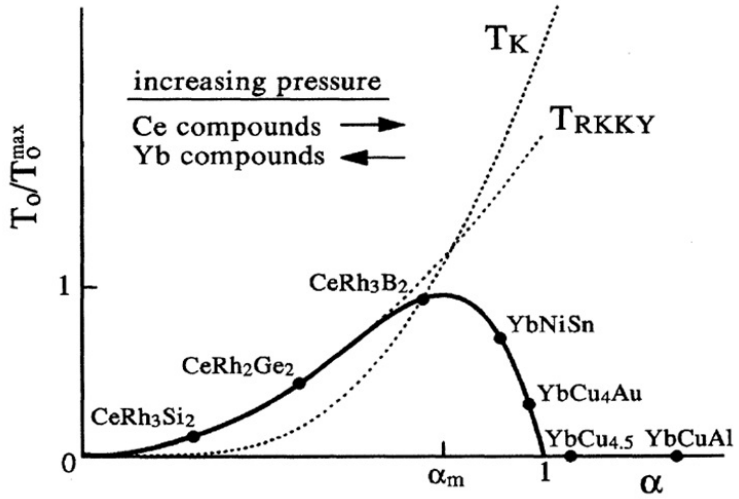

Figure 2.3 The generic Doniach diagram with the ambient pressure positions of several heavy fermion compounds. The characteristic asymmetric curve is the result of two competing magnetic interactions. Source: Ref. [12]

Specifically, it is useful to introduce parameter $\alpha = |J_f N(E_F)|$, where J_f is the magnetic exchange coupling strength and $N(E_F)$ is the density of states at the Fermi surface, a product which is familiar from earlier discussion on the Stoner criterion. Increasing α increases both T_{RKKY} and T_K, but the former scales as $T_{RKKY} \propto \alpha^2$ while the latter scales as $T_K \propto \exp(-1/\alpha)$. The magnetic ordering temperature, denoted T_0 in figure 2.3, depends on the relative strength of the two effects: starting from low α the RKKY interaction increasingly dominates and T_0 increases with α up to a maximum at α_m before the exponentially rising T_K becomes dominant and the system is increasingly non-magnetic due to Kondo screening until T_0 reaches zero Kelvin. This zero point, called a quantum critical point, is of particular interest because novel quantum states such as superconductivity can emerge in the vicinity, as discussed in section 2.6.

As mentioned earlier following the introduction of the direct exchange interaction, the effect of high pressure on a Heisenberg-type ferromagnet may be expected to increase the strength of the magnetic ordering by bringing lattice sites closer together. However, after the subsequent introduction of itinerant magnetism, it was seen that variation of the density of states can also play an important role in the strength of magnetic ordering, as well as indirect exchange interactions, as captured by the parameter α introduced above. Furthermore it was mentioned earlier that UGe_2 is an intermediate valence compound, with the $5f$ electrons having a mixed character, partly localised and partly itinerant. Application of pressure can change the level of this mix, altering the intermediate valence to

produce either stronger or weaker localised moments. The interplay between all these effects makes predicting how the strength of magnetic ordering will vary with pressure rather complicated.

A useful case study is presented in Ref. [12] regarding cerium and ytterbium compounds and their differing responses to high pressure. Application of pressure tends to squeeze valence electrons out of the $4f$ band and into the conduction band in these materials, which can either enhance or reduce the strength of the localised moments depending on the pairing of the valence electrons. Explicitly, for cerium increasing pressure leads to $Ce^{3+} \rightarrow Ce^{4+}(4f^1 \rightarrow 4f^0)$ and the reduction of the $4f$ orbital occupancy tends toward a non-magnetic state due to the lack of unpaired electron spins, whereas for ytterbium $Yb^{2+} \rightarrow Yb^{3+}(4f^{14} \rightarrow 4f^{13})$ and the increase in unpaired $4f$ electron spins leads to an increase in magnetization. Of course the situation is slightly more complicated than that.

For example, although the valence change in cerium compounds tends toward demagnetization, the increased delocalisation of the f-orbital electrons with increasing pressure, and the decreased separation between lattice sites, affects both the strength of the exchange coupling and the density of states. Since the magnetism is substantially itinerant in nature the overall result is an increase in the α parameter, which, because of the starting point on the Doniach diagram of most cerium compounds (see figure 2.3), actually strengthens the magnetic order. The increased strength of the RKKY interaction competes against the effects of Kondo screening and fractionally decreasing valence to increase T_0. Experimentally, it is observed that these compounds do indeed roughly follow the Doniach diagram curve as a function of pressure, with T_0 initially enhanced before dropping sharply.

By contrast, ytterbium is a much more localised system than cerium, with smaller $4f$-orbital radius, and so has reduced hybridisation with the conduction electrons. In this case the effects of the fractional valence change might be expected to be more dominant and lead to increased magnetic ordering with application of pressure. As can be seen from figure 2.3, the starting point for the ytterbium compounds is to the right of the peak in T_0 on the Doniach diagram, implying that an increase in strength of the magnetism would correspond to a decrease in α and therefore a decrease in both T_{RKKY} and T_K. Experimentally, this is indeed observed to be the case, with application of increasing pressure revealing a mirror-image of the Doniach diagram's asymmetric peak, i.e. traversing the curve shown in figure 2.3 from right to left.

Thus it would appear that in ytterbium compounds α decreases with pressure, while in cerium compounds it increases with pressure, with both resulting in an initial increase in the magnetic ordering temperature, despite also having opposite responses to the change in valence. In conclusion, the effects of pressure on the strength of magnetic ordering in these heavy fermion compounds, with dual natured (both local and itinerant) f-orbital electrons, is difficult to predict without the aid of experimental probes. Explaining the decrease in critical temperature T_X under increasing pressure for UGe_2 is also complicated by the dual nature of the f-electrons and the chosen experimental probe of the magnetic transition for this PhD project is the Hall effect.

2.2.4 Domains and Hysteresis

Before leaving the discussion on ferromagnetism it seems pertinent to describe a few important properties of the state. Firstly, upon transition from paramagnetism to ferromagnetism, order parameter M will often remain zero in a bulk measurement of sample magnetization. Application of a small field can then produce dramatic increases in the measured M, despite the internal fields being so much larger than the external field that it seems unlikely that a small applied field could possibly have such a large effect. The resolution of this puzzling behaviour is the idea of the magnetic domain structure.

The exchange field responsible for the ferromagnetic order is short-ranged but the classical interaction between the moments as magnetic dipoles, though very weak compared to the exchange field, is comparatively long-ranged and can span large numbers of lattice spacings. Over the scale of the system as a whole the dipolar energy can sum to be influentially substantial. In order to reduce the large dipolar energy, with minimal cost to the exchange energy reduction from parallel spin alignment, domains of opposite spin alignment will be created. Only over the short distance that the spin alignment flips orientation will the exchange energy not be fully minimised; across the majority of the domain volume the spins will be coaligned. Across the material as a whole the opposing regions of spin alignment will prevent the dipolar energy from accumulating and the domain structure results in an overall non-magnetic material, with M averaging to zero. The domain boundaries, or 'walls', are typically of the order 10 to 100 lattice sites in width, which allows the spin orientation to be gradually rotated instead of abruptly flipped. This is less costly to the exchange energy since over the

exchange interaction range of $1 \sim 2$ lattice spacings the spins are still roughly aligned.

Application of an external field readjusts the domain structure, moving the positions of the domain walls, enlarging the domains where the spin orientation is aligned to the the external field and shrinking domains where it is anti-aligned, leading to a rapid increase in M. Such a dramatic rise in M is possible because the relatively weak external field energy is competing only with the weak dipolar energy and not with the large exchange field energy, which is still the driving force behind parallel-spin alignment and the generation of ferromagnetic moments. As external field strength increases further the domain structure will adjust until the system is composed entirely of co-aligned spins, a situation known as the mono-domain state, and M is said to be saturated at the large value expected for a ferromagnet. Increasing the external field further will then produce only a relatively small change in M as the ferromagnetic ordering is gradually strengthened.

Domain wall motion can be reversible but more often it is hindered by defects in the crystal structure or any other 'potential well' imperfections that cause domain walls to become stuck at particular positions. To move past the position of a defect requires a certain strength of external magnetic field to force the walls out of the potential well. This means that, after reaching saturation of the magnetization, when the external field is removed any defects in the material may prevent the original domain structure from forming and M returning to zero. Instead the hindered wall motion leaves domains with alignment parallel to the past external field larger than domains anti-aligned to the field, resulting in a finite average magnetization with the same direction as a field that is no longer present. Hence the state of the domain structure depends on the past, on the history of the material: a so-called hysteresis effect. The finite M observed in the absence of any external field is called the remnant magnetization, and the field required to be applied in the direction opposite the remnant magnetization to force domain walls to move past the defects and return the system to a fully demagnetized state is called the coercive field.

2.3 The Hall Effect

The classical Hall effect is a relatively simple phenomenon. Under the influence of an externally applied magnetic field, the moving charges that constitute an electric current will be subject to a force, the Lorentz force, a cross product of the magnetic field and the charge velocity. The Lorentz force pushes charges transverse to the direction of current, one way for holes and the other for electrons, creating a transverse potential difference known as the Hall voltage, as shown by the diagram in figure 2.4.

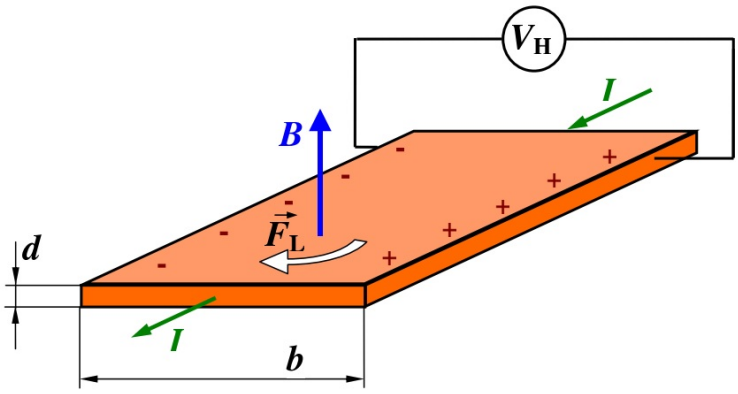

Figure 2.4 Diagram of the Hall effect. Field B produces a Hall voltage V_H transverse to current I due to the Lorentz force $\vec{F_L}$. Source: Ref. [13]

In an equilibrium state the Hall voltage, V_H, depends on the applied field, H, the number density of charge carriers, n, and the current, I. Defining a 'Hall resistivity', usually denoted ρ_{xy} to represent voltage in the y direction for current in the x direction (and therefore magnetic field in the z direction), where $\rho_{xy} = V_H\, d/I$ for some length scale d, the basic formula for the Hall effect is written:

$$\rho_{xy} = \frac{1}{ne}(\mu_0 H) = R_0(\mu_0 H) \tag{2.18}$$

where R_0 is the Hall coefficient and is negative for electrons and positive for holes. The length scale d is, by the van der Pauw method (see section 3.4), equal to the thickness of the sample. Using the same method, the component of resistivity parallel to the current, denoted ρ_{xx} and sometimes referred to as the longitudinal resistivity, can be defined using a different length scale based on the sample dimensions (again, see section 3.4), and in an applied field could be called 'magnetoresistivity'.

In this thesis, the terms longitudinal resistivity and magnetoresistivity, to refer to component $\rho_{xx}(H)$, will be used almost interchangeably. The term magnetoresistance will more often be used for the relative change in resistance with field, the $\Delta\rho_{xx}/\rho_0$ quantity first defined in section 2.1.2. Similarly, the terms transverse resistivity and Hall resistivity, to refer to component $\rho_{xy}(H)$, will also be used interchangeably.

For a multi-band material, such as UGe_2, there are often both hole and electron bands at the Fermi level. In this case two different Hall coefficients can be defined, $R_e = -1/n_e e$ for electrons and $R_h = 1/n_h e$ for holes, and the relationship between the Hall coefficient and the resistivity becomes more complicated. The relevant formulae are given very neatly in Ref. [65], with reference to Ref. [16], as:

$$\rho_{xy}(H) = \frac{\sigma_h^2 R_h + \sigma_e^2 R_e + \sigma_h^2 \sigma_e^2 R_h R_e (R_h + R_e)(\mu_0 H)^2}{(\sigma_h + \sigma_e)^2 + \sigma_h^2 \sigma_e^2 (R_h + R_e)^2 (\mu_0 H)^2} (\mu_0 H) \tag{2.19}$$

$$\rho_{xx}(H) = \frac{\sigma_h + \sigma_e + \sigma_h \sigma_e (\sigma_h R_h^2 + \sigma_e R_e^2)(\mu_0 H)^2}{(\sigma_h + \sigma_e)^2 + \sigma_h^2 \sigma_e^2 (R_h + R_e)^2 (\mu_0 H)^2} \tag{2.20}$$

where σ_h and σ_e are the mean conductivities of the hole bands and the electron bands respectively (sometimes expressed as mobilities, in Ref. [35] for example).

Straightforward derivations of equations 2.19 and 2.20 can be found in chapter 1 of Ref. [28], chapter 7 of Ref. [66] or chapter 7 of Ref. [52]. Essentially the the electron or hole currents from the different bands, in both x and y directions, are calculated and the resultant current due to the magnetic field is then simply given by the sum over all bands. After what Ref. [66] calls "some tedious algebra" the components of the current can then be converted into resistivities ρ_{xx} and ρ_{xy}.

It is worth recalling that these formula are only really valid in the same conditions as Kohler's law (section 2.1.2) is valid, and are subject to the same invalidating circumstances.

There is technically no limit to the number of bands, or their type, and the formulation presented on page 251 of Ref. [52] allows for easy expansion to an arbitrary number of bands. Usually just two bands are considered, one electron and one hole, in order to keep the formulae meaningful. A two band model is more useful, regarding the pragmatic interpretation of experimental results, than a model where the resistivity is related to a great number of different terms practically inseparable from one another.

Having said that, at the very least a model for UGe_2 should include four bands, both spin up and spin down bands for both holes and electrons. Band structure calculations, and data from de Haas-van Alphen oscillations,[5] suggests that there are four Fermi surfaces in the ferromagnetic state, in which case an eight band model should ideally be employed, considering the spin splitting. However, since there is a conductivity and a Hall coefficient for each band, such a model would involve 16 free parameters and interpreting a simple resistance measurement in terms of 16 parameters is somewhat meaningless.

A simplification can be introduced if the material is compensated, such that the number density of holes is equal to the number density of electrons (for a particular spin state at least). Retuning to equations 2.19 and 2.20 for a two-band model, setting $R_e = -R_h = R_H$ gives:

$$\rho_{xy}(H) = \frac{(\sigma_h^2 - \sigma_e^2)R_H}{(\sigma_h + \sigma_e)^2}\,(\mu_0 H) \tag{2.21}$$

$$\rho_{xx}(H) = \frac{\sigma_h \sigma_e R_H^2 (\mu_0 H)^2 + 1}{\sigma_h + \sigma_e} \tag{2.22}$$

From equation 2.22 it can be seen that an obvious characteristic of a compensated metal is quadratic magnetoresistance (though ρ_{xx} saturates at some constant value at high field according to equation 2.26). This is in accordance with Kohler's law, the form of which is more easily recognised in equation 2.22 by replacing $1/(\sigma_h + \sigma_e)$ with ρ_0 and approximating $\sigma_h \sigma_e \sim 1/\rho_0^2$. Rearranging then produces the relation $\Delta\rho/\rho_0 \sim R_H^2(\mu_0 H)^2/\rho_0^2 \sim (\omega_c \tau)^2$.

It should be noted, however, that all of the discussion in this section is strictly only correct for an isotropic system. For an anisotropic material the conductivities will be different in different directions and equations 2.19 and 2.20 would become much more complicated. In this case the behaviour of the magnetoresistance need not be perfectly quadratic even for a compensated metal.

It should also be noted that compensation does not necessarily imply, for a multi-band material, that the Hall coefficient will be zero. Equation 2.21 shows that there can still be a finite Hall resistivity due to differing carrier mobilities on each band. Also it is likely that in the four-band model mentioned earlier, although pairs of Fermi surfaces are compensated, such as up spin electron and up spin hole, it does not necessarily follow that all four are compensated such that the up spin electron band is as densely populated as the down spin hole band for

instance.

A good discussion on the topic of compensation in metals can be found in Ref. [67]. In UGe_2 there are an even number of formula units (four) per unit cell, and both uranium and germanium have even atomic numbers, therefore there should be even numbers of electrons involved and the material *is* expected to be compensated.[30] In this case a four-band analysis of the Hall resistivity might be possible due the reduction in the number of free parameters and the reduced complexity of the relevant formulae.

Complexity can easily be added back into the model though, considering things like open Fermi surfaces (it is difficult to characterise an open sheet as either electron-like or hole-like and so the restrictions imposed by compensation become rather vague) or the shape of the surfaces (introducing sharp corners, such as for a square-like geometry, changes the behaviour of the resistivity from quadratic in field to linear; see Ref. [28] for example), and also the effects of anisotropy as mentioned earlier.

Significant simplification in the analysis of the Hall resistivity can also be achieved by consideration of the high and low field limits of the theory, as discussed earlier in section 2.1 with reference to chapter 1 of Ref. [51]. The now-familiar expression $\omega_c\tau = \sigma R_H(\mu_0 H)$ makes it obvious how the two criteria ($\omega_c\tau \gg 1$ or $\ll 1$ respectively) will affect equations 2.19 and 2.20. Essentially the terms near the right-hand side of these equations differ from those on the left by a factor of $(\omega_c\tau)^2$ and the two formulae can easily be simplified into high and low field limits.

In the low field limit, such that $\sigma R(\mu_0 H) \ll 1$, the Hall coefficient simplifies to:

$$R_0 \simeq \frac{\sigma_h^2 R_h + \sigma_e^2 R_e}{(\sigma_h + \sigma_e)^2} \tag{2.23}$$

and the longitudinal resistivity simplifies to the obvious constant:

$$\rho_{xx} \simeq \frac{1}{\sigma_e + \sigma_h} \equiv \rho_0 \tag{2.24}$$

In equation 2.23 the conductivities are essentially weighting factors, with R_0 given by the weighted average of the hole and electron Hall coefficients. In this case a change in sign (or absolute value) of R_0 is somewhat difficult to interpret, since this indicates a change in dominance (or magnitude) of the product of

conductivity and carrier density of electrons and holes rather than simply a change in dominance (or magnitude) of the type of charge carrier.

In the high field limit, such that $\sigma R_0(\mu_0 H) \gg 1$, the interpretation is simpler. In this case the formulae become:

$$R_0 \simeq \frac{R_h R_e}{R_h + R_e} = \frac{1}{e(n_h - n_e)} \tag{2.25}$$

$$\rho_{xx} = \frac{\sigma_h R_h^2 - \sigma_e R_e^2}{\sigma_h \sigma_e (R_h + R_e)^2} \tag{2.26}$$

In the high field limit the magnetoresistivity saturates at some constant value, leading to a stretched-S-shape behaviour in a plot of ρ_{xx} as a function of field, where the H^2 behavior at lower field changes curvature at some critical value to level out at the high field limit. The critical value where the curvature changes is, of course, the $\omega_c\tau = 1$ point, and around this field the magnetoresistivity will be roughly linear. For an example, the line of best fit seen in figure C.1 in appendix C demonstrates this S-shape.

The high field limit Hall coefficient is simply related to the inverse of the difference between the hole and electron density. This means that if there are more holes than electrons R_0 is positive. This is in contrast to the low field limit stated in equation 2.23, where, supposing that the conductivities were roughly equal, a greater number of holes than electrons results in a negative R_0 (since $R_e > R_h$ and R_e is negative).

Thus the interpretation of R_0 must be approached carefully, taking into account the value of $\omega_c\tau$ over the measurement range. Of course if the system is compensated then equation 2.21 applies for any value of $\omega_c\tau$ and the interpretation of the Hall coefficient is much simplified.

After analysis of the results obtained in this project, the $\omega_c\tau = 1$ critical field for UGe_2 around 2 K was found to be about 10 T, placing the material awkwardly between the two simplifying limits for most of the measurement range (0.25 to 9 T). Of course the quantity $\omega_c\tau$ is specific to each individual band and so there is technically no single, defining limit for the material as a whole, but 10 T is a good order-of-magnitude estimate. At higher temperatures, τ decreases, or equally σ decreases, and so the material moves closer to the low field limit.

Initially the results of the UGe_2 investigation seemed to suggest that the system

was well within the low field limit. The conductivity is typically $\sigma \sim 10^7\,\mathrm{Sm}^{-1}$ and the ordinary Hall coefficient $R_0 \sim 3\times10^{-10}\,\mathrm{m}^3\mathrm{C}^{-1}$, thus at 1 tesla $\sigma R(\mu_0 H) \sim 0.003 \ll 1$ and even at at 10 tesla $\omega_c\tau < 1$. Hence it appeared at first that equation 2.23 should be used to fit and interpret the resistivity data.

In the two-band formulation, the magneoresistance is defined as:

$$\frac{\rho_{xx}(H)-\rho_{xx}(0)}{\rho_{xx}(0)} = \frac{\Delta\rho_{xx}}{\rho_0} = \frac{\sigma_h\sigma_e(R_h\sigma_h - R_e\sigma_e)^2(\mu_0 H)^2}{(\sigma_h+\sigma_e)^2 + \sigma_h^2\sigma_e^2(R_h+R_e)^2(\mu_0 H)^2} \tag{2.27}$$

The quantity on the left hand side of equation 2.27 is referred to in Ref. [66] as "the relative increase in resistivity." This is a particularly useful quantity to work with if the magnetoresistivity is not quantitatively accurate (as in the basic van der Pauw set-up for Hall effect measurements), because by using the *relative* increase the absolute magnitude does not matter as much as the percentage change, which *is* accurately quantified.

An interesting point to note here is that $\Delta\rho_{xx}$ as defined above is always positive. When the above formula is valid the resistivity increases quadratically with increasing field (at low to moderate field strength at least) and there is no available criterion for negative magnetoresistance. In the UGe_2 investigation however, there were various instances of negative $\Delta\rho_{xx}$ encountered, indicating the regions, close to phase transitions, where this formula (and so also Kohler's law) is invalid.

Having four free parameters (σ_e, σ_h, R_e and R_h) in equation 2.27 makes experimental data too easy to fit. The fitting procedure becomes heavily dependent on initial guesses for the parameters and inherently unstable (too many different local minima in the least-squares values, essentially). The fitting procedure can be constrained, however, by removing some of the free parameters. Use of the experimentally determined ordinary Hall coefficient and substitution of the formula for the low field limit allows either R_h or R_e to be eliminated.

Rearranging and substituting equation 2.23 to eliminate R_e in equation 2.27 provides the following expression:

$$\frac{\Delta\rho_{xx}}{\rho_0} = \frac{\sigma_h\sigma_e\big(R_h\sigma_h\sigma_e - R_0(\sigma_h+\sigma_e)^2 + \sigma_h^2 R_h\big)^2(\mu_0 H)^2}{\sigma_e^2(\sigma_h+\sigma_e)^2 + \sigma_h^2\big(R_h\sigma_e^2 + R_0(\sigma_h+\sigma_e)^2 - \sigma_h^2 R_h\big)^2(\mu_0 H)^2} \tag{2.28}$$

Equation 2.24 allows another one of the free parameters (either σ_e or σ_h) to

be eliminated from equation 2.28. The quantity $\rho_{xx}(H \to 0)$ is known from measurements and at ~ 0 T the system is definitely in the low field limit, such that $\rho_{xx}(H \to 0) = 1/(\sigma_h + \sigma_e)$.

From experience of fitting the data for the UGe_2 project, this last step was found to be not strictly necessary, however having only two free parameters did help stabilise the fitting procedure and the same results were found as for fitting to 2.28 with three free parameters.

By fitting experimental data to equation 2.28 R_e and σ_e can be determined and then σ_h and R_h found from equations 2.24 and 2.23 respectively. The results from such analysis at low temperature (~ 2 K) are not particularly self-consistent, however.

The resulting values for the conductivities are roughly the $\sigma \sim 10^7\,\mathrm{Sm}^{-1}$ stated earlier, but the individual hole and electron Hall coefficients are found to be significantly larger than R_0, at around $R \sim 2 \times 10^{-8}\,\mathrm{m}^3\mathrm{C}^{-1}$. Therefore at 1 tesla $\sigma R(\mu_0 H) \sim 0.1$ and at 10 Tesla $\omega_c \tau \sim 1$. Thus the system is not actually in the low field limit for most of the field range and the whole analysis procedure at 2 K breaks down somewhat.

Furthermore, the magnetoresistance is found to be negative across much of the interesting range of temperature and pressure and so unfortunately cannot be fitted to equation 2.28. Bearing this in mind, and the result that UGe_2 is in an awkward 'intermediate field' regime, and the fact that it really requires a model with more than two bands, and is electrically anisotropic unlike the isotropic theory, formulae such as 2.27 might be considered of limited use for investigations of real, complex materials.

Having said that, the Hall effect is still a very useful experimental probe, even at the analysis stage of obtaining R_0 and judging it based on equation 2.23 without actually obtaining the quantitative characteristics of individual bands. To truly understand the number, type and size of Fermi surfaces in the material and how these parameters, and the complex shape of the surfaces, evolve under application of pressure it would be necessary to measure quantum oscillations (see section 2.4) while rotating the sample relative to the applied field. There are however many reasons why Hall effect measurements are a preferable experimental probe of the Fermi surface.

Why not measure quantum oscillations instead?

Firstly, since UGe_2 is a heavy fermion material and the effective mass of the charge carriers is expected to be very large, extremely low temperatures and high magnetic fields are required in order to produce quantum oscillation amplitudes larger than the noise level inherent in the measurements. Very high purity samples are also required, as detailed in section 2.4. For the highest quality samples of UGe_2 currently available, the dilution refrigerator base temperature (~ 50 mK in high field conditions) together with the highest fields available in-house (the range from about 10 up to 17 T) were found to be necessary to observe quantum oscillations in the resistivity at ambient pressure. This means that for high pressure measurements around P_X a pressure cell would have to be loaded into a dilution refrigerator, while ideally mounted on a two-axis rotator.

Setting up this experiment encounters a whole host of difficulties. The cell would need to be much smaller than the one used in this PhD project to fit onto the dilution fridge field-center sample stage. It would need to be smaller still to fit onto a two-stage rotator and likely just a single-axis rotator would have to be used, although this would still require a pressure cell not much bigger than a stack of a few large coins. Generating pressures up to ~ 20 kbar from such a small cell would be tricky, but certainly not impossible, a diamond or sapphire anvil cell could do it easily, although maintaining intact measurement wires across an anvil and gasket setup is challenging.

Attempting to measure magnetization, usually by a.c. susceptibility in this situation, is equally challenging since the sample would necessarily be very small (if the pressure cell as a whole is only a few centimeters across then there would only be a tiny space available for the sample within the pressurised environment), which leads to a small measurement signal lost within the background susceptibility. Ideally the pick-up coil would be surrounding the sample within the pressurised environment, which would reduce the background signal, though again the difficulty of passing unbroken, non-shorting wires through the anvil and gasket is encountered. Furthermore, providing enough cooling power to maintain the sample at ~ 50 mK while at ~ 15 T is difficult even when good thermalisation to the dilution fridge mixing chamber is provided; when the sample is within a pressure cell and mounted on a rotator it would be ambitious to maintain such a base temperature.

In summary, high pressure quantum oscillation measurements on a heavy-fermion

compound like UGe_2 are extremely difficult and therefore very time consuming, and to perform them multiple times while stepping across the phase diagram in pressure would require multiple years. Hall effect measurements on the other hand are relatively quick and easy, and measurements (down to 2 K and up to 9 T in this PhD project) can be performed using a quick turnaround cryostat system and relatively bulky piston-cylinder cells. This allows for good resolution in pressure, since a reasonably high number of experimental runs (12 in the vicinity of P_X in this project) can be completed in a timely fashion.

Hall effect measurements also allow a wide temperature range to be probed, unlike any potential quantum oscillation study where measurements above 1 K would almost certainly not be possible with the observed temperature dependence of the oscillation amplitudes for UGe_2. Thus changes across T_X can be observed, as well as any high temperature consequences of crossing the critical pressure. The Hall effect also allows similar flexibility in measuring changes as a function of field, specifically at H_X, whereas the high fields necessary for quantum oscillations would obscure such relatively low field behavior; measuring the FM1 state around P_X would be basically impossible, the high field driving the system into the FM2 state instead (alternatively the field could be applied along one of the hard axes, although that would severely limit the rotation angles at which the extremal areas of the Fermi surfaces could be measured, leading to a markedly incomplete picture).

In conclusion, the Hall effect is, for the aims of this project, the best available experimental probe of the Fermi surface and how it evolves across the pressure-temperature-field phase diagram of UGe_2.

2.3.1 The Anomalous Hall Effect

The presence of magnetism within the material produces a contribution to the Hall voltage in addition to the classical Hall effect due to the Lorentz force, which is henceforth referred to as the 'ordinary' Hall effect. This additional contribution is proportional to the magnetization, M, of the sample, rather than the applied field, and is known as the 'anomalous' Hall effect.

For a theoretical review of the various mechanisms that give rise to the anomalous Hall effect (AHE) the reader is referred to Refs. [14, 68–75] since only a brief summary of what is a complicated field of study will be included below.

Thankfully, despite the theoretical complexity of the AHE, the phenomenological behavior is simple and well known, established empirically by experimental investigations in the 1930s and encapsulated by the equation:

$$\rho_{xy} = \mu_0(R_0 H + R_a M) \tag{2.29}$$

where R_a is the anomalous Hall coefficient. The coefficient R_a can be related to either (or both) the longitudinal resistivity or the resistivity squared depending on the dominant mechanism responsible for the AHE, as discussed below. In general terms this dependency can be written:

$$R_a \simeq R_{a_1}\rho_{xx} + R_{a_2}\rho_{xx}^2 \tag{2.30}$$

and so equation 2.29 can be expanded into the general expression:

$$\frac{\rho_{xy}(T,P,H)}{\mu_0 H} = R_0 + \Big[R_{a_1}\rho_{xx}(T,P,H) + R_{a_2}\rho_{xx}^2(T,P,H)\Big]\frac{M(T,P,H)}{H} \tag{2.31}$$

An important distinction to make here is that in equation 2.31 it is implied that the anomalous Hall coefficient has field dependence, via the field dependence of the resistivity. More accurately, however, R_a is related to powers of τ and is only empirically related to ρ_{xx} due to its direct dependence on the scattering rate. Since τ generally has no field dependence, then generally R_a should have no field dependence, and instead equation 2.29 should be used to fit to experimental data as a function of field, extracting the coefficient R_a as a function of temperature, which then can be related to powers of ρ_0.

The decision to use $\rho_{xx}(H)$ in the expansion of equation 2.29 into equation 2.31 stems from the field dependence of τ when in close proximity to a metamagnetic transition. Since there are different values of τ in the two different ferromagnetic phases of UGe_2 and application of field moves the system around the phase diagram, closer or further away from the phase transition, there will be an unavoidable field dependence to the scattering rate.

Furthermore, since the interesting data for this project is precisely that from very close proximity to the phase transition, performing the investigation away from the critical points, where the field dependence of τ disappears, is not a good alternative. Thus the somewhat unconventional formula shown in equation 2.31

was used for the main analysis of the Hall effect in this thesis, but it should be noted that it is indeed unconventional.

Although phenomenologically straight-forward, the underlying physics expressed by the signs and magnitudes of R_{a_1} and R_{a_2} remains to this day a difficult theoretical problem. The AHE has only been understood with any clarity in the last few years after great progress was made over the first decade of the 21st century. The history of the phenomenon stretches back a long time however, almost as far back as the discovery of the ordinary Hall effect. Indeed it was Edwin Hall who, in 1881, first observed 'anomalous' behaviour in the transverse conductivity of ferromagnetic materials.[76]

The main theories of the AHE were proposed many years later. These were the Karplus-Luttinger (KL) mechanism[77] in 1954, the skew-scattering mechanism[78] by Smit in 1958, and the side-jump mechanism[79] by Berger in 1970. The debate over which theory was primarily responsible for the observed AHE was swiftly resolved by the realisation that all three mechanisms contribute to produce a combined effect and, depending on the regime in terms of interaction strengths and sample purities, all three are relevant. A more extended debate then continued as to exactly what contribution each mechanism made to the combined effect and how these could possibly be untangled and individually determined by their dependence on the resistivity ρ_{xx}, which proved more difficult to resolve.

The three mechanisms contributing to the Hall effect are quantum mechanical in nature but are commonly described in semi-classical language with treatments based on the Boltzmann transport equation. All three arise as a consequence of the spin-orbit interaction (SOI) of electrons in a metal under the influence of an external electric field, and the separation of the full quantum treatment of spin-orbit coupled electron transport into three distinct phenomena is slightly messy, though the categorisation is useful for an intuitive understanding of the AHE.

Skew Scattering Mechanism

Skew scattering is perhaps the easiest of the three to understand intuitively. It refers to the asymmetric scattering of electrons from impurities due to the SOI and is described as extrinsic in origin since it depends only on the presence of impurities and not on properties intrinsic to the material. Since this contribution completely neglects the band structure, and the interband coherence effects that

give rise to the intrinsic AHE, it is the only mechanism that can be satisfactorily described by traditional Boltzmann transport theory.[14]

The Boltzmann transport equation makes use of the principle of detailed balance, that the transition probability from state n to m is the same as the reverse, from m to n. Including the spin-orbit interaction a transition that is right-handed with respect to the magnetization direction has a different probability to the left-handed one, meaning that for a particular spin orientation electrons are preferentially scattered either left or right, leading to a transverse Hall conductivity. These asymmetric contributions to the conductivity appear at 3rd order in a perturbation theory calculation of the scattering amplitude after collisions.[14]

Skew scatting results in an angular deflection of the electron velocity and so the resultant Hall angle is independent (in the 'clean' limit at least) of the impurity density: only occasional collisions are required to produce a transverse current. This suggests that the skew scattering contribution to the anomalous Hall conductivity is proportional to the Bloch state transport lifetime, τ, or, equally, inversely proportional to the scattering rate.

Stated another way, such angular deflections independent of the impurity density implies that the anomalous Hall resistivity is simply proportional to the longitudinal resistivity, i.e. $\rho_{xy}^{\mathrm{AH}} \sim \rho_{xx}$ at $T = 0$. In fact it is this relationship that Ref. [14] uses to *define* skew scattering, and so coefficient R_{a_1} in equation 2.31 would be related to the strength of the skew scattering mechanism simply by definition.

Proportionality to τ also implies that skew scattering is expected to dominate in clean materials and nearly perfect crystals, where the clean limit is defined in Ref. [14] as typically $\rho_{xx} < 10^{-8}\,\Omega\,m$ at $T = 0$. Essentially, skew scattering is dominant when $\hbar/\tau < U_{\mathrm{imp}}\,E_{SO}\,D$ where U_{imp} is the impurity potential, E_{SO} is the energy of the spin-orbit interaction, and D is the density of states at the Fermi level.[71] As temperature increases and the scattering rate increases there is a crossover to a regime where other mechanisms dominate the AHE.

The crossover can be seen in studies of the Lorenz ratio (the ratio of the thermal to the electrical Hall conductivity, divided by temperature), as in Ref. [73], which reports an almost constant Lorenz ratio across the clean regime that then suddenly drops as ρ_{xx} increases through the crossover and the scattering-free intrinsic AHE begins to dominate.

There are also contributions to the AHE from skew scattering that give $\rho_{xy}^{\mathrm{AH}} \sim \rho_{xx}^2$, which Ref. [68] terms 'intrinsic' skew scattering (despite originating from impurity scattering) while Ref. [14] prefers to put these contributions under the banner of the side-jump mechanism due to their similar consequences for ρ_{xy}^{AH} (despite having a different origin). Defining skew scattering as whatever causes a $\rho_{xy}^{\mathrm{AH}} \sim \rho_{xx}$ contribution also avoids complications from phonons.

Even for very pure samples and almost perfect crystals, inclusion of phonon scattering into the skew scattering mechanism changes the characteristic ρ_{xx} dependence to $\rho_{xy}^{\mathrm{AH}} \sim \rho_{xx}^{\beta}$ at finite temperature, with β shifting away from 1 and toward 2 as temperature rises. It is also worth highlighting a theory from Kondo in 1962,[80] which suggests $\rho_{xy}^{\mathrm{AH}} \sim \rho_{xx}^2$ for skew scattering from magnetic excitations at finite temperature. Such complications add to the confusion surrounding the theoretical description of the AHE.

Side Jump Mechanism

The side-jump mechanism is the other extrinsic contribution to the AHE due to electron collisions with impurities and the influence of the SOI. In contrast to skew scattering, however, the magnitude of the side-jump conductivity is independent of the scattering rate and so can dominate in 'dirty' materials at higher temperatures, where the contribution to the Hall conductivity from skew scattering is greatly reduced.

As mentioned earlier, Ref. [14] simply defines the side-jump contribution as any extrinsic mechanism that results in $\rho_{xy}^{\mathrm{AH}} \sim \rho_{xx}^2$, regardless of the physical origin, although the original side-jump mechanism proposed by Berger[79] is indeed based on a single, understandable physical process. A good description of the two possible SOI influenced scattering processes is provided in Ref. [70], which remarks that "the side-jump is a pure quantum effect and has no classical equivalent."

The side-jump mechanism refers to a lateral displacement (typically 10^{-11}m)[70] of the centre of an electron wavepacket during scattering, which, because of the SOI, is asymmetrical in respect to the spin state. The initial plane-wave is transformed by scattering into a spherical wave with its centre displaced from that of the impurity potential in a direction (perpendicular to both the momentum and spin) that is opposite for spin-up and spin-down states. The magnitude of the displacement is found to be dependent on the Fermi momentum and the

Compton wavelength for electrons, as might be expected.

There can also be a longitudinal shift in position during the scattering process, though as Ref. [69] notes, this has no impact on the Hall conductivity so can be ignored. The transverse shifts in position during each scattering event sum to produce the overall side-jump effect, a transverse current measurable as a Hall voltage. According to Ref. [69], the "most important feature of the side-jump contribution is that it yields a Hall conductivity that is independent of the impurity concentration...it is essentially an *intrinsic* contribution just like the Karplus-Luttinger term, and, therefore, yields a contribution to the Hall resistivity that is proportional to ρ_{xx}^2."

In fact, the similarity between the KL and side-jump mechanism goes deeper than yielding a contribution to the AHE with the same proportionality to the longitudinal resistivity. The additional transverse momentum gained by an electron wavepacket during a collision event, in the presence of an impurity potential, which gives rise to the side-jump mechanism, is essentially the same phenomena as the anomalous velocity resulting from the KL mechanism. In the former the driving influence is the local electric field of the impurity and in the latter it is the influence of the external electric field applied to the system as a whole. Thus it is unsurprising that they yield similar contributions to the AHE, though these similarities also add to the general confusion surrounding the topic.

Karplus-Luttinger Anomalous Velocity

The KL theory[77] identifies, by inclusion of the SOI, an additional contribution to the electron velocity, perpendicular to an externally applied electric field and dependent only on the band structure of the material. The independence of the KL contribution from impurity scattering leads to it being called the intrinsic mechanism of the AHE and gives rise to the characteristic $\rho_{xy}^{\mathrm{AH}} \sim \rho_{xx}^2$ relationship.

As with side jump and skew scattering, where the asymmetry of the scattering is due to the spin state and so a definite preference for a particular spin direction (i.e. a finite magnetization) is required to produce a net Hall current, the presence of ferromagnetism is also required for the KL mechanism to produce a net effect. More accurately, the intrinsic AHE is zero unless time-reversal symmetry is broken, as it is spontaneously in a ferromagnet. This is because the anomalous velocity has different sign on different spin bands and cancels out entirely unless

the spin degeneracy of the band structure is lifted by, for instance, the Zeeman-like splitting that occurs for the ferromagnetic state.[68]

Since it is a population imbalance of different spin states that yields both net extrinsic and intrinsic anomalous Hall conductivity, and it is the same imbalance that provides the finite magnetization that characterises ferromagnetism, it is clear why the AHE is proportional to the magnetization, as determined empirically and encapsulated by equation 2.29.

The intrinsic AHE is governed by the perfect crystal Hamiltonian, neglecting lattice disorder and including the SOI term, and is related to changes in the phase of Bolch states under the influence of the electric field, which causes them to evolve in crystal momentum space.[14] This additional phase gives rise to an additional term to the group velocity of the Bloch wavefunctions, transverse to the electric field, and the Hall conductivity is obtained simply from the sum over all occupied states.

The additional velocity term present in the KL theory arises from "interband matrix elements of the current operator" and "quantum coherent band mixing effects", as stated in Ref. [14], but is more easily understood in the modern formulation using the Berry phase and Berry curvature. Indeed it was reformulating the KL mechanism in terms of Berry phase that has allowed advances to deeper understanding of the AHE in the 21st century and a clearer separation of the intrinsic and extrinsic mechanisms and their physical causes.

Berry Phase and the AHE

An excellent introduction to the Berry phase is provided by Ref. [69], starting from classical physics and the concept of anholonomy. The classical analogy to the Berry phase can be seen in 'parallel transport' of vectors in geometry, which refers to the transportation of a vector across a surface without ever rotating it about the surface normal. When the surface is a flat plane there is no change in the vector when transporting it around a closed loop, but when the surface is curved, like that of a sphere, the vector can gain a rotation relative to its initial orientation when it is transported back to the same starting position, as demonstrated by figure 2.5. This phenomenon is called anholonomy.

In general holonomy is defined in terms of connections on manifolds (rather than the more specific case of vectors on curved surfaces). A connection is a

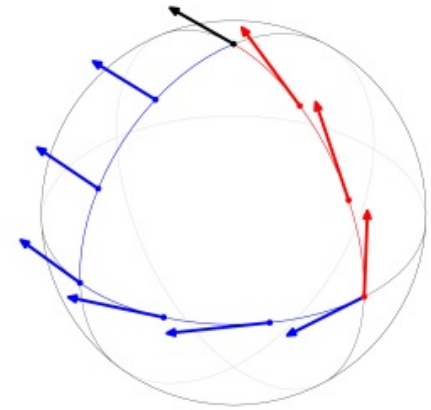

Figure 2.5 Demonstration of anholonomy for the case of vectors on a spherical surface. Starting with the red path, parallel transport to the pole then down along the blue path back to the starting point results in a rotation between the orientation of the initial red arrow and the final blue arrow.

geometric object on a smooth manifold that connects nearby tangent spaces, and the holonomy is a measure of the extent to which parallel transport around a closed loop fails to preserve the geometrical data being transported due to the curvature of the connection. Just as in the above example the vector picks up a rotation due to the curvature of the spherical surface, a quantum state can pick up an additional phase when transported around a closed loop due to the curvature of the Berry connection.

The Berry phase introduced in 1984[81] refers to the phase gained by a quantum system adiabatically transported around a closed circuit C in the space of some external parameter. For the AHE the parameter of interest is the crystal momentum, $\vec{k}$. The Berry phase picked up by the system depends only on the geometry of C and thus the shape and topology of the band structure in k-space.

The importance of what came to be known as the Berry phase was initially overlooked, from the birth of quantum theory until 1984, since in quantum mechanics the expectation value of any observable quantity has no dependence on the phase of the wavefunction. However, the Berry phase is given by the integral around C of the Berry connection, which can be transformed to a surface integral (Stokes' theorem, essentially) by introduction of a gauge field known as the Berry curvature. It is this field that gives rise to the anomalous velocity in KL theory, despite the additional phase of the transported quantum state having no direct effect on observable parameters such as conductivity.

In more mathematical language, consider a quantum state $|\phi_n(t)\rangle$ transported

around a circuit in k-space such that $|\phi_n(t)\rangle = \exp(i\gamma_n(t))|n(\vec{k})\rangle$ where $|n(\vec{k})\rangle$ are fixed eigenstates of the Schrödinger equation and $\gamma_n(t)$ is the phase.

The Berry phase is given by the integral of the Berry connection, $\vec{A}^n(\vec{k}) = i\langle n(\vec{k})|\nabla_{\vec{k}}\, n(\vec{k})\rangle$, as in equation 2.32.[69]

$$\gamma_n(C) = \oint_C i\langle n(\vec{k})|\nabla_{\vec{k}}\, n(\vec{k})\rangle \cdot \mathrm{d}\vec{k} \tag{2.32}$$

The integral in equation 2.32 can be transformed to a surface integral by replacing the Berry connection with the Berry curvature, B, using $\vec{k}_1$ and $\vec{k}_2$ to parameterize surface S. Then $B^n(\vec{k}) = \nabla_{\vec{k}_1} A_2^n(\vec{k}) - \nabla_{\vec{k}_2} A_1^n(\vec{k})$ and the Berry phase is given by equation 2.33.[69]

$$\gamma_n(C) = \iint_S i\left[\langle \nabla_{\vec{k}_1} n(\vec{k})|\nabla_{\vec{k}_2} n(\vec{k})\rangle - \langle \nabla_{\vec{k}_2} n(\vec{k})|\nabla_{\vec{k}_1} n(\vec{k})\rangle\right] \mathrm{d}\vec{k}_1 \mathrm{d}\vec{k}_2 \tag{2.33}$$

The Berry curvature then leads to an addition velocity term, the 'anomalous' velocity, transverse to the electric field. The transverse conductivity is given by the sum over all occupied states of the Berry curvature weighted by the Fermi distribution function $f(\epsilon_n)$ for energy eigenvalues ϵ_n, as in equation 2.34.[74]

$$\sigma_{xy} = \sum_{n,\vec{k}} f(\epsilon_n(\vec{k}))B^n(\vec{k}) \tag{2.34}$$

From this it can be seen that the Berry curvature is essentially the curl (in k-space) of the Berry connection, where in a different phrasing the Berry curvature can be viewed as a fictitious magnetic field (in k-space) and the Berry connection is the corresponding vector potential. More precisely, Ref. [69] states that the Berry curvature is the magnetic field generated by a Dirac monopole and thus the Berry phase of circuit C is given by the flux of the monopole though the surface subtended by C. The relation between magnetic monopoles and the AHE was developed further by Fang *et al* in 2003,[74] who state that the magnetic monopole corresponds to the source or sink of the Berry curvature.

An important development came from Haldane in 2004,[72] finding that the intrinsic AHE is primarily due to Berry phases accumulated by the adiabatic motion of quasiparticles on the Fermi surface and not from the entire Fermi sea. It is proposed that the AHE is dependent on the topology of each distinct Fermi

sheet, though the author calls for the development of a "topological Fermi liquid theory" in order to confirm and progress the idea.

Nagaosa in 2006[82] seconds that call while providing a general overview of the modern Berry phase approach and the "topological picture of the AHE", while Sinitsyn in 2005[83] points out that although in the super clean limit the Berry phase contribution to the AHE can conceivably come from all electrons, even those deep in the Fermi sea, in reality scattering often dominates and the side-jump and skew scattering mechanisms only involve electrons at the Fermi surface anyway.

Wang *et al* in 2007[84] provide support for Haladane's conclusions, that while the intrinsic AHE can be written in terms of an integral of the Berry curvature over the occupied portions of the Brillouin zone, the integral can be manipulated first into a Fermi surface integral of the Berry connection and then ultimately into a Fermi surface integral of a Fermi-vector-weighted Berry curvature. Wang *et al* attempt to calculate this final integral and compare the results to experimental data, and find that the two match reasonably well, suggesting that the Fermi surface topology approach to the intrinsic AHE is a good one.

The work of Shiomi *et al* in 2010[73] refers to topology in terms of magnetic monopoles in k-space, referencing the work of Fang *et al* mentioned earlier, stating that macroscopically the Berry phase originates from band anti-crossing and gap formation due to the SOI, which gives rise to the "novel topological structure of the magnetic monopole." Hence the intrinsic AHE is topologically protected by the band structure, specifically the gap structure at the anti-crossing points, and so is robust against electron scattering.

In summary, of the three mechanisms that yield an 'anomalous' transverse conductivity the intrinsic AHE is by far the most interesting as a probe of Fermi surface topology and the fundamental band structure of the material. However, the individual contributions from the different mechanisms, summarised in figure 2.6, are typically difficult, if not impossible, to untangle in experimental measurements of the Hall effect.

Their differing dependences on the longitudinal resistivity provide a possible means of separating out the skew-scattering contribution, at low temperature and in very clean samples at least, but the side-jump and intrinsic mechanisms are both contained by the parameter R_{a_2} in equation 2.31 and their individual contributions cannot be separated easily. A range of similar samples of varying

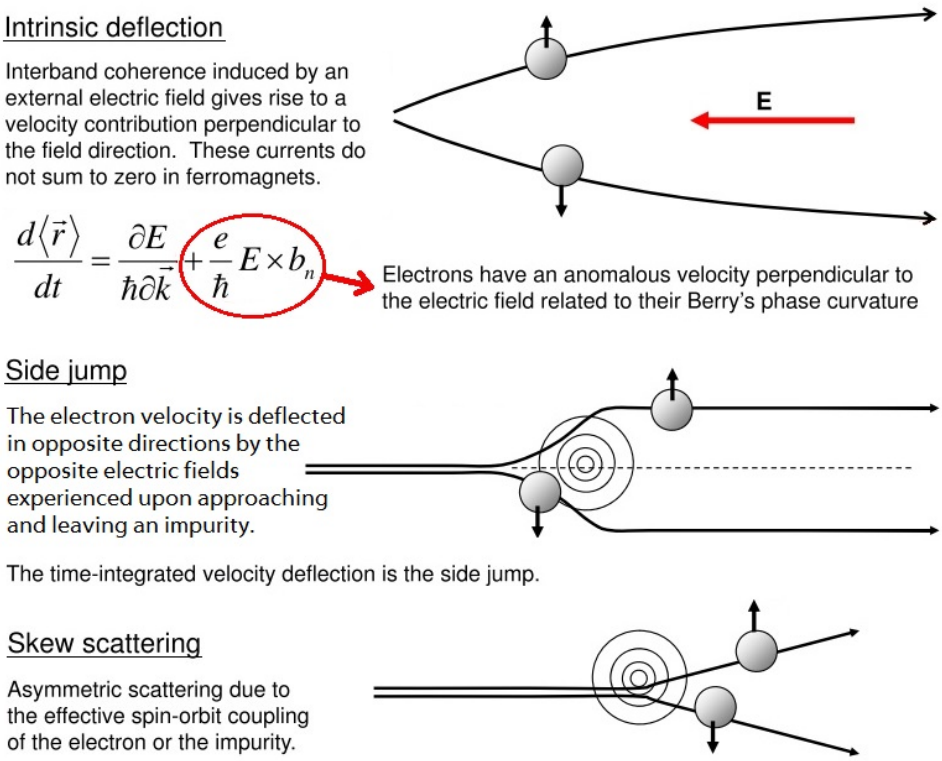

Figure 2.6 Depictions of the three main mechanisms for the anomalous Hall effect with short descriptions of each. Adapted from Ref. [14].

purity can be used to alter the impurity scattering rate, varying extrinsic but not intrinsic effects, but performing this kind of experiment is very labour intensive in terms of measurements and sample preparation.

Recent attempts to calculate the intrinsic AHE from the Berry phase formulation, such as in Ref. [85] and Ref. [75], or of particular relevance Ref. [86] for f-electron heavy-fermion systems and Ref. [87] for ferromagnetic superconductors, have achieved reasonable success but no straight-forward theory has yet emerged that allows for easy analysis of experimentally determined R_{a_2} data.

This is unsurprising considering that, despite the AHE being first discovered in the 19th century, is is only in the 21st century that the relationships between the Fermi surface, scattering mechanisms and the Berry phase, and the anomalous Hall conductivity have been developed and the debate and confusion surrounding the AHE mostly resolved. In some ways the field is still young, and progress on the theory of the AHE is ongoing.

2.4 Quantum Oscillations

2.4.1 Landau Quantization

As is typical when attempting to describe a quantum phenomenon, the simplest derivation of Landau quantization begins with consideration of a particle in a box. For a particle of mass m in a cubic region, side length L with periodic boundary conditions, the free electron Hamiltonian has the usual eigenvalues $\epsilon(k) = \hbar^2 k^2/2m$ with wavevector quantization $k_i = 2\pi n_i/L$ determined by integer n_i for each component $i = x, y, z$. If a magnetic field B is then applied (arbitrarily and without loss of generality) in the z direction, a term involving the electromagnetic vector potential will be added to the Hamiltonian and the energy levels become:

$$\epsilon_\nu(k_z) = \frac{\hbar^2}{2m}k_z^2 + (\nu + \frac{1}{2})\hbar\omega_c \tag{2.35}$$

where $\omega_c = eB/m$ is the cyclotron frequency.

It can be seen from this result that the electron motion parallel to the field is unaffected, as is expected from the nature of the Lorentz force. In the plane perpendicular to the field the orbital motion of the electron has become quantized in terms of quantum number ν in dramatic contrast to the non-localised, plane wave solutions obtained for the zero-field case. The quantized energy levels given by equation 2.35 are known as Landau levels.

The exact form of the Hamiltonian that gives rise to these Landau levels depends on the choice of vector potential, $\vec{A}$, since although the system is both translationally and rotationally (about the z-axis) invariant it is not possible to specify a vector potential that is invariant under both.

Common choices are the symmetric gauge, $\vec{A} = B/2(y, -x, 0)$, or the Landau gauge, $\vec{A} = B(0, x, 0)$, with the latter being more commonly employed for simplicity. The physical properties of the system are however independent of the choice of vector potential due to the gauge invariance of the Hamiltonian, so the final results are generic.

The Landau gauge yields the Schrödinger equation:

$$\begin{aligned}\hat{H}\psi(r) &= \frac{1}{2m}(\hat{p} - e\hat{A})^2 \\ &= \frac{-\hbar^2}{2m}\left(\frac{\partial^2}{\partial x^2} + \left(\frac{\partial}{\partial y} - \frac{ieB\hat{x}}{\hbar}\right)^2 + \frac{\partial^2}{\partial z^2}\right)\psi(r) \\ &= \epsilon(k)\psi(r) \end{aligned} \tag{2.36}$$

A reasonable solution substituted back into this expression transforms equation 2.36 into a second order differential equation with the form of the wave equation of a harmonic oscillator (see chapter 7 of Ref. [66] for example).

The nature of the equation 2.36 can also be recognised, more readily, by noting that the momentum operator $\hat{p}_y$ commutes with the Hamiltonian (since there is no explicit y dependence) and thus can be replaced by its eigenvalue $\hbar k_y$. Then substituting the cyclotron frequency defined earlier gives:

$$\hat{H} = \frac{\hat{p}_x^2}{2m} + \frac{1}{2}m\omega_c^2\left(\hat{x} - \frac{\hbar k_y}{m\omega_c}\right)^2 + \frac{\hat{p}_z^2}{2m} \tag{2.37}$$

This is the Hamiltonian for a quantum harmonic oscillator with centre $x_0 = \hbar k_y/m\omega_c$, plus a term for the unaffected electron energy in the z-axis direction. The corresponding energy eigenvalues are those expressed in equation 2.35, hence it is clear that the quantization of electron orbits in terms of ν is exactly analogous to the quantization of energy levels in a quantum harmonic oscillator.

The Effects of Spin

The discussion thus far has considered only the effect of a magnetic field on the orbital motion of electrons; the effect of the field on electron spin, specifically Pauli paramagnetism, was covered earlier in section 2.2. The orbital motion of electrons in Landau levels produces a magnetization antiparallel, in direct opposition, to the applied field, an effect called diamagnetism. The magnetic susceptibility in this case will be determined by a combination of both Pauli and Landau susceptibilities (and also the Larmor diamagnetic susceptibility, the response of the ionic cores to the applied field), where the two are related (for the free electron case only) by $\chi_{\text{Landau}} = -\frac{1}{3}\chi_{\text{Pauli}}$.

In regards to Landau quantization of free electrons, the interaction of electron spin and applied field separates out the energy levels, creating two different sequences of Landau levels, one for each spin state. Their relative displacement in terms of energy is given by the Zeeman splitting energy $ge\hbar B/4m = \mu_B B$, where the Landé g-factor is taken as equal to 2 and μ_B is the Bohr magneton. Note from equation 2.35 that the separation between Landau levels of subsequent ν is equal to $e\hbar B/m = 2\mu_B B$, which is half that of the Zeeman splitting.

The Landau levels are highly degenerate, with many different electron orbits sharing the same energy. For each energy level, for given quantum number ν and arbitrary k_z, there exist $2eBL^2/h$ degenerate states, collectively known as the ν^{th} Landau level, where the factor of 2 comes from spin degeneracy.

The value of the degeneracy is calculated by realising that the average density of states in k-space (in 2 dimensions, the x-y plane) is unaltered by the application of a magnetic field, remaining equal to $(L/2\pi)^2$. In k-space the Landau levels can be represented as a series concentric cylinders, with the z-axis as the axis of symmetry, and the total area attributed to each Landau level is $2\pi eB/\hbar$. The degeneracy per state is the total area divided by the density of states, giving the value $2eBL^2/h$ stated above.

2.4.2 The de Haas-van Alphen Effect

The number of degenerate states per Landau level is directly proportional to the field, as is the energy of the levels and also the separation between them. At very low temperature the Fermi surface is a sharp boundary between occupied and unoccupied states and electrons will thus occupy sections of the cylinders representing Landau levels that fall within the Fermi surface (a sphere for free electrons) as seen in figure 2.7.

Increasing the applied field increases the energy, or radius in k-space, of the highest occupied Landau level, moving it beyond the Fermi surface. As this happens the number of states available in lower levels also increases, allowing electrons to move down from the highest Landau level, depopulating it. Increasing the field further will bring the next highest Landau level to the Fermi surface and then beyond, at the same time creating more low-level states for electrons to move into.

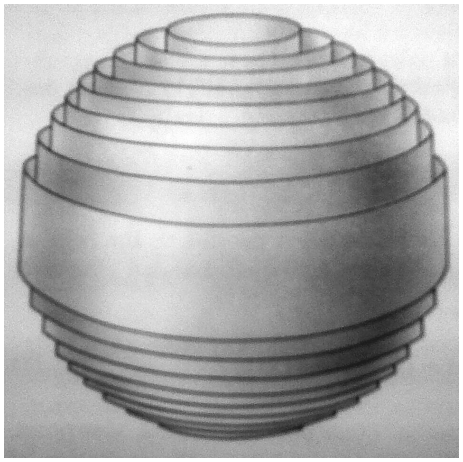

Figure 2.7 Landau quantization of electron orbits in k-space for a vertical magnetic field. Landau levels for free electrons are a series of concentric cylinder surfaces. Only the occupied portions of the Landau levels, contained within the Fermi surface, are shown. Source: Ref. [15].

Therefore the population of electrons near the Fermi surface is constantly changing with field in an oscillatory manner as successive Landau levels are expanded and depopulated (quantified more rigorously in Ref.,[88] p.349-351). The period of these oscillations with field is determined by equating the area of the Fermi surface, $A_F = \pi k_F^2$, with the area associated with successive Landau levels. Thus the period of oscillation, in terms of inverse field, is given by:

$$\Delta\left(\frac{1}{B}\right) = \frac{2\pi e}{\hbar A_F} \tag{2.38}$$

as derived by Onsager in Ref. [89].

This relation becomes of greater importance for real materials where the Fermi surface is not a simple sphere (as in figure 2.1). In this case equation 2.38 still holds but A_F refers to one or more extremal cross-sectional areas of the Fermi surface, perpendicular to the field. Applying the field in different directions thus defines different extremal areas and provides information about the shape and form of complex and unknown Fermi surfaces . Figure 2.8 shows several orbits that bound extremal areas for different field directions.

The oscillations in electron energy give rise to corresponding oscillations in magnetization: at absolute zero the magnetic moment of a system is related to the energy through $\mu \propto -\partial E/\partial B$ and so there is a periodic dependence of susceptibility on field known as the de Haas-van Alphen effect. Using the

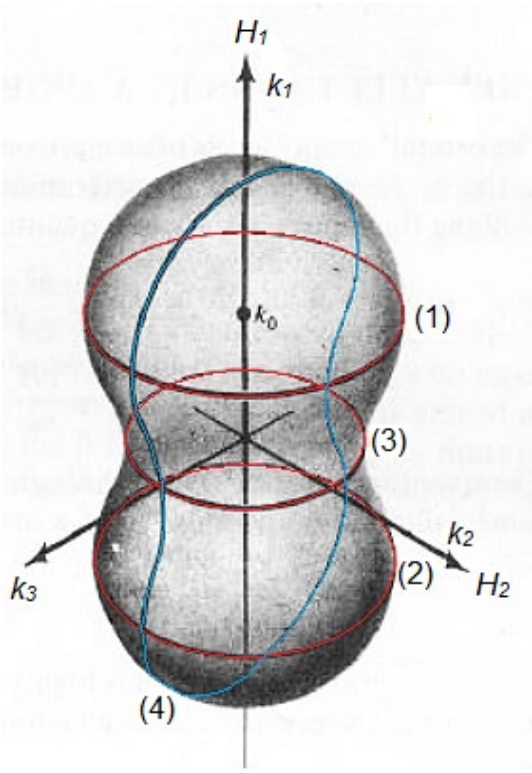

Figure 2.8 Illustration of a hypothetical Fermi surface with variety of extremal orbits highlighted for two different directions of magnetic field. Orbits 1, 2 and 3 (in red) are present for field H_1 whereas only orbit 4 (in blue) is present for field H_2. Adapted from Ref. [16].

Onsanger relation the de Haas-van Alphen effect can be used to probe the Fermi surface by measurements of magnetization and/or susceptibility (for an overview see Ref. [90]). Essentially, rotating the sample within the magnetic field and analysing how the quantum oscillation frequencies vary allows for the construction of a 3d picture of the Fermi surfaces.

For full determination of Fermi surface geometry a two-axis rotator is required, since a single-axis rotation provides only the extremal orbit size and how it varies with angle, not the full shape of the surface, which can be constructed after a full rotation in the other plane.

It is common that a particular field direction defines two or more extremal orbits simultaneously, and so there will be an oscillation period for each of them superimposed to give the overall behaviour of the magnetization with field, as seen in figure 2.9. A Fourier transform can then be used to extract the individual frequencies of each oscillation.

The conditions under which de Haas-van Alphen oscillations are expected to be

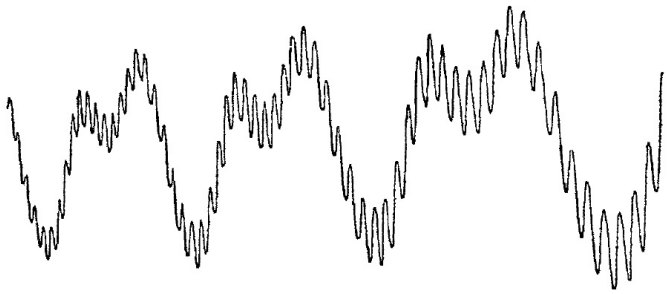

Figure 2.9 Several different oscillation periods superimposed in a single measurement, from different extremal orbits present simultaneously for a particular direction of applied field. Source: Ref. [16].

seen can be determined by considering thermal fluctuations around the Fermi surface. If the thermal energy is greater than the typical energy separation of Landau levels then thermal fluctuations will obscure any effects due to Landau quantization. Equating the thermal energy with the energy separation from equation 2.35 gives the limiting value $T/B = e\hbar/k_B m = 1.34$ K/T for free electrons, so very low temperatures and high fields are required. For example, at liquid helium temperature fields greater than 3 T are typically required before de Haas-van Alphen oscillations are observed.

Moving beyond the free electron gas, the oscillation amplitude is more realistically determined by proportionality to the factor $[x/\sinh(x)]$ where parameter $x = 14.7m^*T/B$.[91] This is known as the thermal attenuation factor in the well-established Lifshitz-Kosevich formula for quantum oscillation amplitude.

The thermal attenuation factor comes from the Fermi-Dirac distribution: at lower temperature the edge of the distribution is sharper, giving a sharper Fermi surface, without the typical thermal broadening of width $k_B T$. This means less smearing out of the Landau levels, or equivalently less smearing out of the oscillations, providing larger amplitudes. Since the function $[x/\sinh(x)]$ is maximised for small x this implies that large oscillation amplitudes require low temperature, high field, and small effective mass.

From measurements of how the oscillation amplitude changes as a function of temperature (for the same field strength) it is therefore possible to experimentally determine the effective mass of charges on a particular band, and from measurements of oscillation amplitude over different field ranges it is possible to extract information about the scattering rate, as well as all the information gained about the Fermi surfaces from the extremal areas from the frequencies of

the oscillations.

Including the effects of scattering into the Lifshitz-Kosevich formula adds the dependence of the oscillation amplitude on the factor $\exp(-\pi/\omega_c\tau) = \exp(-\pi m^*/eB\tau)$.[91] This is known as the Dingle damping factor and it is important to be aware that the τ used here is related to the scattering rate for impurities only, and as such has no temperature dependence, being proportional to the residual resistivity and thus to the purity of the sample.

Maximising the quantum oscillation amplitude according to the Dingle damping factor therefore further requires small effective mass, high field and high sample purity, in addition to the high field, low temperature and small effective mass conditions required by the thermal attenuation factor.

Finally, it should be noted that Landau quantization results in quantum oscillations in many other system parameters (summarised in chapter 14 of Ref. [16]), such as the Shubnikov-de Haas effect which refers to oscillations in magnetoresistance. These are the main type of quantum oscillation studied in this thesis for URhGe.

2.5 Capacitive Torque Magnetometry

Torque magnetometry is at first glance fairly simple. Application of field perpendicular to a magnetic moment will produce an effective torque as the moment attempts to align with the field in order to reduce the magnetic interaction energy.

In an isotropic paramagnet the moments will simply do so, generating a net magnetization parallel to the field. However, in a ferromagnet with a definite easy axis of magnetization, such as low-temperature URhGe, the net moment is fixed in alignment to the easy axis and, for a modest field strength, will move very little from that orientation. Therefore, in order to align the magnetic moment to the field, the sample as a whole must rotate under the influence of the magnetic torque.

If the sample is fixed to the end of a cantilever, the magnetic torque will bend the lever. The magnitude of the torque is directly related to the magnitude of the net moment perpendicular to the field, and thus measuring the strength of the torque

is a form of magnetometry. The torque can be determined by the displacement of the lever from its position in the absence of field, and such small distances can easily be measured by changes in capacitance, where the lever forms one plate of the capacitor and a stationary base plate forms the other. To visualise this, see figure 4.2.

There are several good reasons to use capacitance to measure magnetic torque, and thus magnetization, but the real strength of the method is the amazing precision that can be achieved in a measure of capacitance, especially when coupled with the outstanding voltage measurement capabilities of a lock-in amplifier. For example, the latest Quantum Design MPMS, a high-specification SQUID magnetometer and an impressive instrument itself, can measure magnetic moments to a sensitivity of $5 \times 10^{-11}\mathrm{Am}^2$.

The experimental set-up utilized in this PhD project resulted in a voltage change of 23 μV per fF, and with typical lock-in amplifier sensitivity around 5 nV that gives a sensitivity in capacitance of about 0.2 aF, which was indeed observable when adjusting the attofarad levers on the capacitance bridge instrument. This implies that, at a field of 1 T for example, the minimum measureable change in magnetization was $3 \times 10^{-11}\mathrm{Am}^2$, and the sensitivity scales with the applied field, such that at 15 T the sensitivity reaches $2 \times 10^{-12}\mathrm{Am}^2$.

In addition to this very high sensitivity, capacitive torque magnetometry allows measurements at milikelvin temperatures and tens of tesla. With an in-house dilution refrigerator, measurements were performed below 50 mK up to 17 T. Furthermore, the sample can be easily rotated with respect to the applied field, allowing a high precision angle study under at these conditions, and electrical contacts can also be placed on the sample without affecting the magnetization measurement, allowing electrical transport properties to be measured simultaneously.

It is also possible to simultaneously measure both the bulk magnetization and the differential susceptibility of the sample, which can be dramatically different in a ferromagnetic superconductor where the susceptibility is negative due to the diamagnetism of superconductivity but gradually increasing the field will increase the equilibrium magnetization as is usual for a ferromagnet.

Finally, torque magnetometry gives a bulk measurement of magnetic moment in such a way that both vector components, parallel and perpendicular to the applied field, can be determined independently and concurrently. This is important for

URhGe because as field increases the magnetization vector will gradually rotate away from the easy axis to align with the field, before the easy axis abruptly changes at the 'moment rotation transition' (see section 1.4).

Thus to fully characterise the magnetization it becomes necessary to know not just the perpendicular moment but the parallel component too. Thankfully, although determining the latter is a much more complicated measurement than the former in torque magnetometry, both components can be obtained by the methods detailed below.

2.5.1 Introduction to the Method

Magnetic torque, τ, is related to the magnetic moment of the sample, m, and the external field, $(\mu_0\vec{H})$, by the cross product:[92]

$$\vec{\tau} = \vec{m} \times (\mu_0\vec{H}) \tag{2.39}$$

where the magnetic moment has units $\mathrm{Am}^2 = \mathrm{NmT}^{-1}$ and the field has units T such that the torque is measured in Nm as expected. The torque is essentially related to a perpendicular force F at distance L from the origin for small deflections of a cantilever with the sample a distance L from the bending point (i.e. $\vec{\tau} = \vec{r} \times \vec{F}$ where $\vec{r} = L\hat{r}$). This force causes a deflection Δd from equilibrium position d_0 according to Hooke's law:

$$F = \frac{\tau}{L} = -k\Delta d \tag{2.40}$$

where k is the spring constant of the lever. The spring constant is determined by the physical properties of the lever according to:[93]

$$k = \frac{Ewt^3}{4L^3} \tag{2.41}$$

where E is Young's modulus (124 GPa for BeCu) and w is the width, t the thickness and L the length of the lever. The sample is placed at the end of the lever such that the force F is applied approximately a distance L from the bending point.

More generally $k = 3EI/L^3$ for moment of inertia I, where for a cantilever with

the force applied at the end $I = wt^3/12$.

The deflection Δd can be measured by capacitance. The capacitance, C, of two parallel plates of over-lapping area A is inversely related to the distance between the plates, d, by the simple formula:

$$C = \frac{\epsilon A}{d} \tag{2.42}$$

where ϵ is the permittivity. For air, and especially within the vacuum of the cryostat, $\epsilon \simeq \epsilon_0$, where ϵ_0 is the permittivity of free space. Thus for a change in the gap between the plates caused by a deflection in cantilever Δd there is a corresponding change in capacitance ΔC from its equilibrium value C_0, given by:[94]

$$\Delta C = \frac{\epsilon_0 A}{d_0}\left(-\frac{\Delta d}{d_0} + \frac{2(\Delta d)^2}{d_0^2} - ...\right) \tag{2.43}$$

which for small deflections can be approximated to a simple linear relationship:

$$\Delta C = -\frac{\epsilon_0 A \Delta d}{d_0^2} \tag{2.44}$$

Then substituting the equilibrium gap size for the equilibrium capacitance by $d_0^2 = \epsilon_0^2 A^2/C_0^2$ (equation 2.42) the expression becomes, rearranging for the deflection:

$$\Delta d = -\frac{\epsilon_0 A \Delta C}{C_0^2} \tag{2.45}$$

Thus the torque is related to the change in capacitance by:

$$\tau = FL = -kL\Delta d = \frac{Ewt^3}{4L^2}\frac{\epsilon_0 A \Delta C}{C_0^2} = \alpha\frac{\Delta C}{C_0^2} \tag{2.46}$$

where the constant α can be calculated from the following numbers, specific to the experiment. $E = 124$ GPa, $w = 2$ mm, $t = 100$ μm, $\epsilon_0 = 8.854$ pFm^{-1}, $A = 4.5$ μm^2, $L = 5.2$ mm, and so $\alpha = 9.13 \times 10^{-17}$ S.I. units. The spring constant $k \simeq 400$ Nm^{-1}.

The important formula for the experimental method, relating capacitance to magnetization, can then be obtained by a simple combination of equations 2.39

and 2.46 to arrive at the expression:

$$m = \frac{\alpha}{(\mu_0 H)} \frac{\Delta C}{C_0^2} \tag{2.47}$$

where the quantity m here is the magnitude of the net magnetic moment perpendicular to vector $\vec{H}$.

There are several assumptions made here. The first is that only the linear term in beam deflection in equation 2.43 is considered, such that $(\Delta d/d_0)^2 \simeq 0$ and so $\Delta C \propto \Delta d$. For this project, d_0 was typically around 50 μm so an error less than 1% required that $\Delta d < 0.5\mu$m. Hence the general aim with cantilever magnetometry is to minimise d_0 in order to maximise capacitance and so the accuracy of the measurement, while also maximising the typical Δd for the best resolution, under the constraint of $\Delta d/d_0 < 0.01$. A small ratio of Δd to d_0 is also required to maintain the parallel-plate approximation of the capacitor when the lever is bent.

Another assumption is that Δd is small enough that the angular deflection is negligible compared to the angular resolution of the sample alignment relative to the applied magnetic field. Consider the angular resolution of the rotator, 0.01 degrees, which corresponds to a lever deflection of roughly 1 μm. Depending on the orientation of the sample, the maximum lever deflections observed (for the lever properties listed above and a URhGe sample mass of 0.15 mg) are also about 1μm at maximum field, so it seems more reasonable to quote sample alignment to a precision of 0.1 degrees. A deflection of 1μm also barely satisfies the constraints listed in the previous paragraph, and in this case the error due to the higher-order terms in equation 2.43 can approach 2 %, although it should be remembered that this is for the combination of sample orientation and field that results in the most extreme deflection and for most of the measurement range the error is well below the 1% aimed for.

Yet another assumption is that the deflection follows Hooke's law. In a generalised form Hooke's law states $\sigma = \epsilon E$ where σ is normal stress, ϵ is strain, and E is Young's modulus. For an externally applied load a "load parameter" can be defined, denoted by γ.

$$\gamma = \frac{FL^2}{2EI} \tag{2.48}$$

where load F is applied at length L to a lever with moment of inertia I.

It can be shown[93] that if deflections of the lever are small, such that for angular deflection θ the approximation $\sin(\theta) \simeq \theta$ can be made, then $\theta \simeq \gamma$. Specifically $\sin(\theta) \simeq \theta \simeq \Delta d/L$ and it can be shown that in this case of small deflections $\theta = \frac{2}{3}\gamma$. Substituting this into the expression for the load parameter it can be seen that it all works out to verify that this small deflections regime is where Hooke's law holds true.

$$\gamma = \frac{3}{2}\theta = \frac{3\Delta d}{2L} = \frac{FL^2}{2EI} \tag{2.49}$$

Rearranging the above, and recognising the expression for the spring constant, returns a statement of Hooke's law as expected.

$$F = \frac{3EI}{L^3}\Delta d = k\Delta d \tag{2.50}$$

To estimate the load parameter the typical moment of $m \simeq 8.15 \times 10^{-7}\text{Am}^2$ for the URhGe sample at a field of $B = 12$ T can be used to calculate a maximum torque of about $\tau \simeq 9.8 \times 10^{-6}\text{Nm}$ and thus a force of $F \simeq 1.88 \times 10^{-3}\text{N}$ and the calculated value of $\gamma \simeq 0.0013$. This can then compared to $\sin(\gamma) \simeq 0.0012999996$ to confirm that the experiment is well within the small deflection limit for Hooke's law to hold.

One final assumption is that the torque arising from the demagnetizing field is negligible compared to the torque due to the applied field as described by equation 2.39. Introduced in section 2.2, the demagnetizing field reduces the strength of ferromagnetic ordering and is governed by the shape and orientation of the sample with respect to the field. Thermodynamically, the system will attempt to decrease the demagnetizing field, in order to increase the magnetization, by rotating the sample such that its major length is more aligned to the field. For example, this torque would be maximised for a thin needle lying horizontal within a vertical field.

More generally, the strength of this effect is expected to be proportional to the difference between the demagnetization factor when the minor sample length is aligned with field, n_r, and the factor when the major length is aligned with field, n_a, where $n_r \geq n_a$. For a perfect sphere the torque due to the demagnetizing field would be zero, since both demagnetization factors are the same and rotation of the sample makes no difference. The strength of the effect is also expected to be proportional to the magnetization, since the product of demagnetizing factor and

magnetization defines the demagnetizing field, and also to the magnetic moment, since magnetic torque is given by the product of moment and field.

An expression for the magnetic energy due to the demagnetizing field is derived in Ref. [59], which goes on to determine the conditions under which the energy is minimised for a soft magnetic body, both above and below saturation of the magnetization, and provides formulae for the maximum possible torque. For a saturated magnetization, M_s, which is the case encountered for almost the entire field range in the URhGe experiment, the torque is given by equation 2.51, which has exactly the expected form. As Ref. [59] points out, "the model only requires the knowledge of the body geometry and the saturation magnetization of the material."

$$\tau_{\text{demag.}} = \frac{n_r - n_a}{2} \mu_0 V M_s^2 \sin(2\phi) \tag{2.51}$$

The URhGe sample is close to a sphere and so the torque is expected to be small, with $n_r \sim 0.4$ and $n_a \sim 0.3$. The magnetic moment at high field, $m_s = VM_s \sim 8 \times 10^{-7}\,\text{Am}^2$, and the magnetization $\mu_0 M_s \sim 0.1\text{T}$. The angle ϕ is the angle between the magnetization and the axis of symmetry for a sample taken as an oblate ellipsoid. From equation 2.51 it can be seen that the torque is maximised at $\phi = 45°$ such that $\sin(2\phi) = 1$. Thus the *maximum* torque for the URhGe sample is calculated as $\sim 4 \times 10^{-9}\,\text{Nm}$.

The torque due to the interaction of the moment with the main field, roughly equal to $m_s\,\mu_0 H$, is usually several orders of magnitude greater than the $\tau_{\text{demag.}}$ calculated above. Depending on the field the main torque varies between 10^{-6} and 10^{-5} Nm across the measurement range, and even at $\mu_0 H \sim 0.1\text{T}$ the torque is $\sim 4 \times 10^{-8}$ Nm, which is still $10\times$ larger than $\tau_{\text{demag.}}$ although the latter is starting to become significant.

Therefore at very low field the effects of $\tau_{\text{demag.}}$ must be considered, just as at very low $\mu_0 H$ the effects of the demagnetizing field must be taken into account and the usual approximation $H \simeq H_{\text{ext.}}$ is no longer valid. Thankfully, as mentioned in section 2.2 when this approximation was first stated, the field range of interest for the URhGe project is around 12 T where these effects are small enough to be mostly disregarded.

2.5.2 Two-Component Magnetometry

The method outlined above, using a spatially uniform field, provides only the magnetic moment perpendicular to the applied field. In order to get the other component of interest, the moment parallel to the field, a field gradient technique known as Faraday magnetometry can be employed. In contrast to the cross product seen in equation 2.39, the dot product features in the formula for Faraday magnetometry, which allows measurement of the component of magnetization parallel to an applied field gradient.

In Faraday magnetometry a spatially varying magnetic field strength is used to create a gradient, ideally linear across the sample volume, which generates a magnetic force. The standard formula is:[2]

$$\vec{F} = \left(\vec{m} \cdot \vec{\nabla}\right)(\mu_0 \vec{H}) \tag{2.52}$$

There are various ways that a field gradient can be established across the sample space. In Ref. [95] a pair of canted Helmholz coils are used to generate a vertical gradient, while in Ref. [96] a vertical gradient is created in a horizontal field modified by a stack of additional coils. Both rely on very careful and precise positioning of the sample within the spatially varying field, a regularly occurring issue with Faraday magnetometry. In fact one method of applying a field gradient, used in Ref. [97] for example, is to simply move the sample away from the centre of a solenoid magnet, where the field is approximately uniform, toward the end, where gradients begin to enter the field profile.

Most often additional coils with their axes aligned to the direction of the intended field gradient are employed, as in Ref. [98] or Ref. [99]. By varying the current in different coils, usually by having the current flow in opposite directions for coils either side of the sample, a controlled and variable field gradient can be established while also keeping the magnitude of the field at the sample approximately zero.

In Ref. [100] a set of four coils, two horizontal and two vertical, is used for full vectorial control over the field profile. The experimental setup for this PhD project uses six coils in addition to the main magnet for similar vectorial control,

[2]There is some confusion in the literature as to the correct formula for the force on a magnetized material within a spatially varying field. The discussion is covered in this thesis in appendix B.

shown in the diagram in figure 4.4.

For the URhGe investigation the large direct-current (d.c.) generated field is the control parameter of interest, the tuning parameter by which the phase transition is crossed, and so any field gradient must necessarily be applied in addition to the tuning field. However, there is of course only one sample and one cantilever, and so the torque from equation 2.39 and the torque from the force from equation 2.52 simply combine to produce a single measurable effect: the bending of the cantilever.

In order to resolve the individual contributions to the total torque, to separate the effects of the main field and the additional field gradient, an alternating-current (a.c.) generated field gradient is used to modulate the cantilever deflection at the a.c. frequency.

The "alternating gradient force magnetometer", as it is referred to in Ref. [99], is a useful technique anyway, even without the presence of a d.c. field, because "the force, or the displacement produced by the force, can be converted to a voltage and analyzed using a lock-in amplifier to discriminate against unwanted background noise." This is particularly useful at cryogenic temperatures when, if the gradient coils are resistive, dissipative heating limits the current, and so the strength of the field gradient, that can be applied.[98]

Even for non-dissipative, superconducting coils it is infeasible, in practice, to generate gradients as strong as the main field. Typical gradients are $\sim 0.1\,\mathrm{Tm}^{-1}$ whereas for the URhGe experiment the control field is $\sim 10\,\mathrm{T}$.

If the experiment involved only Faraday magnetometry then more sensitive measurement devices could be employed to measure the deflection due to the field gradient, as in Ref. [101]. However, to measure both components of the magnetization simultaneously in URhGe up to 17 T a stiff cantilever is required, and making the cantilever stiff enough to perform well under the effects of the large control field means that the deflections due to the field gradient are very, very small. By modulating the deflection and using a lock-in amplifier even these very small signals can be measured.

Thus in the URhGe experiment the equilibrium position of the lever changes with d.c. field strength according to equation 2.39, while the amplitude of the oscillations of the lever deflection, caused by the a.c. field gradient, changes according to equation 2.52. It is therefore imperative, in order to fully resolve the

two different torques, that only a.c. field *gradient* is present, and not any a.c. field, since an a.c. field would cause an effect governed by equation 2.39 that would be indistinguishable from the Faraday magnetometry signal at the a.c. frequency.

This requirement to eliminate any a.c. fields at the sample, while creating a strong a.c. field gradient, is easier to discuss once the problem is written out mathematically. For the following section, the applied field $\mu_0 H$ is denoted by the less clumsy B for clarity, though it should be remembered that this is not truly the B field.

2.5.3 Simultaneous Torque and Force Magnetometry

Using a coordinate system where z is vertical and x is horizontal, in the crystallographic b-c plane of URhGe, the total applied magnetic field can be written as:

$$\vec{B}(t,x,z) = B_{0z}\hat{z} + B_x(x,z)\sin(\omega t)\hat{x} + B_z(x,z)\sin(\omega t)\hat{z} \tag{2.53}$$

assuming that at the sample B_{0z}, the main d.c. field, is uniform whereas the a.c. fields B_x and B_y vary in space. Relative to the main magnet, the z direction could be called axial, and the x direction radial; it is assumed that there is no radial component to B_0 in the field centre (i.e. $B_{0x} = 0$).

The corresponding magnetic moment is:

$$\vec{m}(t,x,z) = m_{0x}\hat{x} + m_{0z}\hat{z} + m_x(x,z)\sin(\omega t)\hat{x} + m_z(x,z)\sin(\omega t)\hat{z} \tag{2.54}$$

An assumption made here is that the magnetic moment will oscillate precisely in phase with the field, which may not always be the case. In the superconducting state, for example, strong diamagnetism would result in a response that is completely anti-phase with the modulation field.

The magnetic moment could thus be written more accurately in terms of $\sin(\omega t + \varphi)$ for arbitrary phase φ, but an assumed $\varphi \simeq 0$ response will be considered here for mathematical simplicity. The idea of an out-of-phase response is discussed further in section 6.6.

At this point it becomes important to consider the resonant frequency of the

cantilever, in order to avoid choosing a field modulation frequency that would cause the lever to oscillate at resonance and disrupt the measurement.

The resonant frequency of the lever is easily calculated using the spring constant $k \simeq 400$ Nm^{-1} and the relation $\omega = \sqrt{k/m}$ where $\omega = 2\pi f$ gives the frequency f and the mass m is the mass (not the magnetic moment here) of the lever plus sample. The density of copper is 8940 kg m^{-3} and the volume of the lever is $\simeq 1 \times 10^{-9}$m^3, giving a mass of about 10 mg, which is significantly more than the 0.15 mg of the sample. The resulting resonant frequency is $f \simeq 1000$ Hz. This is much, much higher than the chosen field modulation frequency, which is constrained to a low value ($\sim$1 Hz) by the necessity of avoiding heat generation on the sample platform.

The interaction of the magnetization and the field gives rise to two torques: the torque due to the magnitude of the field at the sample, $\vec{\tau}_1$, and a torque due to the spatial gradient of the field at the sample, $\vec{\tau}_2$.

$$\vec{\tau}_1 = \vec{m} \times \vec{B} \tag{2.55}$$

$$\vec{\tau}_2 = \vec{r} \times \left(\vec{m} \cdot \vec{\nabla}\right)\vec{B} \tag{2.56}$$

For a lever of length L oriented at an angle θ from vertical (i.e. the angle of the platform rotator) then $\vec{r} = (L\sin\theta)\hat{x} + (L\cos\theta)\hat{z}$ and torque 1 and 2 can be expanded to:

$$\begin{aligned}\vec{\tau}_1(x,z,t) = \hat{y}\Big[&\big(m_z(x,z)\sin(\omega t) + m_{0z}\big)\big(B_x(x,z)\sin(\omega t)\big) \\ &- \big(m_x(x,z)\sin(\omega t) + m_{0x}\big)\big(B_z(x,z)\sin(\omega t) + B_{0z}\big)\Big]\end{aligned} \tag{2.57}$$

$$\begin{aligned}\vec{\tau}_2(x,z,t) = \hat{y}\,\Bigg[&(L\cos\theta)\,\Big[\big(m_x(x,z)\sin(\omega t) + m_{0x}\big)\frac{\partial}{\partial x}\big(B_x(x,z)\sin(\omega t)\big) \\ &\quad + \big(m_z(x,z)\sin(\omega t) + m_{0z}\big)\frac{\partial}{\partial z}\big(B_x(x,z)\sin(\omega t)\big)\Big] \\ &-(L\sin\theta)\,\Big[\big(m_x(x,z)\sin(\omega t) + m_{0x}\big)\frac{\partial}{\partial x}\big(B_z(x,z)\sin(\omega t) + B_{0z}\big) \\ &\quad + \big(m_z(x,z)\sin(\omega t) + m_{0z}\big)\frac{\partial}{\partial z}\big(B_z(x,z)\sin(\omega t) + B_{0z}\big)\Big]\Bigg]\end{aligned} \tag{2.58}$$

The "first demodulation signal" is a phrase used to refer to the lock-in amplifier voltage directly proportional to the output from the capacitance bridge. This varies in time, as small oscillations about a large field-dependent background value, but the time-average gives the equilibrium deflection of the cantilever due to τ_1 since there are no τ_2 terms without sinusoidal time dependence (which average to zero) that do not vanish after a spatial derivative has been applied.

The first demodulation signal is therefore simply related to the perpendicular magnetization:

$$\bar{V}_{\text{demod 1}} \propto -m_{0x}B_{0z} \tag{2.59}$$

where $\bar{V}$ is the time-averaged lock-in amplifier voltage at field B_{0z}.

The "second demodulation signal" from the capacitance bridge lock-in amplifier is the voltage measured at the frequency of the a.c. field modulation, essentially giving the amplitude of the cantilever oscillations from equilibrium. More details of lock-in amplifier 'tandem demodulation' can be found in section 4.5.

The second demodulation signal can originate from both τ_1 and τ_2, though in the absence of spatial field gradients clearly only the τ_1 contribution will be present. For example, if a purely axial field modulation is applied, parallel to the main field, without significant gradient such that $B_z(x,z) \simeq B_z$, then:

$$V_{\text{demod 2}} \propto -m_x B_{0z} - m_{0x}B_z \simeq -\big(\frac{\partial m_x}{\partial B_z}B_{0z} + m_{0x}\big)B_z \tag{2.60}$$

The susceptibility introduced above is based on the assumption:

$$\chi_{xz}(B_{0z}) = \frac{\partial m_{0x}}{\partial B_{0z}} = \frac{\partial m_x}{\partial B_z} \simeq \frac{m_x}{B_z} \neq \frac{m_{0x}}{B_{0z}}, \tag{2.61}$$

i.e. the magnetization responds approximately linearly to the tiny modulation field at some particular B_{0z} but the response of the magnetization across the whole range of B_{0z} is *not* linear.

The introduction of the susceptibility makes it clear that the second demodulation signal in this case is simply related to the derivative of the first demodulation signal, as might be expected when modulating the field in the same direction as

B_{0z}. Explicitly:

$$\frac{d}{dB_{0z}}\bar{V}_{\text{demod 1}} \propto \frac{d}{dB_{0z}}(-m_{0x}B_{0z}) \propto V_{\text{demod 2}}/B_z(x,z) \tag{2.62}$$

In other words, the integral of the second demodulation field, divided by the strength of the modulation field and B_{0z}, provides the magnetic moment m_{0x}.

If a purely radial field modulation is applied, transverse to the main field, without significant gradient such that $B_x(x,z) \simeq B_x$, then:

$$V_{\text{demod 2}} \propto m_{0z}B_x - m_x B_{0z} \simeq \big(m_{0z} - \frac{\partial m_x}{\partial B_x}B_{0z}\big)B_x \tag{2.63}$$

In this case the other component of the moment, m_{0z}, seems tantalisingly close to being determined. The applied fields are all known, and the value of m_{0x} is measured by the first demodulation signal. The only issue is that $\chi_{xz} \neq \partial m_x/\partial B_x = \chi_{xx}$. Unfortunately, χ_{xz} is known but χ_{xx} is not, and there is simply not enough information available to calculate m_{0z}.

Of course this conclusion merely highlights the necessity for Faraday magnetometry and the requirement for strong field gradients, ideally in the complete absence of any a.c. fields, such that $B_x = B_z \simeq 0$ T at the sample, in order to avoid any contributions to the second demodulation signal described by equations 2.60 and 2.63.

The spatial profile of the field modulation in 'gradient mode' can be seen in figure 2.10, which shows that $B_x(0,0) = B_z(0,0) = 0$T. Exactly in the field centre the contribution from τ_1 is therefore trivially zero. Roughly a centimeter from the field centre typical values of the undesired a.c. fields are around $B_x \sim 6 \times 10^{-4}\,\text{T}$ and $B_z \sim 1.2 \times 10^{-3}\,\text{T}$.

Close to the field centre the gradients $\partial B_x/\partial z$ and $\partial B_z/\partial x$ are generally small enough to be neglected. The largest gradient is the intentionally applied one, $\partial B_z/\partial z \simeq 0.12\,\text{T}\,\text{m}^{-1}$. The radial gradient, ideally zero, is unfortunately exactly half the strength of the axial gradient, an unavoidable consequence of satisfying Maxwell's equations.

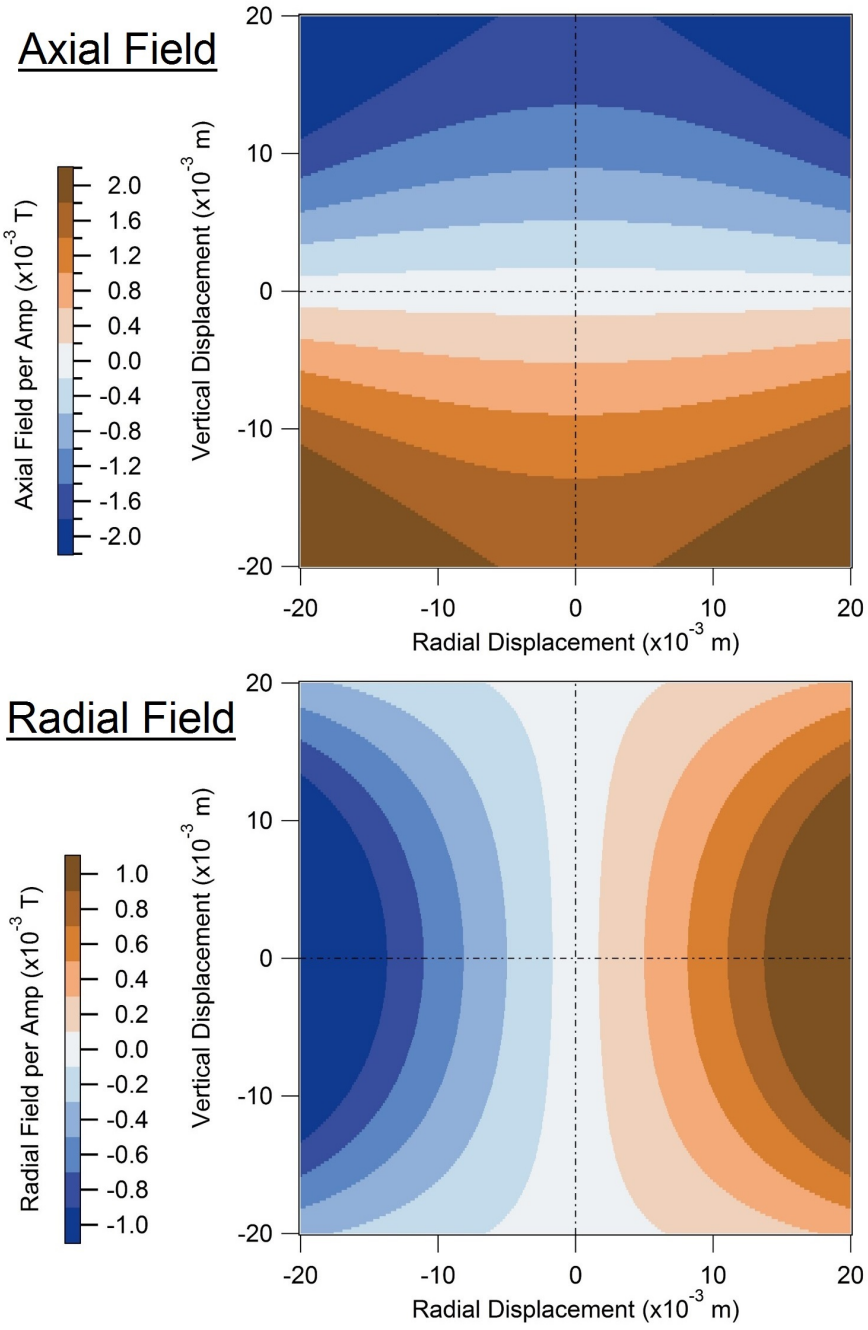

Figure 2.10 The field modulation strength as a function of position, relative to the field centre, for small distances surrounding the centre point. The magnet system is in 'gradient mode' in these calculations, and the field strength plotted is per ampere of current supplied to the magnet coils. **Top:** The field strength in the axial $\hat{z}$ direction. **Bottom:** The field strength in the radial $\hat{x}$ direction.

Specifically the divergence of the field must be zero for any particular volume in space. Writing $\vec{\nabla} \cdot \vec{B} = 0$ in cylindrical polar coordinates, and assuming azimuthal symmetry, gives $\partial B_z/\partial_z = -(\partial B_x/\partial_x + B_x/x)$. Assuming linearity, such that $\partial B_x/\partial_x = B_x/x$, the radial field gradient is thus necessarily half that of the axial, as the calculated field profiles in figure 2.10 show.

At the sample rotations of interest, $35^\circ < \theta < 45^\circ$ and $L\sin\theta \sim L\cos\theta \sim 2.5$mm. The product of the main field gradient and this length-scale prefactor is thus 3×10^{-4} T, significantly smaller then the stray fields at a centimetre from the field centre. At a millimeter from the field centre $B_z \sim 1.2 \times 10^{-4}$ T, which is still relatively substantial.

Hence the sample needs to be less than a millimeter from the $x = z = 0$ point if the force from the field gradient is going to be the dominate cause of oscillations in the torque and the second demodulation signal can be analysed as a Faraday magnetometry measurement. Experimentally, such precise positioning is not easily achievable, and the degree of litotes in that statement can be gauged from the discussion in sections 4.3 and 4.6.

Assuming that, using a vector magnet system, the fields B_x and B_z can be tuned to a level of negligible influence, making gradients $\partial B_x/\partial z$ and $\partial B_z/\partial x$ completely negligible, the second demodulation signal would then be entirely due to τ_2, as described by equation 2.58, and given by:

$$\begin{aligned} V_{\text{demod 2}} &\propto L\cos(\theta)\, m_{0x}\, \frac{\partial B_x}{\partial x} - L\sin(\theta)\, m_{0z}\, \frac{\partial B_z}{\partial z} \\ &= L\, \frac{\partial B_z}{\partial z} \left(\frac{1}{2}\, m_{0x}\, \cos(\theta) - m_{0z}\, \sin(\theta) \right) \end{aligned} \tag{2.64}$$

Thus both components of magnetization can be obtained from the following two formulae.

$$m_{0x} \propto \frac{-\bar{V}_{\text{demod 1}}}{B_{0_z}} \tag{2.65}$$

$$m_{0z} \propto \frac{-1}{\sin(\theta)} \left(\frac{V_{\text{demod 2}}}{L\,(\partial B_z/\partial z)} - \frac{1}{2}\, m_{0x}\, \cos(\theta) \right) \tag{2.66}$$

Obviously the ideal experimental condition is therefore at $\theta \simeq 90^\circ$, in which case equation 2.66 is greatly simplified to $m_{0z} \propto -V_{\text{demod 2}}/L(\partial B_z/\partial z)$, but this is not always possible in practice, especially when performing a study in which the sample is rotated.

Finally it is worth returning to equation 2.57 to consider the $\sin^2(\omega t)$ terms. Although these terms will not contribute to the second demodulation signal measuring at the fundamental frequency, sending the signal to another lock-in amplifier measuring the 2F signal (see section 4.5 for details) can provide the amplitude of these terms via the relationship $\sin^2(\omega t) = \frac{1}{2}(1 - \cos(2\omega t))$.

Thus the Y component of the second demodulation 2F signal will provide the magnitude of the $\sin^2(\omega t)$ terms according to $V_{2F} \propto m_z B_x - m_x B_z$. If there is only B_x modulation present then $V_{2F} \propto \chi_{zx} B_x^2$ and if there is only B_z modulation present then $V_{2F} \propto -\chi_{xz} B_z^2$, which can be a useful avenue for determining two components of the susceptibility tensor.

2.6 Ferromagnetic Superconductivity

The basic principles of superconductivity can be found in any graduate textbook on solid state physics (e.g. chapter 11 of Ref. [54], chapter 11 of Ref. [52] or chapter 34 of Ref. [16]) and so only a brief introduction to the phenomena will be included here. The textbooks Ref. [102], Ref. [103] and Ref. [104] are also good sources for deeper discussions on the topic.

Superconductivity is a state of quantum ordering of the conduction electrons, which, through some attractive interaction, are loosely associated in Cooper pairs. The formation of Cooper pairs allows these boson-like combinations to condense into a single ground state, in contrast to the unpaired electrons which, as fermions, must obey the Pauli exclusion principle.

Condensation opens a gap in the band structure at the Fermi level of width 2Δ, where Δ is the order parameter associated with the superconducting state, growing from zero at the transition temperature to a maximum at 0 K. To scatter a paired electron into a higher momentum state a collision must provide excitation energy of at least the gap size.

Failing this there will be no electrical resistance, a defining characteristic of superconductivity. As well as perfect conductivity the other property characteristic of superconductors is perfect diamagnetism and the complete expulsion of any externally applied field (up to some critical value), a phenomena known as the Meissner (or Meissner-Ochsenfeld) effect.

For studies of UGe_2 and URhGe the crucial concept from the short introduction above is the requirement of an attractive interaction between the conduction electrons, a microscopic pairing mechanism that can overcome the Coulomb repulsion (or at least the reduced, short-range Coulomb interaction due to Thomas-Fermi screening). In the conventional theory, the so-called BCS theory,[105] the attraction is mediated by the ionic lattice, specifically by lattice distortions, and can be described by the emission and absorption of virtual phonons.

In phonon-mediated superconductivity the pairing mechanism can be described as follows. An electron interacts with the lattice, attracting nearby ions, drawing them slightly toward it, and then swiftly moves on. The lattice reacts relatively slowly, creating a region of space with a higher than average concentration of positive charge. A second electron is then attracted to the increased charge density of that lattice distortion, effectively interacting with the first electron. This retarded interaction couples the two electrons as a Cooper pair.

The formation of Cooper pairs for conventional superconductivity requires particularly favorable conditions, typically very low temperatures and/or low magnetic fields and currents, as well as high crystal purity. The desirability of materials that remain superconducting up to higher temperatures (ideally something in excess of 300 K) and high magnetic fields motivates the search for unconventional superconductors, whose pairing mechanisms cannot be described by the BCS theory.

Arguably the most important of these were discovered in the late 1980s – the so-called 'high-temperature' superconductors – starting in 1986 with a new record for the highest transition temperature, slightly above 30 K, and quickly progressing to ever higher records such as YBCO at over 90 K, BSCCO at over 100 K, and TBCCO at 127 K.[106] The crucial advancement was passing the boiling point of nitrogen at 77 K, which allowed these materials to be easily and cheaply cooled to the superconducting state and used for practical purposes outside of academic research.

UGe_2 and URhGe have comparatively low transition temperatures, both below 1 K, but are of particular interest in the pursuit of superconductors that can operate at high magnetic fields. Superconductivity and magnetism are fundamentally incompatible by conventional theory but UGe_2 and URhGe are ferromagnets, magnetism is inherent to their nature and apparently exists cooperatively with

the superconducting state, a property that, particularly in the case of URhGe, allows them to remain superconductors up to unusually high magnetic fields.

Unsurprisingly, the critical temperature for superconductivity, T_{SC}, is related to the order parameter, the gap size. Specifically, for a BCS superconductor $\Delta(T \to 0) = 1.76 k_B T_{SC}$. The important parameter for superconductivity in a magnetic field, however, is the coherence length, ξ. The upper critical field for a type II superconductor is inversely proportional to the square of the coherence length: $B_{c2}(T) \sim \Phi_0/\xi^2(T)$, where $\Phi_0 \equiv h/2e$ is the flux quanta.[102] Ergo, if the coherence length is large then the critical field is small.

In order to enhance the upper critical field the coherence length can be reduced by lowering temperature. Immediately below the transition temperature $\xi(T) \sim (T_{SC} - T)^{-1/2}$, but there is a limit to how far reducing temperature can boost B_{c2} and the coherence length drops to a fairly constant ξ_0 once far below T_{SC}. The coherence length is also inversely proportional to the effective mass, and so B_{c2} is also enhanced by the heavy fermion nature of UGe_2 and URhGe (and, importantly, at any points on the phase diagram where m^* is significantly increased).[107]

The upper critical field is generally governed by two effects imposing two different limits, the Pauli paramagnetic limit and the orbital limit. In a conventional BCS superconductor, the Cooper pairs are formed by electrons with opposite spin, i.e. a singlet state, often described as an s wave state. In this case, flipping one of the spins will destroy the Cooper pair and thus destroy the superconducting state. This is the Pauli paramagnetic limit, where application of an external field provides sufficient energy for spin-flip excitations that break Cooper pairs.

From this is should be immediately obvious why ferromagnetism and superconductivity were traditionally thought of as competing states of matter, as antagonistic phases unable to coexist, since the large internal field responsible for spin alignment in the ferromagnetic state easily destroys the Cooper pairs required for conventional s-wave superconductivity.[107] The strong ferromagnetic ordering does however mean that the Pauli paramagnetic limit is not applicable to the unconventional superconductivity that somehow does arise in UGe_2 and URhGe, and thus these compounds are described as 'orbitally limited' superconductors.

In contrast to a type I superconductor, in which the Meissner effect will result in the expulsion of all flux from the interior of the sample, a type II superconductor can exist in a 'mixed state' above critical field B_{c1}, below which the full Meissner

effect is also present. Above B_{c1}, but below the upper critical field B_{c2}, the magnetic flux from an external field will penetrate the material as a vortex lattice, where a vortex describes a small region of the normal state residing within the bulk superconductivity (hence 'mixed state').

Each vortex contains precisely one flux quanta, so increasing the field increases the number of vortices and so the density of the lattice. The orbital limit occurs when the separation between vortices approaches the vortex size, essentially overlapping the normal state regions such that the entire material becomes normal. The radius of a vortex is related to the coherence length, leading to the expression $B_{c2}(T) \sim \Phi_0/\xi^2(T)$ seen earlier.

With a small enough coherence length and the absence of the paramagnetic limit, ferromagnetic superconductors can thus have very high upper critical fields. For example, URhGe remains superconducting in excess of 30 T. Millikelvin temperatures are required, and also very high purity samples because the mean free path needs to exceed the coherence length, but the upper critical field is nevertheless impressive.

The ferromagnetic order means that Cooper pairs must be formed from an aligned spin state, a spin-triplet state, rather than the anti-aligned, singlet state described by conventional theory. Ferromagnetic superconductors therefore require an unconventional pairing mechanism, likely based on magnetic fluctuations rather than lattice distortions. Any effective attractive interaction between electrons, involving the exchange of bosons other than phonons, can give rise to superconductivity, in which case the electron pairing may have p-wave or d-wave character instead of the s-wave form assumed by the BSC theory.[104] Unconventional pairing also typically means that the symmetry of Δ is lower than that of the underlying crystal, unlike for s-wave pairing, which has spherical symmetry.[104] A good review titled "Superconductivity without phonons" can be found in Ref. [108].

The usual starting point for discussions on pairing mechanisms in ferromagnetic superconductivity is the Fay and Appel theory,[27] published in 1980. The theory considers equal spin pairing by the exchange of longitudinal paramagnons, fluctuations in the spin structure parallel to the magnetization, in an itinerant system where the same electrons are responsible for both superconductivity and ferromagnetism. The authors conclude that it is indeed possible for spin fluctuations to produce a p-wave superconducting state within a ferromagnetic

phase near the border with paramagnetism.

In a 1988 publication[109] Millis, Sachdev and Varma investigated the effect of magnetic fluctuations on the transition temperature of unconventional superconductors, seeking to clarify which were beneficial to the emergence of superconductivity and which were 'pair breaking'. The results were a critical frequency in the boson spectrum, with low frequency fluctuations being pair breaking and higher frequency bosons enhancing T_{SC}.

In Ref. [110] a generic phase diagram is presented for a metal in which magnetic order is driven to ever lower temperature by increasing lattice density. Near the critical density where the magnetic transition temperature reaches absolute zero the magnetic interactions become strong and long-range, leading to Cooper pair formation and the emergence of a superconducting phase. This generic diagram is compared to the phase diagram for several real, heavy fermion materials, where the Néel temperature is reduced to zero by the application of pressure and the superconducting state emerges in the vicinity. The authors note that "our evidence speaks strongly in favour of the existence of a superconducting state which arises because of magnetism rather than in spite of it."

Essentially, since spin-order fluctuations are greatly enhanced in the vicinity of a magnetic phase transition is it likely that magnetically mediated superconductivity can be found in regions of the phase diagram where such a transition occurs at temperatures low enough to meet the conditions typically required for the emergence of such unconventional superconductivity.

The point on the phase diagram where a magnetic transition temperature is reduced to absolute zero, by varying conditions such as chemical doping concentration, magnetic field strength, hydrostatic pressure or uniaxial stress or strain, is known as a quantum critical point (QCP), and is therefore the perfect place to look for the emergence of superconductivity.

Quantum criticality is a more general phenomena than a simple indicator of potential superconductivity, and quantum critical points occur in many different materials. A good example is $YbRh_2Si_2$ where the Néel temperature is driven to zero by application of magnetic field and the quantum fluctuations between two incompatible ground states at the QCP influences the properties of the material at finite temperature over a large area of the phase diagram. The critical fluctuations associated with the competition between the RKKY interaction and Kondo screening at $T = 0$ K produce a region of so-called non-Fermi-liquid behavior

above the QCP, with a characteristic T-linear dependence to the resistivity. In general the appearance of exotic or novel phases in the vicinity of QCPs is what makes them particularly interesting to study.

The Fermi surface reconstruction at the critical point in $YbRh_2Si_2$ is studied in Ref. [111] by measurements of the Hall coefficient, which shows a dramatic jump at the transition and provides insight into the formation of the heavy fermion state. These measurements are possible because of the absence of superconductivity in this case, allowing the QCP to be studied in more detail, as in Ref. [112] or Ref. [113]. Much of the discussion surrounding $YbRh_2Si_2$ is applicable to UGe_2 too, though the two are obviously very different, and it is this universality of behavior that also makes quantum criticality an interesting topic.

Regarding UGe_2 and URhGe, however, since the ferromagnetic transition becomes first order before reaching absolute zero, the 0 K point is technically not a QCP, which is only strictly defined for a continuous phase transition. The critical points in UGe_2 and URhGe could perhaps be called unconventional QCPs, since the general idea of strong fluctuations between incompatible ground states leading to the emergence of exotic or novel phases remains the same. The bifurcation of the phase transition line at a tricritical point, and the resulting first order wing structure, is proposed in Ref. [114] to be a universal low-temperature property of ferromagnets, and so it seems unlikely that a true QCP exists for the FM-PM transition.

The important point as far as superconductivity is concerned is the presence of strong magnetic fluctuations, which may possibly be more closely related to the QCEPs at the feet of the wings than the unconventional QCP, or possibly even related to the tricritical point. The three occur in a relatively small area of the phase diagram for both UGe_2 and URhGe and it is difficult to distinguish which phenomena are associated with which critical point.

In Ref. [45] it is "demonstrated that re-entrant superconductivity in URhGe can arise even in the absence of critical fluctuations due to a drastic increase in longitudinal susceptibility." Hence it is arguably the high susceptibility (of the correct type) and not strictly quantum criticality that is required for the superconducting pairing. An expansion of the Landau free energy is used in Ref. [45] to explore this idea, working in terms of the longitudinal and transverse components of the magnetization and the susceptibility.

Were these components fully characterised across the URhGe phase diagram it

would allow the coefficients of the free energy expansion to be calculated and, after minimising the expression, the relative strengths of the magnetic fluctuations to be judged regarding which are beneficial to superconductivity and which are antagonistic. This is essentially an ultimate aim of the URhGe project outlined in this thesis, a goal unfortunately not yet reached but hopefully achievable in the future.

As a more simplistic analysis, the transverse and longitudinal susceptibility could simply be compared to each other directly. In Ref. [115] it is shown that "the critical temperature for spin-triplet, p-wave superconductivity mediated by spin fluctuations is generically much higher in a Heisenberg ferromagnetic phase than in a paramagnetic one, due to the coupling of the magnons to the longitudinal magnetic susceptibility."

However in Ref. [116] it is observed that "the natural direction for a spin-rotation excitation to propagate is along the direction perpendicular to the plane of rotation", which would be transverse to the magnetic moment, suggesting that it might be enhanced transverse, rather than longitudinal, magnetic fluctuations at the moment rotation transition in URhGe that are beneficial for superconducting pairing. Simultaneous measurements of both components of the magnetization as a function of the tuning field should elucidate the situation and provide useful information about the type of magnetic fluctuations responsible for superconductivity in URhGe.

Chapter 3

Hall Resistivity Experimental Methods

3.1 Introduction

The main sample of UGe_2 used for the Hall effect project was a high-quality (RRR $\simeq$ 70) single-crystal grown by the Czochralski method, orientated by Laue diffraction and cut by spark erosion to produce a thin plate, roughly rectangular, with faces normal to the a-axis and sides aligned parallel to the b and c-axes. It should be noted that crystal growth and cutting was preformed by others in the research group before this project began (see acknowledgments). At the start of the project Laue diffraction was used to confirm the single-crystal nature of the sample and to check the crystallographic orientation, which was indeed aligned to the sample geometry to within $\sim 1^\circ$.

The sample was then mounted within a BeCu piston-cylinder pressure cell, capable of applying precise and easily adjustable hydrostatic pressure up to 20 kbar (at room temperature). Daphne oil was used as a pressure medium and a coil of Manganin wire utilised as a pressure gauge: the resistance of Manganin varies linearly with pressure and the coefficient of that linear relation varies linearly with temperature.

A closed circuit helium-4 refrigerator and superconducting magnet system was employed to provide temperatures down to 2 K and magnetic fields up to 9 T. Resistance measurements were made using a standard low-noise a.c. set-up, with

lock-in amplifiers and (room temperature) pre-amplifier transformers. The Hall effect was measured according to the van der Pauw method, using four gold contacts spot-welded to the perimeter of the sample plate surface and the usual field reversal techniques, which will be described in detail in section 3.4. Current was typically applied parallel to the c-axis and magnetic field applied parallel to the a-axis, the axis of easy magnetization.

3.2 Sample Preparation

The UGe_2 sample used for the high pressure study is shown in figure 3.1 along with a sketch showing the sample dimensions and orientation. Also accompanying this is a pattern-matched Laue diffraction image, demonstrating the alignment of the sample plane normal with the a-axis. At the bottom of figure 3.1 the pressure cell is shown in detail. The 'L' shaped sample table is indicated in the labeled diagram; the sample was mounted horizontally, onto the bottom of the 'L', such that the a-axis points vertically in the diagram and photographs.

A coil of Manganin, a couple of millimeters in diameter, was placed into the cylindrical space below the sample table. For a sense of scale, the internal bore of the cell is 4 mm in diameter. Daphne oil filled the volume between the upper and lower copper seals, providing a reliable hydrostatic pressure medium.[117] Measurement wires for the sample and Manganin coil were threaded through the BeCu plug and out the bottom of the cell, the small exit hole being sealed with Stycast epoxy.

The labeled photograph of the pressure cell shows the connection to the cryostat probe and the setup for an initial measurement during testing, whereas the second photograph shows the usual experimental setup. Note that the locking bolt is much lower in the latter, indicating a much higher pressure than the former. Another major difference is in the wiring: for all data presented in this thesis well-secured, twisted-pair wiring was employed for low-noise measurements in high magnetic field.

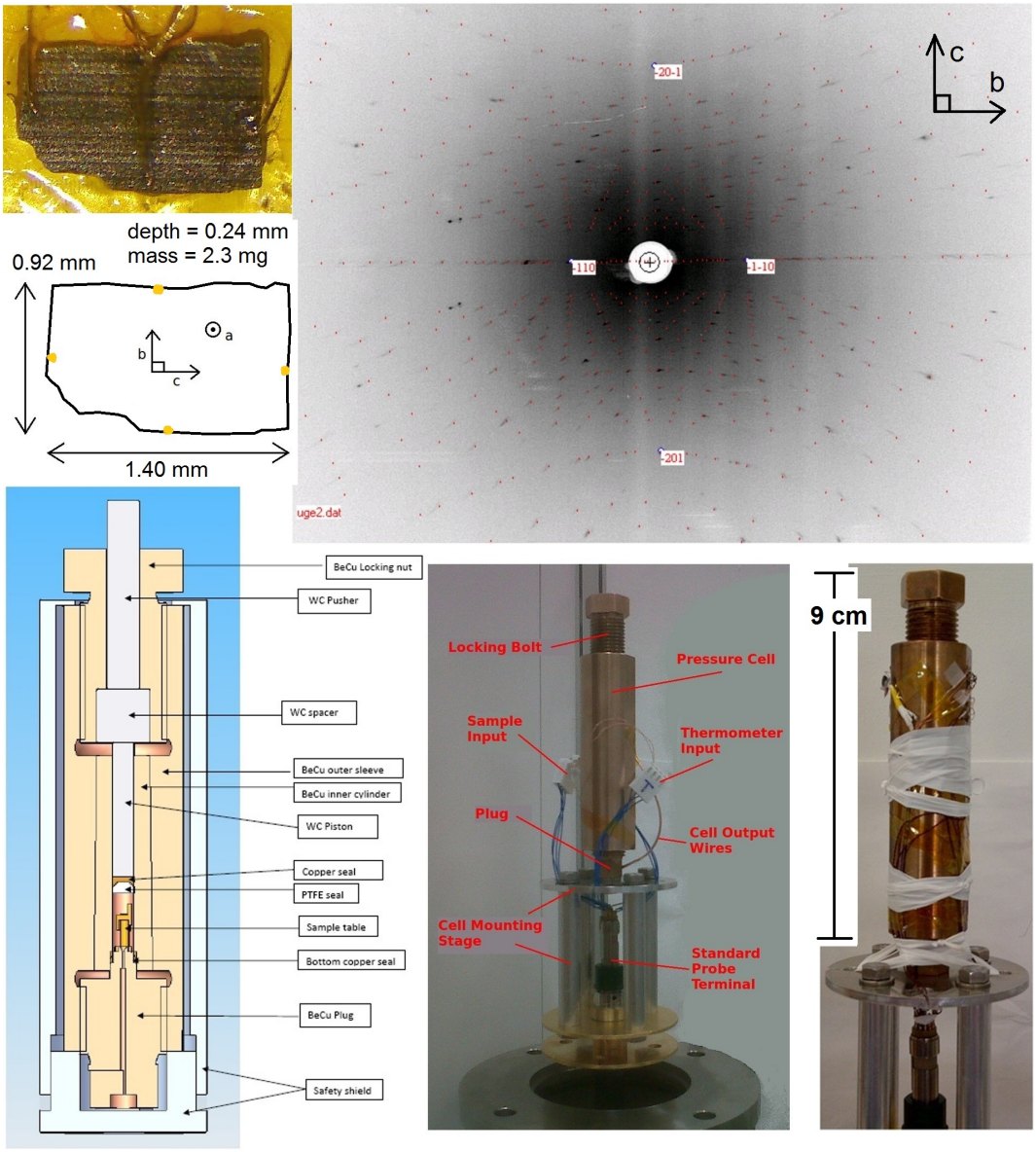

Figure 3.1 **Top Left:** Photograph and sketch of the UGe_2 sample used for the Hall effect study. In the photograph four spot-welded gold wires can be seen. The approximate contact positions of these wires are indicated by gold spots in the sketch, along with the sample dimensions and crystallographic orientation. **Top Right:** The Laue diffraction pattern for the sample, for a backscattered x-ray beam parallel to the crystallographic a-axis, matched to show the c-axis vertical and the b-axis horizontal. **Bottom Left:** Diagram of the piston-cylinder pressure cell showing the sample space within the 4 mm diameter bore. **Bottom Centre:** Labelled photograph of the pressure cell mounted on the cryostat probe stage, showing initial testing at low pressure. **Bottom Right:** Photograph of an actual measurement run at high pressure, showing well secured, twisted-pair wiring.

3.3 Motivation for the Van der Pauw Method

The Hall effect is, in concept, a simple measurement: magnetic field is applied to the sample in one direction, current is applied perpendicular to the field, and the voltage perpendicular to them both is measured. Working with tiny samples, however, at high pressure and very low temperature, makes the measurement procedure somewhat more complicated, as does the ferromagnetic nature of the material.

Measurements at high pressure often require very small samples because the space within the pressurised environment is of the order of millimeters at most, the piston-cylinder cell with its 4 mm bore providing one of the larger sample spaces in high pressure physics, though compromising maximum achievable pressure to do so. While the piston-cylinder cell used in this project had a maximum pressure of around 20 kbar, a standard diamond anvil cell can reach about 4,000 kbar, although the sample space in that case is a mere 8 μm, the size of a single red blood cell. Regardless of the limitations of the pressure cell, high-quality samples of single crystal UGe_2 cannot be grown beyond a few centimeters in size anyway.

Small samples then necessarily require very small measurement wire contacts, which at low temperature have relatively large contact resistances, giving rise to voltage noise of magnitude such that the desired measurement signal becomes difficult to accurately obtain. This difficulty arises partly because of the relatively low signal strength, due to using low currents in order to avoid resistive heating of the sample: power dissipation scales as the current squared. For metallic samples at low temperature the resistance is very low, such that these small currents produce only very small voltages.

Sample heating from larger currents must be avoided for two reasons. Firstly, depending on the amount of cooling power available from the cryostat, resistive heating may prevent the sample stage from reaching the low temperatures desired. And secondly, local heating of the sample may lead to a discrepancy between the temperature of the thermometer and the temperature of the sample, giving inaccurate measurement data. Specially shaped 'bridge-type' samples[118] can reduce the noise introduced by small measurement contacts but this requires intricate cutting that is practically impossible to carry out on millimeter-sized samples of a brittle material such as single-crystal UGe_2.

Several methods exist that provide a solution to the high noise-to-signal ratio encountered in small metallic samples. A number of them are contrasted in Ref. [119], which concludes that "the van der Pauw method yields the most accurate measurement of the Hall constant" provided that a number of conditions are met. The van der Pauw method[118] requires a sample shaped as a thin, flat plate, with four point-contacts placed on the same face and spaced around the edge; magnetic field is applied perpendicular to the face of the plate. The accuracy of this method relies on the contacts being as small as possible, as close to the edge as possible, and the sample being 'thin' and free of holes.

The error introduced due to contact size is discussed in depth in Ref. [120] and calculated as negligible for the spot-welded 25 μm diameter gold wires used in this experiment. The error due to the displacement of contacts from the edge was required by Ref. [119] to be less than 10% for the van der Pauw method to be the most accurate, and calculations estimate the error at 2.8% for this experiment. Finally the thickness of the sample used in this experiment, compared to its other dimensions, meets the criteria of 'thin' as specified in Ref. [121] to require no correction to the determined resistivity.

The van der Pauw method also has the advantage that knowledge of the current flow pattern is not required so the sample can be of arbitrary shape and the contacts arbitrarily spaced along the edge, although in this case the theory only strictly applies to isotropic materials. Subsequent extensions of the theory[122] show that the method can also be applied to anisotropic materials, such as UGe_2, although the results obtained will be averages of the values of the conductivity tensor.

The van der Pauw method is particularly sensitive to anisotropy when the contacts are arranged in a square-like configuration,[123] and for a strictly rectangular-shaped sample with a contact in each corner the individual components of the conductivity tensor can potentially be determined in full.[121] Furthermore it can be shown[124] that both the Hall effect and the components of the conductivity tensor can be determined concurrently from the same contact configuration on such a rectangular sample when the sample edges are cut parallel to the crystallographic axes, although the method outlined in Ref. [124] requires a somewhat time-consuming series of measurements for each data point.

It is noted in Ref. [125] that "despite the complicated, asymmetric distribution of current-density lines in anisotropic samples, the transverse Hall field is uniform.

Hall eddy currents in the contact regions of the sample even out the distribution of Hall electric charges at the faces". By the same author, Ref. [126] goes on to make the observation that "the Hall field potential in the case of point current contacts has a constant value at all points along the specimen perimeter, except at the point of the current input and output" and that even in an anisotropic material the Hall voltage can be simply measured in any sample where "the contacts for measuring Hall electromotive force are placed along the specimen perimeter on each side of the line connecting current electrodes".

Thus, although the conductivity tensor cannot be fully determined, the Hall resistivity of an arbitrarily shaped sample can be measured, even for anisotropic materials, using arbitrarily spaced contacts. As Ref. [126] points out, however, it is best to have symmetrically arranged contacts in order to reduce the voltage measured in the absence of field (Ref. [125] names this zero-field signal the "transverse conduction voltage" (TCV)), which can make the Hall voltage difficult to measure when the Hall effect is comparatively small. The TCV is reduced by having voltage contacts placed along an axis as perpendicular as possible to the axis of alignment of the current contacts, as seen in figure 3.2(a).

In conclusion, using the van der Pauw method the Hall effect can be measured easily and independently from the lengthy procedure and constraints imposed by calculating all components of the conductivity tensor, by way of a simple 4-probe measurement. The Hall voltage could possibly be obtained from the difference between a measurement in an applied field and in the absence of field, although this is not an ideal measurement of the Hall effect since other effects usually contribute to the transverse voltage, as discussed in Ref. [127]. These undesired voltages in the measurement signal are basically impossible to eliminate with d.c. methods and Ref. [127] suggests the use of a.c. current and narrow-band amplifiers, which is indeed the experimental set-up employed in this project (such a set-up would be used for low temperature, low-noise measurements anyway, as discussed in section 4.5).

The issue of magnetoresistance effects in the TCV still remains with a.c. techniques, however, and a field reversal method must be employed to accurately measure the Hall voltage in the case of significant magnetoresistance and a significant TCV contribution, as is the case for the UGe_2 sample in these experiments. More details on field reversal and the van der Pauw method can be found below in section 3.4.

3.4 The Van der Pauw Method in Detail

3.4.1 Placement of Contacts

The ideal setup for measurement of the Hall effect by the van der Pauw method is shown in figure 3.2(a). The contacts are placed in a symmetric configuration where for the UGe_2 sample $x \sim c$-axis and $y \sim b$-axis as defined by the sample geometry, with the orientation of the voltage contacts ideally aligned to the y direction, as perpendicular as possible to the current contacts, which are ideally aligned to the x direction.

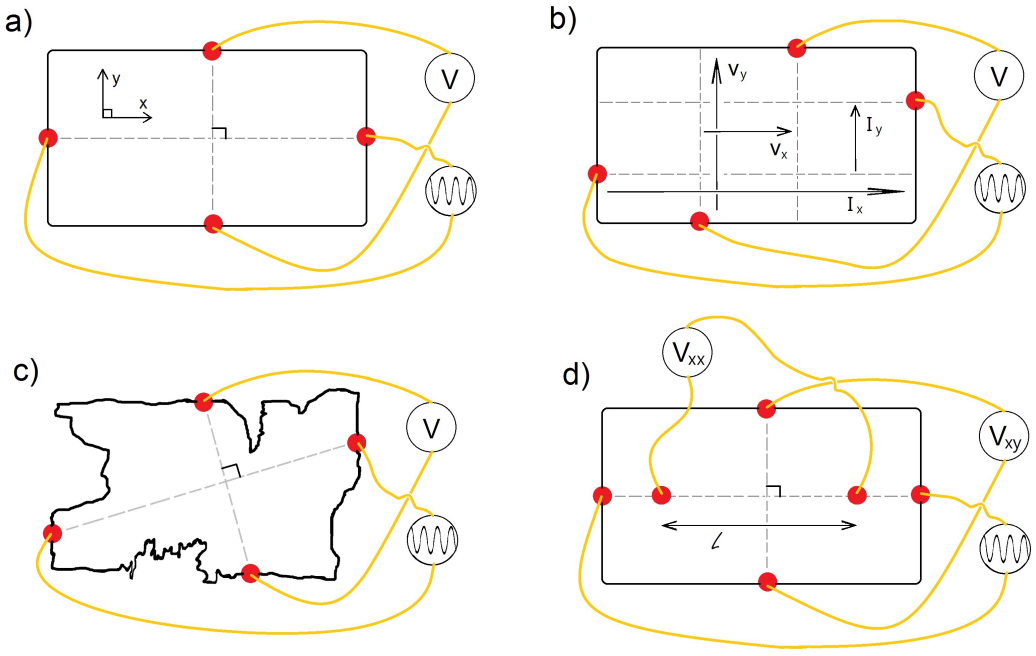

Figure 3.2 Several examples of possible placement of electrical contacts on a sample for Hall effect measurements. **a)** The ideal case of well-aligned and perpendicularly-oriented contacts, placed on the edge of the sample as per the van der Pauw method. **b)** An exaggeration of mis-aligned contacts, where both voltage and current contacts are skewed from ideal alignment with the crystallographic axes and their relative orientations are far from perpendicular. **c)** For a non-ideal sample shape, with rough edges, the orientation of the voltage and current contacts are still perpendicular, however alignment to the crystallographic axes has been lost. **d)** One possible method of quantitatively determining the longitudinal resistivity while also optimising the Hall effect measurement by using six contacts.

Note that even in the case of perfect current contact alignment (and if the x axis is *defined* as the orientation of the current contacts then such perfection can be achieved in practice) the current will not flow directly in a straight line

between the contacts, there will generally be a 3d current flow pattern through the sample.[118, 128] Thankfully, one of the key advantages of the van der Pauw method is that no knowledge of the current flow is required. An unavoidable consequence, however, is that there will be potential differences throughout the sample whenever a current flows, which is the origin of the TCV introduced in section 3.3.

For UGe_2 the longitudinal resistivity ρ_{xx} is of the order $\times 100$ the magnitude of the Hall resistivity and so any slight deviation from perfectly perpendicular will result in a measurement signal comprised of both the Hall voltage and the TCV. Explicitly, if the angle between the orientation of the contacts is ideally 90° then a single degree mis-alignment from this, around 1%, coupled with the factor of $\times 100$, produces a TCV of similar magnitude to the Hall signal.

Figure 3.2(b) shows an exaggeration of this effect, where both the current and voltage contacts are severely skewed from alignment. Here there is a significant contribution to the voltage signal from $V_x \parallel I_x$ and $V_y \parallel I_y$ in addition to the Hall voltage, which is a mix of predominantly $V_y \perp I_x$ with some $V_x \perp I_y$. The skewed alignment might not actually matter if there is no interest in keeping to crystallograpic axes, which is a major strength of the van der Pauw method: as long as the contacts are spaced along the edge of the sample the Hall voltage can be measured reliably by reversing the direction of the magnetic field (see equation 3.1).

However, for UGe_2 where $\rho_{xx} \sim 100 \times \rho_{xy}$, for such a configuration of contacts the Hall voltage may be just a tiny fraction of the measurement signal, meaning that it suffers from excessive noise when extracted from the mix. Thus the ideal setup of symmetric contacts, as seen in figure 3.2(a), becomes almost a necessity under such conditions.

Figure 3.2(c) also shows a skewed configuration, but here the $\sim 90°$ between voltage and current contact orientations is preserved, allowing a low-noise measurement of the Hall voltage; only the alignment of the current and voltage to the crystallographic axes is lost in this case. If there is limited freedom in the placement of current or voltage contacts, perhaps due to the sample shape and its edges, if it is not possible or desirable to cut a well-formed rectangle, then a skewed yet perpendicular orientation of contacts should still be aimed for in order to reduce the ratio of TCV to Hall voltage.

Explicitly, the measured signal in the positive field direction can be written:

$V_+ = V_H + V_{\mathrm{TCV}}$. In the opposite field direction the sign of the Hall voltage is flipped, giving: $V_- = -V_H + V_{\mathrm{TCV}}$. Either adding or subtracting these measurements allows the two components of the voltage to be separated.

$$V_H = \frac{V_+ - V_-}{2} \qquad\qquad V_{\mathrm{TCV}} = \frac{V_+ + V_-}{2} \tag{3.1}$$

To convert these voltages to resistivities some length scale is required, and for the van der Pauw method this is d, the depth of the thin, plate-like sample. As discussed in section 2.3 the Hall resistivity is given by $\rho_{xy} = V_H\, d/I$. Determination of the magnetoresistivity ρ_{xx} is based on all the dimensions of the sample, specifically the ratio of the length to the width, which enters calculations in Ref. [121] with reference to Ref. [128] to produce the numeric prefactor factor in $\rho_{xx} \simeq 4.53\, V_{\mathrm{TCV}}\, d/I$.

The 4.53 prefactor is calculated by approximating the sample as electrically isotropic, giving ρ_{xx} as a vague average of the b and c-axis resistivities (something akin to $\rho \sim (\rho_b \rho_c)^{1/2}$), and as such the calculated values used henceforth should only be considered a rough estimate of what in UGe_2 is actually a tensor quantity.

Furthermore, the calculations that provide the value of 4.53 are strictly only correct for contacts placed in the corners, as in the Montgomery method (an extension of the van der Pauw method; see Ref. [121]), rather than on the sides of the sample. As such the values of ρ_{xx} determined in this project, though measured to high precision, are perhaps only accurate to an order-of-magnitude, which, as the discussion in section 2.3 hopefully illustrates, makes complete analysis of the Hall coefficient more challenging. For a true determination of the resistivity ρ_{xx}, which in this case would be the c-axis resistivity, the Montgomery method would have to be followed in full.

Alternatively, three long and thin bar-shaped samples, with their edges cut parallel to different combinations of the crystallographic axes, provides a more straightforward way to obtain all components of the resistivity tensor. Or, if merely a more accurate ρ_{xx} is required, a 6 contact setup could also be utilised, as seen in figure 3.2(d), whereby the displacement L provides a more quantitatively correct way of calculating ρ_{xx} than using the TCV and the approximations stated above.

The focus of this investigation, however, is on the Hall effect and the simple arrangement of contacts seen in figure 3.2(a) was chosen with that focus in mind.

3.4.2 The Sign of the Hall Voltage

From equation 3.1 it can be seen that the sign of the Hall voltage is rather arbitrary if based solely on that simple piece of mathematics. The choice of $V_+ - V_-$ could equally be $V_- - V_+$ and the sign would be different, though in reality the sign is fixed by the cross product in the Lorentz force and only one choice is actually correct. Thus it was necessary to first verify the order of terms in equation 3.1 and then ensure that every experimental run was consistent about the direction of the current and the polarity of the measured voltage.

One way of maintaining consistency between experimental runs was use the sign of ρ_{xx} as a fixed certainty: it should generally be positive and increase with increasing field, and does not depend on any choice of mathematics. Since the TCV is definitely positive and the contacts have the slight misalignment shown, as an exaggeration, in figure 3.3, then the current flow must be in the negative x direction. In this case a positive voltage measurement must be potential difference $V_2 - V_1$.

The raw data for a typical measurement is shown in figure 3.3 for both directions of applied field. The formula defined by equation 3.1 would therefore give the Hall voltage as negative and suggest that in positive field, for current in the negative x direction, the Hall voltage must be in the negative y direction.

The positive field direction was vertically upward within the cryostat, though the sample was mounted upside-down meaning that positive H was into the page for the diagram presented in figure 3.3. This implies that the cross product from the Lorentz force produces a Hall voltage in the negative y direction, as concluded earlier. Hence everything is consistent and the order of terms in equation 3.1 is correct.

3.4.3 Experiment Details

The current supplied for all Hall effect measurements was 0.1 mA by way of 0.1 V applied across a 1 kΩ low-TCR resistor. A pre-amplifier gain of ×500 was applied to the voltage signal by way of an active, room-temperature transformer. The a.c. frequency was set to 37 Hz, chosen as high enough to ensure a proper response from the transformer while low enough to minimise the pick-up of inductive voltages and stray capacitance. Twisted-pair wiring was also used throughout

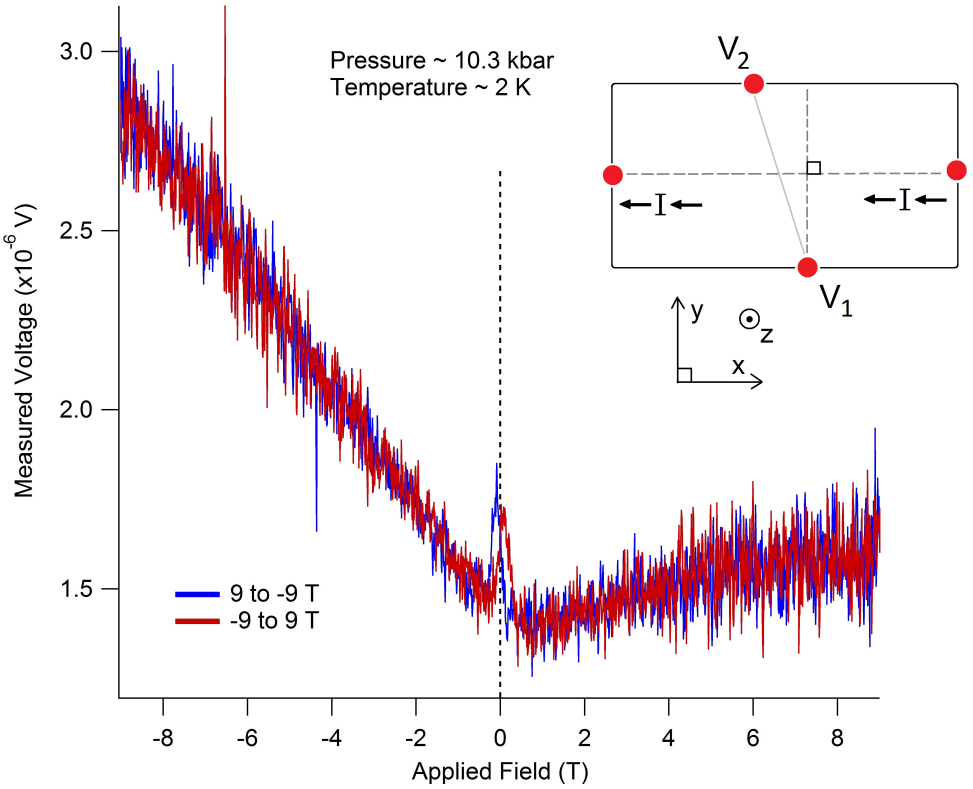

Figure 3.3 **Main:** The measured voltage as a function of field at 2 K and 10.3 kbar. At positive field the reduced magnitude, relative to negative field, suggests that the Hall voltage has opposite sign to the current. From the physical direction of the field, this implies that the Hall voltage is negative. **Inset:** A sample diagram showing the positions of the electrical contacts, where the voltage contact mis-alignment has been exaggerated.

the circuit to this effect.

The Cernox thermometer (CX-1050-SD type) measuring sample temperature was affixed as close as possible to the sample on the outer body of the pressure cell using General Electric varnish. The sample was themalised to the pressure cell by the pressure medium (frozen Daphne oil) and by contract with the metalwork of the cell through a thin sheet of Kapton film. The large thermal mass of the pressure cell helped to maintain stable temperature control on gradual sweeps.

Thermal lag between the sample temperature and thermometer temperature was minimised by using slow temperature sweep speeds and no significant effects of thermal lag were observed in the results. Typically the time constant between a sudden change in temperature according to the thermometer and the corresponding sudden change in the resistance of the sample was roughly 10 seconds, and the standard rate of temperature variation was 0.5 K per minute.

The effects of magnetic field on the output of the thermometer were also considered, though calculations based on Ref. [129] show that the magnetoresistance of the thermometer is negligible above 4K and even at cryostat base temperature only becomes a consideration above about 8 T. For example, at 4 K and 9 T the calculated correction to the thermometer read-out is around 0.03 K, which is a small systematic error of less than 1% even at this extreme.

The field was always applied parallel to the crystallographic a-axis, the easy axis of magnetization, to ensure that the magnetization remained in a fixed orientation relative to the field. Having the two vectors aligned also simplifies analysis of the ordinary and anomalous Hall effects to a 1d problem and makes correcting for the demagnetizing field easier. Applying field in any other direction would result in a gradual rotation of the magnetic moment (as discussed at length in regards to the URhGe project) and would needlessly complicate the experiment.

Measurements were primarily performed over a range of fixed magnetic fields, sweeping temperature between 2 and 60 K, as seen in figure 5.7, which gives the Hall effect data presented in figure 5.3. Measurements were also taken at various fixed temperatures, sweeping field between -9 and 9 T, a few examples of which are presented in figure 5.8.

A full data set was collected for each of 13 different pressures, 12 points between 7.8 and 14.3 kbar (at low temperature) in addition to ambient pressure measurements (with the sample remaining within the pressure cell for consistency).

3.5 Measuring Pressure

In order to construct a precise, sample-specific phase diagram, necessary to attribute sub-ranges of the Hall resistivity data to the correct phase, an accurate method of pressure determination was essential, allowing for the precise positioning of the Curie temperature and the metamagnetic critical points T_X and H_X as described later in sections 5.1 and 5.2. The chosen method for determining pressure within the BeCu piston-cylinder cell for this project was the resistance measurement of Manganin wire.

3.5.1 Advatages of the Manganin Pressure Sensor

Pressure within a piston-cylinder cell can be determined in many different ways, the most common being to measure the resistance of a sample of lead or tin, or essentially any superconductor with a well characterised relationship between the superconducting transition temperature and hydrostatic pressure. This method, however, provides only a single data point as a function of temperature and it is not precisely known how the pressure varies over the measurement range (2 to 60 K in this case).

Although pressure typically does not change dramatically with temperature within a piston-cylinder cell there is nevertheless a noticeable variation (see figure 3.5 for example) and for fine steps in pressure, seeking data-point resolution of fractions of a kilobar, that temperature variation becomes important. It is also important when seeking fine, controlled steps to have a measure of pressure at room temperature while the cell is being adjusted (which was done with a bench-top hydraulic press).

A potential solution is to use ruby fluorescence,[130] whereby laser light is shone onto a small chip of ruby within the pressure cell and a spectral analysis of the fluorescence acts as a pressure sensor: the peaks in the fluorescence spectrum shift in frequency as a function of pressure. In a piston-cylinder cell, however, this method is hampered by the lack of optical access. Unlike a diamond or sapphire anvil cell, for example, where the laser can be shone through the transparent anvils and directly onto the ruby from outside the cell, the piston-cylinder cell is constructed of opaque BeCu walls and an equally opaque tungsten piston.

Optical access could still possibly be provided by use of fibre optics, the glass filaments passed through the epoxy-sealed hole in the BeCu plug along with the measurement wires, but this has some issues. Firstly, resistance measurements are simply easier to perform. The experimental set-up for ruby florescence is more complicated, requiring optical equipment within the cryostat, a lens and a collimator at least, and more complicated usually means less reliable. Also, resistance can be measured to very high precision and very small differences in pressure determined that way, resulting in finer resolution at the pressures relevant for the UGe_2 project than ruby florescence can provide, the latter being more suited to measurements at very high pressure $\sim$1 Mbar.[130]

Hence in this investigation pressure was determined by resistance measurement

of a small coil of Manganin wire, which once calibrated allows the pressure to be measured continuously as a function of temperature. There exist other alloys that have similar responses to pressure and are often used as pressure sensors, but Manganin was chosen for its high resolution and reliability.[17, 131–134]

3.5.2 Pressure Sensor Calibration

Calibration required both the resistance of the Manganin at ambient pressure, as a function of temperature, and the calibration coefficients found in Ref. [17]. The coefficient α is the constant of proportionality between the change in resistance and the change in pressure, defined as:

$$\alpha = \frac{1}{R_0}\frac{dR}{dP} \tag{3.2}$$

where R_0 is the resistance at ambient pressure. This coefficient was found[17] to be constant as a function of pressure from approximately 0 to 14 kbar but does have a strong temperature dependence.

The temperature variation of α is approximated in Ref. [17] by two regions of linearity, above and below 110 K, though the approximation was only verified by measurement down to 77 K. The authors note, however, that their linear relationship fits well with similar behaviour reported in Ref. [134], where measurements were performed to 4 K. The value of α proposed by Ref. [17] extrapolated down to 2 K is shown in figure 3.4.

The variation of α and its temperature dependence between different coils of Manganin was investigated in Ref. [133], which concluded that the general result for the material could be used reliably without the need to individually calibrate every newly created coil. The pressure is thus calculated by simple rearrangement of equation 3.2 to:

$$P = \frac{1}{\alpha}\frac{R(P) - R_0}{R_0} = \frac{1}{\alpha}\frac{\Delta R}{R_0} \tag{3.3}$$

The measured resistance at high pressure and the ambient pressure measurement used for calibration were both smooth and low-noise, and both show a significant decrease on cooling as is typical for a metal. The difference between the curves, ΔR, varies only slightly however, making this value comparatively rough and noisy. While ΔR decreases slightly on cooling, dividing by the substantially

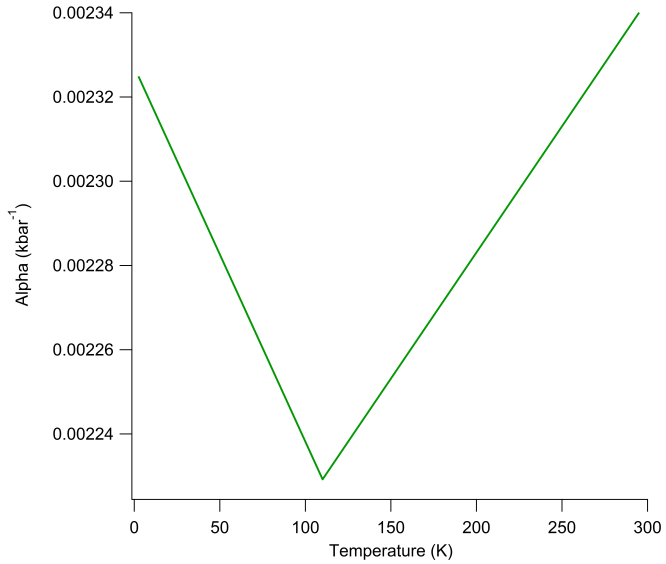

Figure 3.4 A plot of α, the change in Manganin resistance with change in pressure, relative to the ambient pressure resistance, as a function of temperature, according to the approximation to experimental data determined in Ref. [17]. It is worth reiterating that this is a plot of two temperature regions characterised by different linear equations, developed for generic use with Manganin pressure sensors, which are only approximations to the real behavior.

decreasing R_0 produces an increasing quantity that leads to an overall increase in the calculated pressure. The final calculations shown an increase of over 1 kbar for the higher pressure cool-downs, gradually reducing to about 0.3 kbar for the lowest pressure.

The final step of the calibration was to use the position of T_X to ensure that P_X, the pressure at which T_X becomes zero, lies at 12.5 kbar in accordance to the value from published literature,[21] since the absolute values of the pressure calculated from equation 3.2 were found to be about 1.5 kbar too high.

The main reason why this adjustment was necessary was a mistake in the experimental method: current was applied using the lock-in amplifier signal generator and a 10 kΩ resistor in-series with the Manganin, which is not the most accurate way of doing so. The problem is that different resistors were used to generate the current for different experimental runs, and since there was an uncertainty in their resistance of about 1% the applied current included an error of about 1% too. At the time of the experiment it was not realised that the calculated pressure would be so sensitive to the absolute value of Manganin resistance. In hindsight, using a high-accuracy current source instrument would have been better.

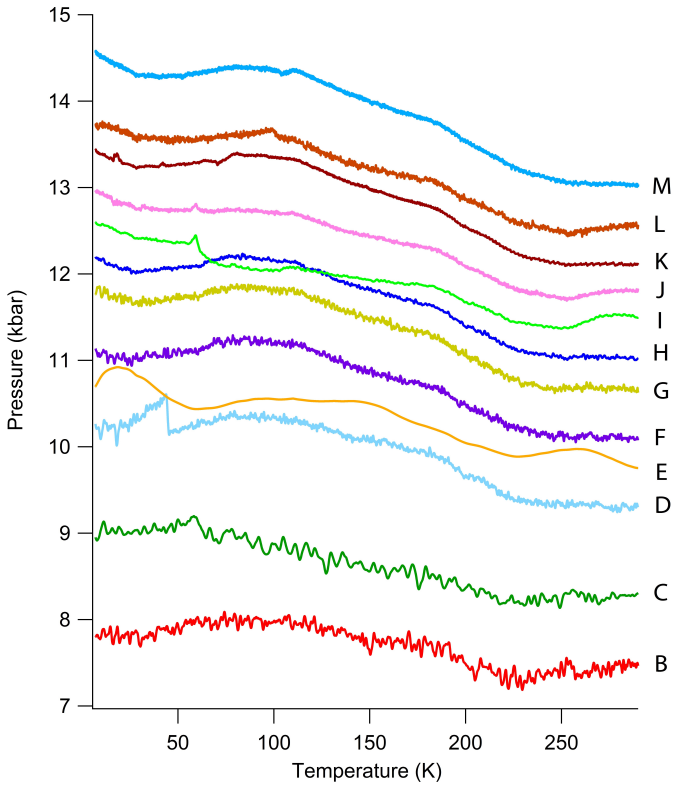

Figure 3.5 The pressure determined by the Manganin pressure sensor, plotted as a function of temperature for every high-pressure experimental run. Note that the E run has been fitted with a smoothing interpolation because of excessive noise that obsured the other plots on the graph. The increase in pressure from room temperature down to 2 K becomes greater as the runs progress from B to M.

The calculated room-temperature values of pressure from the Manganin, measured using a Keithley Multimeter while the cell was being pressurised in the hydraulic press, were used to ensure consistency in the pressure spacing of different experimental runs and to verify the aforementioned 1.5 kbar adjustment. Crucially, though there was some confusion over the absolute value, the variation of the pressure with temperature was still determined accurately and precisely by the lock-in amplifier measurements.

The final results can be seen in figure 3.5, which shows the calibrated data for all experimental runs (labeled with letters B to M where A is the ambient pressure run). As mentioned earlier, the calculated value of pressure is very sensitive to slight changes in ΔR and small irregularities in the resistance measurement produce very noticeable noise and kinks in the data, but the general trend with temperature should be robust.

Finally, the pressure at 30 K as seen in figure 3.6 was used to label the

experimental runs after calibration. It should be noted that the pressure varies only slightly over the temperature range presented in figure 3.6 and so using the 30 K value (in the centre of the main measurement range, 2 to 60 K) to refer to the whole data set and the positions of both T_C and T_X was deemed sufficient for the purpose of constructing the phase diagram.

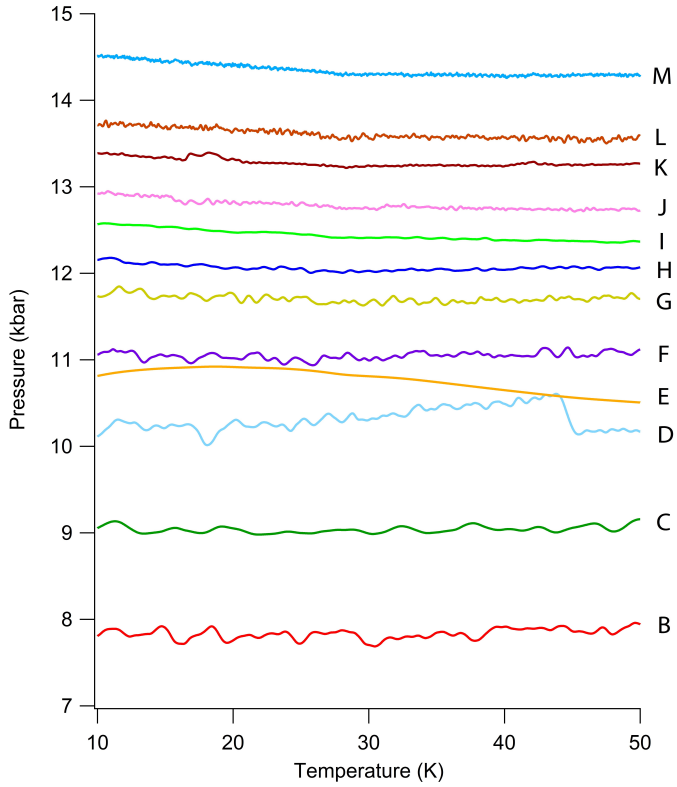

Figure 3.6 The pressure determined by the Manganin pressure sensor, plotted over the low-temperature measurement range for the main Hall effect dataset, for every high-pressure experimental run. Note that the E run has been fitted with a smoothing interpolation because of excessive noise that obscured the other plots on the graph. Compared to the variation in pressure observed at higher temperature, seen in figure 3.5, there is relatively little change in pressure at low temperature. The value at the centre of this graph is the pressure used to label the whole experimental run for subsequent Hall effect analysis.

Chapter 4

Torque Magnetometry Experimental Methods

4.1 Introduction

The main sample of URhGe used for the torque magnetometry project was a small, high quality (RRR $\simeq$ 100) single crystal selected from the fragments of a crushed and broken polycrystalline, annealed, quenched-melt growth. It should be noted that crystal growth was performed by others in the research group, as named in the acknowledgments. X-ray diffraction and the Laue method were used to check the single crystal nature of the sample. A number of electrical contacts were created on the sample surface by spot-welding gold wires, then the sample was oriented by Laue diffraction and glued to the end of a beryllium-copper (BeCu) cantilever.

The cantilever was cut from BeCu sheet by wire erosion and annealed prior to sample mounting. The lever was then placed into the capacitive torque magnetometry device shown in figure 4.2 and the gold wires connected for the resistivity measurement. The magnetometer was mounted onto a single-axis rotator platform in such a way that the b-c plane was oriented vertically and the rotation axis was aligned to the crystallographic a-axis, which was also the magnetic torque axis and so the rotation axis of the cantilever.

The rotator platform was then placed within a cryostat at the field centre of a 17 T superconducting magnet and dilution refrigerator system, capable of cooling the

sample to a base temperature of 20 mK in the absence of field and around 60 mK at 17 T. In addition to the main field, applied vertically, a set of six magnet coils surrounding the sample space, oriented both vertically and horizontally, allowed vectorial application of field modulations and field gradients, in the *b*-*c* plane, at low a.c. frequencies.

Field modulation was applied in order to determine the rotation angle of the sample platform, using a pair of perpendicular pick-up coils, while alternating field gradients were used to perform magnetic force (Faraday) magnetometry. Torque magnetometry was performed using the main d.c. field. Capacitance measurements were primarily performed by a passive bridge instrument, which returned a voltage signal proportional to the unbalanced arm of the capacitance bridge circuit, subsequently measured by a lock-in amplifier. Resistivity measurements were performed simultaneously by standard low-noise a.c. techniques, using a lock-in amplifier and low temperature transformer. Motorised rotations of the sample platform were performed to a precision of $\sim 0.01^{\circ}$.

4.2 Sample Preparation

The primary sample of URhGe used for the torque magnetometry project is shown, stuck to the end of a wooden cocktail stick, in figure 4.1. The sample is roughly spherical with a diameter of $\sim 280\,\mu$m. The original polycrystalline growth of URhGe, a nugget a couple of centimeters across, was crushed by mortar and pestle into tiny fragments and examined under a microscope. Candidate samples were identified as potential single crystals by an apparent clean break from the larger polycrystal, which results in smooth and particularly shiny surfaces. Around a dozen candidates were examined by x-ray diffraction before a genuine single crystal was found. The Laue patterns of failing candidates were disordered with a multitude of blurred spots of low intensity, indicative of polycrystals. The Laue diffraction image of the single crystal sample is shown in figure 4.1, demonstrating a clear and ordered pattern of spots.

Having been identified as a single crystal the sample was removed from the cocktail stick, cleaned by an ultrasonic bath of ethanol, and five gold wires, $25\,\mu$m in diameter, were spot-welded to the surface. There was no particular arrangement to these electrical contacts because the sample was too small, and the uncut surface too uneven, to reasonably pursue methods such as those discussed

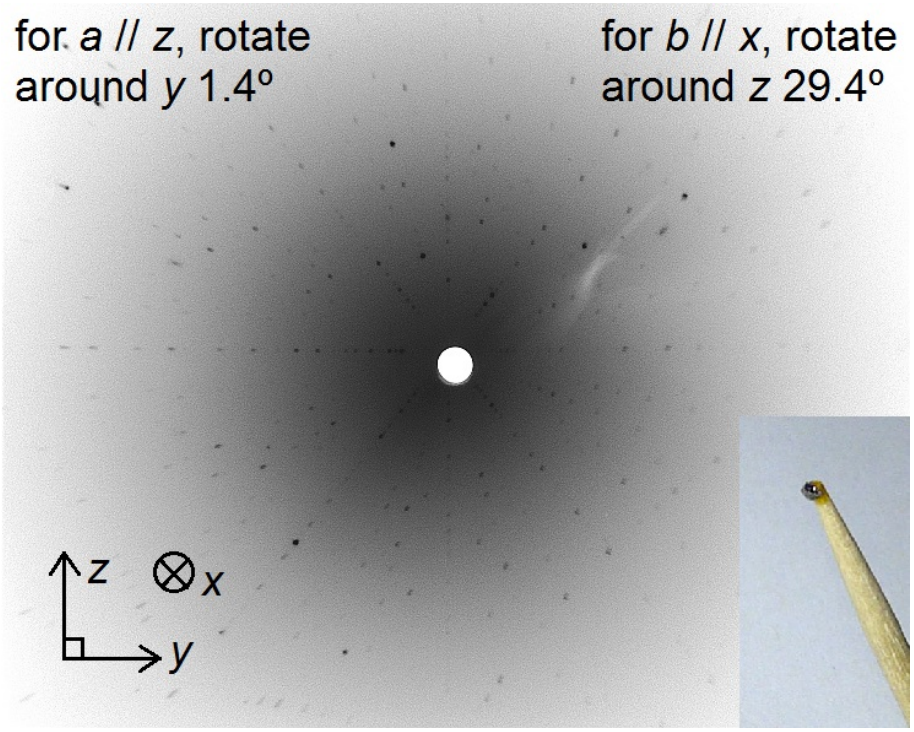

Figure 4.1 The Laue diffraction pattern for the primary sample of URhGe, shown on the tip of a wooden cocktail stick in the photograph in the bottom right corner. The coordinate system for the Laue pattern is shown in the bottom left corner; the x-ray beam direction was parallel to the x-axis. The sample was positioned 5 cm from the backscatter image plate. The a-axis of the sample is almost parallel to the vertical z-axis. The b and c axes have no particular alignment.

in section 3.4. Instead contacts were simply placed wherever possible in a rough line across the naturally curving surface, with sufficient spacing for a reliable four-probe resistance measurement. In this case the resistance is unrelated to any particular component of the resistivity tensor. The fifth gold wire was an ultimately unnecessary spare, used instead for additional thermalisation of the sample.

The sample was suspended by the spot-welded gold wires and oriented by Laue diffraction. The end of the cantilever, hosting a single drop of a weak solution of GE varnish, was then brought gradually closer to the suspended sample until it entered the varnish. Direct contact between the cantilever and the sample was avoided in order to avoid altering the orientation of the sample. Once the varnish was dry a few more drops of the weak solution were added, and allowed to dry, and then the sample was covered by a layer of full strength varnish to glue it securely to the lever.

The gold wires were then unstuck from the support beside the x-ray beam and the cantilever stuck to the support instead, in order to re-analyse the sample in its new position glued to the lever. This Laue pattern is shown in figure 4.1 with details of the final orientation. The gluing procedure was fairly successful, with only a slight twisting of 1.4° leading to a mis-alignment of the a-axis. There was a larger mis-alignment in the b-c plane, of around 30° (or conversely 60°), but since this was the plane of rotation of the sample platform within the cryostat any mis-alignment in the b-c plane was not actually detrimental.

The ideal setup for Faraday magnetometry would be to have the cantilever horizontal relative to the field, the $\theta \simeq 90°$ position. Equation 2.64 shows the consequences, essentially that the torque due to the horizontal field gradient $\partial B_x/\partial x$ would be minimised and the term could be disregarded from the expression, simplifying the analysis.

This is only a minor advantage, however, since the contribution from the $\partial B_x/\partial x$ term is easily characterised from torque measurements and can be subtracted, as it would have to be at any other rotation angle than $\theta \simeq 90°$ anyway. For the URhGe project it was far more important to minimise any mis-alignment of the a-axis and so, having achieved an acceptable outcome in this respect after several attempts at sample mounting, the less than ideal orientation of the b-c plane was also deemed acceptable.

The only mounting mis-alignment with severely detrimental consequences would be if the $\theta = 0°$ position was encountered during the rotation study, in which case the vertical field gradient and vertical force would have no effect on the vertically oriented cantilever. The mounting of the sample described above ensured that this did not happen, since from a starting position of $\theta \simeq 30°$ the angle only increased during the rotation study.

The cantilever was cut by wire erosion from 100 μm thick BeCu sheet and annealed at 320°C for 2 hours to allow the beryllium to diffuse within the alloy, increasing both tensile strength and, more importantly for this experiment, homogeneity of the material. Annealing may also help to soften any stresses and strains introduced to the cantilever during the cutting process. The cantilever was also handled very delicately, with soft plastic tweezers rather than the usual metal ones, to avoid deforming the material and introducing stresses and strains.

The cantilever was prepared after the single crystal sample was found, since the thickness of the cantilever is dependent on the sample size, which determines the

magnitude of the ferromagnetic moment and therefore how stiff the lever must be in order to fulfill all the requirements detailed in section 2.5. Equation 2.41 shows that, with the length of the lever being set by the dimensions of the device shown in figure 4.2, varying thickness is by far the most effective way to vary the stiffness of the lever. At 100 μm thick the maximum deflection of the cantilever, under any conditions, was about 1 μm, roughly 2% of the separation between the capacitor plates (at low temperature). Typical deflections were around a third of that.

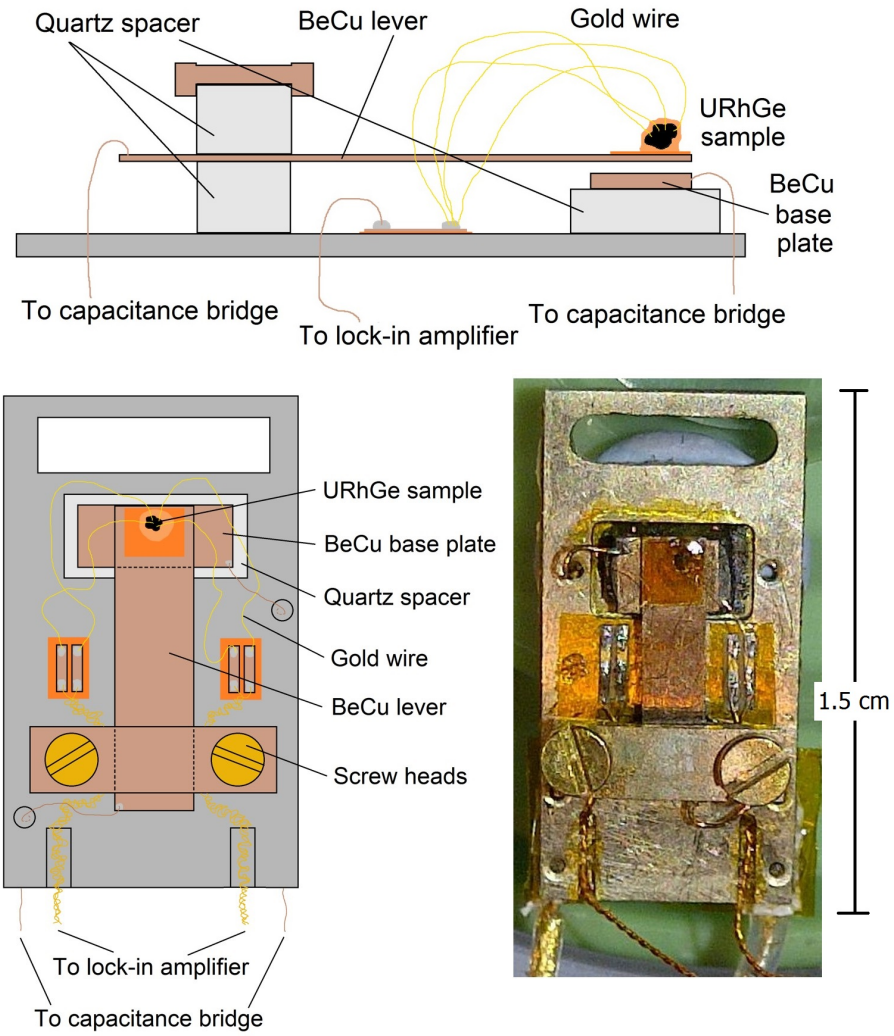

Figure 4.2 Diagrams and a photograph of the torque magnetometer. **Top:** A labelled, side elevation diagram showing the small gap between the cantilever and base plate and also the loose nature of the gold wires. **Bottom Left:** Labelled, plan view diagram of the magnetometer showing the screws used to clamp the cantilever between the quartz blocks that comprised the fulcrum. **Bottom Right:** Plan view photograph for comparison.

The separation between the capacitor plates was controlled by the thickness of the quartz support upon which the base plate was fixed, relative to the height of the quartz fulcrum upon which the lever was fixed. The pieces of quartz indicated in figure 4.2 were cut, by wire erosion, from a larger piece of quartz plate. The fulcrum sections were unaltered while the spacer used as a support for the base plate was gradually polished to a height calculated to provide a separation of $80\,\mu$m between the base plate and the cantilever.

The base plate itself was cut, by wire erosion, from $200\,\mu$m thick BeCu sheet. The polished quartz spacer was fixed in place by Stycast epoxy, which was also used to glue the base plate to the quartz. A layer of hardened Stycast epoxy was estimated at $10\,\mu$m. After assembly, the resulting gap between base plate and cantilever was about $75\,\mu$m, only slightly lower than aimed for, although after reaching cryogenic temperatures the gap apparently shrunk to $50\,\mu$m.

The cantilever was secured by clamping it between two pieces of quartz forced together, with considerable strength, by a metal bracket screwed down hard into the base of the torque magnetometer device. All of the metal components of the magnetometer presented in figure 4.2, except for the cantilever and base plate, were constructed from phosphor bronze. The substantial force exerted on the quartz clamp ensured that the lever would only bend in the length beyond the fulcrum and also aided in good thermalisation of the sample.

Copper wires were soldered to the cantilever and base plate and immediately threaded through individual holes to the underside of the magnetometer, where they entered separate tunnels through the metal, which acted as initial shielding. The wires were then connected to thin co-axial cables, with the join occurring within the tunnels. The co-axial shielding was continuous through the various stages of the dilution refrigerator, using shielded connectors, and maintained to the point where the co-axial cables entered the capacitance bridge instrument.

The gold wires were left long and loose to avoid placing any stress on the cantilever or interfering with the bending moment. Tighter connections may have loaded some additional force on the lever due to the pull of the wires. This unfortunately creates some extra noise in the resistance measurement, since large and unsecured loops of wire pick up induced voltages that scale as the magnetic field squared, but the torque measurement was of primary importance and took priority over noise reduction in the resistance. The gold wires were connected to well-secured, twisted-pair copper wiring as soon as possible and the resulting noise in the

resistivity measurements was well within the limits of acceptability.

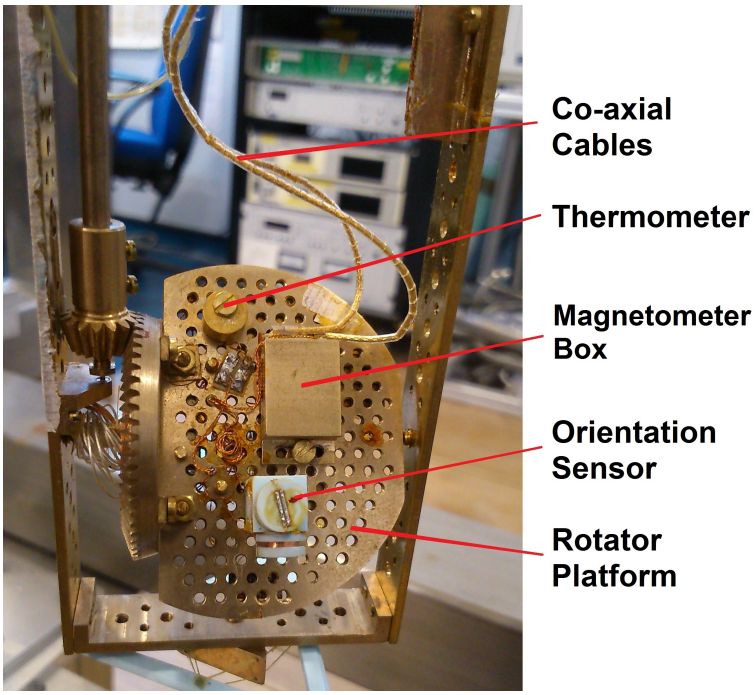

Figure 4.3 Labelled photograph of the rotator platform and gearing; the axis of rotation is the horizontal in this image. The magnetometer is positioned such that the sample, located near the screw that secured the box to the platform, is close to the rotation axis and as such will change position relatively little when the platform rotates.

The magnetometer was enclosed by fitting a tight-sealing lid and the closed, phosphor bronze box was then mounted onto the rotator platform, as shown in figure 4.3. The box was attached to the platform by a tightened screw, ensuring good thermalisation. The co-axial cables were bent into an S shape to allow the length to expand and contract when rotating the platform. The magnetometer was positioned such that the sample was as close to the field centre, and the axis of rotation, as possible. The a-axis of the sample, and the axis of torque and rotation of the cantilever, was thus aligned to the rotation axis of the platform, which in figure 4.3 is the horizontal direction.

The thermometer indicated in figure 4.3 is a field calibrated, ruthenium oxide sensor, also placed within a metal box and screwed onto the rotator platform for good thermalisation. The bundle of silver wires, seen to the left of the gear, are thermally connected to the dilution fridge mixing chamber and clamped hard beneath screws on the opposite side of the rotator platform. The platform itself is constructed from phosphor bronze but is gold plated to aid thermal conductivity. This ensured that the temperature of the sample was very close to the temperature

set by the mixing chamber except at the very lowest temperatures and highest fields.

Also seen in figure 4.3 is the sensor used to determine the orientation of the platform relative to the magnetic field. The orientation sensor consists of a pair of perpendicular pick-up coils wound around a plastic former and mounted atop a plastic pillar, which elevates them from any surrounding metal that could potentially interfere with the measurement. The induced voltage picked up by the coils is a result of an a.c. field applied by the additional magnet coils within the cryostat, as discussed in the next section.

4.3 Field Modulations and Gradients

The magnet coils used to apply the a.c. field for the orientation sensor were a set of four superconducting solenoids, two pairs, where each pair was wired in series as seen in figure 4.4. The current for these magnets was supplied by two voltage-to-current power amplifiers, with the input voltages coming from two lock-in amplifiers such that the pick-up voltages of the orientation sensor coils could easily be measured by the same lock-in amplifiers.

Determining the orientation of the rotator platform was always done with the main d.c. field set to zero (primarily because rotating the platform in a high field caused severe, undesirable heating), although the a.c. field could be applied in addition to the main magnet to create high d.c. fields with low-level modulation. A typical current of 1 A supplied to the modulation coils provided a field modulation amplitude of just 3.1 mT. To avoid induction heating of the sample platform a low frequency of 1 Hz was used for orientation sensing, placing the power amplifiers in d.c. mode and setting the lock-in amplifiers to be d.c. coupled.

By changing the phase of the current supplied to coils 1 & 3 from 0° to 180°, from in-phase to entirely out-of-phase relative to coils 2 & 4, the combined output could be changed from a uniform field modulation to an alternating field gradient, as illustrated by figure 4.4. Another advantage of using lock-in amplifiers as the input source for the voltage-to-current power amplifiers was their ability to produce an output signal phase and frequency locked to the reference signal but phase shifted by an arbitrary angle. This meant that the magnet system could be switched from modulation to gradient mode without manually changing any

physical connections.

In gradient mode the magnet coils at maximum output provide a field gradient of $0.855\,\mathrm{T\,m^{-1}}$ from 7.65 A. In practice the maximum current supplied to the magnet coils in gradient mode was around 1 A at 1.4 Hz, limited by system heating partly caused by the oscillating field but mainly by heat dissipation from the transverse field coils, which were necessarily powered by currents proportional to the current supplied to the gradient coils. In contrast to the superconducting modulation/gradient coils, the transverse field coils were created in-house from resistive copper wire, as detailed in section 4.3.1. Had they been created from superconducting wire it is possible that higher field gradients could have been applied.

The transverse coils, included in the diagram in figure 4.4, were necessary in order to correct the horizontal positioning of the sample with respect to the modulation field centre. A current of 170 mA in the transverse coils, the maximum possible due to the heat dissipation, provided a horizontal field of approximately 1.0 mT. As discussed in section 2.5, this is the same order of magnitude as the fields encountered by the sample should it be a centimeter from the modulation field centre with the gradient coils running at 1 A.

The field centre can be moved vertically by adjusting the ratio of the currents supplied to the gradient/modulation coil pairs. The usual procedure was to keep the current in coils 1 & 3 fixed while varying the current in coils 2 & 4. With coils 1 & 3 running at 1.2 A the modulation field was typically centred on the sample by running coils 2 & 4 at about 0.5 A, depending on the rotation of the sample platform. At these currents the required horizontal adjustment to the field centre was always within the limit of the 1.0 mT available from the transverse coils.

Estimating the magnitude of the field gradient from the provided calibration constant of $0.112\,\mathrm{T\,m^{-1}}$ per amp is made more complicated by running the magnet coils at different currents. A sensible calculation would be to simply take the average, 0.85 A, which gives $0.095\,\mathrm{T\,m^{-1}}$ as the gradient, though a more thorough discussion of the calibration of the magnetometer can be found in section 4.4.

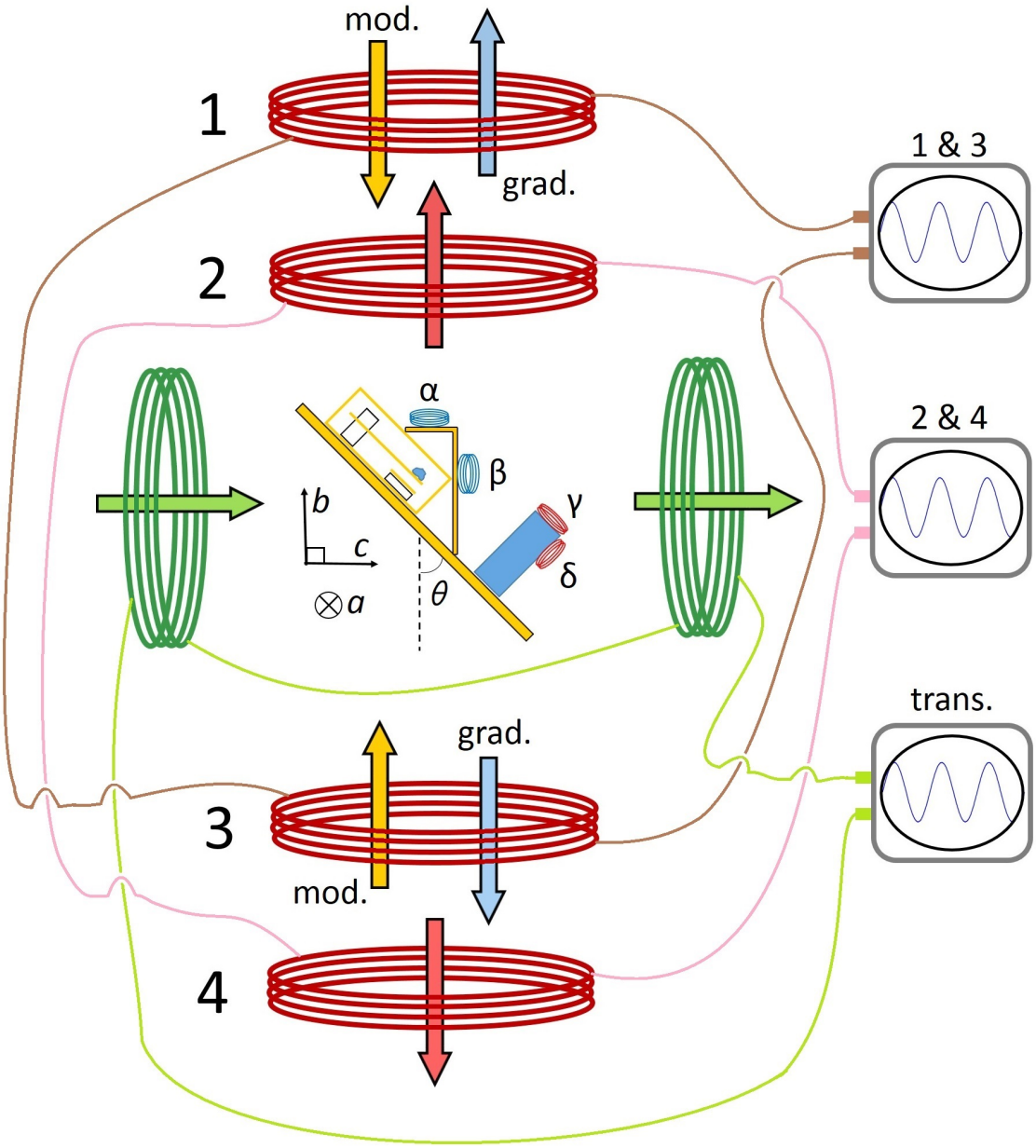

Figure 4.4 A diagram of the six magnet coils surrounding the sample space. Coils 1 & 3 are wired in series, as are coils 2 & 4. When current is supplied to both circuits in-phase the direction of the field generated by each coil is indicated by the arrows marked 'mod'. This is the 'modulation mode', providing a uniform field across the sample space. When the direction of current supplied to coils 1 & 3 is reversed, such that it becomes 180° out of phase with that supplied to coils 2 & 4, the field directions are those marked by 'grad'. This is the 'gradient mode', where the field in the centre is approximately zero but has opposite sign immediately above and below the sample space, creating a strong gradient. The two transverse coils are also wired in series and always provide horizontal field modulation. In this diagram the rotator platform is oriented such that the crystallographic b-axis of the sample is vertical and the c axis is horizontal, which occurs at $\theta \simeq 35°$. The pick-up coils labelled α and β are angled to probe the vertical and horizontal field modulation at this orientation, while the pick-up coils labelled γ and δ are angled to primarily probe the orientation of the rotator platform.

4.3.1 Transverse Field Coils

The field profile for the modulation coils working in field gradient mode was calculated using the known dimensions and vertical spacing of the four magnet coils and a short piece of code to numerically determine the various elliptic integrals (first, second and third kind) involved in the calculation of the field generated by an arbitrary solenoid. The result is shown in figure 2.10, demonstrating that radial fields of the order 1 mT may be encountered by the sample due to a horizontal displacement a few centimeters from the exact centre of field.

The same code was used to calculate the size and number of turns required in a pair of Helmholtz-like coils to provide, for a reasonable current, a horizontal field of about 1 mT in the sample space of the dilution refrigerator. For coils 6 cm in diameter and spaced 6 cm apart a total of $\sim$500 turns were required for a current $\sim$ 150mA. This seemed reasonably achievable, however there were a number of challenges involved in introducing such magnet coils to the system.

Firstly, the decision was made to use copper wire rather than superconducting wire, like niobium titanium, since the coils were required to work up to 17 T and it seemed unlikely that a 'homemade' magnet would remain superconducting at such high fields, especially if the coils were not immersed in the main helium bath. Superconducting wire is also difficult to work with and expensive, and generally thicker than the copper wire available. Copper is cheap and easy to manipulate; coils with many turns can be made quickly and relatively easily using thin and flexible, enamelled copper wire.

The main drawback with copper, however, is that it is resistive and therefore dissipates heat, with power $P = I^2R$ for current I and resistance R. Thus heat dissipation is minimised most effectively by reducing the required current, although this path of optimisation has limits. The magnetic field was fixed by the experiment requirements and the field produced by a solenoid is proportional to the product of the current and the number of turns.

Hence decreasing the current necessitates increasing the number of turns to generate the same field, which increases the resistance of the coil since the resistance is proportional to the length of wire. This extra resistance increases the heat dissipation, though obviously not as much as the decrease from reducing the current. Therefore this is clearly *not* the aforementioned limit on the optimum

design for the transverse field magnet.

The limiting factor was the space available for any additional magnet coils, which restricts the maximum number of turns, depending on the thickness of the wire. A sketch of the sample space and surroundings within the cryostat is shown in figure 4.5. The outer diameter of the inner vacuum can (IVC) surrounding the dilution refrigerator was very close to the inner diameter of the main magnet bore, leaving insufficient space between them to introduce additional magnet coils.

Another possibility considered was the space within the radiation shield, but the volume swept out by the rotator platform effectively fills almost all of the available space and it was deemed impractical to attempt to introduce the transverse field coils there. There was, however, a 4 mm gap between the IVC and the radiation shield, shown as an exaggeration in figure 4.5. More precisely there was a measured difference of 9 mm between the inner diameter of the IVC and the outer diameter of the radiation shield. Leaving a couple of millimeters clearance, since it was imperative that there was no contact between the IVC and the radiation shield, there was about 2 mm 'spare' either side of the radiation shield to insert a transverse field magnet.

The decision was made to thermally couple the transverse field coils to the IVC and not the radiation shield since the IVC has all the cooling power of the liquid helium bath whereas the radiation shield has only the limited cooling power provided by the dilution fridge. Thermally connecting the resistive copper coils to the radiation shield would have produced a heat load beyond what the fridge is capable of handling, preventing the mixture from condensing and warming up the entire experiment. This meant that the transverse field coils could not simply be fixed to the outside of the radiation shield.

Instead the coils were mounted onto a holder, only 2 mm thick, which was sprung to secure itself, by friction, to the inner surface of the IVC. The spring force was sufficient to both support the weight of the holder and to make a strong thermal connection to the IVC wall. The chosen design can be seen in figure 4.6, constructed in phosphor bronze. The bands around the top and bottom are the full 2 mm thickness and were the main contact areas between the holder and the IVC wall. The middle section was cut out to be only 1 mm thick and is where the coils were stuck, such that the coils are also pressed against the IVC wall for thermalisation.

Imposing a maximum solenoid height of only 1 mm, including layers of electrical

insulation and glue such that the actual copper coil was only about 0.5 mm high, the number of turns was thus restricted by the practicalities of coil winding, at least with the equipment readily available. The minimum diameter of enamelled wire that could be mechanically wound without it regularly snapping in the process was found to be 50 μm. Winding was done, by machine, by guiding the wire between two custom-made, hard plastic washers that fitted tightly to a 55 mm diameter former.

A weak solution of GE varnish was regularly dripped between the washers during winding to bind the coil together. After 200 turns the coil was allowed to dry and then, by careful application of ethanol to dissolve only the layer of varnish that glued the coil to the former, the washers were slid off and pulled apart. An example of the resulting coil is seen in figure 4.6, with a height of 0.5 mm as planned and a width of 2.5 mm. Two of these coils were then affixed to the holder as shown in the photograph, one opposite the other to create a Helmholtz-like pair – an actual Helmholtz coil has radius equal to the separation, rather than the diameter as in this case, but the curvature of the available space prevented such large coils.

The room temperature resistance of the two coils, a combined 400 turns, was 756 Ω. At 4 K the resistance dropped to about 10 Ω because of the large RRR of copper. For the 170 mA current required to produce 1 mT at the field centre the I^2R heating was safely dissipated into the IVC and the liquid helium bath. Roughly 200 mA was discovered to be a hard upper limit for the current, however, because of the large RRR. If the coils began to heat up even slightly then the resistance would increase, leading to greater heating, leading to greater resistance, and so on until the entire system began to warm up.

A final consideration was the self inductance of the coils, and also the magnetic torque placed on them by the main magnet running at 17 T. The latter was found to be negligible for the materials used (lots of glue essentially), while the former required more careful calculations. The self inductance of the transverse field coils, producing around 1 mT by way of 170 mA, was calculated as $\sim$0.01H. In order to keep everything in phase for the magnetometry measurements, to keep the transverse field alternating in phase with the field gradient, the reactance of the coils was required to be small compared to the resistance. Fortunately the frequencies involved were very low, to avoid eddy current heating. At 1.4 Hz the reactance was $\sim 0.1\Omega$ and so only 1% of the resistance, resulting in a phase rotation of less than 1°.

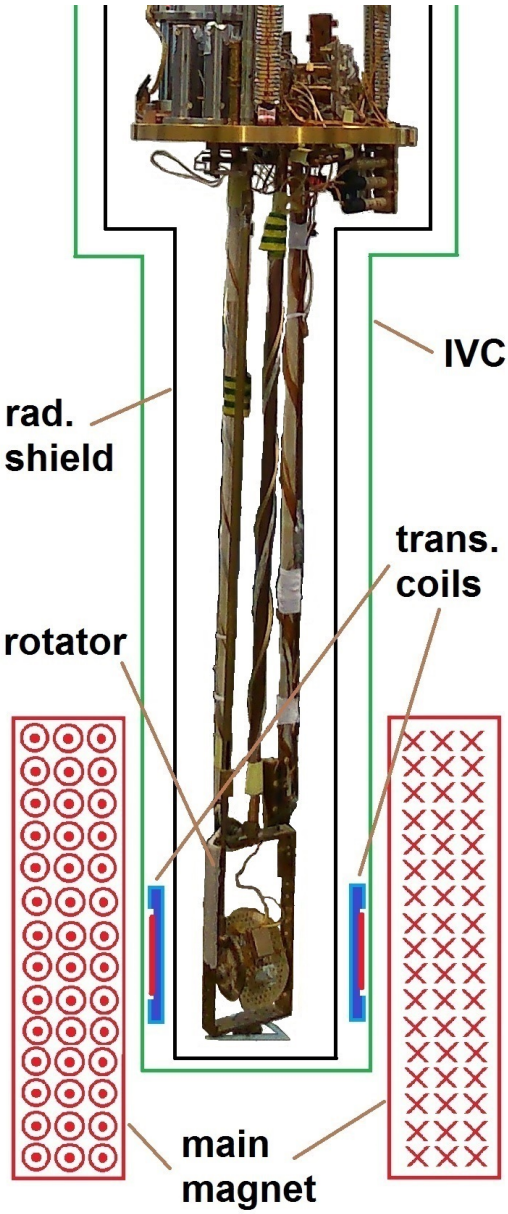

Figure 4.5 An illustration of the space surrounding the rotator platform, not-to-scale, with the separation between the inner vacuum can (IVC) and the radiation shield exaggerated. A photograph of the rotator has been inserted instead of a diagram, showing the connection to the dilution fridge mixing chamber at the top of the figure.

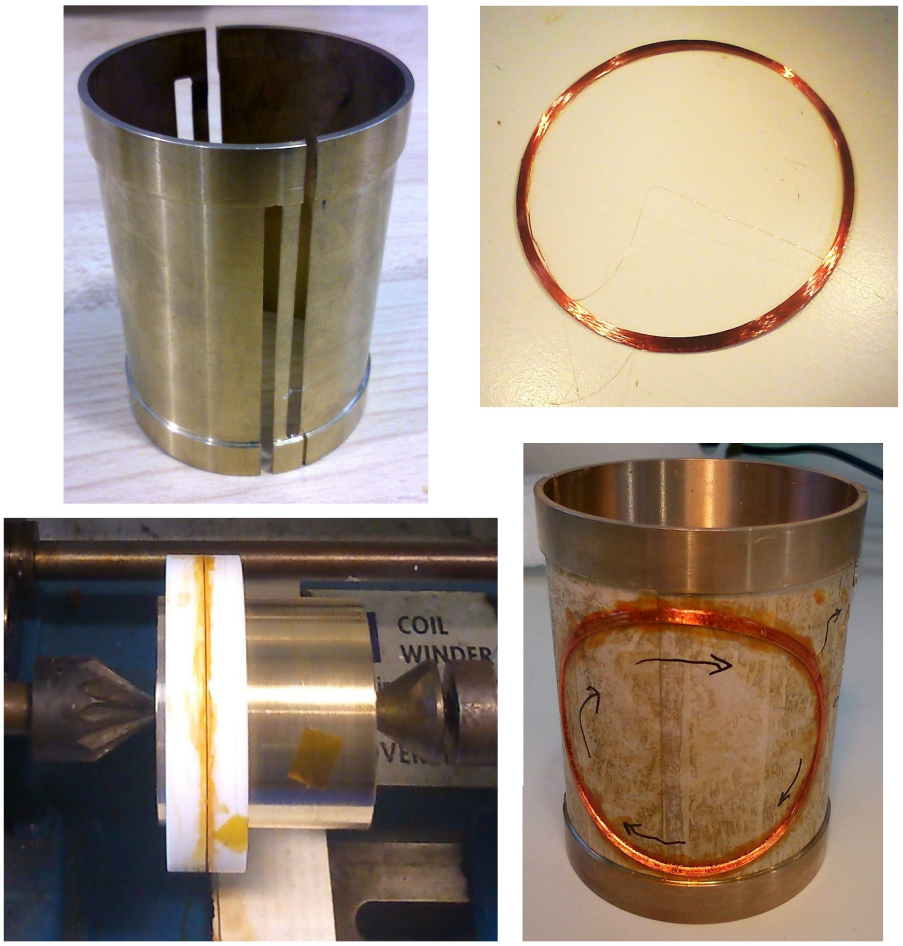

Figure 4.6 **Top Left:** The phosphor bronze coil holder, designed to be sprung against the inside wall of the dilution refrigerator IVC. The ends of the vertical slits close up as the holder is squeezed into the tail of the IVC. **Bottom Left:** The coil winding equipment used to make the transverse field coils. The white plastic washers are a tight fit to the metal former but are free to slide. The gap between them in this photograph is approximately 0.5 mm, the intended height of the coils. **Top Right:** The resulting coil, 200 turns of 50 μm diameter enamelled copper wire, weakly held together by diluted GE varnish. **Bottom Right:** The coils mounted onto the holder (a second coil is mounted on the other side). The holder has been covered by electrical insulation and the coils have been covered by a substantial layer of full-strength GE varnish. The two coils are wired in series, with the arrows indicating the relative direction of current flow, such that the generated magnetic fields are parallel rather than anti-parallel.

4.4 Magnetometer Calibration

Equations 2.65 and 2.66 relate the perpendicular and parallel components (respectively) of magnetization to the measured demodulation voltages from the lock-in amplifier. The purpose of this section is to determine the constant of proportionality necessary to calibrate that relationship.

The calibration constant can be estimated from the properties of the lever, as detailed in section 2.5, but a great many quantities are involved in the calculation and the estimate is only good to an order of magnitude. Finer calibration is accomplished by simple comparison to some well known fixed points, such as the spontaneous ferromagnetic moment in the easy axis direction at low field. An order-of-magnitude estimation from the physical properties of the lever, however, is a good check on the reliability of the measurement and the experimental set-up, and is therefore still a useful calculation.

Capacitance measurements using the passive bridge instrument were always performed with a voltage of 100 V, which resulted in a output voltage of 23.1 μV per fF difference from the null value, which was typically $C_0 \simeq 793$ fF. The formula given in equation 2.46 relates the torque to change in capacitance, which for this typical value of C_0 can be written: $\tau \simeq 1.45 \times 10^8 \ \Delta C$. In SI units the output from the GR bridge is 1 V $= 4.33 \times 10^{-11}$ F and so the torque measured per volt is $\tau \simeq 6.29 \times 10^{-3}$ N m.

The perpendicular component of magnetization is the simplest to use for calibration purposes, near $\phi \sim 2^\circ$ where the domain structure does not interfere with the measurement beyond a couple of tesla but the perpendicular magnetization is still approximately the same as the total magnetization. By 2 T the magnetization vector will have rotated slightly in the direction of the field, and so the measured perpendicular component will be slightly less than the expected total magnitude of $0.42\,\mu_B$ per formula unit (f.u.), but for an order-of-magnitude calculation it will suffice.

The sample mass was measured as 0.15 mg. Using the atomic masses of U, Rh and Ge to find the mass of a formula unit, 6.867×10^{-25} kg, the sample mass equates to roughly 2.2×10^{17} formula units. For a magnetization of $0.42\,\mu_B$/f.u. this gives a total magnetic moment of $m = 8.15 \times 10^{-7}$ Am^2.

At 2 T the measured first demodulation voltage at $\phi \simeq 1.8^\circ$ is (as seen in figure

6.22) $V_{\mathrm{demod1}} = 55.55\,\mu\mathrm{V}$, which converts to a torque of $\tau = 3.49 \times 10^{-7}\,\mathrm{N\,m}$. Simply dividing by the field gives the measured perpendicular moment as $m = 1.75 \times 10^{-7}\,\mathrm{A\,m^2}$.

Measurements reveal that rotation of the moment by 2 T has reduced the perpendicular component to about 90 % of the total ferromagnetic moment. Thus the figure calculated above can be boosted from 1.75 to roughly $1.95 \times 10^{-7}\,\mathrm{A\,m^2}$, which nevertheless fall far short of the expected value of $8.15 \times 10^{-7}\,\mathrm{A\,m^2}$.

There are several possible reasons for the factor of 4 between the expected and the calculated value. The obvious one is that the determined α factor from equation 2.46 is too low. The Young's modulus of the cantilever could easily be different from the standard value for beryllium copper, especially after the annealing process. The stiffness of the lever could also be affected by the presence of the sample and the transport measurement wires, though the majority of the bending occurs near the point where the cantilever is clamped, which was intentionally left completely bare for that reason. The thickness and length of the lever were well characterised, by a micrometer and observations through a microscope respectively, so there is also little room for error there.

Another possible source of error in the calculation of α is in the capacitor plate area A, to which α is directly proportional. As can be seen in figure 4.2, there is more metallic material than simply the two capacitor plates and there will be stray capacitance between the whole lever and the whole base plate and wiring (which could be incorporated as an effective increase in A). This additional capacitance will be very small, according to equation 2.42, because the distances involved are much grater than the few tens of microns between the main capacitor plates.

All of these inaccuracies could combined to produce a significant effect, however it seems unlikely that a mis-estimated α is solely responsible for the factor of 4 underestimation of the moment.

A significant source of error could be the mass of the sample, which is used to convert the known magnetization into the expected moment. It could be the expected value, rather than the calculated estimation, which is out by a factor of 4. The uncertainty in the mass measurement is $0.15 \pm 0.05\,\mathrm{mg}$ from the scale reading uncertainty of the laboratory balance, which is obviously quite large. The mass can be checked using the sample dimensions, as observed under the microscope, and the density of URhGe.

Calculating the volume of the unit cell from the lattice parameters stated in Ref. [40], and recalling the fact that there are 4 formula units per unit cell, gives the volume per f.u. as $5.585 \times 10^{-29}\,\mathrm{m}^3$. From the mass of a formula unit found earlier, this gives the density of URhGe as $12295\,\mathrm{kg\,m}^{-3}$.

The sample is seen to have dimensions of approximately $320 \times 240 \times 240\,\mu\mathrm{m}$, though being crudely spherical in shape an approximate diameter of $280\,\mu\mathrm{m}$ is perhaps more appropriate. The volume $V = \frac{4}{3}\pi r^3 = 1.15 \times 10^{-11}\,\mathrm{m}^3$ gives a mass of 0.14 mg, which is remarkably similar to the value from the balance and clearly *not* a factor of 4 too large.

In conclusion, the experimental evidence suggests that the lever does not appear to bend as much as it should. One possible explanation may be that that extra stiffness was introduced to the lever by the cutting procedure, adding increased thickness and strain along the edges. Since the stiffness scales as thickness cubed it only takes a slight, effective increase in this parameter to produce a substantial increase in the α prefactor.

Pragmatically, the resolution to these issues in accurately determining α is to instead define the calibration constant according to the spontaneous ferromagnetic moment, which is well known and highly accurate. The two agree to within an order of magnitude, which at least provides reassurance that the experimental method is working as expected and there are no major problems.

The estimated torque per volt from the calculated α prefactor is $\tau \simeq 6.29 \times 10^{-3}\,\mathrm{N\,m}$, but since this provides a magnetic moment apparently 4 times smaller than the known quantity the calibration used to analyse the final results of this project was a value of torque per volt: $\tau \simeq 25 \times 10^{-3}\,\mathrm{N\,m}$.

4.4.1 From Torque to Magnetization

Calculating the component of magnetization perpendicular to the main field is relatively easy. After converting the measured first demodulation voltage signal into torque using the calibration constant stated above, the net magnetic moment is found by simply dividing by the field, according to equation 2.65.

From the sample mass and the density of URhGe it was determined earlier that the sample was composed of roughly 2.2×10^{17} formula units. Dividing the determined magnetic moment by this value, and the Bohr magneton, provides

the magnetization in units of μ_B/f.u. as is typical.

Calculating the component of magnetization parallel to the main field is more complicated. First the second demodulation signal must be adjusted for the amplification added by the tandem demodulation process, as described in section 4.5. Then, according to equation 2.66, the signal is divided by $(L \sin\theta)(\partial B_z/\partial z)$ and the contribution from the m_{0x} component subtracted. Finally, multiplying by the calibration constant to convert the voltage into torque gives the net magnetic moment. The moment is then converted to magnetization in the same way as before.

The value of L is fixed by the magnetometer, at 5.2 mm. The platform rotation angle θ is given by $35° + \phi$ where ϕ is the angle measured from the position of alignment of the field and the b-axis of the sample, as detailed extensively in section 6.2. Rotation in the positive ϕ direction ensures that θ increases, rather than approachs zero, which severely reduces the sensitivity of the measurement, catastrophically so for ϕ approaching $-30°$.

The field gradient $(\partial B_z/\partial z)$ was estimated in section 4.3 as $0.095\,\mathrm{T\,m^{-1}}$, based on the average current provided to the field modulation coils. This varied slightly as θ varied, changing the sample position and changing the current in coils 2 & 4 required to precisely cancel the field modulation at the sample. These variations were small, however; the current supplied ranged from 0.45 to 0.51 A, having a relatively small effect on the average.

Ultimately, the gradient could be judged from the experimental results contrasted with the known total magnetization at high field, after the moment rotation transition, in much the same way as the capacitance to torque calibration was judged and adjusted earlier. From the experimental results, however, a gradient of $0.095\,\mathrm{T\,m^{-1}}$ appears to be fairly accurate.

4.5 Lock-In Amplifiers and Tandem Demodulation

In order to accurately and precisely measure very small voltage signals it is highly beneficial to use a.c. transformers and lock-in amplifiers. The lock-in amplifier has a built-in signal generator, which is commonly used to produce the excitation current for the measurement. In the case of torque magnetometry, the currents required for various field modulations and gradients are produced by voltage-to-current power amplifiers as discussed in section 4.3. For a simple resistivity measurement the voltage from the signal generator is dropped across a large resistor, typically $10\,\mathrm{k}\Omega$, to produce a small current, usually $\sim 100\,\mu A$ for the study of metals at dilution fridge temperatures.

The signal generator also produces a reference signal at the same frequency and phase as the output. The lock-in amplifier then compares the input voltage signal from the experiment to the reference. The input signal will contain noise across all frequencies in addition to the result of the measurement, a response purely at the frequency of the applied current. By multiplying the input signal by the reference, and using the orthogonality of sine waves and a high quality low-pass filter, the lock-in amplifier essentially acts as a very narrow band-pass filter, separating the measurement signal at the reference frequency from the noise at every other frequency.

Additionally, a second reference, shifted 90° out of phase with the original, is used for phase sensitive detection. Varying the phase of the reference relative to the measurement signal will produce variations in the amplitude of the resultant product, and a turning point will be found when the two are exactly in phase. In this way the lock-in amplifier 'phase locks' the reference to the measurement, which also aids in the rejection of noise. The second reference can then show the component of the measurement signal that is 90° out of phase with the input current.

The in-phase component of the measurement is labelled X and the 90° out of phase component labelled Y, where both quantities refer to the RMS amplitude of the detected signal. The ability of lock-in amplifiers to use two phase sensitive detectors in this way is particularly useful when making measurements with magnetic fields, as any inductive voltages are related to the rate of change of the current, or a modulated field, and so are indicated by the Y component. In this way any inductive noise in a resistivity measurement (from loops of current-

carrying wire mechanically oscillating within the magnetic field) can be separated from the measurement voltage too.

Pre-amplifier transformers also significantly increase the accuracy of voltage measurements where the currents and resistances involved are very small. For the URhGe resistance measurements transformers with gain $\times 300$ were used to boost the tiny voltage signals and make them easier for the lock-in amplifier to detect, especially important when trying to capture fine details like quantum oscillations. The transformers can however introduce additional noise to the measurement, something mostly avoided by use of a low-temperature transformer (LTT). Being at very low temperature, within the cryostat and thermally coupled to the liquid helium bath, significantly reduces any thermal noise (usually called Johnson noise) produced by the transformer coils.

A potential drawback of using pre-amplifier transformers is that, depending on the resistance of the remainder of the circuit (i.e. the sample), the a.c. frequency must be carefully selected in order to produce the expected gain and there can also be a phase rotation of the measurement, mixing the X and Y components (as determined by the lock-in amplifier) such that some small part of the Y signal is rotated into the X signal. This is most obvious in the superconducting state, where the in-phase voltage measuring the sample resistivity should be zero and the out-of-phase signal (the inductive noise, proportional to the magnetic field squared) is non-zero.

In this case a phase rotation can be applied to the lock-in amplifier measurement, separating the X and Y components into the correct in-phase and exactly 90° out of phase signals. The standard rotation matrix is defined as:

$$R = \begin{bmatrix} \cos(\varphi) & -\sin(\varphi) \\ \sin(\varphi) & \cos(\varphi) \end{bmatrix} \tag{4.1}$$

Thus the rotated X component is calculated as $X_{\text{rotated}} = X\cos(\varphi) - Y\sin(\varphi)$ for a phase rotation of φ radians.

For the URhGe resistivity measurements a phase rotation of 7° was applied. This value was found entirely empirically by simple observation of the data, seeking a rotation angle that resulted in the measurement of zero resistance in the superconducting regions as expected. As an example, the effects of a 7° phase rotation can be seen in figure 4.7 (for the resistance data shown in figure 6.2),

bringing the X signal to the expected, unvarying zero in the superconducting state between 9 and 13 T by rotating away the contribution from the negative Y signal.

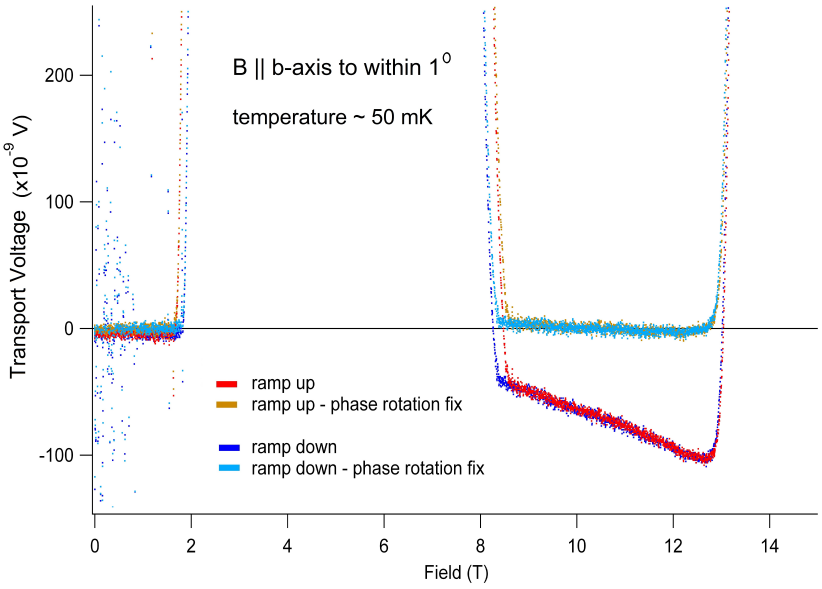

Figure 4.7 An example of the phase rotation applied to the lock-in amplifier measurements of the sample transport voltage. The phase angle was found empirically, by ensuring that the X component was constantly zero within the superconducting regions. The data before and after the phase rotation is shown, for both up and down field ramps.

The lock-in amplifier instruments used for the URhGe project actually contained two lock-in circuits (so four phase sensitive detectors) allowing them to perform tandem demodulation. In this way the instrument can analyse the input signal in two different ways. One common use was to measure the response of the sample at the fundamental frequency, the frequency of the applied current, and at $3\times$ the frequency, the so-called 3F signal. The 3F response is usually zero, and if the sample is entirely Ohmic (i.e. follows Ohm's law exactly such that voltage is always directly proportional to current) then the 3F signal is identically zero. One example of non-Ohmic behaviour, particularly relevant for this project, is superconductivity, where up to some critical value increasing the current does not result in any change in voltage.

If the critical current is not exceeded then the zero voltage response is simply recorded by the fundamental X signal, as seen in figure 4.7. If the a.c. amplitude does exceed the critical current, however, then for part of the sinusoidal excitation the voltage response will be zero, but for the peaks, above the critical value, the response will be Ohmic. This non-sinusoidal voltage response will

register as a non-zero 3F signal, and can be used to detect the departure from purely Ohmic behaviour in systems with superconductivity of very low critical current (since the excitation amplitude is only $\sim 100\,\mu$A). Examples may be surface superconductivity, domain wall superconductivity, grain boundary superconductivity, or essentially any superconducting system where the current resides within a very small volume such that the density is high.

The second main use of tandem demodulation in the URhGe project was to measure the amplitude-modulated voltage response from the capacitance bridge when the torque magnetometer was operating within an alternating field gradient. In this mode of operation, the 'first stage' lock-in amplifier measures the amplitude of the voltage signal from the capacitance bridge, at a frequency of 1 kHz, then passes that measurement to the 'second stage' lock-in amplifier, which measures the oscillations in capacitance due to the field gradient, at 1.4 Hz.

This procedure could also be achieved by use of two separate lock-in amplifier instruments, as could the measurement of the 3F signal (and in fact a second tandem demodulation instrument was used in this way to additionally measure the 2F and 5F signals), but the reason why tandem demodulation is preferred is best illustrated by use of an example from the experiment data.

A quick glance at figure 6.24 and then figure 6.25 may cause some confusion, since in the former there are clear oscillations of amplitude, at 620 mK and 10 T for example, of around $0.5\,\mu$V, but in the latter the second demodulation signal is given as about $35\,\mu$V. This is a result of the tandem demodulation circuit, where the output from the first stage demodulation is passed to the second stage internally, within a single instrument. An extra amplification is applied between the stages, which for this specific experimental setup was $\times 100$. It should be noted that lock-in amplifiers always work with RMS voltages and so although the peak-to-peak amplitude appears to be $0.5\,\mu$V the RMS value is closer to $0.35\,\mu$V, which after gain of a factor 100 gives the observed $35\,\mu$V second demodulation signal.

The typical resolution for the first demodulation signals measured (at $\phi > 1^\circ$ at least) was about $0.05\,\mu$V, which is a result of the lock-in amplifier sensitivity being set to $500\,\mu$V, the range required to comfortably measure the signal magnitudes observed in figure 6.22. A quick calculation using the second demodulation signal at $\phi \simeq 6^\circ$, for example, seen in figure 6.30, reveals that even at peak

magnitude (applying division by a factor of 100 as discussed above) the oscillation amplitude in the first demodulation signal will be below this sensitivity limit, at around $0.03\,\mu$V. Thus an inspection of the first demodulation signal at $\phi \simeq 6^\circ$ should reveal no clear evidence for any amplitude modulation at all, and closer observation of the data does indeed confirm that hypothesis.

This ability to measure signals below the output sensitivity of the first stage lock-in amplifier is the real strength of tandem demodulation in comparison to passing the signal from the first to second demodulation stage via data digitization and output to a second instrument, which as noted earlier is an alternative solution. In a setup involving two separate instruments it becomes very difficult to pass the output from the first to the second stage with enough sensitivity to measure the tiny amplitude modulations encountered in this project.

The signal can of course be amplified using a pre-amplifier transformer but then the relatively large magnitude of the carrier signal, the first demodulation signal, often overloads the input stage of the second instrument. Keeping the input signal to the second lock-in amplifier small enough to avoid any risk of overload usually resulted in a second demodulation signal that, while just about measurable by the instrument even when oscillations were not obvious in the digital data, was significantly more noisy than the result of the tandem demodulation.

4.6 Experiment Details

While the experiment was being set up and the dilution fridge loaded into the cryostat and cooled, and for field ramps used as initial testing, the capacitance was measured using the electronic Andeen-Hagerling (AH 2550A) 'ultra-precision' capacitance bridge instrument. This was much easier to use than the passive bridge and lock-in amplifier setup employed for the main measurements and gave an instant read-out of the capacitance. The bridge instrument used for the two-stage demodulation measurements was the General Radio (GR) 1616 capacitance bridge, which involved using mechanical levers on the front panel to balance the capacitance and nullify the bridge circuit.

The difference between the measured capacitance and the value set by the front panel levers was output as a proportional voltage. The usual measurement procedure was to set the temperature and orientation of the magnetometer in

the absence of field, manually balance the bridge circuit by adjusting the levers such that the output voltage was zero, and then begin a field ramp and measure the change in capacitance using a lock-in amplifier.

For the GR bridge, the capacitance registers as the X component of the lock-in amplifier, while the 'loss' is output as the Y component. The loss simply refers to any contribution to the total impedance that is 90° out-of-phase with the capacitance (such as any resistance in the circuit). The GR bridge measured the loss in units of conductance, i.e. siemens, and also determined by balancing the voltage to zero by adjusting front panel levers.

The separation of capacitance and loss into X and Y components was not always perfect and a small phase rotation was often required in order to correct the output. In the corrected state of operation moving one of the levers to create a large off-balance capacitance reading, and a large X component, would leave the Y component unaffected, and vice versa. The phase rotation angle was determined empirically and regularly checked, though the variation between experiments was small and the phase applied to the lock-in amplifier measurement was always around 12.5°.

The GR bridge was supplied a 1.0 kHz input voltage of 100 V for all measurements, provided by a Keithley 6221 current source, passing 10 mA through a 10 kΩ resistor in parallel. A trigger link cable from the Keithley 6221 was used to frequency and phase lock the reference signal of the first demodulation stage lock-in amplifier used to measure the capacitance.

The internal signal generator of the same lock-in amplifier instrument was used to generate the reference signal for the second demodulation stage. This reference signal was also passed to several other lock-in amplifiers, and those internal signal generators used as the inputs to the power amplifiers that provided current to the field modulation and alternating gradient magnet coils. In this way everything remained phase and frequency locked to each other.

The voltage-to-current power amplifiers employed in this project, the Labworks PA-138, provided 22 amps output per volt input, up to a maximum of 30 A. However, high-power-rated 10 Ω resistors in series with the superconducting modulation/gradient magnets limited this maximum to 4 A, since the amplifiers had a maximum 40 V output. This restriction ensured that the applied current was always well below the absolute maximum, which if accidentally applied was somewhat catastrophic (a main magnet quench at 15 T with a full helium reservoir

was sufficient motivation for this precaution).

In the case of the transverse field coils a 100:1 voltage divider was placed on the output of the signal generator, since currents much smaller than 1 A were required. The voltage divider reduced the maximum output from the lock-in amplifier from 5 V to 50 mV, which when converted into 1.1 A would definitely cause excessive heating of the sample platform and dilution fridge but would not cause any lasting damage.

The current for the resistivity measurement was also provided by the lock-in amplifier, as mention in section 4.5. The current is limited by the necessity to avoid resistive heating of the sample, which can be difficult to detect if the heating is local and does not register on the thermometer. Often a sub-optimal current is used because of this difficulty, however the presence of quantum oscillations in the resistance measurement of URhGe allowed precise current optimisation in this instance as the amplitude of the oscillations provides a sensitive measure of the sample temperature.

Measuring resistance over a number of field sweeps, the current was gradually increased such that initially the oscillation amplitude increased, as expected, until the sample began to warm and the trend halted and then reversed. The peak in quantum oscillation output occurred around 400 μA so a current of 350 μA, safely below the critical value, was chosen as the standard excitation for all subsequent measurements.

To ensure that the measured second demodulation signal from the capacitance bridge was entirely the result of Faraday magnetometry, and the modulated torque on the cantilever had no contributions from alternating fields, only field gradients, the currents in the three pairs of coils shown in figure 4.4 had to be precisely adjusted such that there was no field modulation at the position of the sample, i.e. the sample was in the exact centre of the field profile shown in figure 2.10. To probe the magnetic environment around the sample and to detect any field modulation several different pickup coils were used, and the currents in the field gradient coils tuned such that measurements of the pickup coils returned minimal voltages.

Initially the orientation sensors were co-opted for this purpose. In normal operation, supplying 1 A at 1 Hz to the magnet coils in field modulation mode, the pick-up coils registered roughly 60 μV on the lock-in amplifier when aligned to the modulation field. In order to calculate the orientation angle the maximum

voltages from each of the perpendicular pick-up coils was found by a test rotation, from approximately $\theta = 0°$ to 90°, and then any particular measurement, voltages V_1 and V_2, at an arbitrary rotation provided the orientation angle from $\tan(\theta) = (V_1/V_{1_{\max}})/(V_2/V_{2_{\max}})$.

The sample platform was rotated to the $\theta = 0°$ position, such that orientation sensor 1, measuring any horizontal field modulation, registered $\sim 0V$ while sensor 2, measuring the vertical field modulation, registered $V_{2_{\max}}$. The phase of modulation coils 1 & 3 was then shifted 180° to put the magnet into gradient mode and voltages V_1 and V_2 became small but not zero, as the would be in ideal circumstances. By adjusting the relative magnitudes of the currents supplied to coils 1 & 3 and 2 & 4, as discussed in section 4.3, the voltage pick-up from orientation sensor 2 could be tuned to zero, leaving only a small voltage on sensor 1 from the undesired radial a.c. field.

The horizontal, radial field was then tuned to zero by applying an in-phase field from the transverse magnet described in section 4.3.1, adjusting the current supplied to the transverse field coils until orientation sensor 1 also registered $\sim 0\,\mathrm{V}$. This method for finding the field centre was unfortunately not quite accurate enough, since the orientation sensors are in a slightly different position to the sample. Also, the main measurements were made with the rotator platform at around $\theta \sim 35°$ such that the orientation sensors were no longer aligned to the horizontal and vertical field directions, which made the tuning procedure somewhat more complicated and confusing.

To mitigate these issues a second pair of pick-up coils was added to the setup, mounted on a right-angled copper bracket and placed over the magnetometer box such that the pick-up coils surrounded the sample and were roughly aligned to the horizontal and vertical field directions, as illustrated in figure 4.4. After rotating to the $\theta \sim 35°$ position these additional pick-up coils were used to fine-tune the magnet currents to maneuver the sample into the exact field centre, or more precisely to shift the field centre to the position of the sample.

Since these additional pick-up coils were also not exactly at the position of the sample, and as stated in section 2.5.3 sub-millimeter precision is required, tuning both pick-up voltages simultaneously to zero would not actually ensure that the sample resides in the field centre. Careful consideration of the field profile in figure 2.10 and the diagram in figure 4.4 suggests that small fields of opposite sign should instead be picked-up by the coils. From this information the field

centre was shifted as close to the sample position as possible, though achieving this to sub-millimeter precision was challenging. The final results of the project show that it was unlikely that the sample was sufficiently centred within the field profile to obtain a pure Faraday magnetometry signal.

It should be noted that the same effect could have been achieved by mounting the magnetometer on a multiple-axis translational displacement stage, most likely a piezoelectric one, to physically move the sample to the natural field centre, without altering the field profile by difficult methods such as the introduction of additional transverse field magnets. Implementing such an idea would have had its own difficulties however. The magnetometer box was relatively large and the space on the rotator platform relatively limited, and a device capable of executing the necessary displacements would almost certainly be too bulky for the circumstances. Such a device would also be mechanically complex and therefore somewhat unreliable, a heavy disadvantage in a slow-turnaround dilution refrigerator system.

In summary, the usual measurement procedure was to rotated the magnetometer to the desired orientation, using an a.c. field and the orientation sensors, and then set the temperature. The modulation coils were then placed into gradient mode, with differing currents in the coils to roughly place the sample in the field centre. An in-phase transverse field was also applied and then the pick-up coils over the sample were used to adjust the currents in all three pairs of magnet coils to exactly center the alternating field on the sample. Finally the capacitance bridge was manually balanced by adjusting the front panel levers such that the output voltage was reduced to zero. The field was then ramped up to 17 T and back down to zero, slowing the ramp rate for the highest fields to keep the sample temperature constant, measuring the magnetic torque via the capacitance and the sample resistance simultaneously.

Chapter 5

UGe_2 Hall Resistivity Results and Discussion

Measurements for the UGe_2 project generated a large quantity of data, the result of covering a substantial region of temperature, pressure and magnetic field paramater space in fine detail and having the means and motive to plot both Hall resistivity and magnetoresistivity as a function of any combination of these parameters.

To familiarise the reader with this large dataset, the initial results of the project are introduced in this chapter within a narrative framework of determining critical points T_C, T_X and H_X, which allows various, selected results to be shown in a logical and structured way.

To this end, multiple methods for determining these critical points are demonstrated below, with an overview of the results presented in appendix A.

The sample resistance is a complex and somewhat indirect measure of magnetism and the measurements reveal broad, difficult-to-interpret features at both T_C and T_X. These critical temperatures can be identified more easily in measurements of magnetization, as a direct measure of the metamagnetic transitions, although high-pressure, high-field magnetization measurements are more difficult to accomplish and also unnecessarily time-consuming if performed in addition to extensive resistivity measurements.

Hence for this investigation T_C and T_X were determined by the resistivity and

then compared to previously published values from magnetization measurements in order to refine the method and check its accuracy. The data used for this purpose originates from Ref. [18], the essential figures from which, showing the determined critical points as a function of pressure, are presented in figure 5.1.

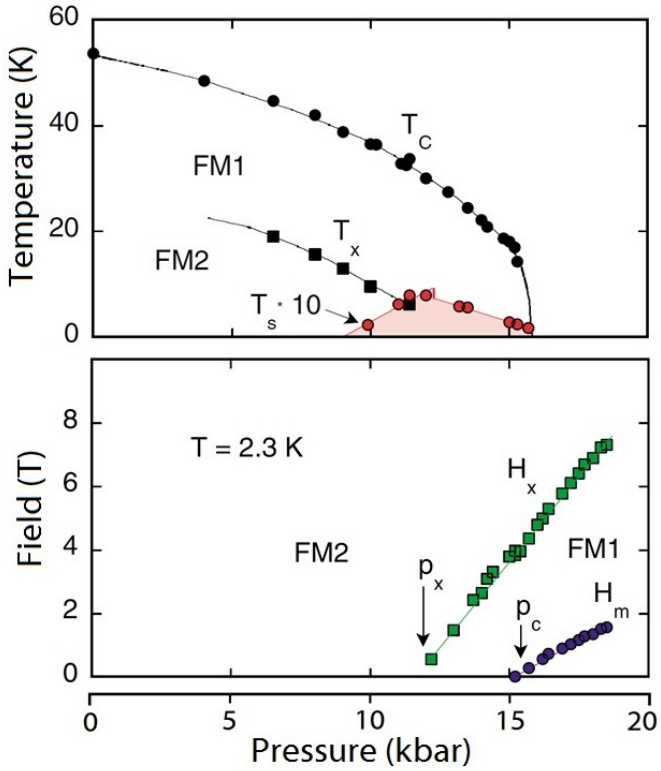

Figure 5.1 The positions of critical points T_C, T_X and H_X as determined by magnetization measurements in Ref. [18], which is also the source of the figure.

5.1 Determining Curie Temperature

5.1.1 Method 1

The resistivity as a function of temperature, in the absence of a magnetic field, for the H run, is shown in figure 5.2 as the derivative of the curve with respect to temperature. In contrast to the sharp kink seen at T_C in the ambient pressure data, at high pressure the changes in slope associated with the transitions at T_C and T_X are very subtle in the raw data and not easily visable by eye, but differentiating makes any structure in the resistivity vs temperature curves easy to see.

The low-temperature pressure associated with the H run is 12.0 kbar, just below P_X, making it particularly useful for demonstrating various aspects of the data analysis. From the magnetization data T_C is expected to be around 31 K at this pressure.

The feature in the differentiated resistance extends from about 30 to 38 K, encompassing several peaks, troughs and points of maximum slope to choose from as the position of T_C. Phenomenologically, the rate of change of the resistivity with temperature is related to the specific heat capacity, and a thermodynamic phase transition accompanied by a jump in the specific heat (i.e. a second-order transition, such as that from the paramagnetic to ferromagnetic state at the Curie temperature) is thus indicated by a change in the rate of change of the resistivity, or in other words a feature in the second derivative.

By this logic, the positions of T_C and T_X are indicated by the peaks highlighted in figure 5.2. The values are $T_C = 34.1$ K and $T_X = 7.6$ K.

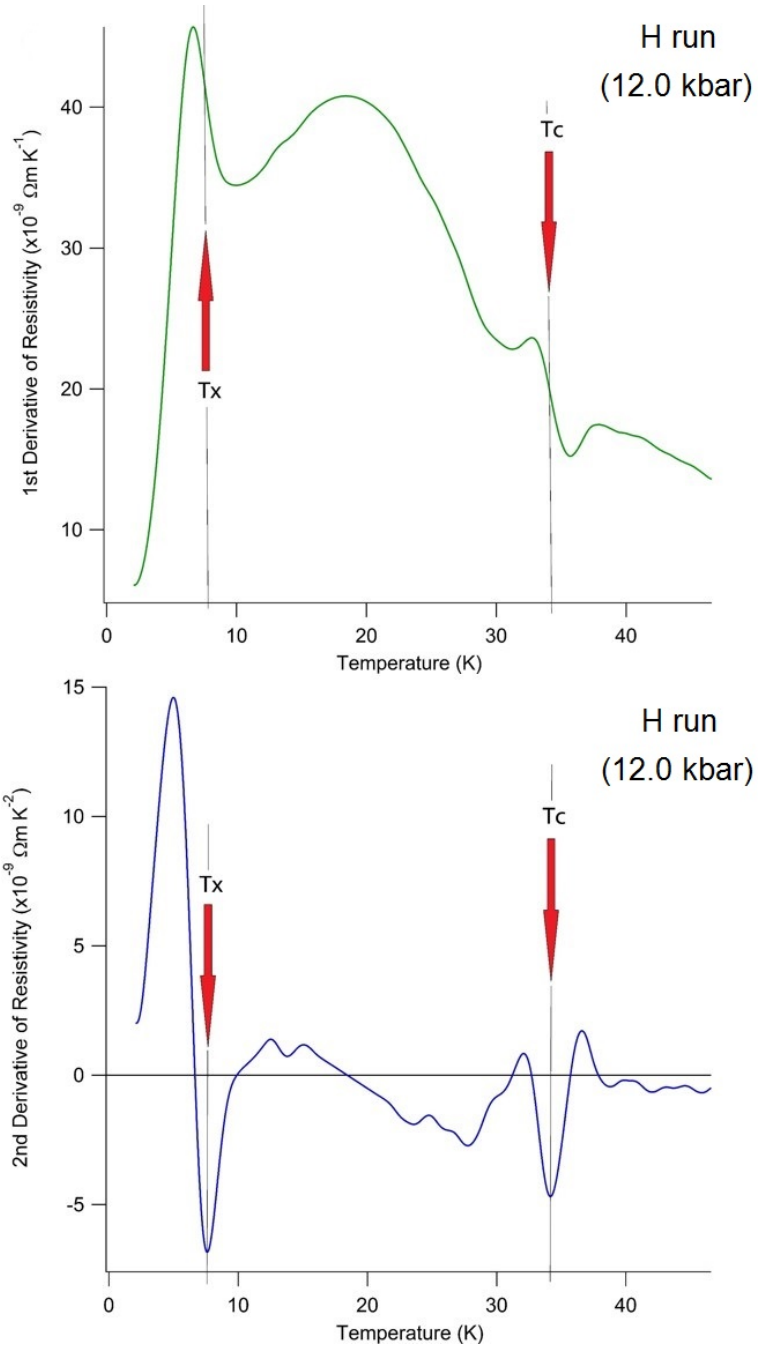

Figure 5.2 **Top:** The first derivative of the resistivity with respect to temperature, plotted over the low temperature range, showing the features associated with the Curie temperature, T_C, and the metamagnetic transition at T_X, for the experimental H run at 12.0 kbar, just below P_X. **Bottom:** The second derivative of the same dataset, indicating that T_C and T_X correspond to the positions of a negative troughs.

5.1.2 Method 2

The Hall resistivity is a good indication of the Curie temperature due to the influence of the anomalous Hall effect. At low temperature the anomalous Hall coefficient is small, since it scales with resistivity and for a high RRR metal the resistivity is small at low temperature. As temperature rises the anomalous Hall coefficient increases rapidly while, within the ferromagnetic state, the magnetization remains large.

Approaching the Curie temperature, however, the magnetization quickly falls toward zero and, despite the increase due to the increase in resistivity, the anomalous Hall effect rapidly decreases too. This is more easily seen in the Hall effect at low field, where the difference between ferromagnetism and paramagnetism is sharp and the Curie temperature is accompanied by a large change in magnetization.

The Hall resistivity as a function of temperature for a number of different applied fields is shown in figure 5.3. As field is increased the Curie temperature moves to higher temperature and therefore so does the position of peak anomalous Hall coefficient. The height of the peak also increases as field increases, since at higher temperatures the sample resistance is larger. Thus the point of rapid decrease in Hall resistivity (i.e. a trough in the first derivative) at the lowest applied field, 0.25 T, is a good measure of the Curie temperature, but a better one is to extrapolate to zero field and find the critical point from that. This can be done in two ways.

Firstly (method 2a), the positions of the troughs in the first derivative for various low fields (say the lowest 5 fields shown in figure 5.3) can be plotted and these values extrapolated to zero field, as in figure 5.4.

Alternatively (method 2b), an extrapolation as a function of field at each temperature data point can be done, to construct a Hall resistivity curve at the limit of zero field (which of course is not physically measurable), and then this curve differentiated to find the critical point, as shown in figure 5.5.

The values found by these methods are slightly different; by the first $T_C = 33.6$ K and by the second $T_C = 34.6$ K. The value of $T_C = 34.1$ K found earlier (from method 1) lies right in the middle of the two, and so gains a certain credibility for its robustness as an indicator of the Curie temperature.

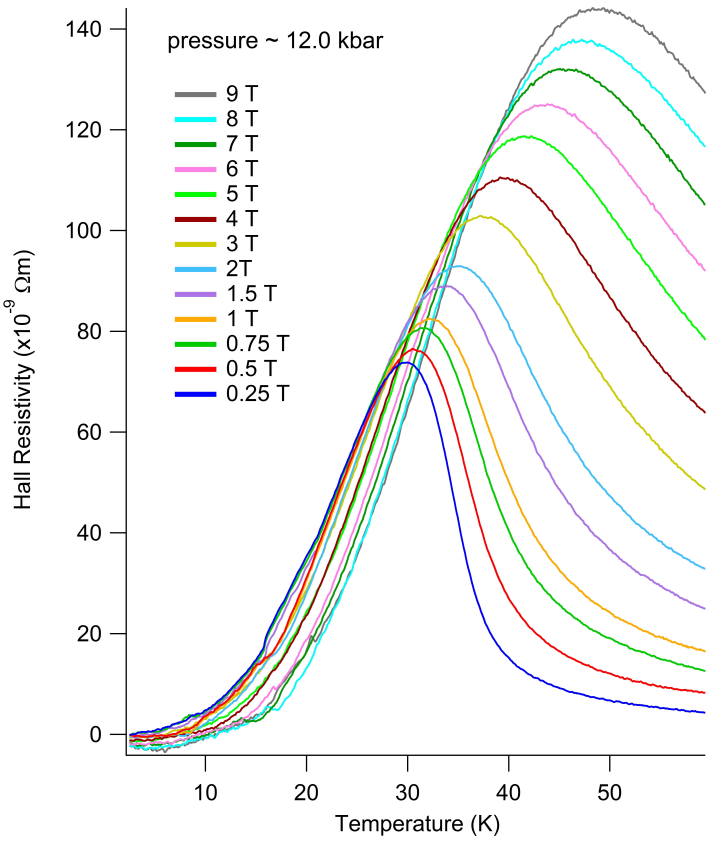

Figure 5.3 The Hall resistivity as a function of temperature for a number of different applied fields. The peak is a result of the anomalous Hall effect, proportional to both the longitudinal resistivity and the magnetization. The dramatic decrease in the Hall resistivity at the Curie temperature, ~ 34 K, at the lowest fields is due to the sudden drop in magnetization at the transition from ferromagnetism to paramagnetism.

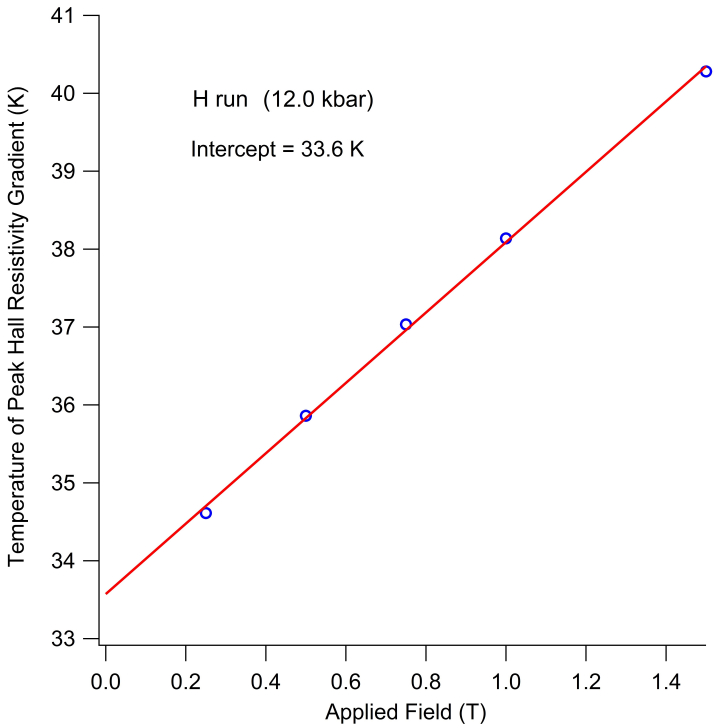

Figure 5.4 The temperature of the trough in the first derivative of the Hall resistivity with respect to temperature, indicative of the Curie temperature, as a function of field using the dataset shown in figure 5.3. A linear fit provides a y-axis intercept that is therefore related to the Curie temperature in the limit of zero field.

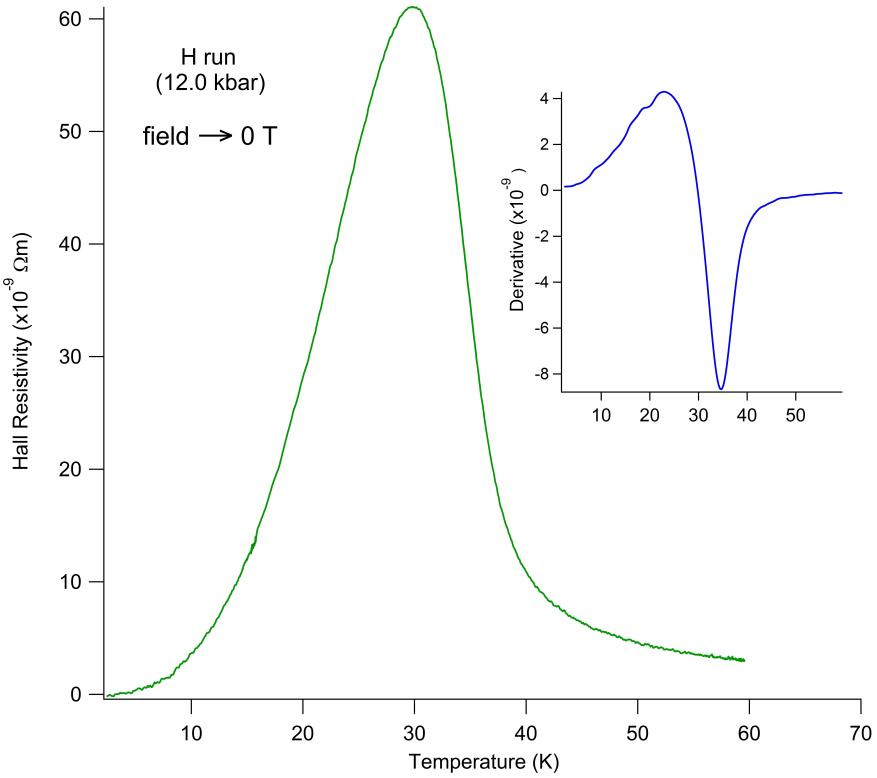

Figure 5.5 **Main:** The Hall resistivity as a function of temperature. Each data point is the result of an extrapolation to zero field of a number of measurements in field, using the data set shown in figure 5.3. **Inset:**The derivative of the curve in the main figure with respect to temperature. The position of the negative trough is related to the Curie temperature in the limit of zero field.

5.1.3 Method 3

As a further test of credibility, the position of T_C can also be found from the magnetoresistance, using differentiation in a similar way to method 1. Application of a small field appears to suppress some of the complexity of the feature in the resistivity data at the Curie temperature, as seen in figure 5.6, which shows the first derivative with respect to temperature of the magnetoresistance at a selection of fields.

Greater field strength reduces the difference between paramagnetism and ferromagnetism, and for high fields where the paramagnetic state is fully polarised there are little to no identifying features of the phase transition in the resistivity. At a low field such as 0.5 T however, the Curie temperature is still evident and identified by a simple maximum in the first derivative.

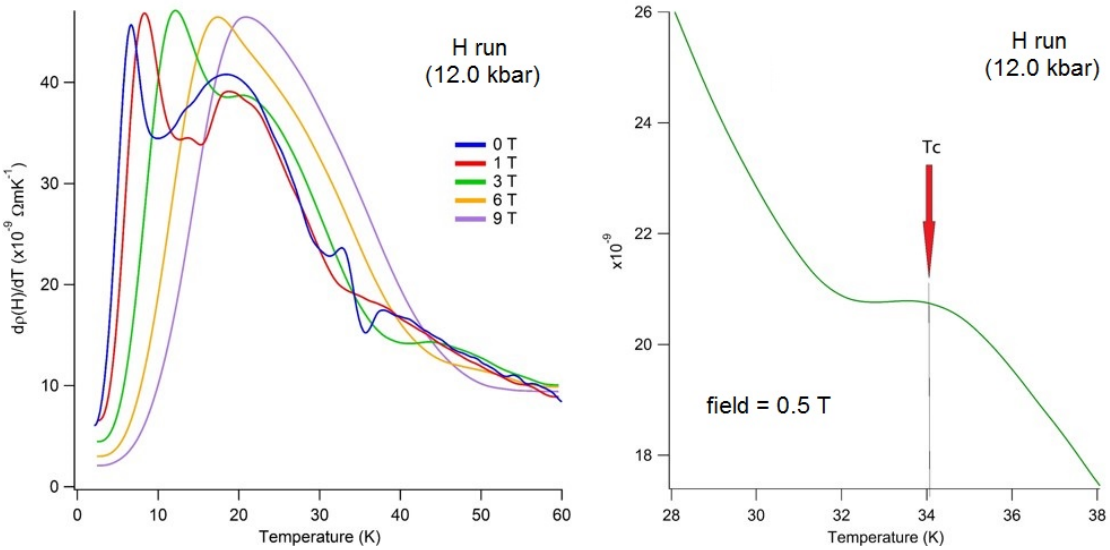

Figure 5.6 **Left:** The first derivative of the magnetoresistivity with respect to temperature, for a small selection of different applied fields, as a function of temperature. Application of field suppresses the feature related to the Curie temperature. **Right** A close-up of the 0.5 T data around the Curie temperature demonstrating how the complicated feature observed at zero field has simplified into a single hump.

For a more accurate position of T_C from this indicator, the magnetoresistance can be extrapolated to zero field in a manner similar to the treatment of the Hall resistivity in method 2. The main raw data for the H run can be seen in figure 5.7, showing the measured resistance before separation into Hall resistivity and magnetoresistance. Two data sets are presented, one for each direction of field, parallel or anti-parallel to the a-axis. At each temperature point the data can be

plotted as a function of field, for both positive and negative field directions, and a zero-field extrapolation value found for, slightly perversely, both 'positive zero' and 'negative zero'.

In practice, the data for the zero-field extrapolations looks almost indistinguishable from the curves at 0.25 T and averages to the dashed line in figure 5.7, which is almost identical to the directly measured curve. The difference between the direct measure and the extrapolated curve can only really be seen when the data is differentiated with respect to temperature.

Instead of the complicated feature at T_C observed in figure 5.2, the extrapolated data gives a simple peak similar (as expected) to the 0.5 T graph seen in figure 5.6. The value of T_C found in this instance is 34.2 K, very close to the value $T_C = 34.1$ K under scrutiny.

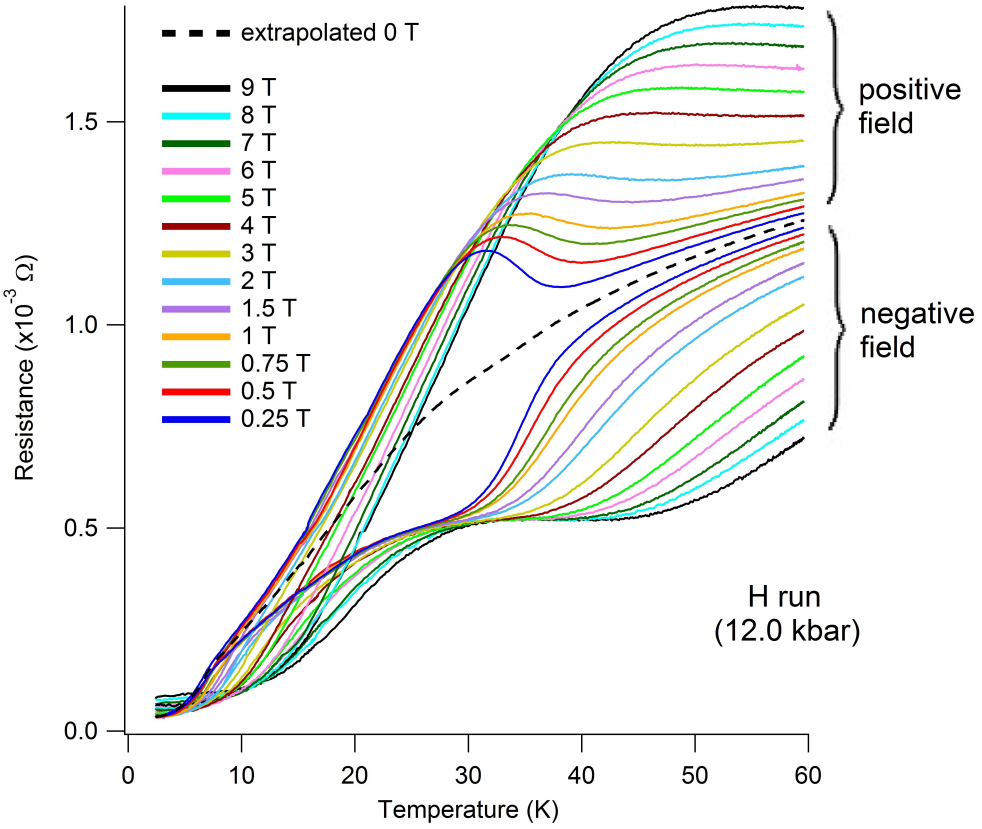

Figure 5.7 Raw experimental data for measurements at 12.0 kbar, before separation into Hall resistivity and magnetoresistivity, for a number of different field strengths applied in both directions, plotted as a function of temperature. The extrapolation to a zero-field curve is also shown, lying between the datasets for opposite field directions as expected.

In general, the value of Curie temperature ultimately attributed to each

experimental run was an average of these three methods. For the H run the Curie temperature was deemed to be 34.15 K. Occasionally, due to the nature of the data at a particular pressure, one or more of these methods could not be applied, which makes having multiple ways of determining the critical points especially useful.

5.2 Determining T_X and H_X

In figure 5.2 the critical temperature T_X was already identified by method 1 of determining the Curie temperature, a sharp trough in the second derivative of the zero-field cooldown resistance. This criterion can be verified in a similar manner to the extrapolation methods described previously, in this case by finding the temperature at which the critical field H_X extrapolates to zero. Therefore it is more constructive to first find a method for accurate determination of H_X and then return to the corresponding critical temperature.

5.2.1 Method A

For an examination of H_X it is beneficial to move from working with run H, just below P_X, to working with run M, far above P_X, where the critical field lies somewhere in the middle of the measurement range and its effects are easier to observe. The Hall resistivity and magnetoresistance, as a function of field, for a selection of low temperatures, for the M run, are shown in figure 5.8. At this pressure H_X appears to be around 4 to 4.5 T, where there is a change in slope in the Hall resistivity and a broad feature in the magnetoresistance characterised by a region of negative gradient.

These features are contrasted in figure 5.9, which shows the data at 3.5 K, near the base temperature of the cryostat. From this more detailed view of the data, the point of change of slope of the Hall resistivity looks to be closer to 4 T, which would coincide more closely with the peak in the magnetoresistivity rather than the point of maximum negative gradient.

In order to resolve this ambiguity and uncertainty a second method of determining H_X is required.

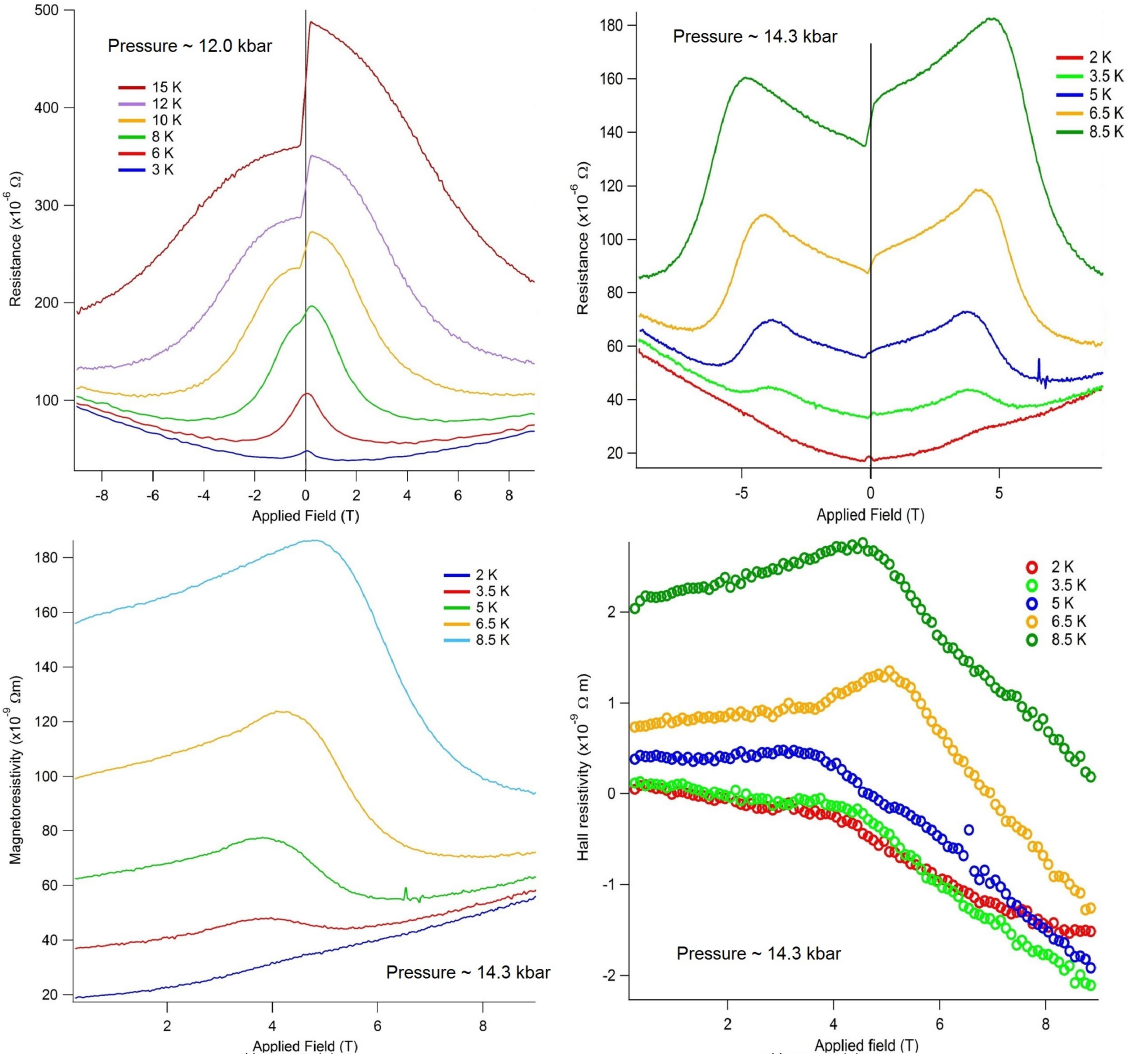

Figure 5.8 **Top Left:** The measured resistance as a function of field for a few low temperatures at 12.0 kbar, below P_X. **Top Right:** The resistance as a function of field for a few low temperatures at 14.3 kbar. The influence of crossing H_X is obvious in comparison to the 12.0 kbar data. **Bottom Left:** The magnetoresistivity (ρ_{xx}) as a function of field for a few low temperatures at 14.3 kbar. **Bottom Right:** The Hall resistivity (ρ_{xy}) as a function of field for a few low temperatures at 14.3 kbar.

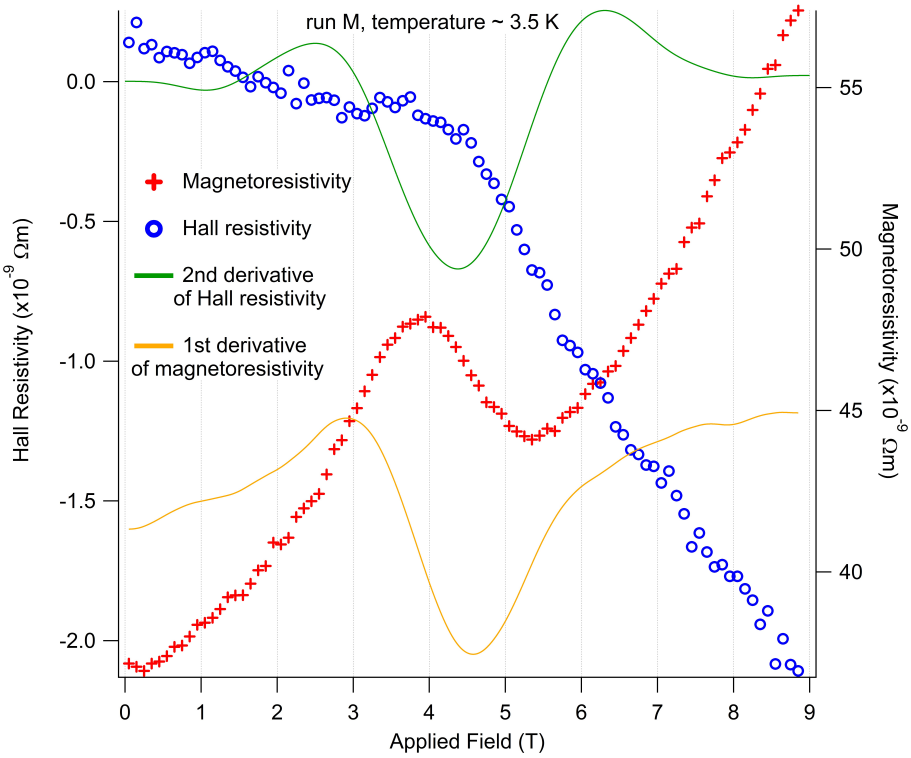

Figure 5.9 The magneto- and Hall resistivity as a function of applied field at 3.5 kbar at 14.3 kbar, along with first and second derivatives (with respect to field) respectively. The troughs in the derivatives may aid in determining the exact position of the critical field H_X, which appears to be around 4 to 4.5 T.

5.2.2 Method B

H_X can also be determined from the magnetoresistivity measured as a function of temperature, differentiated in order to highlight the structure in the data, a technique seen several times before but most relevantly in figure 5.6.

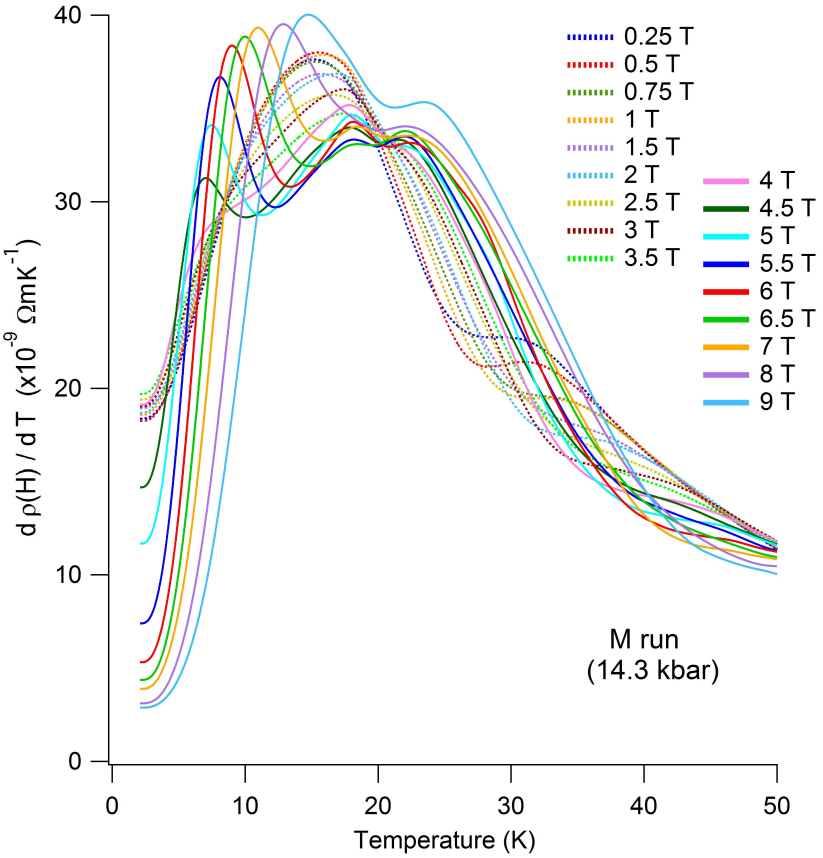

Figure 5.10 The derivative of the magnetoresistivity with respect to temperature, at 14.3 kbar, as a function of temperature for a range of field strengths. Above 4 T a low temperature peak can be seen, a feature associated with T_X, first emerging around 7 K before moving to higher temperature with higher fields. There is also a notable difference between the y-axis intercept of the plots above and below H_X. The data below H_X has been plotted with broken lines in order to make the graph clearer.

The data for run M is shown in figure 5.10. At low field there is the expected feature in the data at the Curie temperature (25.3 K at 0 T) but no other features are present at lower temperature. At 4 T a low temperature peak begins to emerges from the smooth background curve, at about 7 K, and shifts to higher temperatures as field increases further. This peak indicates the value of T_X at fields above H_X, whereby application of field at low temperature has driven the system through the crossover into the FM2 state and then raising the temperature

above T_X crosses back into the FM1 state.

Hence from the graph in figure 5.10 the value of H_X could be estimated as roughly 4 T, which agrees with the values found by method A, although it does suggest that the peak in magnetoresistance in figure 5.9, rather that the point of maximum (negative) slope, is a better indicator of the critical point.

However, some slight difference between the values of H_X determined from method A and method B might actually be expected, since the datasets involved explore fundamentally different cuts through the pressure-temperature-field phase diagram.

The difference essentially lies in whether the metamagnetic transition is crossed by measurements as a function of temperature or as a function of field. The critical end point (CEP) of the FM1-FM2 phase transition is around 7 K, above which the transition becomes a crossover (see figure 1.2). This CEP varies very little with field, remaining at roughly 7 K across the whole field range accessed in this project. Below 7 K the transition line is almost vertical, dropping to absolute zero within a fraction of a kilobar, as seen in figure 1.6.

Because of this steep curvature, measurements of T_X below the CEP are never observed in any experimental dataset constructed from temperature sweeps at discrete values of field and pressure, as is the case for the data presented in figure 5.10. In this graph the feature that emerges above 4 T is not an indicator of the first order transition but rather the crossover above the CEP.

This is in contrast to measurements of H_X at low temperature, below 7 K, when sweeping field at pressures above P_X. In this case a true phase transition line *is* encountered while traversing the temperature-pressure-field phase diagram. For example, the 3.5 K data shown in figure 5.9 are for measurements crossing the plane of first order transitions shaded gray in figure 1.6.

This behaviour can be summarised by the graph presented in figure 5.11, which shows plots of T_X as a function of field, as determined by 'method B'. Above P_X the 0 K values of H_X are estimates based on both 'method A' and the fact that a clear peak, corresponding to T_X in 'method B', is not seen at that field but then *is* seen at the next highest field value.

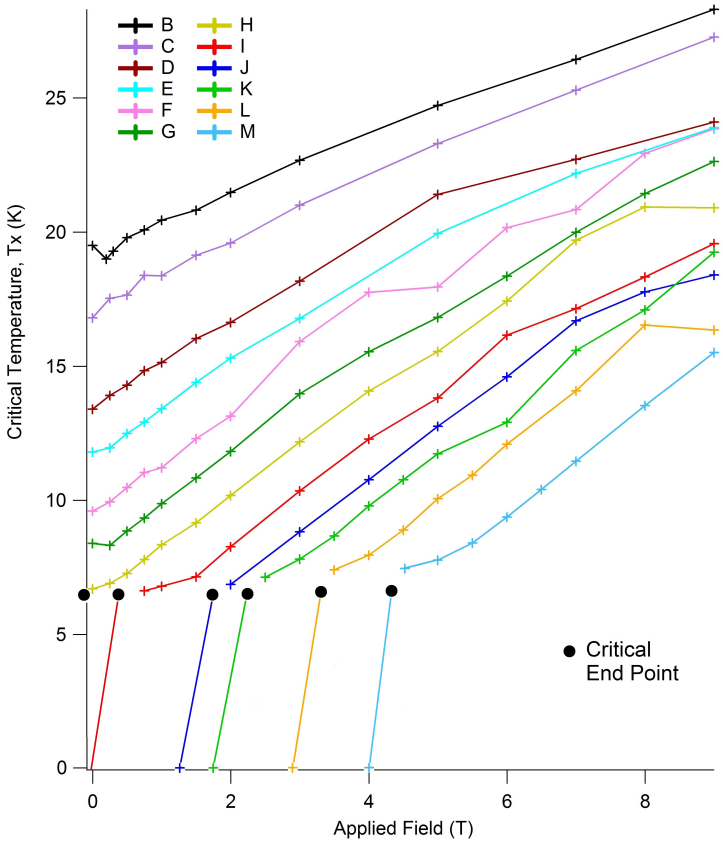

Figure 5.11 The critical temperature T_X plotted as a function of field for every experimental run. For high pressure runs J, K, L and M, above P_X, the field corresponding to 0 K is referred to as H_X. For the I run the extrapolated 0 K value of H_X may lie below 0 T, which is unphysical and would indicate that the pressure is below P_X. The positions of the critical end points drawn on this graph are crude estimates, based on drawing a straight line from H_X at 0 K to the first finite-temperature data point for each high pressure plot.

5.2.3 Method C

Having developed two methods for finding H_X, two extrapolation methods for finding T_X at pressures below P_X can then be employed in order to check method 1, exemplified by figure 5.2.

The H run once again provides a good example and the field-sweep dataset is shown in figure 5.12. At this pressure the metamagnetic transition is a crossover and the shape of the curves is slightly different to the high pressure data shown in figure 5.9, but a clear feature in the magnetoresistance can be identified (especially at low temperature) and extrapolated back to zero field, indicating a value of T_X between 6 and 8 K as expected.

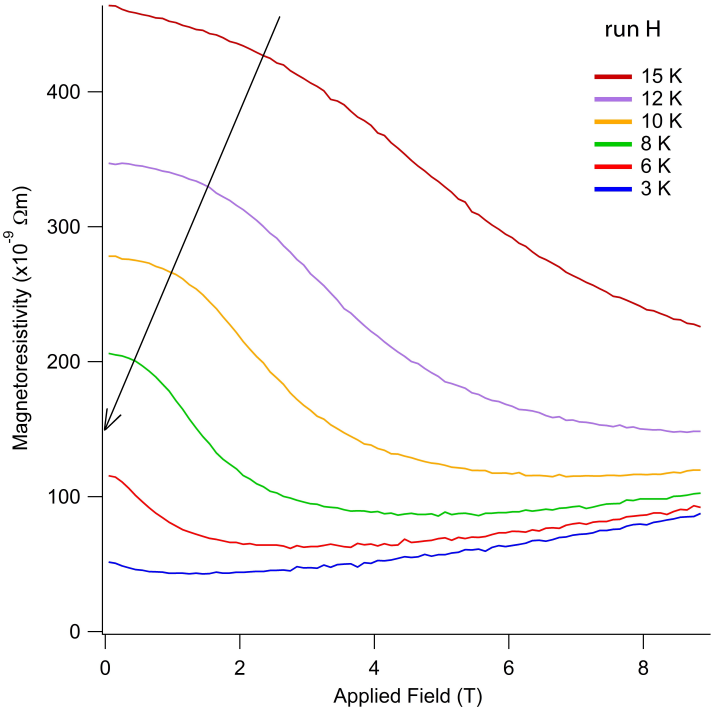

Figure 5.12 The resistivity as a function of field at 12.0 kbar for a few low temperatures. The line of the arrow roughly indicates the feature associated with H_X, which refers to a broad crossover at this pressure, and points toward a zero field extrapolation, an estimate of T_X, of between 6 and 8 K. A more accurate extrapolation, defining the position of H_X as the point of maximum curvature, using the second derivative, provides the result $T_X \sim 6.2$ K.

A more rigorous extrapolation (similar to the graph in figure 5.4, using the second derivative to find the exact position of the feature) gives the intercept as 6.2 K, which is actually significantly lower than the 7.6 K found from the zero-field resistance (method 1) but similar enough to confirm the credibility of that method

as desired.

The other extrapolation method for finding T_X involves using the method B definition of H_X, summarised by figure 5.11. These values of T_X, found by extrapolating to zero field at pressures below P_X, are consistently below the values found by method 1 but are comfortably within the range bounded by the values found from magnetization measurements.

It is the results of this second extrapolation method that are labelled as method C in the table presented in appendix A.

5.3 UGe_2 Phase Diagram

The phase diagram of UGe_2 is fairly complicated and the exact positions of the phase lines can vary between samples, depending on things like the material purity and quality of the single-crystal. As such a precise and sample-specific diagram is ideally required in order to be confident in accurately separating experimental data into sub-sets for the FM1 and FM2 phases.

The various methods employed for exact determination of the critical points T_C, T_X and H_X, and the corresponding values of pressure, scaled against a fixed P_X of 12.5 kbar, are outlined in sections 3.5, 5.1 and 5.2. The temperatures T_C and T_X are found from the average result of these different methods, at each pressure including in the average only the methods that were deemed to produce valid results, since not all of the methods were applicable to all the datasets.

For example, at the highest pressures (runs K, L and M) the feature at T_C in the zero-field resistance is significantly different from the more understandable form seen at lower pressure (see figure 5.13). This is likely due to crossing the tri-critical point (the TCP, as seen in figure 1.2) and the Curie temperature changing from a point of second-order phase transition to that of a first-order transition.

Thus for runs L and M the Hall effect was the only method used to determine T_C and for runs I, J and K the values derived from the Hall effect had greater dominance in the average than the values found from the zero-field resistance. Similarly, by observation of figure 5.13, at low pressures such as the B, C and D runs the zero-field resistance data does not provide a particularly robust way of determining T_X and the other methods discussed in section 5.2 are used in

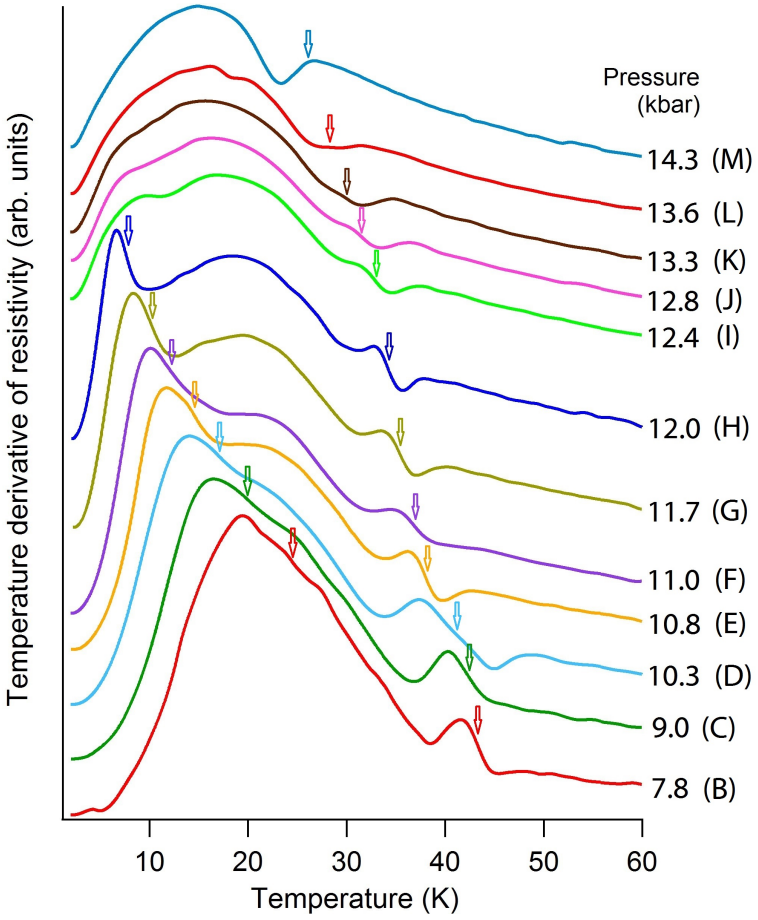

Figure 5.13 The gradient of the Hall resistivity with temperature, $\partial\rho_{xy}/\partial T$, for the 12 pressures measured between 7.8 and 14.3 kbar. The high temperature arrows, ranging from 25 to 42 K, indicate the position of the Curie temperature. The low temperature arrows indicate the position of T_X at pressures where it is observable. The letters used to label each experimental run are also shown, alongside the pressure at 30 K.

collaboration to arrive at the final value.

The determined critical points, plotted as a phase diagram, are shown in figure 5.14. The exact values, including the individual values from each method, are tabulated in appendix A. For comparison the values of T_X and H_X found from magnetization measurements are also shown, using the data published in Ref. [18]. As mentioned in section 3.5, the data from Ref. [18] is used in this project in lieu of sample-specific magnetization measurements to aid in both calibration of the Manganin manometer and in analysis of the Hall effect.

In figure 5.14 the plotted values of magnetization-derived T_X and H_X are those corresponding to particular values of T_C (those seen in figure 5.1), rather than the

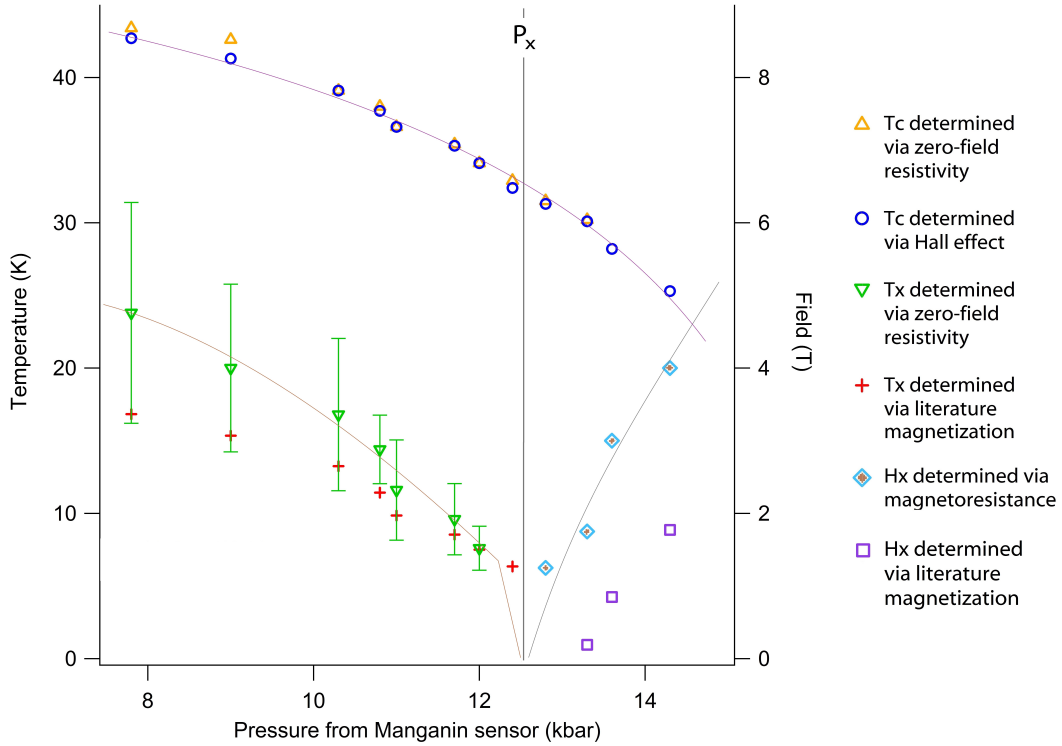

Figure 5.14 The experimentally determined pressure-temperature-field phase diagram for UGe_2. The differences between the determined values for T_X and H_X and the literature values are likely due to the literature value marking the begining of the transition and the value determined by the resistance indicating the midpoint of the transition. The error bars included here are not true errors (the uncertainties in the data points have been omitted from this graph); instead the 'error bars' provide an estimate of the width of the critical region of the crossover. The solid lines are rough guides for the eye.

value of pressure, the determination of which varies significantly between different experiments and was deemed less reliable for cross-experiment comparison than matching up the Curie temperature.

The error bars in figure 5.14 indicate a measure of uncertainty in the position of T_X, such that by a different method of determination (i.e. from the magnetization data) a different value within this range could also be attributed to the critical temperature. Here T_X merely indicates a point within a broad crossover that broadens further as pressure decreases from P_X. It is likely that the values determined via the resistivity indicate the midpoint of the crossover region, while those determined via the magnetization indicate the initial departure from the FM2 state.

The error bars in figure 5.14 show the width of the trough in the second derivative of the zero-field resistance, which is the main definition of T_X used in section 5.2.

For runs D to H this is the width at half-maximum of an easily identifiable trough. For the lowest two pressures, runs B and C, it is obvious from the data shown in figure 5.13 that the second derivative will not have a clear, single, negative peak at T_X. Rather T_X can be estimated in this case from smaller, more local features in the second derivative, which are not sufficiently deep to have a full-width at half-maximum. In this case, a half-width at half-maximum is determined and then doubled.

For the I run, at 12.4 kbar, resistivity methods appear not to provide a reliable value for T_X, as demonstrated by the absence of a low temperature peak in figure 5.13, although measurements of the Hall effect (see figures 5.27 or 5.33 for example) do indeed suggest that the I run lies immediately below P_X, as also suggested by the finite value of T_X from the literature magnetization data, as plotted on the phase diagram in figure 5.14.

It could be that T_X is very low at this pressure, just 0.1 kbar below P_X, perhaps lower than the 2 K base temperature of the cryostat, and therefore would not be evident in the I run plot in figure 5.13. As mentioned in the caption of figure 5.11, it may also be the case that although the I run is marginally above P_X, application of even the smallest field used for measurements (0.25 T for the main dataset) is enough to shift the system into the FM2 state. In this case, pragmatically, the I run would have to be considered just below P_X for the analysis of the Hall effect.

It should be noted that the value of T_C corresponding to P_X from the literature magnetization data is slightly lower than that at P_X as plotted on the phase diagram in figure 5.14, which means that the value of T_X for the I run given by the magnetization, around 6 K, is likely far too high. This also explains why the values of H_X from the literature magnetization data appear to be far too low in figure 5.14. Essentially, it is difficult to compare results across different samples and different experimental probes to such high precision.

The magnetization-derived values for H_X also appear to be significantly smaller than those derived from resistivity measurements, a difference again likely due to differences in how the critical point is defined (as either the start or the mid-point of the transition). For both T_X and H_X the resistivity-derived values were used in the following Hall effect analysis, incorporating a metamagnetic 'transition width' of around 2 T such that the data $\sim$1 T above and below the determined H_X was disregarded when fitting to find separate FM1 and FM2 values.

5.4 Separating the Ordinary and Anomalous Hall Effects

As mentioned at the very start of section 3.3, one of the complicating factors in measurement of the Hall effect in UGe_2 is ferromagnetism, the presence of which results in substantial sample magnetization and so a significant anomalous Hall effect, as discussed in section 2.3.1.

If the magnetization is known then equation 2.29 can be re-written as $\rho_{xy}/(\mu_0 H) = R_0 + R_a M/H$ and a plot of $\rho_{xy}/(\mu_0 H)$ against M/H will provide the normal Hall coefficient as the y-axis intercept of a straight line with gradient equal to the anomalous Hall coefficient. This is the approach taken by Ref. [35] for example, for ambient pressure investigations where the magnetization is quick and easy to measure. At high pressure, however, the magnetization is much more difficult to measure and a limited range of reliable data is available for UGe_2.

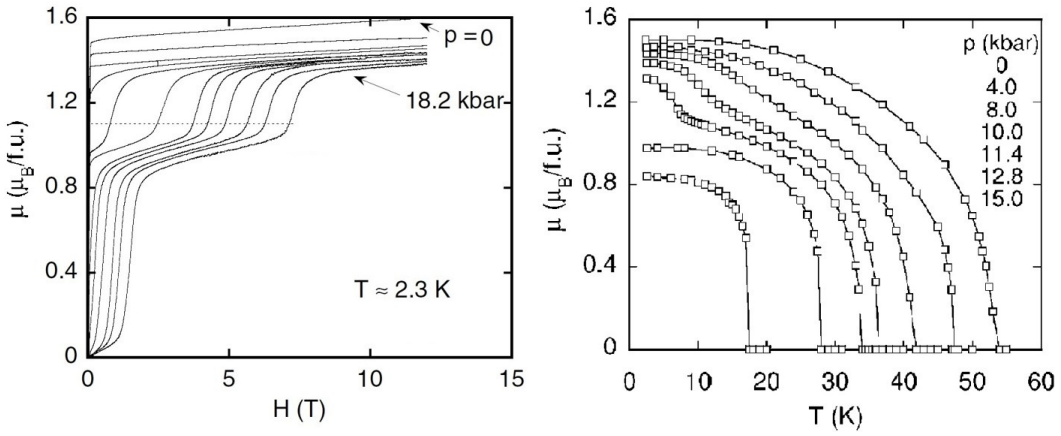

Figure 5.15 The magnetization data presented in Ref. [18], which is also the source of the figures. **Left:** Magnetization as a function of field for the following pressures: 0, 6.5, 9.0, 11.1, 12.8, 13.8, 15.3, 15.5, 16.0, 16.7, 17.3 and 18.2 kbar. **Right:** Magnetization as a function of temperature at several pressures ranging from 0 to 15 kbar.

The magnetization data from Ref. [18] covers the entire range in pressure relevant for this project, but covers the relevant range in field only at ~ 2.3 K (the base temperature of the helium-4 cryostat) and the whole temperature range only at $H \to 0$ T. Except for these two 2d cuts through the 3d pressure-temperature-field phase space there exists no readily available magnetization data for all combinations of temperature and field encountered in this project. Thus for a full dataset of $M(P, T, H)$ various approximations are made by reasonable

extrapolation and interpolation of the data from Ref. [18] presented in figure 5.15.

There are two important observations to make regarding these datasets. Firstly, the magnetization as a function of field is approximately linear within a particular phase (FM1 or FM2) and as such could potentially be approximated by the spontaneous magnetization at $H \to 0$ plus a linear increase with an estimated, pressure-dependent gradient. Secondly, the spontaneous magnetization as a function of temperature makes a series of complicated curves with increasing pressure and so a full 2d interpolation is required to find an estimation of this data at precisely the pressure values measured in this project.

In addition to complications arising from the lack of magnetization data, the complicated nature of the anomalous Hall coefficient results in an expansion of equation 2.29 to equation 2.31, making simple linear fits like that described above invalid. To properly fit to this formula the magnetoresistivity data will be required, as well as a model for finding approximate values for $M(T, P, H)$.

However, since there *does* exist a full dataset for the magnetization at 2.3 K it makes sense to first calculate the Hall coefficients at this base temperature before extending the method to higher temperatures using interpolated data from figure 5.15. Working at 2 K also means that the metamagnetic transition between FM1 and FM2 is sharp and a true phase transition, rather than a broad cross-over, and has well defined critical points in pressure and in field.

5.4.1 A Case Study at 2 K

At a particular temperature, using 2 K as an example, the following quantities can be introduced.

$$\begin{aligned}
\frac{\rho_{xy}(2K, P, H)}{\mu_0 H} &\longrightarrow \Gamma_{2K}(P, H) \\
\frac{\rho_{xx}(2K, P, H) M(2K, P, H)}{H} &\longrightarrow \alpha_{1_{2K}}(P, H) \\
\frac{\rho_{xx}^2(2K, P, H) M(2K, P, H)}{H} &\longrightarrow \alpha_{2_{2K}}(P, H)
\end{aligned} \tag{5.1}$$

This leads to the simplified expression below (equation 5.2), which can then be

fitted using measurement data to provide the values of Hall coefficients R_0, R_{a_1} and R_{a_2}.

$$\Gamma_{2K}(P,H) = R_0 + R_{a_1}\alpha_{1_{2K}}(P,H) + R_{a_2}\alpha_{2_{2K}}(P,H) \tag{5.2}$$

It is beneficial to proceed by focusing on the experimental D run, at 10.3 kbar, as an example, which is sufficiently below the critical pressure that at 2 K the effects of the metamagnetic transition are negligible: all the data is all safely within a single phase, that of FM2, across the whole field range. There is a small temperature range below T_X available for fitting too, which can also be considered to be comfortably within a single phase, FM2, and the data unaffected by the transition.

Figure 5.14 suggests that, although T_X is positioned at 16.8 K the region of influence of the cross-over extends down to about 12 K, encompassing the value of $T_X \simeq 13.2K$ from the published magnetization data. Thus to be fully certain of remaining comfortably within the FM2 phase, without any influence of the transition at T_X, only the data up to 12 K was used for fitting the FM2 phase at 10.3 kbar.

The Hall resistivity and magnetoresistivity for the experimental D run are shown in figure 5.16. The value of magnetic field plotted against here is the actual H field at the sample, including the effects of the demagnetizing field, as discussed in section 2.3, which is why the scale only extends to 8.7 T (reduced from the 9 T field supplied by the cryostat magnet).

Both plots show simple, roughly linear behaviour except for at very low field, below about 0.25 T, where there is an altered slope to the Hall resistivity and, more noticeably, a sharp drop in magnetoresistance. The latter is caused (at this pressure) mainly by the removal of domain walls and the suppression of ferromagnetic fluctuations, both of which are sources of additional scattering. The sharper gradient of the Hall resistivity around $H = 0$ is due to the rapidly changing magnetization, from zero to the saturation value, which influences the Hall resistivity by way of the AHE.

For the majority of the field range both the Hall resistivity and the magnetoresistivity are approximately linear. While the magnetoresistance is generally expected to increase steadily with field, the slope of the Hall resistivity, positive or negative, is entirely variable and contains potentially useful information. From equation 2.29 it can be seen that the gradient of the Hall resistivity plotted

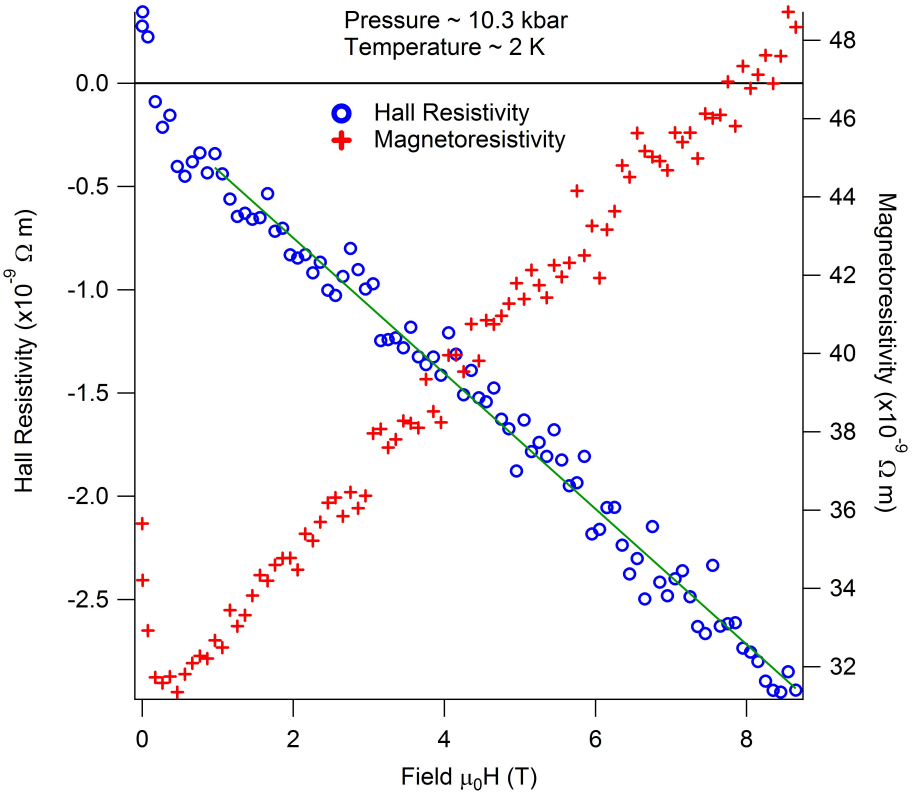

Figure 5.16 The magneto- and Hall resistivity as a function of field at 10.3 kbar and 2 K. Both appear approximately linear at high field, with a negative gradient to the Hall resistivity. The linear fit gives the gradient as $-328 \times 10^{-12}\,\mathrm{m^3 C^{-1}}$. The departure from linearity, in both plots, at very low field is primarily due to changes in the domain structure.

against field is roughly equal to the normal Hall coefficient, R_0, especially at low temperature when the resistivity ρ_{xx} is relatively tiny and so the influence of the AHE is small (this can be seen by the fact that the y-axis intercept is approximately the origin). Here, at 10.3 kbar, the gradient of the Hall resistivity is negative and, except for the low field behaviour mentioned above, is fairly constant across the field range; fitting a straight line between 1 and 9 T gives a constant R_0 of approximately $-328(10) \times 10^{-12}\,\mathrm{m^3 C^{-1}}$.

A constant R_0 would indicate that there are no major changes to the Fermi surface, as might be expected when remaining entirely within the FM2 phase. This is in contrast to the high pressure data shown in figure 5.9, for example, where there is an obvious change in slope at H_X when transitioning from FM1 to FM2. The magnitude of R_0 is related to the charge carrier density, with the sign related to the dominance of either electron or holes, although for a multi-band material such as UGe_2 the relationship is somewhat complicated and encapsulated

by equation 2.23.

The constant negative slope of the Hall resistivity observed in figure 5.16 would thus initially, naively, suggest an electron dominated charge carrier density. For a more accurate and reliable determination of R_0 the AHE must be taken into account, making use of equation 2.31 in full by fitting to equation 5.2.

The two variables α_1 and α_2 are plotted for the D run at 2 K (where they can be calculated exactly, from measurement data) as a function of field in figure 5.17. As before, the field here refers to the H field at the sample, taking into account the demagnetizing field, as will be the case for all field values referred to henceforth unless otherwise stated. Clearly both α_1 and α_2 are sensible and monotonic, and so neither term can be immediately discounted from equation 5.2.

Plotting $\Gamma_{2\mathrm{K}}(P, H)$ as a function of either of these provides roughly the same y-axis intercept; another value, like the gradient of the Hall resistivity plotted in figure 5.16, that is roughly equal to R_0. These intercepts are found by a crude linear extrapolation to $\alpha = 0$ to be around $-350(30)\times10^{-12}\,\mathrm{m^3C^{-1}}$, which agrees fairly well with the previous estimate of $-328(10)\times10^{-12}\,\mathrm{m^3C^{-1}}$.

5.4.2 Fitting the Data

For a proper fit to equation 5.2 approximate values for R_{a_1} and R_{a_2} must be found in advance, to accompany the rough estimate of R_0 already obtained. These rough values are then used as 'initial guesses' for the multi-variable, least-squares fitting procedure. Alternatively, it may be the case that either the α_1 or α_2 term dominates over the other in equation 5.2, allowing one of these terms to be ignored as negligible and thus reducing the formula to a simple linear equation. Depending on the mechanisms responsible for the AHE this may be fairly likely and a perfectly reasonable approach to the analysis.

In order to obtain these rough estimates a possible method lies in analysis of the Hall resistivity at a fixed field over a range of temperature (up to a maximum of 12 K, as discussed earlier). The key assumption here is that the magnetization at some specific field will remain relatively constant across this low temperature range when compared to the change in resistance (specifically the change in ρ_{xx}). At fixed field and pressure, and making the approximation of relatively constant

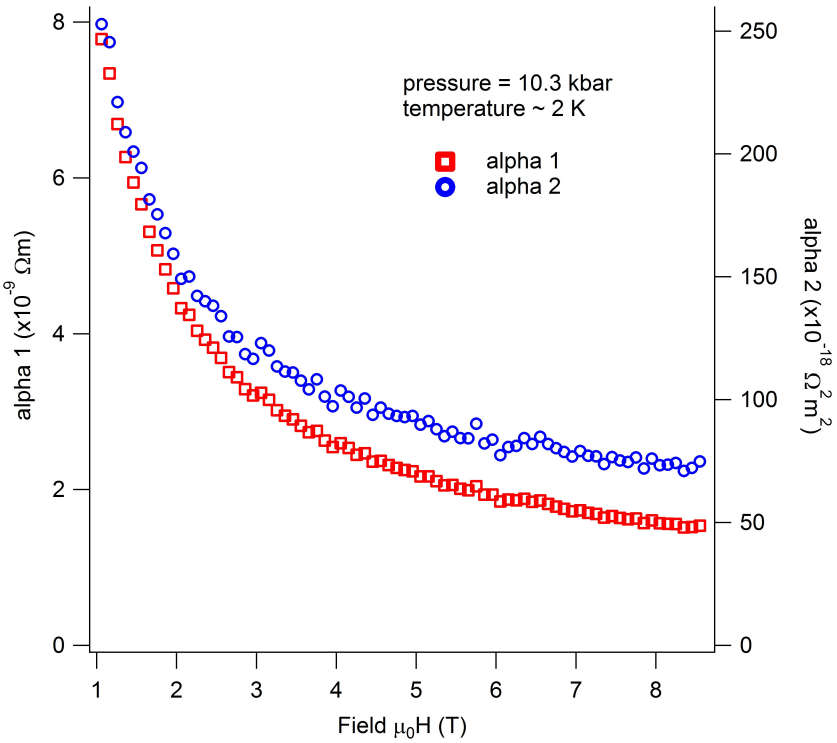

Figure 5.17 The variables α_1 and α_2 as a function of field at 10.3 kbar and 2 K. The field range begins at 1 T instead of zero partly because the data at very low field is not included in the fitting procedure for finding the Hall coefficients and partly because the exponential rise due to dividing by H as $H \to 0$ obscures the behaviour of the rest of the plot.

$M(H)$ across the low temperature range 2 to 12 K, the following expression (a special case of equation 2.31) can be defined.

$$\begin{aligned} \frac{\rho_{xy}(T)}{\mu_0 H} &= R_0 + R_{a_1}\frac{M(T)}{H}\rho_{xx}(T) + R_{a_2}\frac{M(T)}{H}\rho_{xx}^2(T) \\ &= R_0 + A\rho_{xx}(T) + B\rho_{xx}^2(T) \end{aligned} \tag{5.3}$$

where H is constant, and A and B are approximately constant prefactors.

Another assumption key to the validity of this expression is that, as well as the magnetization, the Hall coefficients R_0, R_{a_1} and R_{a_2} are all approximately constant across the temperature range. Comfortably within a single phase this is likely true for the anomalous Hall coefficients, and if R_0 was simply related to the inverse of the carrier density this would also be true for the ordinary Hall coefficient, however for a multi-band material this analysis breaks down somewhat.

Looking at equation 2.23 it is clear that if there is a temperature dependence to the conductivities σ_e and σ_h then R_0 will vary with temperature even when the carrier concentrations are constant. Later results, however, show that R_0 can indeed be considered as roughly constant with temperature within the FM2 phase. See for example the final results for R_0 presented in figure 5.30.

In summary, although this method admittedly relies on various shaky assumptions and thus the results cannot be considered as particularly reliable, the analysis should be robust enough to provide order-of-magnitude estimates of R_{a_1} and R_{a_2} to check the validity of the main method, fitting to equation 5.2.

When attempting to plot Γ as a function of resistivity ρ_{xx} at any particular fixed field, where the underlying control parameter is actually the temperature, defining the x-axis requires careful attention. The physical reality is that ρ_{xx} typically reaches a minimum finite value as $T \to 0$, the residual resistivity ρ_{xx_0}, and therefore never actually reaches zero.[1]

This is a obvious issue with plotting against an 'independent' variable that is not actually the control variable but is in fact *dependent* on the control variable, which is the parameter that truly approaches zero; the result can be large regions of the x-axis which are physically inaccessible, requiring long extrapolations or interpolations to bridge them, and the absolute value of the y-axis intercept is likely to be incorrect.

Thus fitting Γ as a function of resistivity is more accurately performed by plotting against $(\rho_{xx} - \rho_{xx_0})$ as the independent variable, where the zero point of the x-axis is thus the zero point of the actual control parameter, temperature. This is the approach taken for the graph presented in figure 5.18, which shows the 10.3 kbar data at roughly 3 T, fitted by a second-order polynomial between 2 and 12 K.

A reasonable conclusion to draw from this specific example would be that Γ is mostly linear in ρ_{xx}, and so perhaps the quadratic term in the AHE can be neglected. This would immediately suggest that skew-scattering is the dominant mechanism responsible for the anomalous Hall current in UGe_2. However, it should be remembered that this is the result of one plot, at one combination of pressure and applied field, and over one small temperature range. The more

[1] In reality, for UGe_2 the superconducting state would be entered below $T \sim 700$ mK and a zero resistance state reached then, very suddenly, but the behaviour of every variable involved would no longer fit formulae such as equations 2.31 or 5.2 which apply only to the normal metallic state.

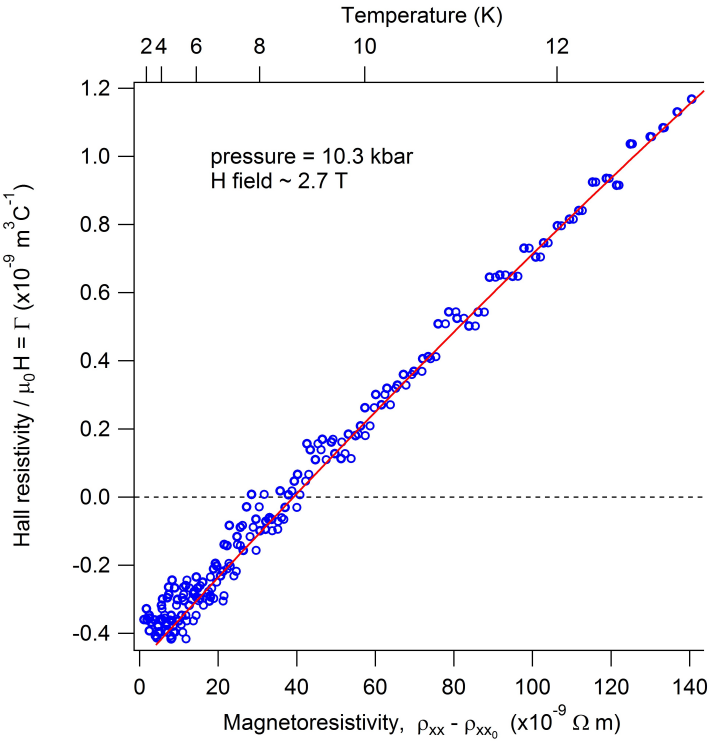

Figure 5.18 The Hall resistivity divided by field, the variable Γ, as a function of magnetoresistivity at 10.3 kbar and approximately 2.7 T. Although the data from 2 to 13 K is shown, only the range 3 to 12 K was fitted, though the line of best fit is plotted across the whole x-axis range.

cautious approach would be to include both α terms in 5.2 in subsequent data analysis, until there is stronger evidence, over a broader parameter space, that the α_2 term can be neglected.

The values of A and B found from the fit shown in figure 5.18 are 0.013 and -7000 respectively, in SI units, which converted to rough values for R_{a_1} and R_{a_2}, after division by $M/H \sim 0.1$, gives $0.13\mathrm{T}^{-1}$ and $-7\times10^4\,\Omega^{-1}\mathrm{m}^{-1}\mathrm{T}^{-1}$ respectively.

These values are then used as initial inputs for the final fit of Γ according to equation 5.2, which is shown in figure 5.19. The 'initial guess' for R_0 was taken from the estimates made earlier, using a rough value of $300\times10^{-12}\,\mathrm{m}^3\mathrm{C}^{-}1$. Note that here the least-squares fit is also weighted by the uncertainty on each data point, as indicated by the error bars.

The resulting values are $R_0 = -269(42)\times10^{-12}\,\mathrm{m}^3\mathrm{C}^{-}1$, $R_{a_1} = 0.033(42)\mathrm{T}^{-1}$, and $R_{a_2} = -1.66(1.47)\times10^6\,\Omega^{-1}\mathrm{m}^{-1}\mathrm{T}^{-1}$.

The first observation to make from these numbers is that R_{a_2} is much larger than the initial guess, while R_{a_1} is significantly smaller, and so the earlier idea of

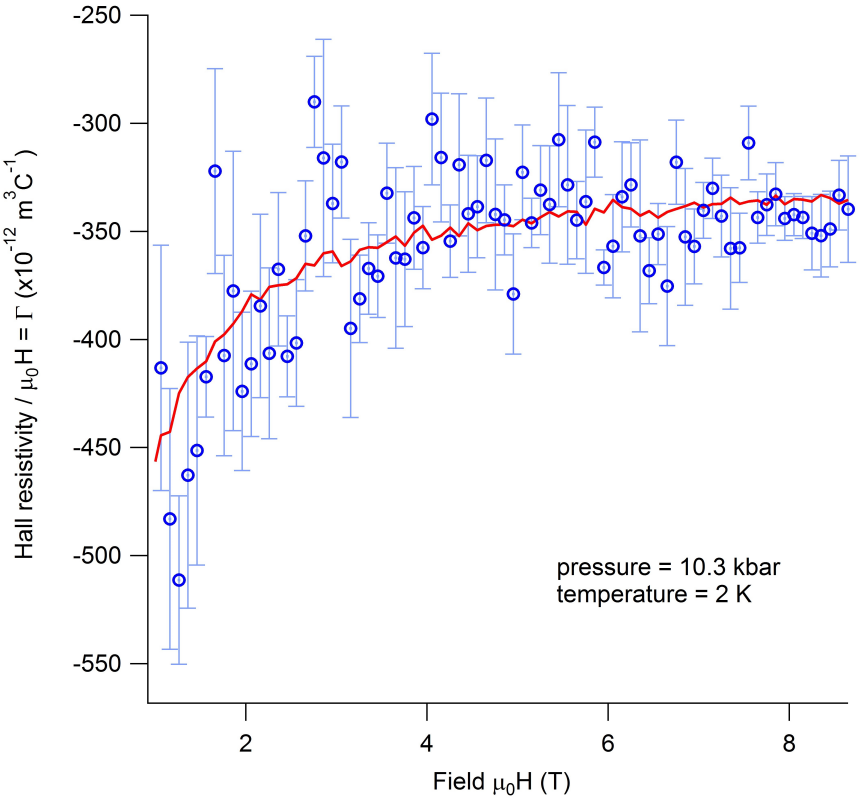

Figure 5.19 The Hall resistivity divided by field, the variable Γ, as a function of field at 10.3 kbar and 2 K. The line shows the fit to equation 5.2, which fits the data reasonably well, although it should be noted that the data scatter is quite large with generally large uncertainties.

neglecting the α_2 term from equation 5.2 based on the apparent linearity of the plot in figure 5.18 will probably have to be set aside.

The larger than ideal uncertainties in these values come from the large uncertainties in Γ due to the high noise level in the Hall resistivity, which can be seen from the scatter of data points in figure 5.16. At the lowest temperatures the measured voltage signal (of which the Hall voltage is only a fraction, the larger fraction being the TCV) typically becomes very small, while the noise is an absolute, and so the ratio of signal-to-noise is worst at 2 K. In addition to this, the variation of the signal with field is smallest at low temperatures and so the data scatter due to noise becomes comparable to any trends in the data, leading to uncertainties in R_{a_1} and R_{a_2} of the order 100%.

On a more positive note, the fitting procedure proves to be highly robust against changes in the 'initial guess' input values, finding the same fit parameters for input values spanning several orders of magnitude. Hence the results appear reassuringly reliable despite the high uncertainties at this temperature.

Interestingly, the uncertainty in R_0 is a comparatively low 15.6% and the value determined here differs from the simple approximation used earlier (the gradient of the Hall resistivity as a function of field) by about 20%, which makes the difference statistically significant.

It is difficult from the fit parameters alone to judge to what extent the ρ_{xx} term or the ρ_{xx}^2 term, if either, dominates the AHE and whether or not either of these terms can be neglected to simplify equation 5.2 as previously discussed. For comparison of their relative magnitudes, multiplying the final values of R_{a_1} and R_{a_2} by α_1 and α_2 respectively, the three terms comprising the full Hall effect are graphed in figure 5.20.

The α_2 term is about 4× the size of the α_1 term, which is actually the opposite of the earlier hypothesis that the α_2 term was potentially negligible. Thus for subsequent data analysis both terms of the AHE will have to be included in the fitting procedure. It may be the case that at other pressures and temperatures one term *does* dominate over the other, but this would have to be an observation made in hindsight, post-analysis.

5.4.3 Extensions to Higher Temperature

The method outlined in the previous section allows the Hall coefficients, both ordinary and anomalous, to be determined at any pressure at 2 K where the magnetization is known from experimental data. At higher pressures, above P_X, there is a phase change at H_X which must be incorporated into the method. In this case the two phases are treated separately and the data in a region 0.5 T above and below the determined critical field is disregarded, defining a 1 T critical region.

Consider the 2 K data presented in figure 5.8 for example, where H_X was determined to be 4 T. Here the FM1 dataset is taken from 0.25 T (once the magnetization has saturated) to 3.5 T, and the FM2 dataset is taken from 4.5 T to 9 T. The Hall coefficients are then found by the usual procedure of fitting Γ with α_1 and α_2 for each dataset individually to get values for each phase.

The procedure is much the same at higher temperatures, although there are two major differences. Firstly the magnetization must be approximated. Secondly the experimental dataset is drawn from measurements as a function of temperature at

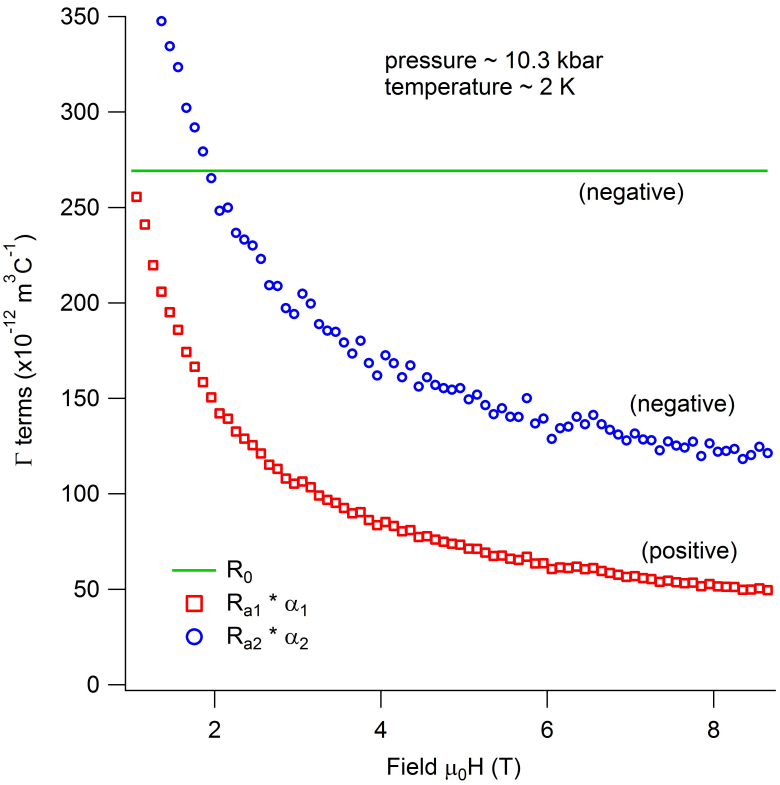

Figure 5.20 The three terms seen in equation 5.2 plotted as a function of field, at 10.3 kbar and 2 K, in order to compare magnitudes. The ordinary Hall coefficient is a constant. The second anomalous Hall coefficient is larger than the first across the whole field range, though both are similar in magnitude and neither dominates over the other. None of the three terms are negligible.

a fixed field rather than measurements as a function of field at a fixed temperature. Measuring over temperature sweeps allows the Hall coefficients to be determined with a much higher data density as a function of temperature than measuring at discrete values of temperature, although the accuracy of the fitting procedure at each temperature data point is of course sacrificed. Fitting is performed using the same method as described above, however the Hall resistivity as a function of field must be constructed by taking the data at the same temperature for each sweep at a different fixed field.

Below P_X a typical choice of field values were those seen in figure 5.7. The smaller spacing of these values below 2 T was chosen because there is usually more variation in the Hall effect and magnetoresistance data at low field than at higher fields. Above P_X a few extra points were added in the middle of the range to cover the region around H_X in more detail, as can be seen in figure 5.21. Data points for each temperature value were found by binning the data for each sweep, usually into a temperature interval of 0.1 K. An example of

the resulting constructed dataset, in comparison with some direct-measure field sweeps, is presented in figure 5.21.

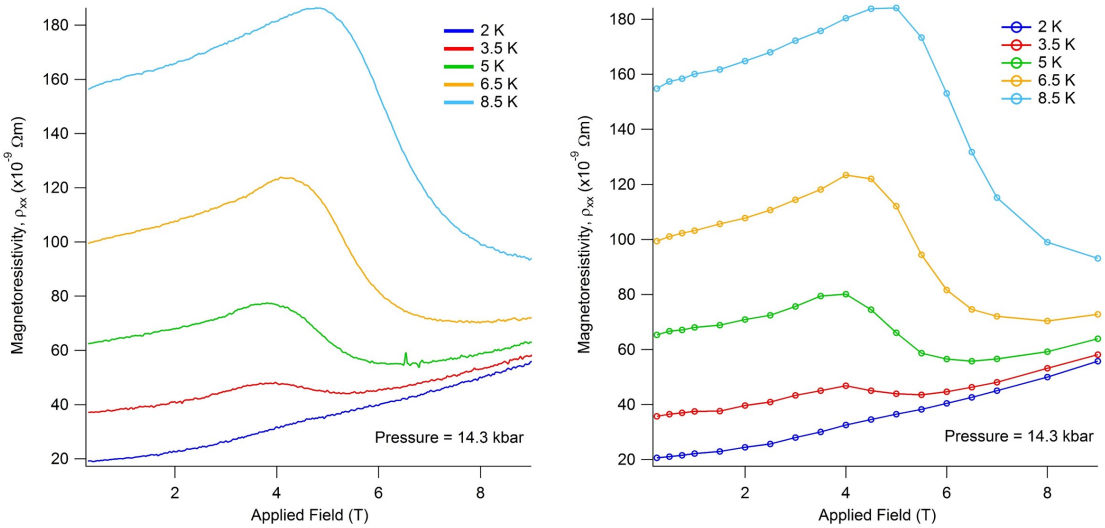

Figure 5.21 **Left:** The magnetoresistivity as a function of field for several low temperatures at 14.3 kbar, directly measured by experimentally sweeping the field. **Right:** The same data set but constructed from temperature sweep measurements at various fixed field strengths, as indicated by the symbols.

In order to approximate the magnetization the roughly linear nature of the susceptibility within a single phase, as observed in figure 5.15, was used in conjunction with the known variation of the spontaneous moment with temperature, also seen in figure 5.15. Explicitly, the following approximation was made:

$$M(H) = M(H \to 0) + \frac{\Delta M}{\Delta H} H = M_0 + \chi_L H \tag{5.4}$$

where the linear susceptibility χ_L is taken as roughly 0.002 for the FM2 state and roughly 0.01 for the FM1 state.

This may seem rather crude but it is worth bearing in mind that the important variables are α_1 and α_2, the behaviour of which is governed much more strongly by the substantial variation of the resistivity ρ_{xx} over the field range than by the magnetization, which (within a single phase) varies very little, relative to the saturation value, as a function of field.

Various different approximations, ranging in sophistication, were trialled during the data analysis for this project but the differences made little difference to the the calculated variables α_1 and α_2 and so negligible difference to the results of the fitting procedure. As a function of temperature it is the variation in $M(H \to 0)$

that is much more important to capture than the slight variation in χ_L.

Thus the simple approximation of a linear susceptibility, using an order-of-magnitude estimation of $\chi_L \sim 0.002$ or $\chi_L \sim 0.01$, was used for the entirety of the analysis. This approximation obviously worsens further away from 2 K, especially approaching the Curie temperature where the susceptibility rapidly increases and will be much larger than the rough 2 K values previously stated, although at higher temperatures α becomes increasingly dominated by the magnetoresistivity and the magnetization has even less of an impact on its behaviour as a function of field.

Put another way, at higher temperatures the Hall resistivity becomes dominated by the AHE and governed by the resistivity rather than the magnetic field or changes in magnetization (in contrast to the at very low temperatures where the Hall resistivity increases in direct proportion to the field and the behavior of the magnetoresistance is largely irrelevant).

Thankfully, since this project focuses on P_X rather than P_C, even for the highest pressures investigated the Curie temperature remains relatively high, at 25 K for the 14.3 kbar run, and so the analysis up to around 20 K, especially at the lower pressures, should be reliable, even if the exact nature of the susceptibility *did* play an important role.

Analysis of the data at higher temperatures is also complicated by the necessity of involving the effects of the crossover. Above T_X the application of field will strengthen FM2 ordering and the susceptibility will peak as the system crosses from an FM1-like phase to an FM2-like phase. This is handled in the same manner as described for crossing H_X at low temperature above P_X, whereby the data is split into two subsets either side of the critical field and then the subsets fitted individually.

This approach is somewhat questionable for the high field subset, however, since the magnetization of the field induced FM2-like phase is almost completely unknown and even the crude approximations mentioned above are no longer applicable. Therefore the main results presented below focus primarily on the low-field phase, i.e. just FM1 above T_X and P_X.

5.5 Data Analysis Summary

- For each pressure begin with a dataset such as that presented in figure 5.7, measurements of resistance as a function of temperature at various field strengths for both directions of field.
- Bin the data into intervals of 0.1 K, taking the error in the mean as the uncertainty in that data point.
- Determine ρ_{xx} and ρ_{xy} by the van der Pauw method outlined in section 3.4.
- By differentiating ρ_{xx} with respect to temperature, find a value of T_X at each field or, conversely, a value of H_X at each temperature, providing the results presented in figure 5.24.
- For each temperature data point:
  - Plot ρ_{xy} as a function of H, as demonstrated by figure 5.21, and if the metamagnetic transition is crossed within the field range then split the dataset into FM1 and FM2 phases.
  - Determine the gradient $\widetilde{R}_0$ for each phase encountered, should there be sufficient data points for an accurate fit.
  - Also calculate the quantities Γ, α_1 and α_2 then functionally fit $\Gamma(H)$ by $\alpha_1(H)$ and $\alpha_2(H)$ according to equation 5.2 to obtain the ordinary and anomalous Hall coefficients R_0, R_{a_1} and R_{a_2}.
- Calculate the single-band carrier concentration $n = 1/eR_0$ as a function of temperature.
- Use the R_0 and ρ_{xx} data to fit to equation 2.28 and attempt to obtain individual electron and hole concentrations, as a function of temperature.

Repeat all of the above for each pressure, then combine the results to produce full datasets for R_0, n, R_{a_1}, R_{a_2} as a function of both pressure and temperature. It should be noted that an assumption fundamental to this method is that these four quantities have no field dependence within a particular phase; a single data point is returned at each temperature value by the procedure outlined above.

5.6 Base Temperature Hall Coefficients

The Hall resistivity and magnetoresistivity just above cryostat base temperature, as a function of field for several pressures both above and below P_X, are shown in figure 5.22. Although the magnetization data from Ref. [18] is at 2.3 K, slightly higher temperatures around 3 K were used for this figure, and in the following analysis, since at pressures above P_X the influence of H_X is identified much more clearly around 3 K than in the almost featureless 2 K data (see figure 5.8). The necessary assumption is therefore that the magnetization, which at these precise pressures is an interpolated approximation anyway, changes very little across this small temperature variation, which was deemed to be reasonable.

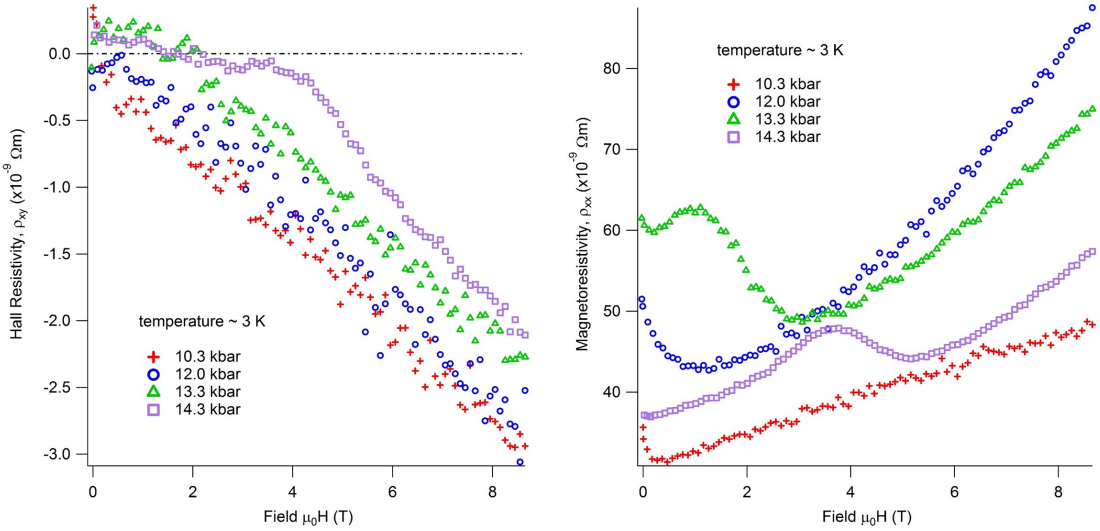

Figure 5.22 **Left:** The Hall resistivity as a function of field for several pressures, two below P_X and two above, around 3 K, showing a change in slope at H_X in the high pressure data but generally negative, constant gradient within a particular phase. **Right:** The longitudinal resistivity for the same dataset, also showing features around H_X but with generally positive gradient away from the transition.

There are several features deserving comment in these graphs. At 10.3 kbar there is a sharp decrease in ρ_{xx} over the initial 0.25 T, likely due to domain restructuring and the suppression of ferromagnetic fluctuations, as noted previously in section 5.4. Much closer to P_X, at 12.0 kbar, the influence of the metamagnetic transition is more obvious and results in a broad minimum in the magnetoresistance at low field, which can be explained as follows.

Immediately below the critical pressure, in the FM2 state but very close to the border with FM1, an applied field will both dampen FM1-FM2 magnetic

fluctuations and strengthen the FM2 order, thus reducing the resistivity. The latter effect can be seen from the higher pressure ρ_{xx} curves, demonstrating that the FM2 state above H_X has significantly lower resistivity than the low-field FM1 state. The curves plotted in figure 5.13 also suggest a sudden drop in resistance below T_X.

Increasing field strength at 12.0 kbar will therefore move the system away from the critical region, resulting in an initially decreasing resistivity. Once further away from the phase transition the influence of this effect is greatly diminished and as the field increases further the expected behaviour of positive magnetoresistance (typically scaling with the square of the field) dominates, and the level of zero-field resistivity is reached around 4 T and then greatly surpassed.

At higher pressure, beyond P_X, there are obvious features associated with H_X as discussed in section 5.2. The Hall resistivity changes slope crossing from FM1 to FM2, with a significantly greater negative gradient in the more strongly polarised FM2 phase. The gradient in both phases at all pressures is always negative at these temperatures.

The gradient of the Hall resistivity with field is strongly associated with the ordinary Hall coefficient. In a simple, single-band model, a negative gradient in the Hall resistivity as a function of field would indicate an electron dominated carrier concentration and a change in slope would indicate a sudden change to greater electron density in the FM2 state.

It is clear from equation 2.23, however, that in a two-band model the gradient of the Hall resistivity is more difficult to interpret. The *relative* concentration of the charge carriers must be considered, the density of both electrons and holes if those are the chosen two bands, and also the relative conductivity of the different bands enters the formula, making it difficult to directly relate any sudden change in R_0 solely to changes in the relative sizes of the Fermi surfaces.

For a two-band, hole and electron model, equation 2.23 suggests that a negative R_0 is more likely an indication of a hole dominated average carrier concentration than an electron dominated one as suggested by the single-band model, although this is not *necessarily* the case, since a relatively large hole band conductivity could result in a negative R_0 even if electrons dominated the average carrier concentration.

Still, the fact remains that the slope of the hall resistivity with field is a useful,

if rather crude, indicator of major changes to the Fermi surface and is often (Ref. [135] for example) plotted as a parameter of interest. The gradient of the Hall resistivity with field, denoted $\widetilde{R}_0 = \partial\rho_{xy}/\partial\mu_0 H$, for the data presented in figure 5.22 is shown in figure 5.23, along with the values of ordinary and anomalous Hall coefficients found by fully fitting the data to equation 5.2 for comparison. The derivative $\widetilde{R}_0$ is referred to as the "estimated" Hall coefficient, while the value of R_0 determined by a functional fit to equation 5.2 is referred to as "full fit".

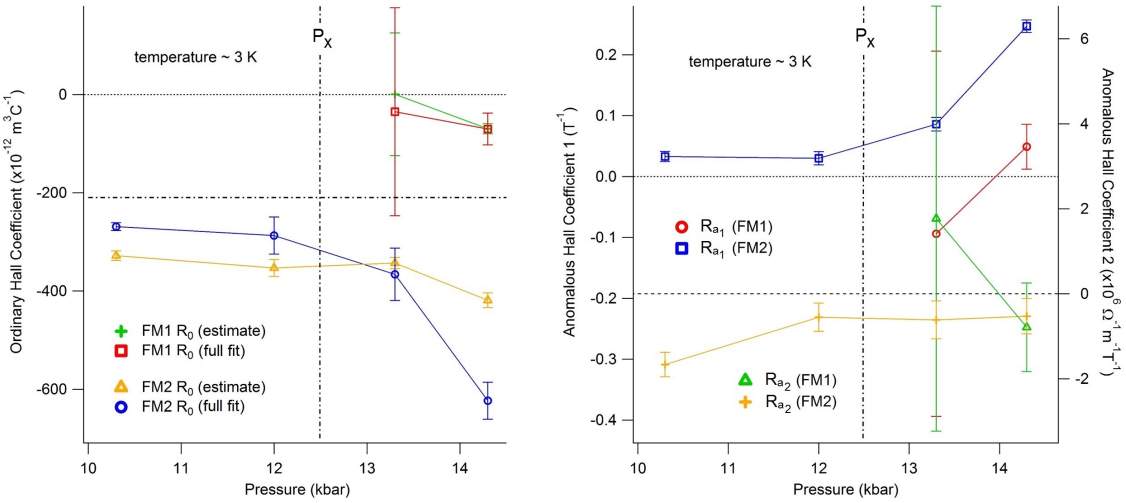

Figure 5.23 **Left:** The ordinary Hall coefficient for several pressures, two below P_X and two above, around 3 K. There is little difference between the FM2 state at low pressure and the induced FM2 state at high pressure, whereas the FM1 values are significantly different at an order of magnitude smaller. The estimated values are reasonably similar to the exact data. **Right:** The anomalous Hall coefficients for the same dataset, showing FM1 values that are not too dissimilar to the FM2 ones. The FM1 data at 13.3 kbar has uncertainty too large to claim significance in any difference from the FM2 values.

A few important conclusions can already be drawn from this initial result. Firstly, there is a significant difference between the FM1 and FM2 ordinary Hall coefficient. In the FM1 state R_0 is small and negative, while in the FM2 state R_0 is still negative but consistently larger. A dividing line at $-210\times10^{-12}\,\mathrm{m^3C^{-1}}$ makes the difference more obvious, with that particular value being chosen for use in later graphs (specifically figure 5.28). As expected, the values of Hall coefficient estimated from the gradient are roughly the same as the 'full fit' values (essentially because of the relatively small contribution from the AHE at this temperature).

The anomalous Hall coefficients appear to change relatively little from FM1 to FM2, disregarding the FM1 result at 13.3 kbar, which cannot be considered

significant because of the large uncertainty. This unreliability is due to the small dataset available for the FM1 state just above the critical pressure where relatively small fields induce the metamagnetic transition to FM2. In the case of the 13.3 kbar run, only the data from 0.5 to 1.5 T was used for fitting to equation 5.2, which is a rather limited range.

To draw more significant conclusions more pressure values must be studied, over a larger temperature range.

5.6.1 Higher Temperatures

From observation of figure 5.8 it is clear that the differences between FM1 and FM2 become more pronounced as temperature, and thus resistivity, increases. The analysis of the Hall resistivity above base temperature is more complicated, however, especially for temperatures above T_X where the metamagnetic crossover is encountered.

Firstly the data must be binned into temperature intervals. The chosen bin size was 0.1 K with each data point positioned at the centre of the interval. For example, the first data point at 2.2 K contains binned data from 2.15 to 2.25 K. The value of a data point was given by the interval mean and the uncertainty was given by the standard error in the mean, i.e. the scatter of data points was the dominant source of experimental uncertainty. For all the graphs presented in this chapter the error bars show the 95% confidence interval, calculated as the standard error multiplied by 1.96.

After binning, datasets as a function of field can be constructed, as demonstrated in figure 5.21. The relatively few data points compared to direct field sweep measurements results in higher uncertainties in the determined Hall coefficients but does provide detailed information on their evolution with temperature. The alternative would be to perform field sweep measurements every 0.1 K, which would greatly reduce the uncertainties but substantially increase the measurement time beyond what was deemed pragmatic, especially for a procedure that had to be repeated numerous times, at different values of pressure.

At each temperature value an estimate of H_X must then be used to divide the data into separate phases. In practice, using temperature sweep measurements, it proves easier to find an estimate of T_X at a particular field and then invert a

plot of T_X vs H to give a plot of H_X vs T. The value of T_X at some particular field strength can be estimated by analysis of $\partial\rho_{xx}/\partial T$ data, as seen in figure 5.10. Taking the peak positions provides the results presented in figure 5.11.

For each pressure, the measurement data was automatically fitted, differentiated and the positions of the peaks identified for each field value. For example, a colour plot of $\partial\rho_{xx}/\partial T$ at 12.0 kbar, just below P_X and so crossing the FM1-FM2 transition for a wide range of temperature above the zero-field T_X of 7.6 K, is shown in 5.24. The automatically detected peak positions are overlaid.

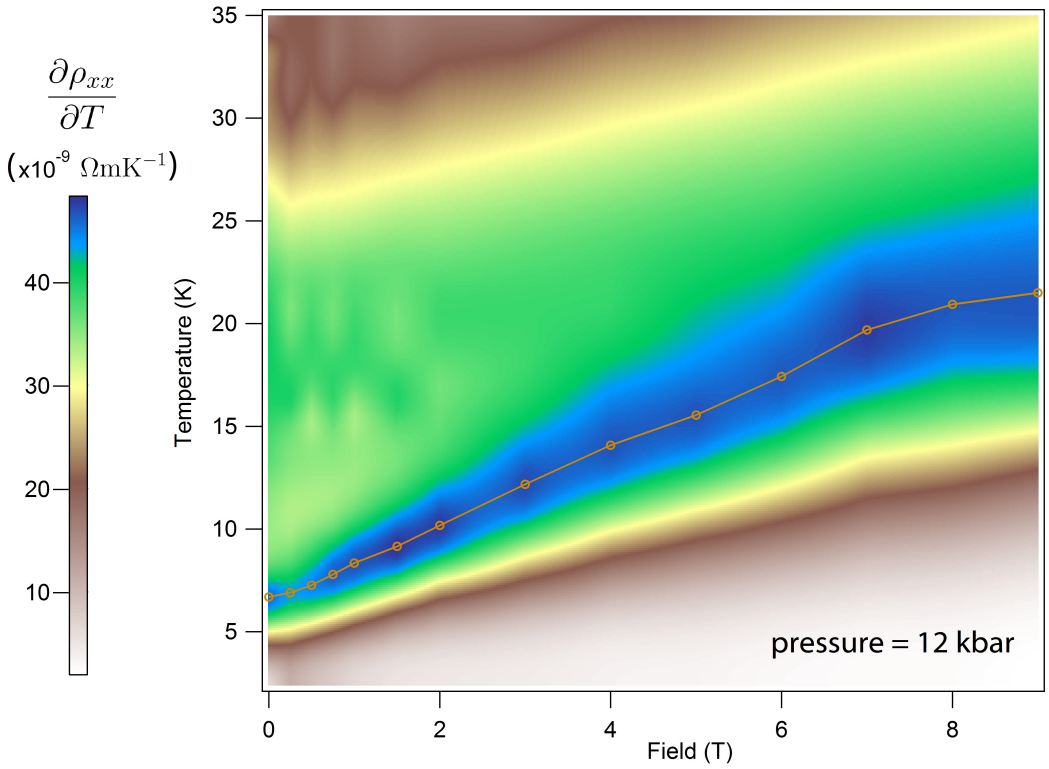

Figure 5.24 Colour plot of the first derivative of the magnetoresistivity with respect to temperature, at 12.0 kbar, plotted as a function of temperature and field. The peak in the derivative, associated with T_X, is coloured blue. The exact peak positions at each measured field are indicated by markers. The value of T_X corresponding to the centre of the crossover region lies slightly above this line.

It should be noted that the temperature values plotted in figure 5.24 (and figure 5.11) are slightly lower than the T_X values determined by section 5.1 method 1, which stated that the point of maximum negative slope (a trough in the second derivative) just to the right of the peak in the first derivative was more closely associated with T_X than the position of the peak itself.

Unfortunately, application of field broadens the peak significantly and it is not possible to identify such a feature in the data at high field. Therefore the peak

position was used as a rough guide, with the accuracy of the method relying on the precaution that data 1 T either side of the determined H_X value at any particular temperature was discarded from the fitting procedure, which ensures that the true H_X value lies somewhere within this critical region.

5.7 The Ordinary Hall Coefficient

The Hall resistivity gradient $\widetilde{R}_0$ is shown for a selection of pressures across the full range (namely runs B, E, H, J, K and M) in 5.25. Both the low-field FM1 phase and the field induced FM2 phase data are included. A limited temperature range, 2 K up to the Curie temperature for each pressure, is shown in these graphs because beyond T_C the values of $\widetilde{R}_0$ become very large (see figure 5.26 for example) and plotting them on the same scale would obscure the behaviour of the low temperature data, which is relatively small in magnitude.

Below P_X the low temperature FM2 values of $\widetilde{R}_0$ are roughly the same across the pressure range. The variation in temperature is also small, with $\widetilde{R}_0$ approximately $-300 \times 10^{-12}\,\mathrm{m^3C^{-1}}$ for the whole FM2 phase except approaching T_X where it curves down to become increasingly negative. The induced FM2 state generally continues this trend.

The FM1 data just above T_X is also negative, though generally smaller in magnitude than the FM2 curve. It also becomes increasingly negative with increasing temperature, before curving back towards zero as T_C is approached. Increasing pressure allows the FM1 data to be calculated to lower temperature, where the value of $\widetilde{R}_0$ becomes less negative, and just below P_X the lowest temperature data reaches zero. Moving beyond the critical pressure sees a sudden jump to positive $\widetilde{R}_0$, with the most positive values around 10 K, as expected from observation of figure 5.8.

As pressure increases further the low temperature region of positive $\widetilde{R}_0$ persists, peaked around a pressure-independent temperature of roughly 10 K, albeit with a diminished magnitude such that the data is scattered either side of zero. By the highest pressure the lowest temperature data is actually negative, again as expected by observation of figure 5.8. It can also be seen that the FM1 data is consistently greater than the field induced FM2 data and that, more easily seen at the highest pressures, the difference increases with temperature.

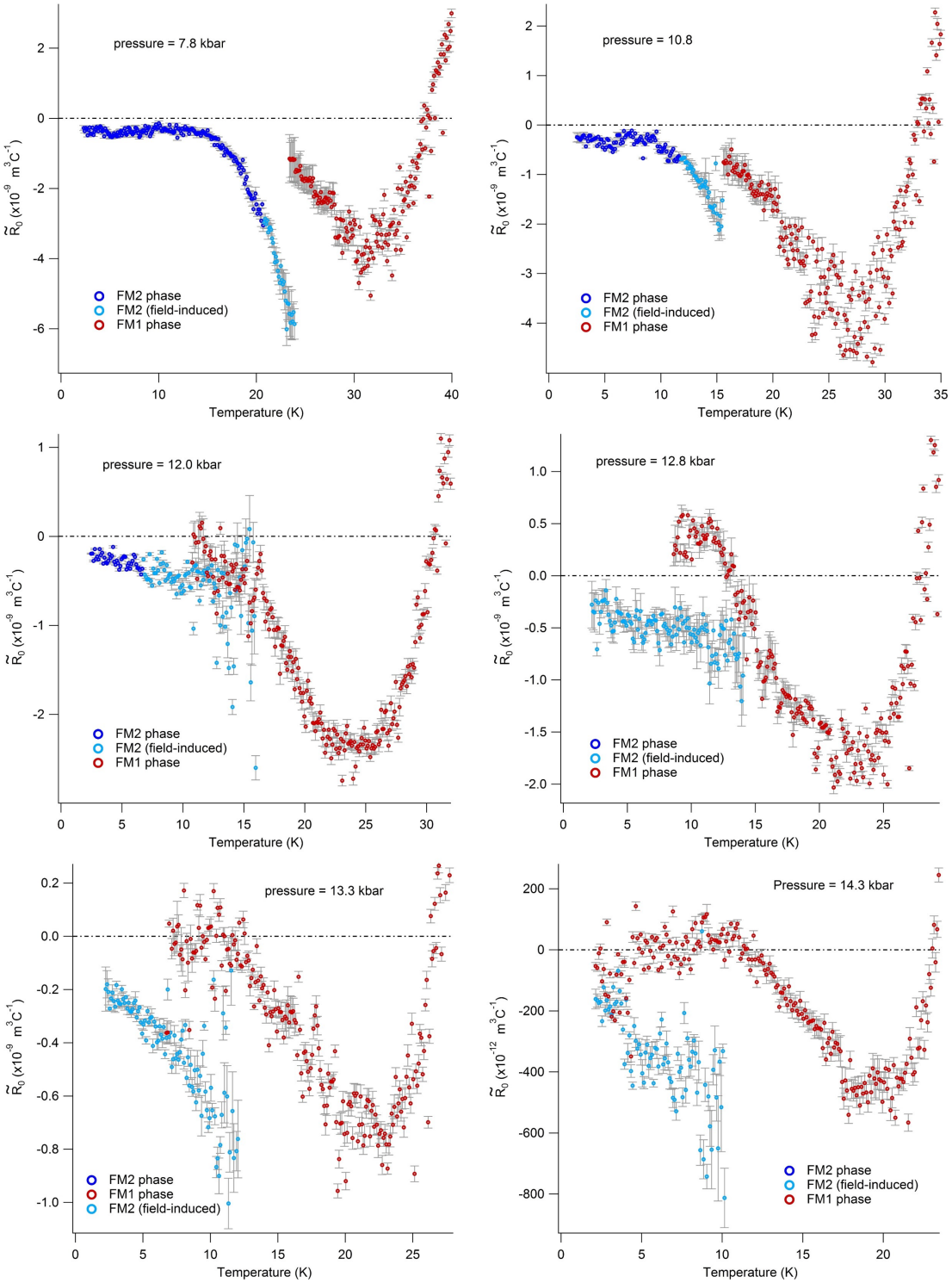

Figure 5.25 The gradient of the Hall resistivity with field, $\tilde{R}_0 = \partial\rho_{xy}/\partial\mu_0 H$, as a function of temperature up to T_C for a variety of pressures, three below P_X and three above. At low pressure, above T_X the field induced FM2 phase is shown in addition to the low field FM1 data.

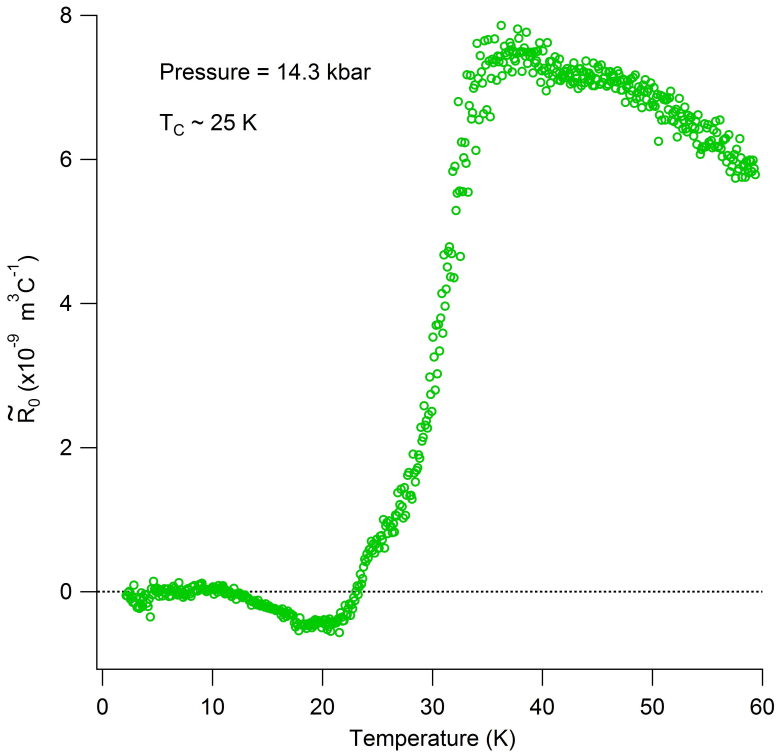

Figure 5.26 The gradient of the Hall resistivity with field, $\tilde{R_0} = \partial\rho_{xy}/\partial\mu_0 H$, as a function of temperature up to and beyond T_C. The highest pressure data has been used as an example, where FM1 data can be shown from 2 K up to a relatively low Curie temperature at 25 K, beyond which the paramagnetic phase is shown up to the end of the measurement range at 60 K. On this scale the Hall coefficient at low temperature, below 10 K, appears to be about zero.

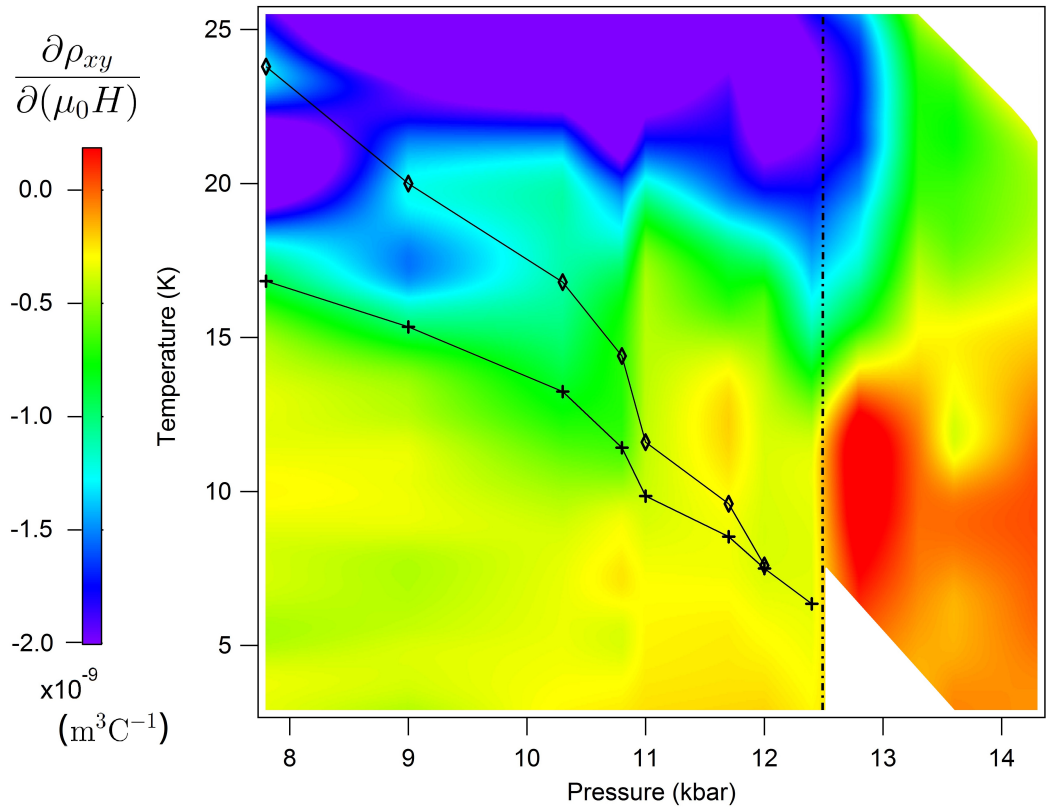

Figure 5.27 Colour plot of the gradient of the Hall resistivity with field, $\tilde{R_0} = \partial\rho_{xy}/\partial\mu_0 H$, as a function of temperature and pressure, created by linear interpolation between discrete pressure values. The T_X and P_X phase lines from figure 5.14 have been overlaid. White triangles have been used to blank areas of unreliable data. At low temperature there is a clear change in $\tilde{R_0}$ crossing the P_X line, from around $-300{\times}10^{-12}$ m^{3}C^{-1} at low pressure to around zero, if not slightly positive, at high pressure. Surprisingly this change is evident at temperatures up to about 13 K, well above the T_X values just below P_X.

The difference between the FM1 and FM2 phases is more easily seen in the colour plot in figure 5.27, which shows the gradient of the Hall resistivity as a function of field plotted across the whole UGe_2 temperature-pressure phase diagram. Here only the low-field phase results are shown, i.e. the FM2 phase below T_X and P_X and the FM1 phase otherwise. The T_X and P_X phase lines from figure 5.14 have been overlaid for reference.

The values for all of the colour plots presented in this section were found by a smoothing 2d grid-style interpolation of the experimental data, which was necessary because of the highly discrete nature of the data points as a function of pressure, despite the data being practically continuous as a function of temperature. The curves fitted to plots against temperature were the result of a smoothing continuous average weighted by the uncertainty on each data

point. The interpolation of the data taken from these curves and plotted for each temperature point as a function of pressure was simply linear.

There are two regions of the phase diagram without reliable data that have been blanked out of the colour plots, despite values being provided by the interpolation procedure. The high temperature, high pressure region in the upper right corner has been blanked out due to the influence of the Curie temperature, which invalidates the analysis that provided the data.

The low temperature region just above P_X has been blanked out because, as observation of figure 5.25 makes clear, there was insufficient data available to accurately fit the FM1 phase under these conditions. Just above the metamagnetic transition application of even a small field moves the system back toward the FM2 phase. For the same reason, it was also impossible to obtain FM1 results for a small temperature range above T_X. However, since in this case there exists reliable data either side of the transition, the interpolated values across the transition region remain visible in the colour plots.

The colour scale in figure 5.27 was adjusted such that the typical FM2 value of $-300 \times 10^{-12}\,\mathrm{m^3C^{-1}}$ is yellow and it can be seen that this colour extends throughout most of the FM2 phase space. Values of $\tilde{R}_0$ closer to zero are coloured red, making the change from low temperature FM2 to FM1 obvious. Interestingly an abrupt change in $\tilde{R}_0$ occurs crossing the P_X line at around 12 K, where it is supposedly the same FM1 phase either side of the line.

Plotting $\widetilde{R}_0$ as a function of pressure for several low temperatures results in figure 5.28, which provides more quantitative information than the colour plot. The dividing line at $-210\times10^{-12}\,\mathrm{m^3C^{-1}}$ utilised earlier in figure 5.23 has been added to highlight the difference between the FM1 and FM2 values. The field-induced FM2 values above P_X have also been added for comparison.

Of course $\widetilde{R}_0$ is only a crude approximation to the ordinary Hall effect, one that although fairly good at the lowest temperatures becomes worse as temperature rises and the influence of the AHE grows. This can be seen in figure 5.29, which shows the ordinary Hall coefficient plotted against temperature for a range of different pressures. Comparing the 7.8 kbar plot of R_0 with that for $\widetilde{R}_0$ in figure 5.25 the difference is clear. In the former R_0 remains relatively constant as a function of temperature across the entire FM2 phase, whereas in the latter significant curvature in the FM2 phase is observed as the temperature increases beyond about 15 K.

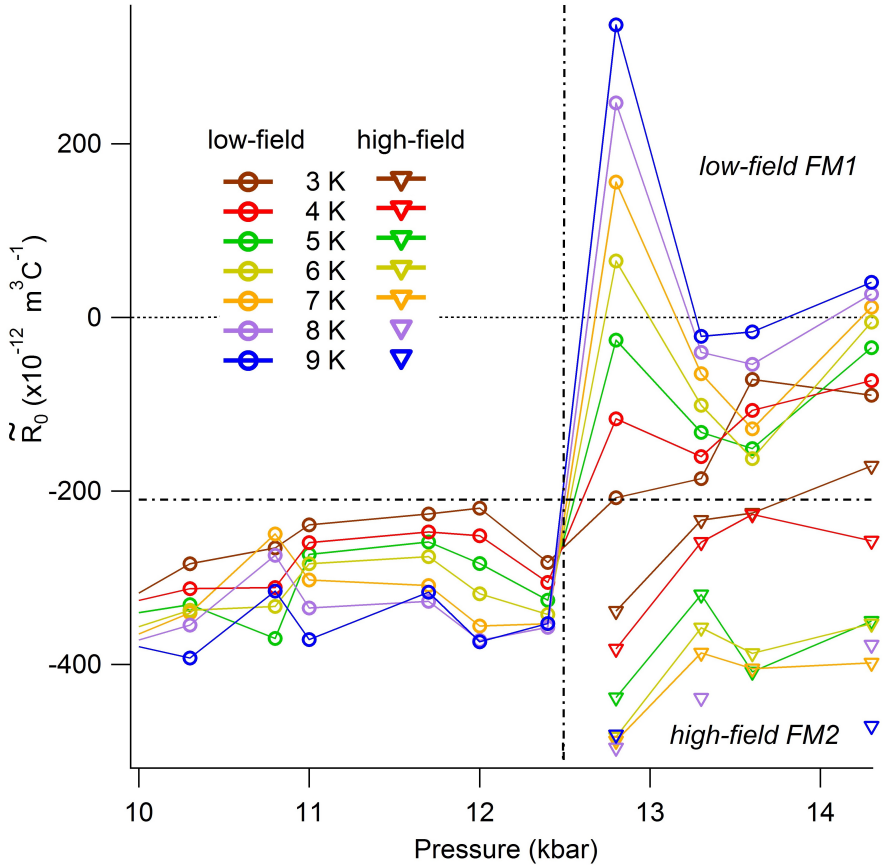

Figure 5.28 The gradient of the Hall resistivity with field, $\tilde{R}_0 = \partial\rho_{xy}/\partial\mu_0 H$, as a function of pressure, plotted for a number of low temperatures. Above P_X the field induced FM2 data is shown in addition to the low field FM1 phase. Error bars have been omitted to avoid obscuring the plots, but typical uncertainties can be gauged from figure 5.25. There is a clear change in $\tilde{R}_0$ crossing P_X, as highlighted by the dividing line at $-210\times10^{-12}\,\mathrm{m^3C^{-1}}$.

Another obvious difference between these two graphs is in the size of the uncertainties in the FM1 data. Just above T_X in the plots of R_0 for 7.8 and 10.8 kbar the calculated uncertainty (the 95% confidence interval) is greater than 100%. Such large values for the uncertainties are essentially indicating that the fitting procedure is invalid for these datasets and that equation 5.2 does not reasonably describe the behaviour of the data. The unacceptably large χ-squared values returned by the fitting procedure for the FM1 data points just above T_X also indicates that the line-of-best-fit, constrained by the formula in equation 5.2, does not fit the data.

As such these data points should strictly be disregarded, but rather than omit these results from the graphs in figure 5.29 (and later figures 5.32, 5.39 and 5.41) they remain plotted for completeness. All interpolation procedures described

in this section use the error bars as weighting factors, so these points are indeed effectively disregarded from any final results presented in the form of colour plots.

The excessively large uncertainties seen in the FM1 state are reduced as pressure increases toward P_X and the crossover sharpens, implying that the large uncertainties at lower pressure are due to the broad nature of the crossover region and the inability of equation 5.2 to describe the data from within this region. The narrowing of the crossover region approaching P_X can be seen from the error bars in the phase diagram (figure 5.14).

At 12.0 kbar the FM1 values just above T_X are roughly zero, with a few data points at the lowest temperatures just crossing the x-axis, similar to the $\widetilde{R}_0$ values. Also in close similarity to the $\widetilde{R}_0$ plots, the low temperature FM1 values of R_0 are strongly positive immediately above P_X, before dropping down toward the x-axis as pressure increases, though the data scatter makes this difficult to see clearly. The general behaviour of R_0 as a function of temperature and pressure is more easily visualised by the colour plot presented in figure 5.30.

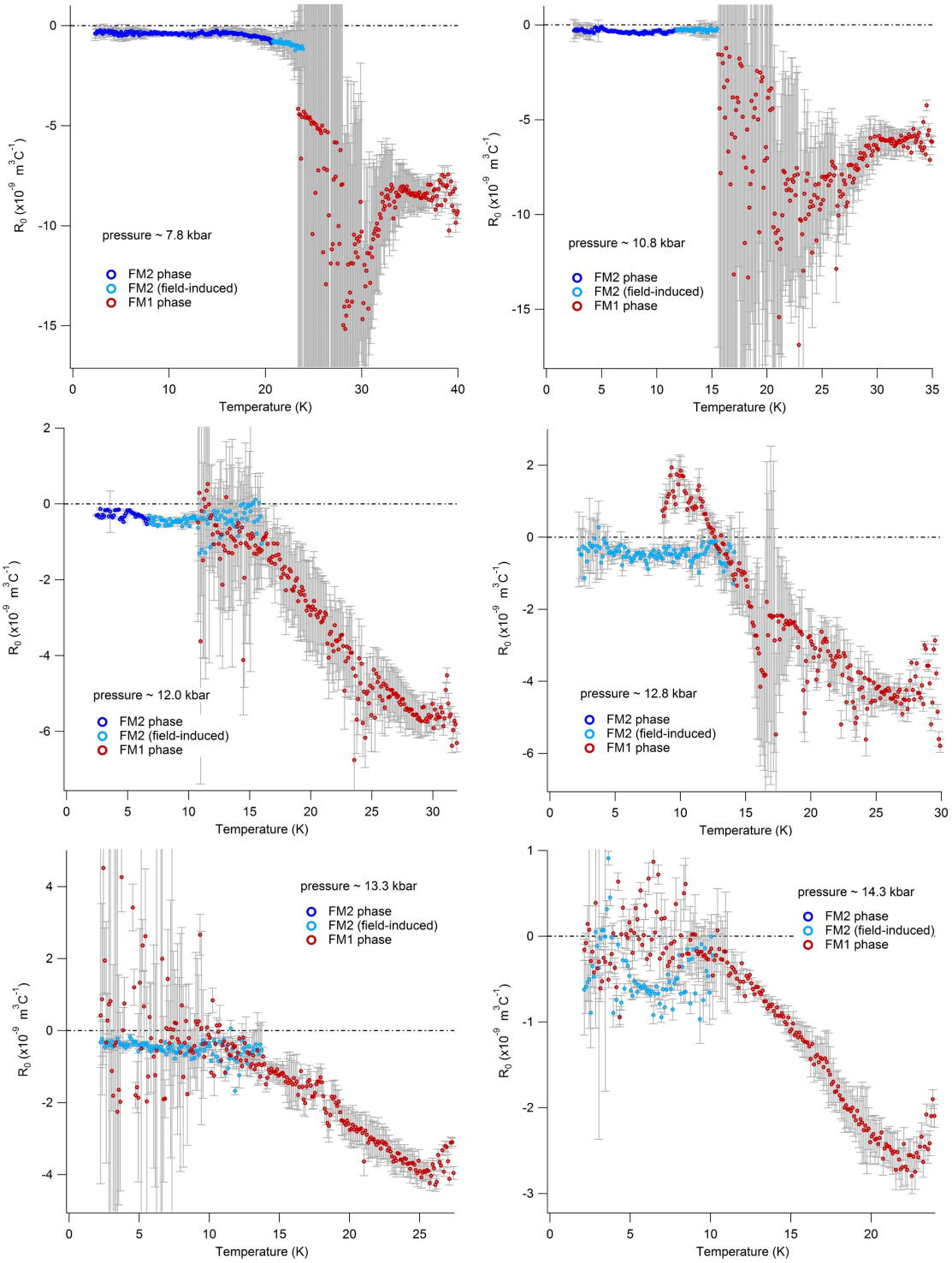

Figure 5.29 The ordinary Hall coefficient, R_0, as a function of temperature up to T_C for a variety of pressures, three below P_X and three above. At low pressure, above T_X the field induced FM2 phase is shown in addition to the low field FM1 data.

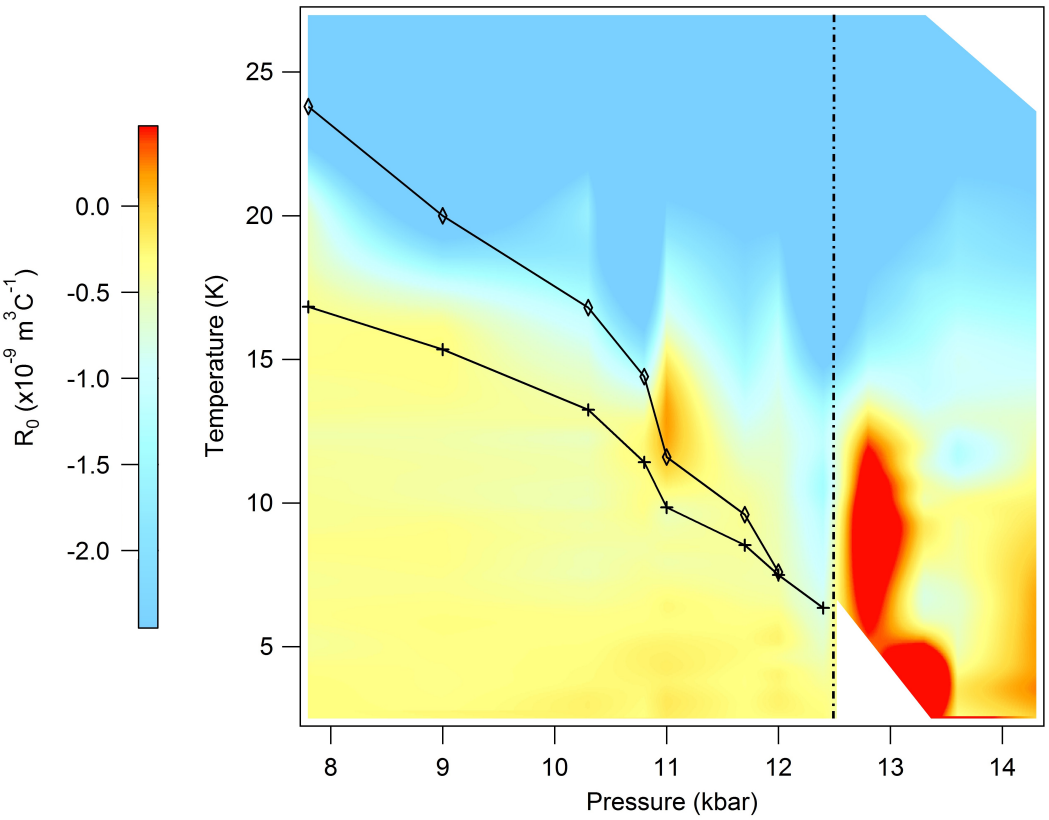

Figure 5.30 Colour plot of the ordinary Hall coefficient R_0 as a function of temperature and pressure, created by linear interpolation between discrete pressure values. The T_X and P_X phase lines from figure 5.14 have been overlaid. White triangles have been used to blank areas of unreliable data. There is a clear change in R_0 from the relatively constant FM2 value of about $-300{\times}10^{-12}\,\mathrm{m^3C^{-1}}$, coloured yellow, to much larger negative values of R_0 in the high temperature FM1 phase, coloured blue. In contrast, at low temperature above P_X, the FM1 phase is characterised by small and positive values of R_0, coloured red, particularly in the region immediately above the critical pressure.

As in figure 5.27 the FM2 phase is a fairly constant yellow colour across the entire phase space, indicating values around the typical $-300\times10^{-12}\,\mathrm{m^3C^{-1}}$ seen before. By contrast, the FM1 phase is somewhat inconsistent between low and high temperature. At high temperature the solid blue seen in figure 5.27 represents large and negative values of R_0, while at low temperature, below about 15 K, the FM1 phase above P_X appears orange and red, indicating small negative and positive values respectively.

There is a particularly strong red region immediately above P_X, as expected from earlier observations in reference to figure 5.28. This suggests that a significant change occurs in UGe_2 crossing P_X, and that it is remarkably different to the FM1-FM2 transition occurring at lower pressure when crossing T_X.

In contrast to the colour plot in figure 5.27 the red region in figure 5.30 does not extend to higher pressures at low temperature, but a quick look at figure 5.29 reveals that the data is so scattered in this region that the results are far from reliable. Although the fitting that produces the colour plots is weighted by the errorbars the resulting curve is basically just a very noisy zero, which shows as a pale orange region in in figure 5.30. It is possible that with less noisy data the high pressure, low temperature region would also be coloured the bright red of a definitely positive R_0 value.

Plotting R_0 as a function of pressure at several low temperatures gives figure 5.31, which allows more quantitative consideration of the changes observed crossing P_X. From this graph the scatter of data points at high pressure seems large and somewhat erratic compared to the values of R_0 seen at low pressure. It is worth remembering, however, that the physically important quantity is actually the inverse of these values. Taking the inverse, the high pressure points will be small, with small variation, and the scatter of the low pressure points actually becomes the more important quantity.

In the simple, single-band model, $R_0 = -1/ne$ for carrier concentration n of charge $-e$. Plotting n instead of R_0 makes any trends in the data easier to understand. Figure 5.32 shows n as a function of temperature for the usual selection of pressures, and figure 5.33 shows the corresponding colour plot.

The colour plot of n is not precisely the inverse of the one for R_0 presented in figure 5.30 because the 2d interpolation procedure used to generate the former was performed on the calculated values of n rather than simply inverting the interpolated R_0 data used for the latter. Therefore there are a few subtle

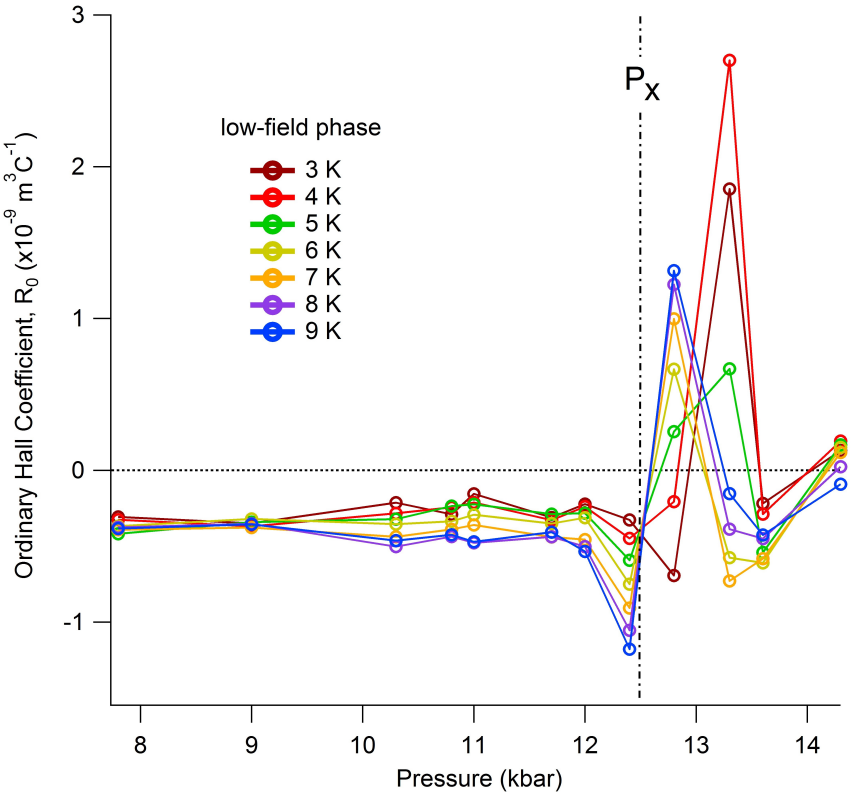

Figure 5.31 The ordinary Hall coefficient, R_0, as a function of pressure, plotted for a number of low temperatures. Above P_X the low-field FM1 phase is shown. Error bars have been omitted to avoid obscuring the plots, but typical uncertainties can be gauged from figure 5.29. There is a significant change at P_X, although the somewhat erratic scatter of data points makes detailed analysis difficult.

differences between the two colour plots that make presenting figure 5.33 worthwhile.

Immediate observations are that at low pressure the single-band carrier concentration is roughly constant within each phase. At low temperature the FM2 value of n is about 1 electron per uranium atom. This drops dramatically crossing T_X into the FM1 phase, decreasing by an order of magnitude to around 0.1 to 0.2 electrons per uranium. Entering the FM1 phase by crossing P_X at low temperature results in an entirely different change, however, to about 0.2 holes per uranium.

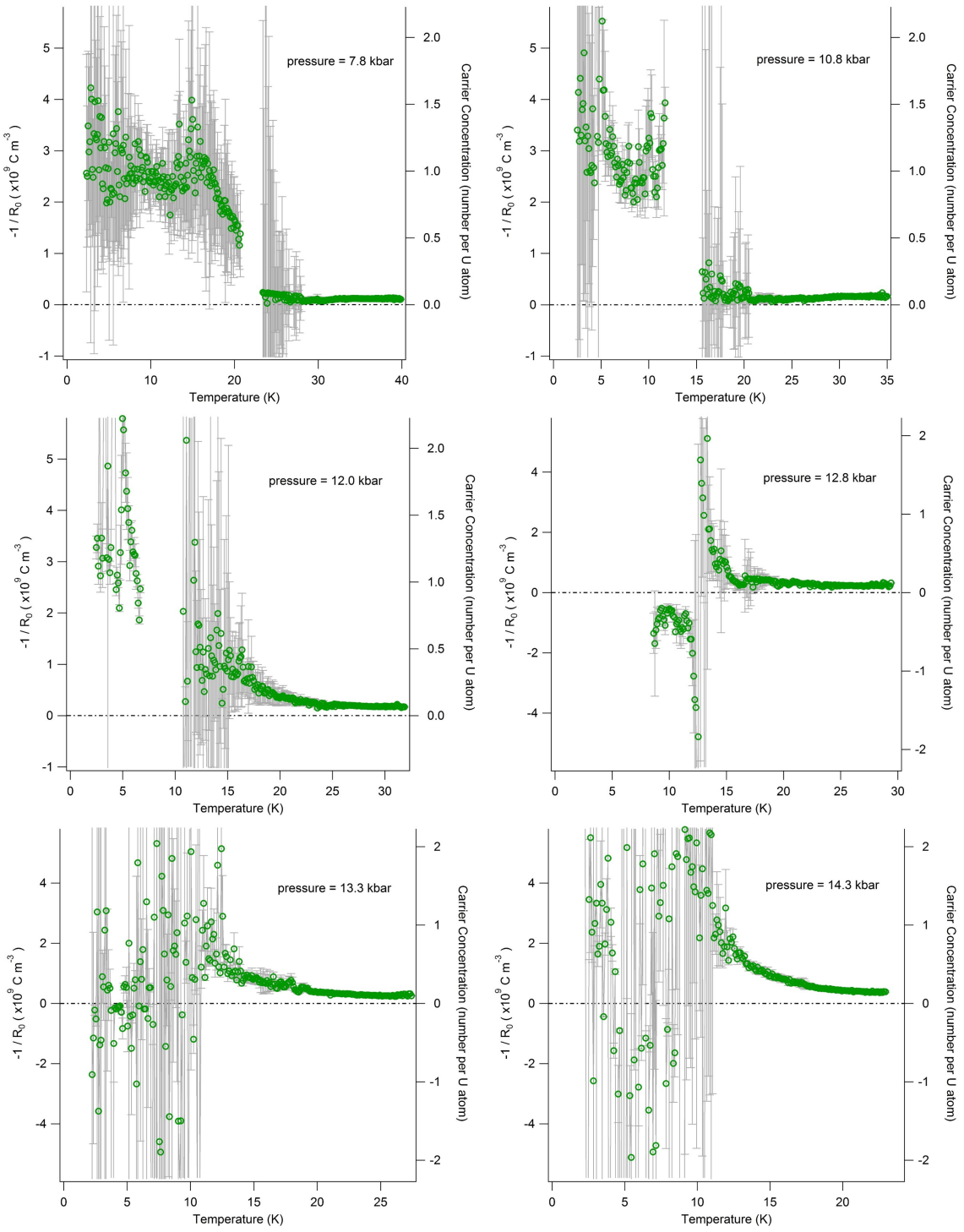

Figure 5.32 The inverse of the ordinary Hall coefficient, and the corresponding carrier concentration for a one-band model, as a function of temperature up to T_C for a variety of pressures, three below P_X and three above. Above T_X or P_X only the FM1 data is shown, for clarity. In general there is a change from $n \sim 1$ per uranium in the FM2 phase to $|n| < 0.2$ per uranium in the FM1 phase, except at the highest pressure where it reaches about 0.3 per uranium.

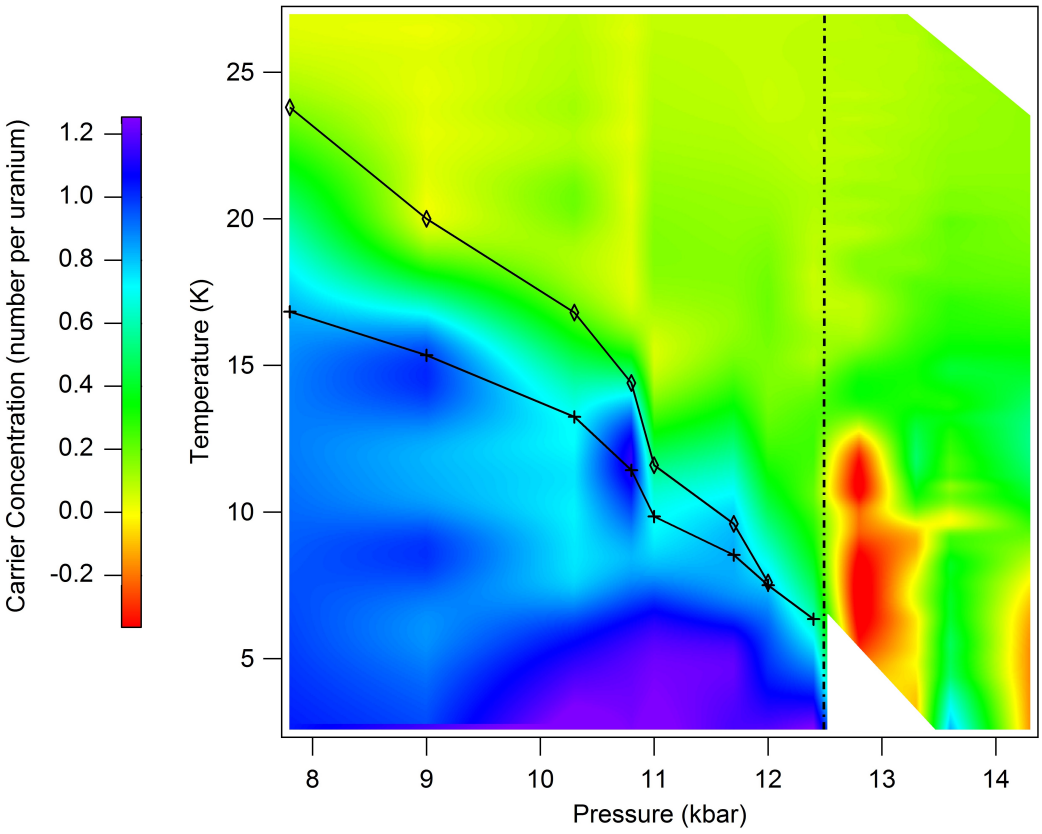

Figure 5.33 Colour plot of the one-band model carrier concentration, essentially the inverse of R_0, as a function of temperature and pressure, created by linear interpolation between discrete pressure values. The T_X and P_X phase lines from figure 5.14 have been overlaid. White triangles have been used to blank areas of unreliable data. There is a clear change from the FM2 value of about 1 electron per uranium to generally much lower values in the FM1 phase, around 0.1 to 0.2 electrons per uranium, with some small regions above P_X at low temperature indicating 0.1 to 0.2 holes per uranium.

The changes crossing P_X can be seen in more detail in figure 5.34, a graph of n as a function of pressure for several low temperatures. The data at 13.6 kbar appears to be something of an outlier to the general trend, but the low temperature data at higher pressures becomes too disordered, with too high uncertainties, to draw any significant conclusions. The error bars seen in figure 5.32 make that clear.

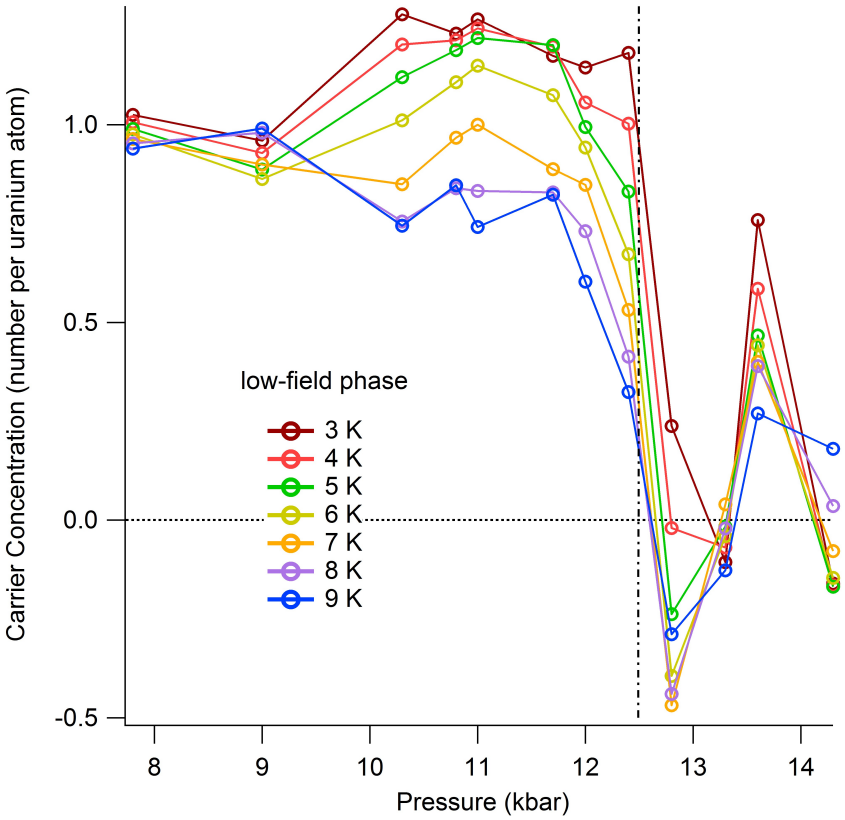

Figure 5.34 The one-band model carrier concentration, n, as a function of pressure, plotted for a number of low temperatures. Above P_X the low-field FM1 phase is shown. Error bars have been omitted to avoid obscuring the plots, but typical uncertainties can be gauged from figure 5.32. There is a significant change at P_X, although the somewhat erratic scatter of data points makes detailed analysis difficult.

Furthermore, if there are both hole and electron bands present at the Fermi surface, and neither charge carrier type dominates, then the simplistic interpretation of n and R_0 discussed above breaks down. In the the multi-band case the negative R_0 and thus positive n observed for the FM2 phase, attributed above to an electron dominated carrier concentration, would most likely be the result of a greater concentration of holes than electrons, depending on the relative conductivities, according to equation 2.23.

As discussed in section 2.3, this would be the interpretation and analysis in the

'low field limit', which is not really the case around 2 K, though the system is indeed closer to the 'low' than the 'high' field regime. At base temperature the Hall coefficient is more accurately described by equation 2.19 but this is rather more difficult to analyse, especially without quantitatively accurate resistivity tensor data. As mentioned in section 2.3 however, the initial results do suggest a low field limit treatment of the data and therefore this will be presented in the following few pages, before going on to discuss more accurate approaches.

Even making the simplifying approximations of the low field limit, finding the individual hole and electron concentrations proves difficult. Fitting to equation 2.27 only works for a limited area of the phase diagram for UGe_2 since the theory that underpins that formula only allows for positive magnetoresistance. As seen in figure 5.12 for example, the change in ρ_{xx} with field is positive only at very low temperatures.

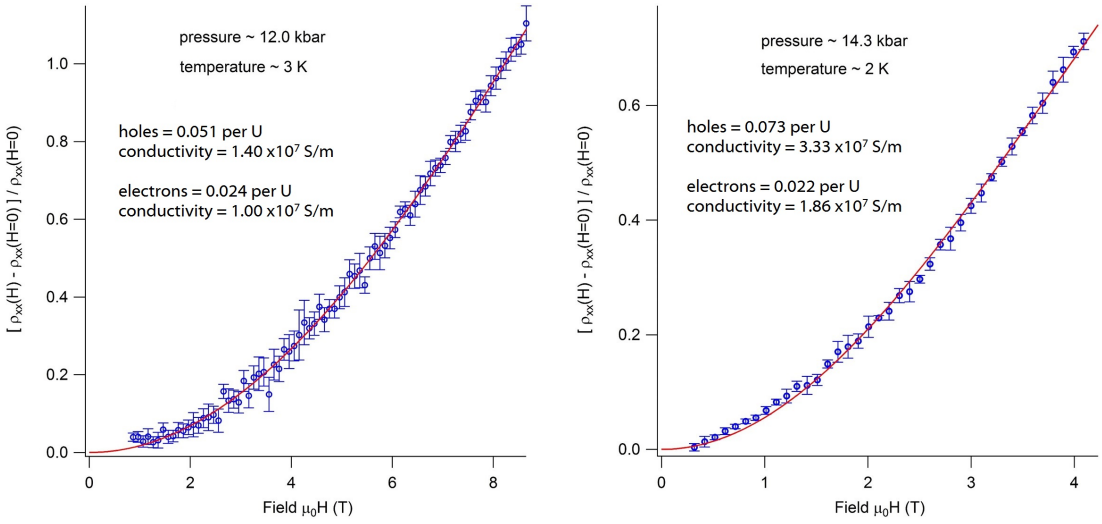

Figure 5.35 The relative increase in resistivity as a function of field, fitted by equation 2.27. **Left:** Just below P_X and in the FM2 phase at 3 K, fitting reveals a hole concentration roughly twice that of the electron concentration, though both are very small, of the order 0.01 charge carriers per formula unit of UGe_2. **Right:** Well above P_X at 2 K the data up to 4 T lies within the FM1 phase. Fitting reveals similar hole and electron concentrations as in the FM2 phase, though the hole concentration has increased by almost 50%.

Figure 5.35 shows good fits to equation 2.27 for the FM1 and FM2 phases at very low temperature, at 2 K and 14.3 kbar, and at 3 K and 12.0 kbar, respectively. Although these regions of temperature and pressure have significantly different values of R_0, seen most clearly in figure 5.23, the determined values for hole and electron concentrations are very similar. The differences between the R_0 values are relatively small, however, when compared to the differences seen across the

whole phase diagram, so perhaps such similarity is unsurprising.

In the FM2 phase at 12.0 kbar the fit gives 0.051 holes to 0.024 electrons per uranium, while in the FM1 phase at 14.3 kbar the fit gives 0.073 holes to 0.022 electrons. These values can then be used to show, as done in section 2.3, that the conditions for the low field limit are not actually fulfilled at these points on the phase diagram.

The shape of the curves in figure 5.35 immediately suggests that the system is not entirely within the low field limit, which should result in magnetoresistance proportional to the field squared. Although there is some evidence of quadratic curvature at low field the magnetoresistance quickly becomes linear, which occurs around the $\omega_c\tau = 1$ point and is the only reason why these plots can be fitted by equation 2.28 despite not having a quadratic field dependence.

An example of where fitting to 2.28 fails to work well is presented in appendix C. In this example the fit suggests that the magnetoresistance should begin to saturate at higher field, resulting in the stretched-S-shape behaviour predicted by the theory. The failure of this fit, and the failure of similar data analysis at other pressures, casts doubt on the validity of the fits shown in figure 5.35 and instead suggests that there might a more fundamental cause for the observed linearity in the magnetoresistance than the influence of the $\omega_c\tau = 1$ point.

As discussed in section 2.3, a reasonable assumption is that the material is compensated, in which case the proper formulae to apply to the data analysis are 2.21 and 2.22. The resistivity in this case still has a quadratic field dependence but only when considering isotropic, spherical Fermi surfaces. Introduction of more realistic Fermi surface shapes to the theory, such as the inclusion of sharp corners with a square-like surface, can result in a linear magnetoresistance. Extensions to a four-band or even eight-band model, as also discussed in section 2.3, would potentially result in more accurate fits to the data too, although then the definition of 'compensated' becomes slightly vague, especially if open Fermi sheets are included in the model as well.

Ultimately, such further analysis is slightly beyond the scope of this thesis. Additional information would be required in order to perform it correctly, without merely introducing various arguably arbitrary artifacts to the model in order to fit the theory to the data instead of using a robust theory to fit the data. Ideally quantitatively accurate components of the conductivity tensor would be needed for proper fitting, and a more detailed knowledge of the Fermi surface

needed to construct a proper model, which is admittedly a demonstration of somewhat circular logic since that is essentially the information that Hall effect measurements aim to provide.

Progressing with the 'simple' analysis of fitting to equation 2.28, ascribing the linear magnetoresistance to approaching the $\omega_c\tau = 1$ point, as dubious as that might be, does at least provide useful information for estimating the critical field that the $\omega_c\tau = 1$ point corresponds to (calculated earlier in section 2.3 as ~ 10 T).

Attempting to fit to equation 2.28 as a function of temperature for each pressure, using the main dataset, provides sparse results. At low pressure reasonable values are returned by the fit only up to a particular temperature, beyond which the uncertainties in the results become extremely large and the scatter of data becomes meaningless. The characteristic temperature beyond which the fitting procedure abruptly fails to provide reasonable results is typically much lower than T_X and simply corresponds to the point where the magnetoresistance transitions from positive to negative.

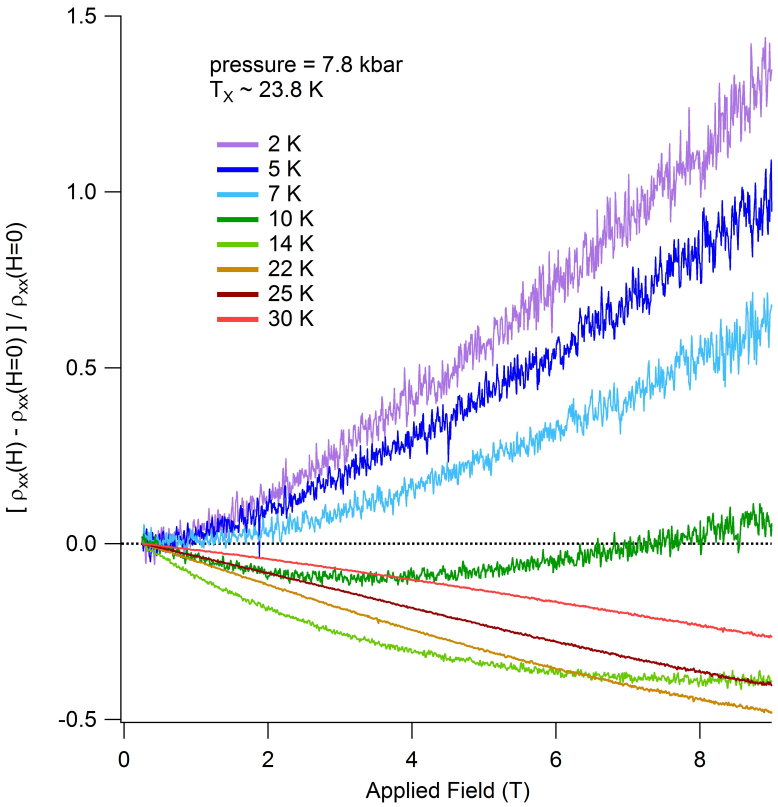

Figure 5.36 The magnetoresistance as a function of field for a range of temperatures at 7.8 kbar where T_X is relatively high at around 20 K. At low temperature the relative increase in resistivity with field can be fitted by equation 2.27 but beyond about 8 K the fitting procedure fails.

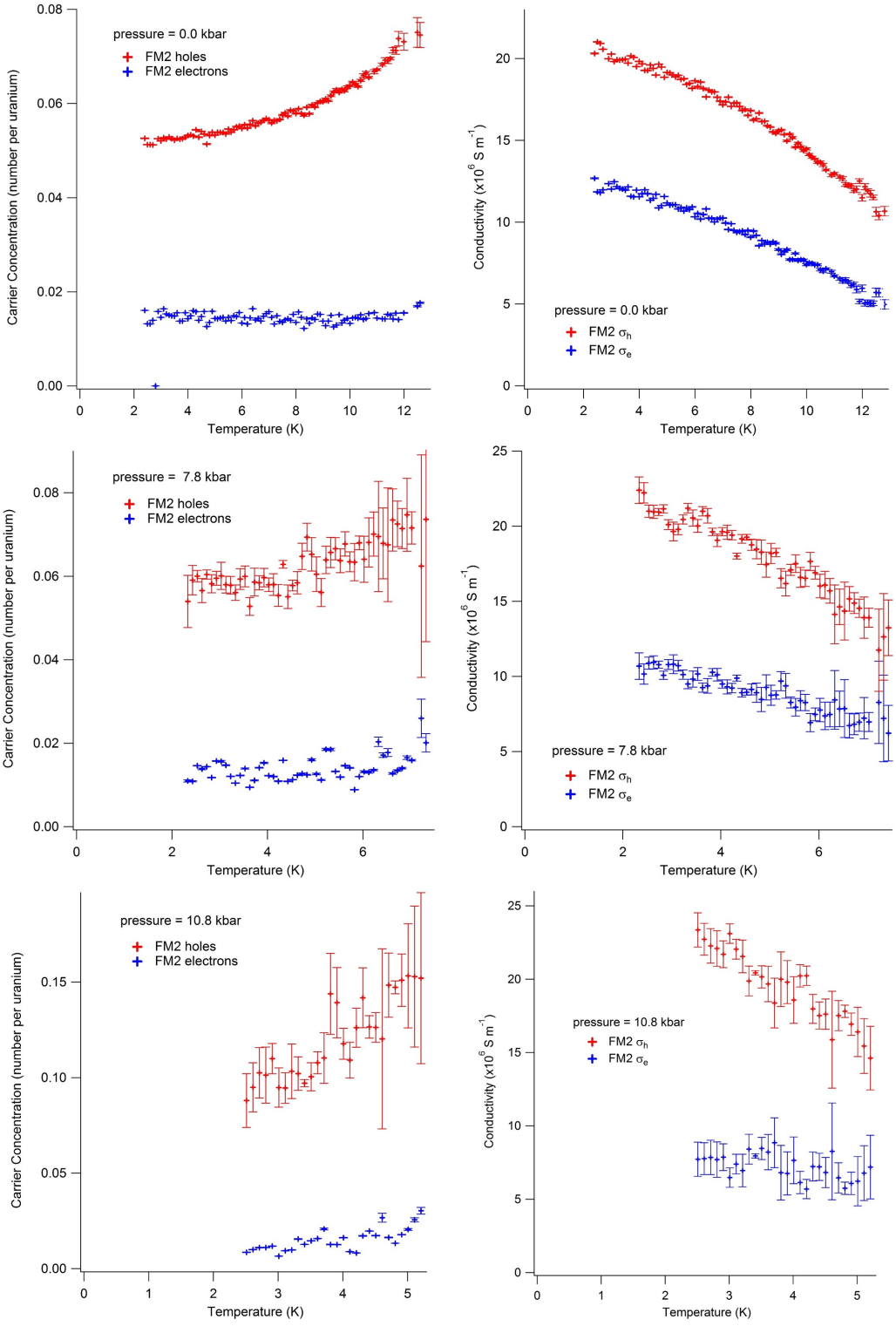

Figure 5.37 The hole and electron concentrations, and the corresponding conductivities, resulting from fits to equation 2.27 for a two-band model, for ambient pressure and two other pressures below P_X. The hole concentration and conductivity are consistently greater than those of the electron band for all pressures. The conductivity generally falls as temperature increases, as expected for a metal. The electron concentration appears approximately constant while the hole concentration seems to increase with temperature.

For example, the magnetoresistance for a wide range of temperatures at 7.8 kbar is shown in figure 5.36. At low temperature the curves are positive but by 10 K the curve becomes mostly negative and clearly cannot be fitted by any function of H^2. This is reflected in the data presented in figure 5.37, which shows the individual hole and electron concentrations and their corresponding conductivities for a few pressures below P_X. The graphs for 7.8 kbar end at 7.5 K, beyond which the fit to equation 2.27 fails.

The existence of this low temperature cut-off is unfortunate because the questionable 'low field limit' analysis applied here becomes increasingly more valid as temperature rises and τ decreases. The occurrence of negative magnetoresistance, however, suggests that the standard theory discussed in section 2.3 does not describe the behaviour of UGe_2 across most of the phase space outlined by the diagram in figure 5.14.

Negative magnetoresistance is to be expected surrounding a metamagnetic phase transition, where additional scattering is introduced in the critical region near the transition from fluctations between the two phases. Applying field moves the system more strongly into a single phase, supressing the influence of this additional scattering and thus lowering the resistance while increasing the magnetic order.

The temperature at which the magnetoresistance changes sign decreases as pressure increases toward P_X, such at by 12.0 kbar the cut-off was only 3.3 K and just a few data points between 2 K and this cut-off temperature were returned by the fitting procedure (with values that match well to those found in figure 5.35).

No reasonable data was returned at any temperature for any of the experimental runs above P_X except for the small temperature range at 14.3 K presented in figure 5.38. This unfortunately makes it difficult, if not impossible, to estimate individual hole and electron concentrations for the strongly red or blue coloured regions (slightly positive or highly negative values of R_0, respectively) of the colour plot in figure 5.30.

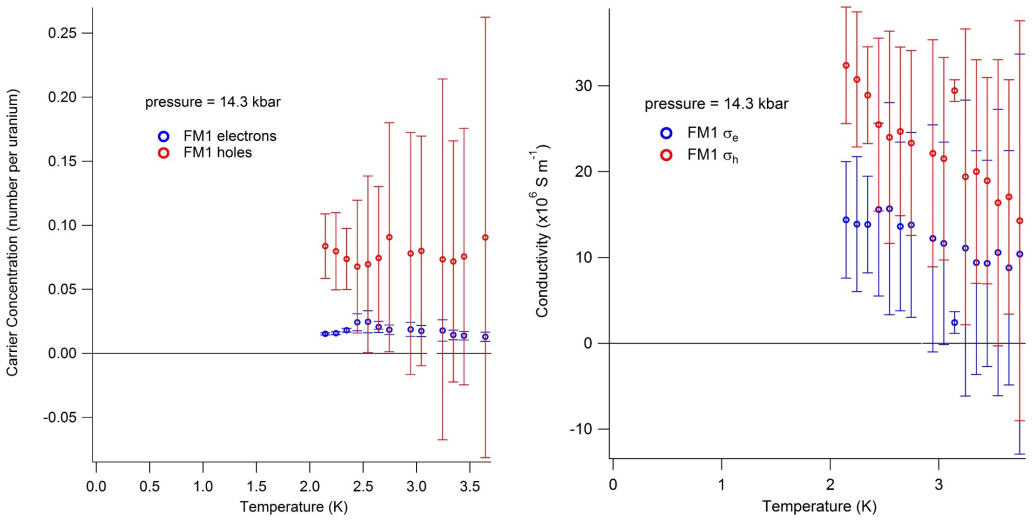

Figure 5.38 The hole and electron concentration, and the corresponding conductivities, resulting from low field (FM1 phase) fits to equation 2.27 for a two-band model, for 14.3 kbar, well above P_X. As for the FM2 data, the hole concentration and conductivity is consistently greater than the electron band values.

5.8 The Anomalous Hall Coefficients

The anomalous Hall coefficient R_{a_1} is shown as a function of temperature for the usual selection of pressures in figure 5.39. Similar to the ordinary Hall coefficient, the error bars just above T_X at low pressure are huge, with the large uncertainty partly due to the large breadth of the transition region far away from P_X. As pressure increases and the crossover narrows the uncertainties immediately above T_X decrease in size, although the error bars for most of the anomalous Hall coefficient data in general are quite large.

The difference between the FM1 and FM2 phases are easier to visualise as a colour plot, as presented in figure 5.40. As in the previous section, the colour plots here are 2d interpolations and show only the data for the low-field phase. Regions where the field range is insufficient to accurately fit the data, or the influence of the Curie point makes the analysis unreliable, have been blanked out as before.

The FM2 values of R_{a_1} are small and positive, as indicated by the fairly uniform red across the FM2 phase space, tinged with yellow, corresponding to the range $0 \sim 0.3\,\mathrm{T}^{-1}$. Crossing T_X is accompanied by a big increase in R_{a_1}, to an FM1 value of $\sim 1\,\mathrm{T}^{-1}$, although this decreases gradually with increasing pressure.

There appears to be little change crossing P_X, with similar values seen either side of the transition at all temperatures. At high pressure a decrease in R_{a_1} is observed, such that a red region covers most of the colour plot above 13 kbar.

Similarly, for the other anomalous Hall coefficient, graphs of R_{a_2} as a function of temperature for a variety of pressures are presented in figure 5.41. The expected large uncertainties just above T_X at low pressure are present and, as before, the behaviour across the pressure-temperature phase space is easier to understand by observation of the corresponding colour plot, shown in 5.42.

It seems difficult to draw any conclusions from the variation of R_{a_2} across the pressure-temperature phase diagram, since there are no significant, structured changes from phase to phase or crossing the P_X line. It might be said that there is a general trend from larger to smaller negative values as temperature increases, but that statement is somewhat unconvincing.

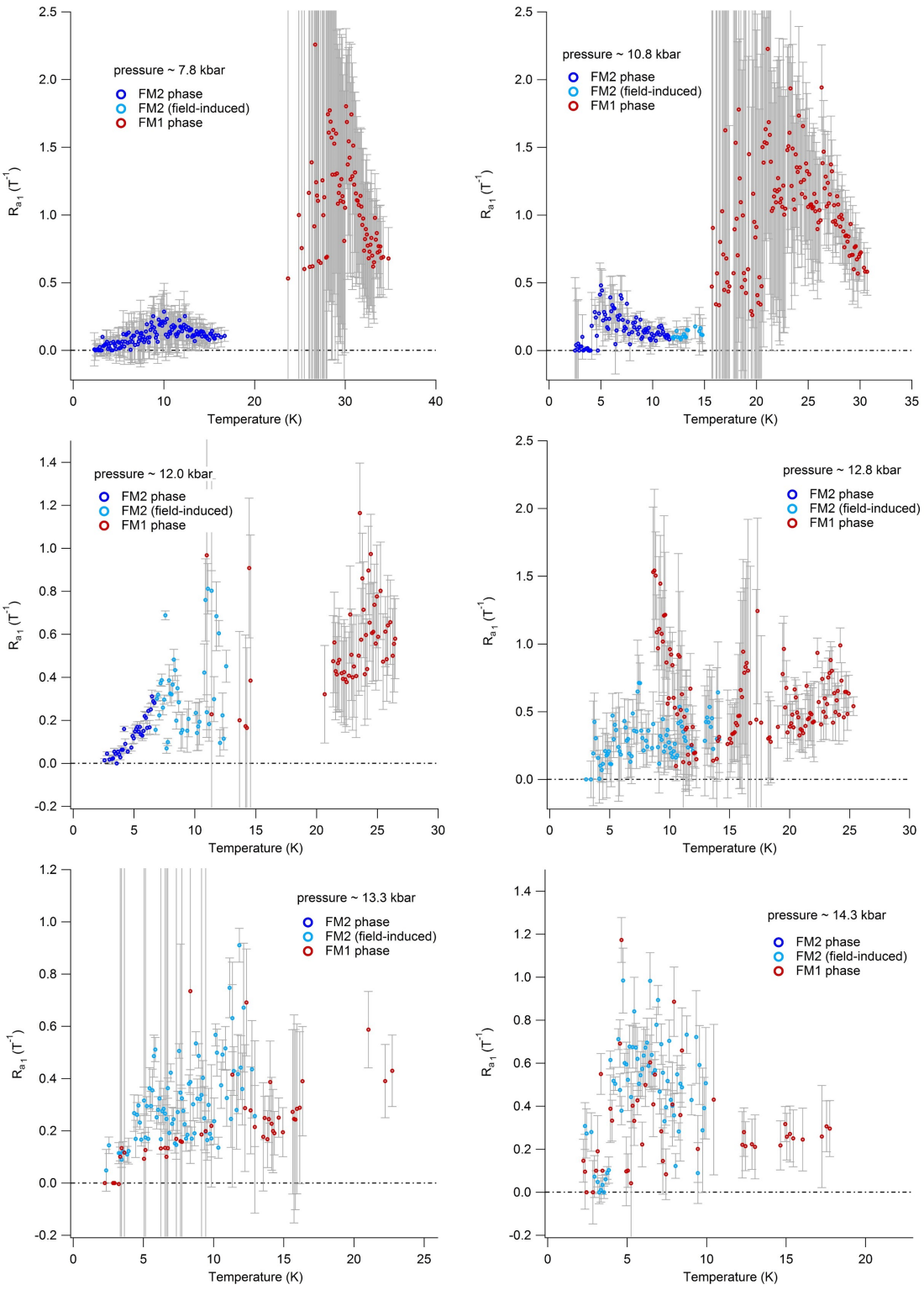

Figure 5.39 The anomalous Hall coefficient R_{a_1} as a function of temperature up to T_C for a variety of pressures, three below P_X and three above. At low pressure, above T_X the field induced FM2 phase is shown in addition to the low field FM1 data.

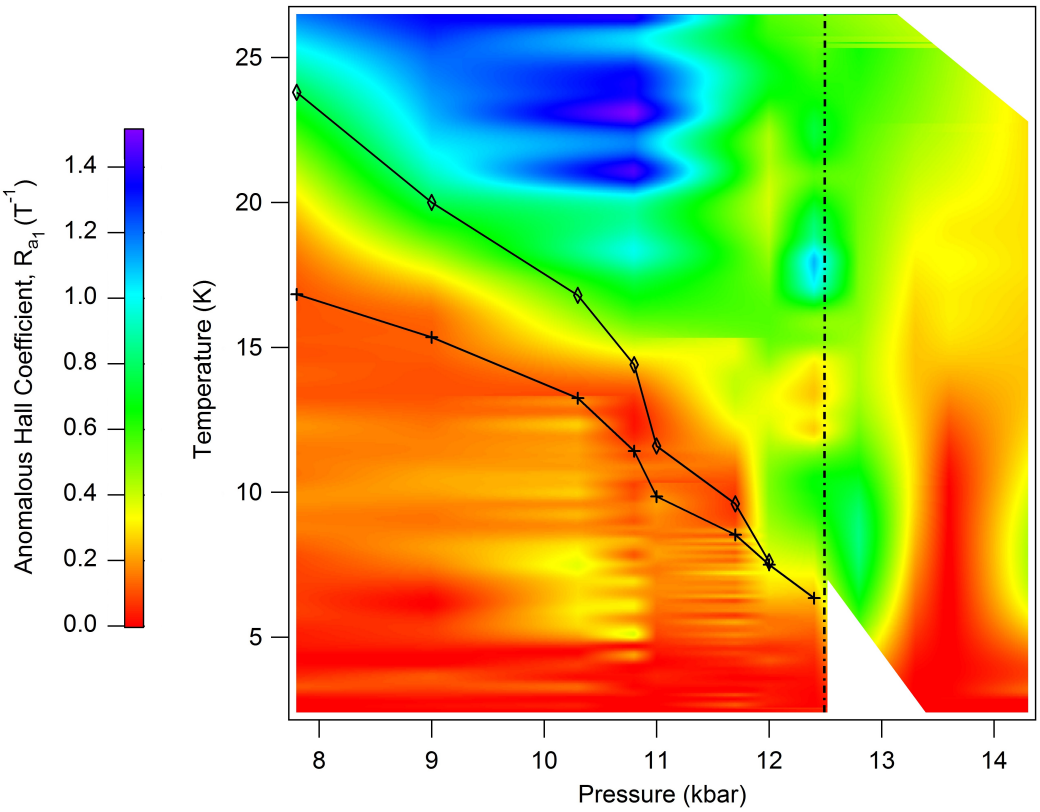

Figure 5.40 Colour plot of the anomalous Hall coefficient R_{a_1} as a function of temperature and pressure, created by linear interpolation between discrete pressure values. The T_X and P_X phase lines from figure 5.14 have been overlaid. White triangles have been used to blank areas of unreliable data.

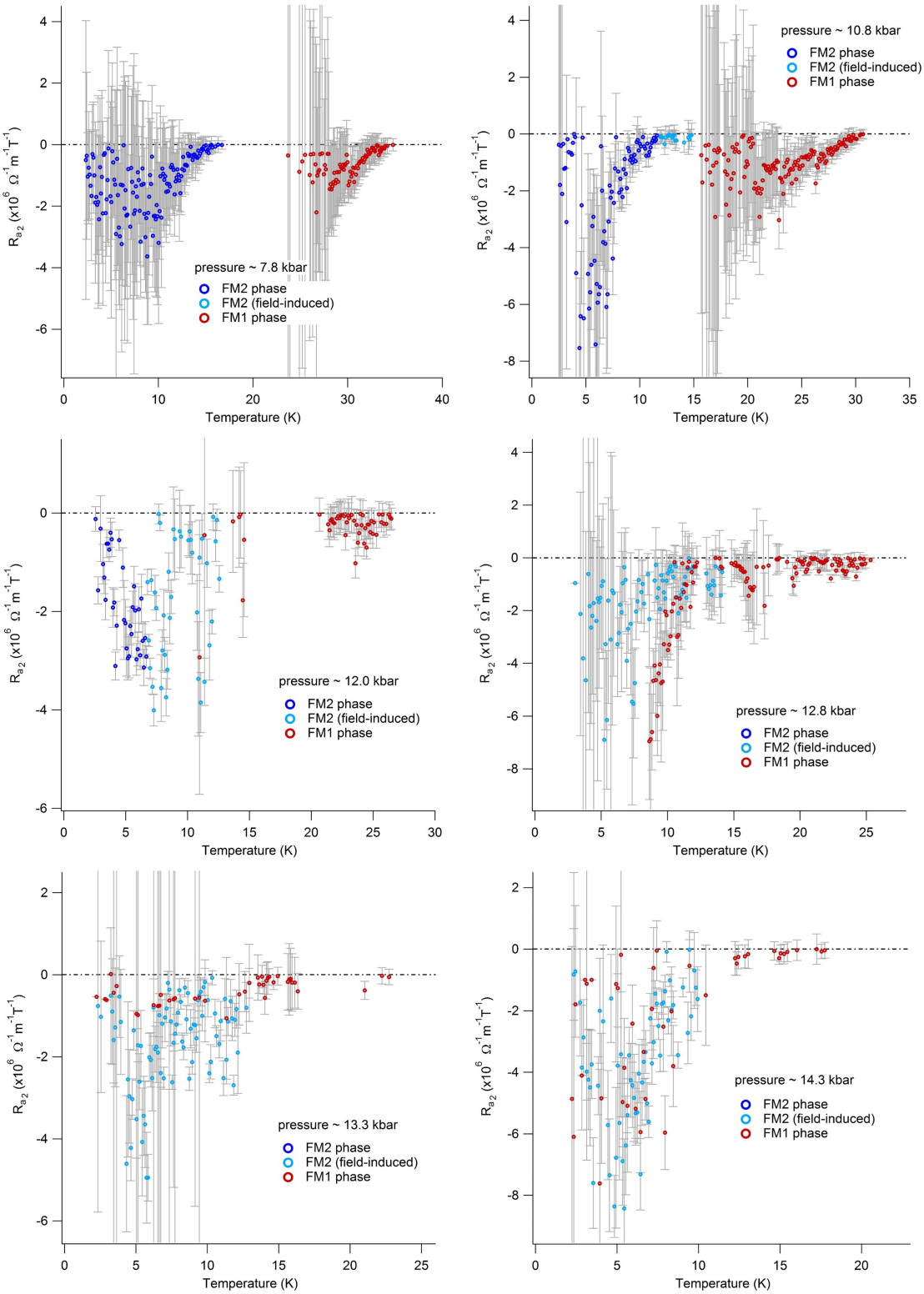

Figure 5.41 The anomalous Hall coefficient R_{a_2} as a function of temperature up to T_C for a variety of pressures, three below P_X and three above. At low pressure, above T_X the field induced FM2 phase is shown in addition to the low field FM1 data.

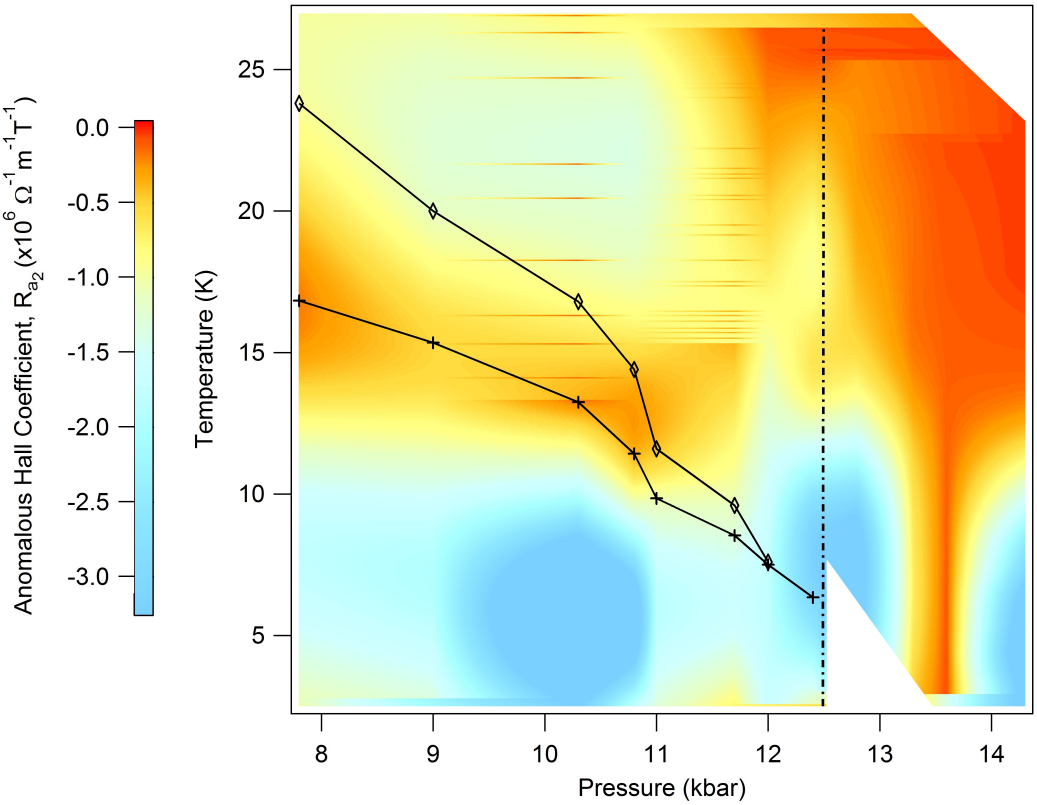

Figure 5.42 Colour plot of the anomalous Hall coefficient R_{a_2} as a function of temperature and pressure, created by linear interpolation between discrete pressure values. The T_X and P_X phase lines from figure 5.14 have been overlaid. White triangles have been used to blank areas of unreliable data.

From the preceding graphs it is difficult to contrast the coefficients R_{a_1} and R_{a_2} and gauge whether or not either can be generally disregarded in order to speculate on which mechanism(s) might be primarily responsible for the AHE.

In section 5.4 it was found that, for the case study of 2 K and 10.3 kbar, neither term of the anomalous Hall coefficient dominated. By observation of the data presented in figure 5.18 it initially appeared that the linear-in-ρ_{xx} term was substantially larger than the ρ_{xx}-squared term, but that analysis was based on various shaky assumptions and the result not very robust.

The full fit to equation 5.2, using real magnetization data and making no assumptions, provided more reliable results. The magnitudes of the three terms of the total Hall resistivity determined by this method, at 2 K and 10.3 kbar, were compared in figure 5.20 and it was seen that the ordinary Hall effect was larger than the anomalous, and that the two AHE terms were reasonably similar in magnitude.

The two terms were also found to have opposite sign, with the linear-in-ρ_{xx} term negative and the ρ_{xx}-squared term positive. Since the latter had a slightly larger magnitude than the former, the anomalous Hall resistivity was negative overall, and combined with the negative ordinary Hall resistivity resulted in a negative total Hall resistivity, as expected.

Observation of figure 5.3 reveals that this cannot always be the case, however, since the Hall resistivity quickly becomes positive as temperature rises. At higher field the ordinary Hall effect, directly proportional to the field, is larger and so the total Hall resistance has a greater negative contribution, but even at 9 T the Hall resistivity becomes positive above about 12 K.

At this pressure, 12.0 kbar, the ordinary Hall coefficient remains negative across the whole temperature range, therefore it must be the total anomalous Hall resistivity that becomes positive at higher temperature. Thus, in contrast to the 2 K result, at higher temperature the linear-in-ρ_{xx} term of the AHE must become larger than the ρ_{xx}-squared term.

This trend is far from obvious in the colour plots of R_{a_1} and R_{a_2} presented in figures 5.40 and 5.42. To properly compare their respective contributions to the anomalous Hall resistivity the coefficients need to be scaled by the longitudinal resistivity. For simple comparison, the zero-field resistivity was used for this purpose, rather than attempting to add a third dimension (magnetic field) to the

resulting pressure-temperature graphs.

'Term 1' and 'term 2' of the anomalous Hall resistivity, the coefficients R_{a_1} and R_{a_2} multiplied by ρ_{xx} and ρ_{xx}^2 respectively, are shown in figures 5.43 and 5.44 respectively.

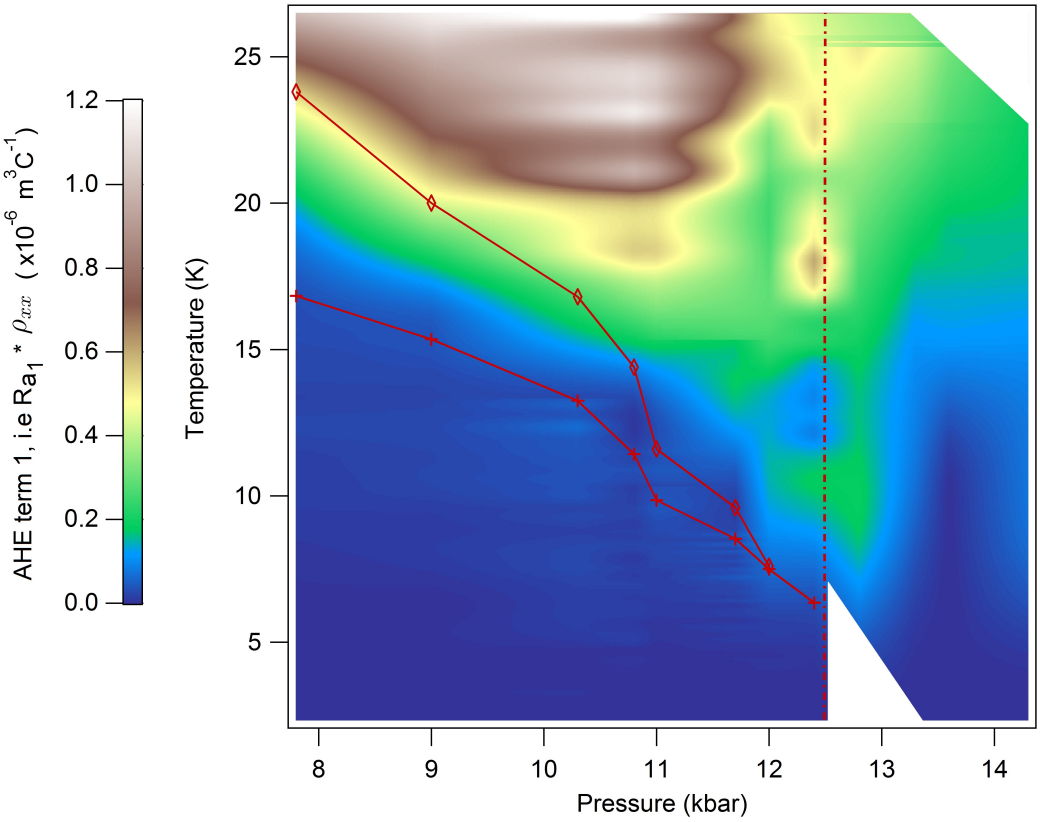

Figure 5.43 Colour plot of the anomalous Hall coefficient R_{a_1} multiplied by the zero-field resistance, a quantity called 'term 1', as a function of temperature and pressure, created by linear interpolation between discrete pressure values. The T_X and P_X phase lines from figure 5.14 have been overlaid. White triangles have been used to blank areas of unreliable data.

Both terms are small below $\sim$10 K but increase rapidly with temperature. The steepest increase at low temperature occurs at pressures near P_X and at 10 K, for instance, there is a peak in both R_{a1} and R_{a2} at the critical pressure (although this is not sustained to higher temperatures where the lower pressure values become much larger much faster).

This behavior might be expected in the region above a quantum critical point. Typically–for a conventional, antiferromagnetic QCP at least–the temperature dependence of the resistivity above a QCP has a lower power than the usual temperature-squared dependence of the Fermi liquid, a phenomenon often

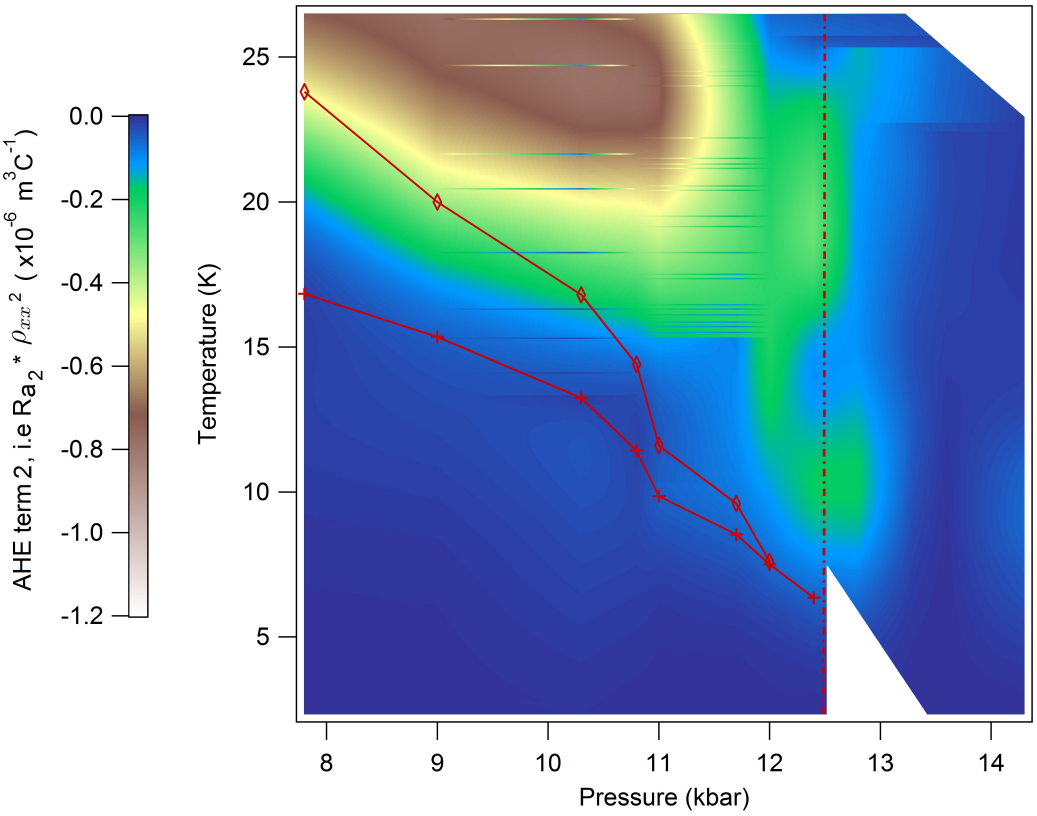

Figure 5.44 Colour plot of the anomalous Hall coefficient R_{a_2} multiplied by the zero-field resistance squared, a quantity called 'term 2', as a function of temperature and pressure, created by linear interpolation between discrete pressure values. The T_X and P_X phase lines from figure 5.14 have been overlaid. White triangles have been used to blank areas of unreliable data.

referred to as 'non Fermi-liquid behaviour'. This behaviour can be attributed to additional electron scattering from spin fluctuations, such as spin density waves, which can result in the emergence of superconductivity as described in section 2.6.

Hence the behaviour of the anomalous Hall coefficients immediately above the QCP in UGe_2 is very interesting, in regards to being indirect evidence of the spin fluctations potentially responsible for superconductivity.

It is still difficult from these plots to compare the magnitudes of the two terms, though the colour scales of each have been set to the same range in order to aid in comparison. At high temperature 'term 1' is clearly larger than 'term 2' across the entire pressure range, as expected, but judging the difference between the two colour plots at lower temperatures by eye is not really possible.

The difference in magnitude between the two terms, i.e. term 1 + term 2, is

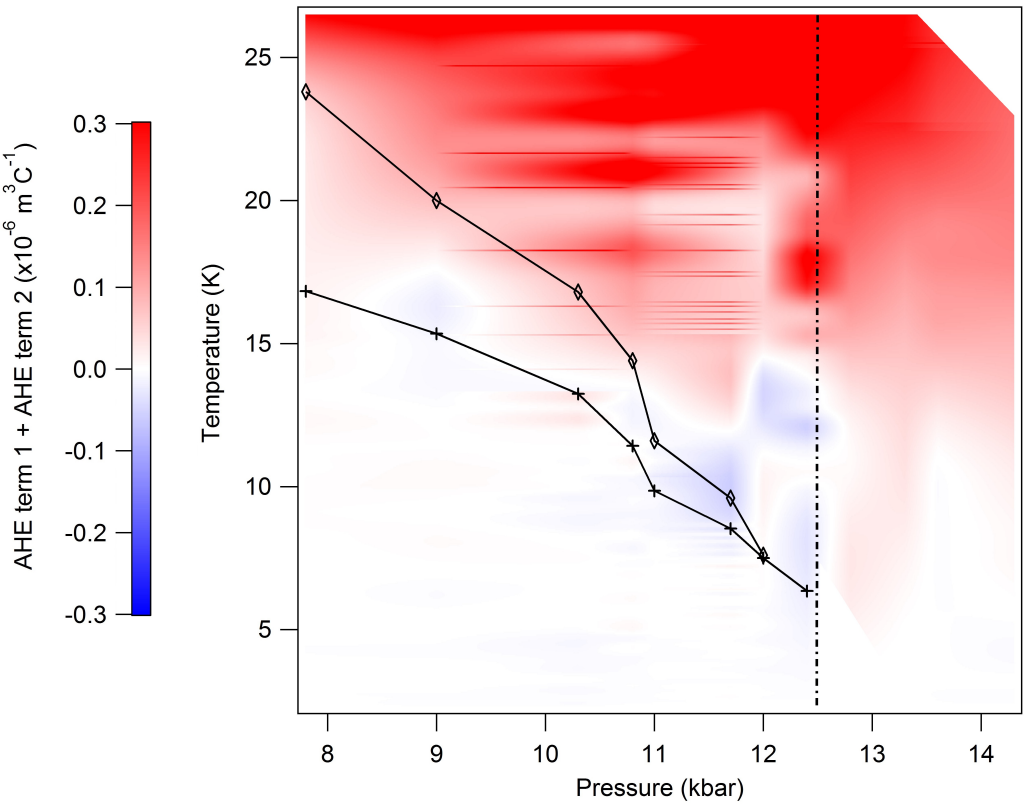

Figure 5.45 Colour plot of the difference between 'term 1' and 'term 2' of the anomalous Hall resistivity, as a function of temperature and pressure, created by linear interpolation between discrete pressure values. Since term 2 is negative, the difference is given by term 1 + term 2. The T_X and P_X phase lines from figure 5.14 have been overlaid. White triangles have been used to blank areas of unreliable data.

plotted in figure 5.45. This colour plot shows a white region, corresponding to approximately zero, across the entire FM2 phase, suggesting that the two contributions to the anomalous Hall resistivity are roughly equal, at least in comparison to the big difference between them at higher temperatures.

This result collaborates well with the conclusion from observation of figure 5.20, which showed that although term 2 was slightly larger than term 1 at 10.3 kbar and 2 K, both terms were small and roughly the same magnitude.

At higher temperature term 1 is clearly much greater than term 2, though the question remains whether or not the ρ_{xx}-squared term can be neglected. In order to see if term 2 is truly negligible, and if term 1 could be said to be dominant, and so skew scattering described as the dominant cause of the anomalous Hall resistivity, the ratio term 1 / |term 2| is plotted is figure 5.46.

The colour scale for this plot was chosen such that there is a transition from blue to green when the two terms are equal. Where term 2 is actually greater than term 1, the colour plot is blue, and where term 1 is the larger of the two, the plot is green. Regions where term 1 dominates are brown and white, although this only occurs at high pressure approaching the Curie temperature, which is where all this analysis breaks down.

For most of the plot, even the high temperature regions identified in figure 5.45 as where the linear-in-ρ_{xx} contribution to the AHE was the largest, term 1 is only about twice that of term 2. Unfortunately, this is far from high enough to justify disregarding the ρ_{xx}-squared term from the anomalous Hall resistivity and simplifying the interpretation of the effect.

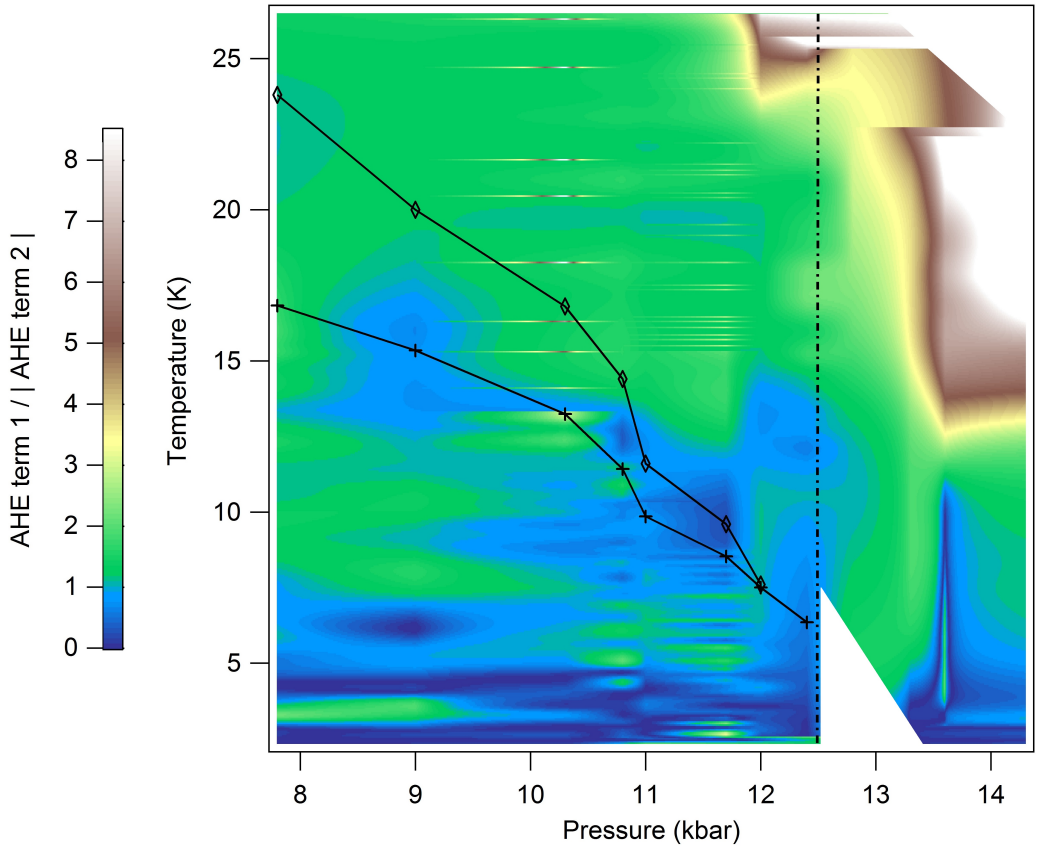

Figure 5.46 Colour plot of the the ratio of the two terms of the anomalous Hall resistivity, i.e.term 1 / |term 2|, as a function of temperature and pressure, created by linear interpolation between discrete pressure values. The T_X and P_X phase lines from figure 5.14 have been overlaid. White triangles have been used to blank areas of unreliable data. The colour scale was chosen such that if term 2 is greater in magnitude than term 1, the region is coloured blue. At higher temperatures, term 1 is mostly about twice the size of term 2, coloured green.

Chapter 6

URhGe Torque Magnetometry Results and Discussion

6.1 Zero-Field Resistance

The resistance of the primary sample of URhGe used for the torque magnetometry project was first measured from room temperature to 1.8 K in a helium-4 refrigerator system. The low temperature behaviour is shown in figure 6.1. At higher temperatures a slight increase in resistance is observed upon cooling, rather unusually for a metal, although this behaviour has been seen in previous resistivity measurements (in-house on other, bar-shaped samples) and suggests that current is applied predominantly in the a or c axis direction. The placement of the chosen voltage and current contacts was very roughly aligned to the a-axis, aiming to apply current transverse to the magnetic field regardless of the rotator platform orientation.

There is a sudden change of slope at 9.80 K, the Curie temperature, indicating the onset of ferromagnetism. The sample was subsequently measured in the dilution refrigerator between 1200 and 20 mK. The resistivity abruptly drops to zero at 255 mK when the sample becomes superconducting. Just above this temperature, around 350 mK, there is a small step in resistivity of roughly 10 % of the normal state value.

This could indicate that the sample is somewhat inhomogeneous and of varying purity, with a small region of higher quality material, with higher superconducting

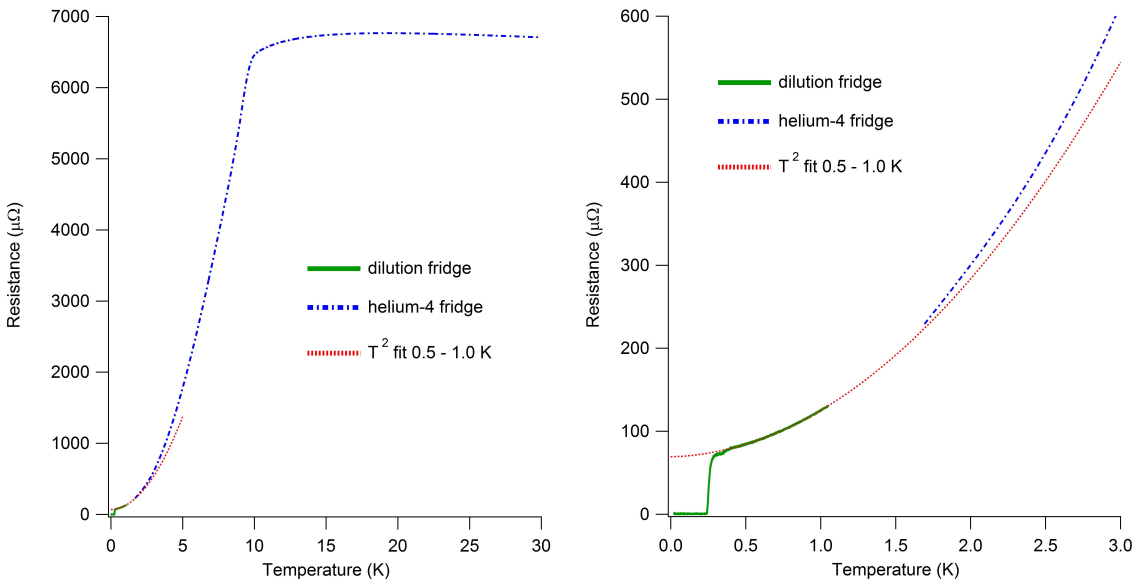

Figure 6.1 **Left:** URhGe resistance as a function of temperature in the absence of field, demonstrating a change in slope around 9.8 K, the Curie temperature, and superconductivity below 255 mK. **Right:** Low temperature close-up showing the superconducting transition in more detail and a small step in resistance around 350 mK. The T^2 fit works well at low temperature but noticeably poorly above about 1.5 K.

transition temperature, mixed in with the marginally lower quality bulk. This seems unlikely though, since there have been no reports of samples with superconducting transitions temperatures as high as 350 mK. Alternatively it could be evidence of surface or domain wall superconductivity, with a higher critical temperature than the bulk.

A T^2 fit to the data between 2 and 3 K gives a residual resistivity ratio (RRR) of several hundred, though the fit is not very good and this value cannot be taken as accurate. As discussed in section 2.1 the RRR provides a quick, rough measure of sample purity but relies upon proper extrapolation of the resistivity data to 0 K, usually by way of a fit to the Fermi liquid theory formula $\rho(T) = \rho_0 + AT^2$.

The poor T^2 fit from 2 to 3 K suggests that phonon (or possibly magnon) scattering is still making a significant contribution to the resistivity, even at these low temperatures. A much better fit is found below 1 K, to about 0.5 K, below which the emergence of superconductivity begins to influence the behaviour of the resistance.

Since the resistance is measured between irregularly placed contacts on the sample surface it is difficult to accurately calculate the resistivity, particularly since

URhGe is a highly anisotropic material. Instead an inverse length scale λ can be defined, with units m^{-1}, such that resistance $R = \lambda\rho$. Then the Fermi liquid formula becomes $R(T) = R_0 + (\lambda A)T^2$, which can be fitted to the experimental data.

Values of $\lambda A = 40{\times}10^{-6}\,\Omega\,K^{-2}$ and $R_0 = 0.086\,\mu\Omega$ are found as fitting parameters, giving a RRR of 98, which for URhGe suggests a sample of high purity, as does the relatively high superconducting transition temperature.

6.2 Finding The $\phi = 0$ Position

As a consequence of the sample mounting technique (detailed in section 4.2) it was necessary to rotate the sample relative to the applied field $\mu_0\vec{H} \simeq \vec{B}$ in order to bring the b-axis parallel to the field. The required $\sim 30°$ rotation from the vertical platform position was known in advance from the Laue diffraction measurements. A basic capacitance and resistance measurement at roughly 34° shows the expected behaviour for $B \parallel b$-axis alignment, as seen in figure 6.2. The characteristic features are a sudden fall in capacitance at 12 T due to the moment rotation transition, when the magnetization becomes parallel to the field, and the region of high-field superconductivity indicated by the zero-resistance state between 8 and 13 T.

Other notable features are an apparent low frequency oscillation in the resistance above 13 T and the evident hysteresis in the resistivity below the high-field superconductivity. Slight hysteresis is also observed in the capacitance. These additional features will be described in more detail later.

Further capacitance measurements were then used to determine the $B \parallel b$-axis rotation angle with much greater precision, a precision necessary due to the large changes in magnetic behaviour with rotation close to $B \parallel b$-axis alignment. The change in capacitance with field, $\Delta C(B)$, is directly proportional to the magnitude of the sample magnetization perpendicular to the field (as detailed in section 2.5) and at low field the magnetization is directed along the easy axis, the c-axis.

Thus it might be expected that at perfect $B \parallel b$-axis alignment the c-axis would be exactly perpendicular to the field and the capacitance would be at a maximum. The domain structure of the ferromagnet, however, means that at perfect $B \parallel b$-

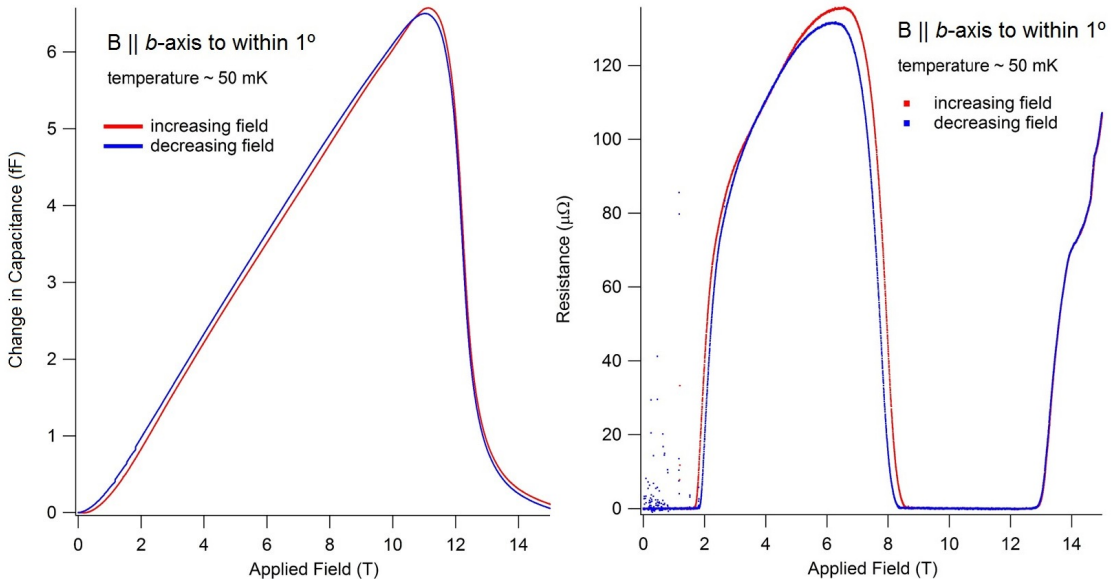

Figure 6.2 **Left:** The base temperature capacitance measured by the digital AH bridge instrument as a function of field, relative to the zero-field value, at a sample platform rotation of roughly 34° from vertical. There is a sudden fall to zero around 12 T due to the magnetic moment rotation transition. **Right:** The resistance measured simultaneously with the capacitance, showing the two regions of superconductivity, with critical fields 2, 8 and 13 T.

axis alignment there is no significant field applied in the easy axis direction to break the symmetry of parallel and anti-parallel moments to the c-axis, and the net magnetization is actually zero.

The actual maximum in net magnetization is expected at $B \parallel c$-axis alignment, where the field swiftly establishes a mono-domain state and increasing field then further strengthens the ferromagnetic moment. However, the perpendicular-to-field component of this large net magnetization would be zero and so ΔC at this rotation would also be zero. A few degrees rotation from $B \parallel b$-axis alignment might therefore be expected to give the maximum ΔC, at moderately low field strength, where there is sufficient field parallel to the c-axis to break up the domain structure and strengthen the moments but the resultant net magnetization remains mostly perpendicular to the field.

At this particular angle, increasing field strength increases the magnetic torque on the net moment and forces it to rotate away from the c-axis and toward the field direction, thus decreasing the perpendicular projection of the magnetization vector while at the same time further increasing its absolute magnitude. At higher fields the balance between these two effects will determine the angle of maximum ΔC. This discussion is essentially captured in figure 6.22 which, empirically, puts

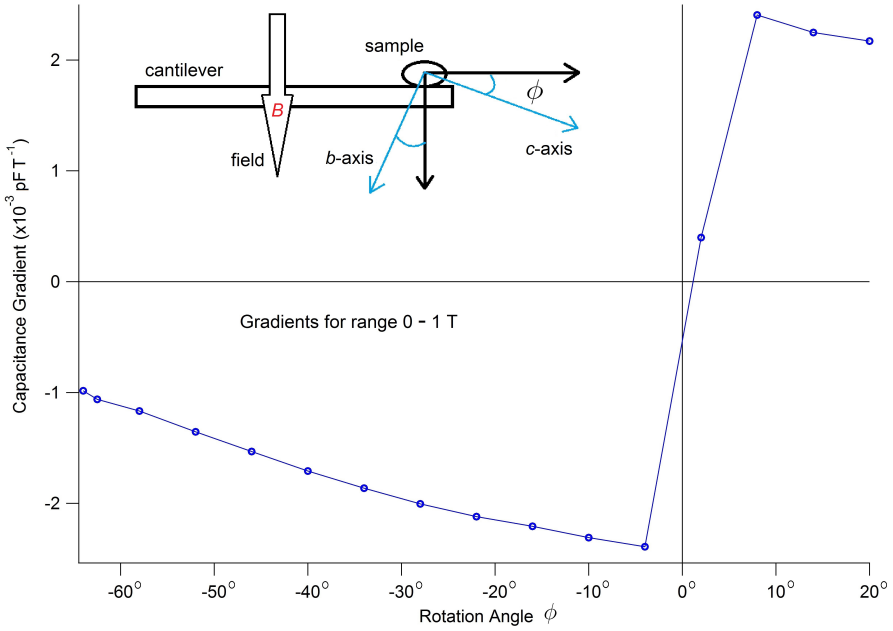

Figure 6.3 The gradient of the capacitance against field over the first 1 T, allowing the zero-crossing point to be determined, which gives the sample platform rotation angle at which $B \perp c$-axis and effectively $B \parallel b$-axis. The angle that ϕ refers to is indicated in the sketch in the upper left corner; variations in ϕ are the result of rotating the cantilever relative to the field, which is always vertical.

the rotation angle of maximum perpendicular moment somewhere between 6 and 9 degrees.

In summary, the behaviour at comparatively low fields, where the moment rotation effect is small, is comparatively easy to understand. The change in capacitance will gradually increase approaching $B \parallel b$-axis alignment, as the mono-domain magnetization becomes increasingly perpendicular to the field, until there is too little field in the direction of the easy axis to prevent the formation of domains and at perfect $B \perp c$-axis alignment ΔC is expected to be zero.

This idea is encapsulated by figure 6.3, where the zero point on the 'Rotation Angle ϕ' axis corresponds to a sample platform rotation of about 34° from vertical, as expected from the Laue diffraction data. The exact $\phi = 0°$ position corresponds to perfect $B \perp c$-axis alignment, and all rotation angles are henceforth quoted as relative to that position unless otherwise stated.

At small angles around the platform rotation of 34° from vertical, the capacitance across the full field range allows an even more precise determination of $\phi = 0°$. Although, as discussed above, the high-field behaviour of the perpendicular component of magnetization is complicated when a few degrees from $\phi = 0°$, for

a very close alignment of $B \perp c$-axis it becomes simple.

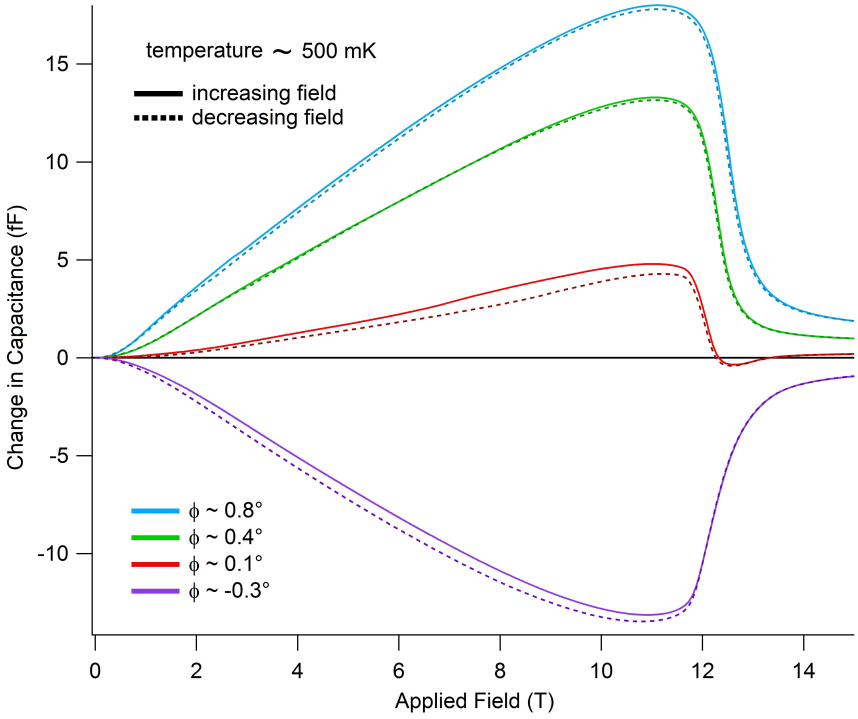

Figure 6.4 The capacitance, relative to the zero-field value, as a function of field for a few small rotation angles around the $B \parallel b$-axis position, as measured by the AH bridge. Even for the smallest angle the capacitance is not zero across the entire field range, as would be the case for a perfectly balanced domain structure, but instead crosses zero in several places. This is due to a small a-axis misalignment.

Even at high fields there is insufficient field strength parallel to the easy axis to fully rearrange the domain structure and produce a large net moment perpendicular to the field, and as the field increases the moment rotates away from the perpendicular easy axis anyway. Then at the metamagnetic transition the easy axis becomes the b-axis and the moment discontinuously rotates to align with it, further decreasing any perpendicular-to-field component. Thus at exactly $\phi = 0°$ the capacitance change should be approximately zero across the entire field range.

A quick look at figure 6.4 reveals that this is evidently not the case, although ΔC does indeed decrease dramatically as the $\phi = 0°$ position is approached. It can be seen that the data for the smallest rotation angle not only deceases to zero at the moment rotation transition but actually changes sign. This is because of a slight mis-alignment of the b-c plane with respect to the plane of the vertically applied magnetic field and the rotator platform normal. The Laue diffraction data shows a degree or two of a-axis misalignment after sample mounting, meaning that

the b-c plane is tilted such that alignment $B \perp c$-axis does not necessarily imply $B \parallel b$-axis, as would be ideal.

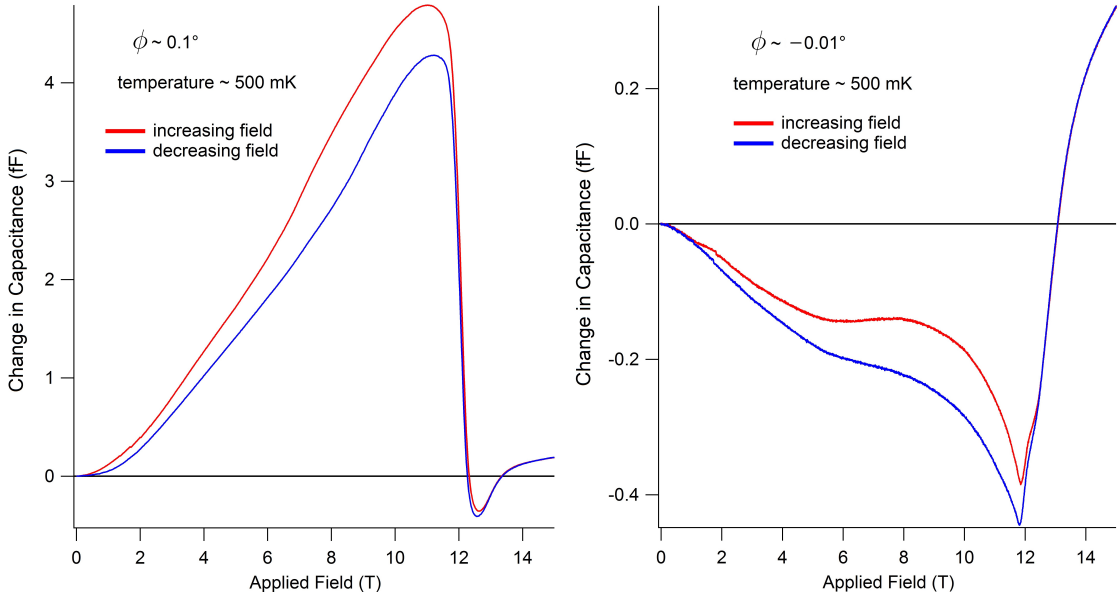

Figure 6.5 **Left:** The capacitance, relative to the zero-field value, as function of field for $\phi \sim 0.1°$. **Right:** The same for $\phi \sim 0.01°$. In both cases there is significant hysteresis below the metamagnetic transition field, and a sign change above. Note that the magnitude of ΔC decreases roughly linearly with ϕ at these tiny angles.

Fortunately the a-axis is magnetically hard compared to both the b and c axes and so there are no significant effects of this slight mixing in of an a-axis component, other than the resulting inability to perfectly align $B \parallel b$-axis from measurements of the perpendicular-to-field component of magnetization. The practical effects of the tilting of the b-c plane are mitigated somewhat by the experiment design, however, since the cantilever cannot twist easily, and so is only sensitive to the particular cross product of moment and field that produces a torque that bends the lever in the expected manner.

That being said, when all other effects have been tuned, by extremely small rotations, to an absolute minimum at the $\phi = 0°$ position, even the mitigated influence of the slight sample mounting misalignment becomes a significant factor. The capacitance measured at $\phi \sim 0.1°$ and $\phi \sim -0.01°$ is shown in figure 6.5.

An important observation to make regarding the $\phi \sim -0.01°$ case is the scale of ΔC compared to that seen in figure 6.4. Typically ($\phi > 2°$) the maximum change in capacitance, at around 11 T, is roughly 20 fF. At $\phi \sim -0.01°$ the maximum change is only about 0.4 fF, and would seem essentially zero if plotted on the

same graph as data from larger rotation angles.

Another important observation to make is the obvious hysteresis in the capacitance measurement at fields below the moment rotation transition. Hysteresis is typically associated with a first-order transition. At low fields there is a c-axis domain structure, up until the transition, when the domain walls shift and the structure destroyed. Decreasing field back through the transition re-assembles a domain structure, though with a larger net moment, as evidenced by the larger magnetic torque and so larger ΔC value, for the $\phi \sim -0.01^\circ$ data at least. The opposite appears to have occurred in the $\phi \sim 0.1^\circ$ case.

This opposite behaviour may be due to the fact that the $\phi \sim -0.01^\circ$ case is, very slightly, a negative rotation angle. This fact is simply deduced from the capacitance measurement, by the observation that the change in capacitance at low field is negative rather than positive, and not from any measured platform rotation. When performing the rotation an angle as close as possible to $\phi = 0^\circ$ was aimed for and the slight negative value was unintentional.

Regardless of intention, the result is potentially very illuminating. The positive value of ΔC observed at the highest fields is evidently unaltered by the change in sign of the rest of the measurement, and the increasing field data appears to be consistently higher in capacitance than the decreasing field data, leading to the opposite hysteresis behaviour observed in the two graphs in the magnitude of ΔC.

These differences are presumably due to the influence of the a-axis misalignment; the unchanging positive values of ΔC above the moment rotation transition confirms the reality of the tilted b-c plane and the impossibility of ever rotating to a perfect $B \parallel b$-axis alignment.

6.3 Resistivity Measurements

Having determined the exact $\phi = 0°$ position a detailed rotation study could then be performed, measuring resistivity and capacitance simultaneously. The resistivity measurements will be presented here first.

As well as the $\Delta C = 0$ condition, the resistivity also provides a method for determining the $\phi = 0°$ position, or more accurately the platform rotation corresponding to $B \parallel b$-axis, which as mentioned in the previous section is technically not quite the same thing. It is expected that at $B \parallel b$-axis the high-field superconductivity will emerge at the lowest field of any rotation angle, with a broad range, returning to the normal state just after the moment rotation transition, which will also occur at the lowest possible field. The sample resistance as a function of field, at the base temperature of the dilution fridge, for a broad range of rotation angles is shown in figure 6.6.

It can be seen that the high-field superconductivity is only present within about 5° of $\phi = 0°$ and is strongly angle dependent. The low-field superconducting transition has a weaker angle dependence, though is still noticeably anisotropic, B_{SC_1} reaching a maximum at $\phi \simeq 0°$.

At base temperature of the dilution fridge quantum oscillations in the resistivity are easily recognisable by eye above 10 T, for angles less than roughly 25° and greater than 6°, below which the high-field superconductivity masks them. These quantum oscillations are investigated in more detail in the next section.

The angle dependence of the high-field superconductivity is examined more closely in figure 6.7. There is more structure to the curves than simply sharp transitions in and out of superconductivity against a background of gradually increasing magnetoresistance. There are kinks entering the superconducting state, most noticeably at $\phi \sim 0.5°$ and 3.0°, followed by features (in the data at the smallest angles at least) around 14 T upon exit.

These 14 T features may be due to magnetic breakdown and the resulting low frequency quantum oscillations, as described in Ref. [28]. They may also be due to sample inhomogeneities, as mentioned earlier when discussing figure 6.1 and the transition temperature of the zero-field superconductivity, T_{SC1}. In fact the same kind of feature can be seen in B_{SC_1} as well as T_{SC_1}, for high data-density measurements at low field, a few examples of which are shown in figure 6.8.

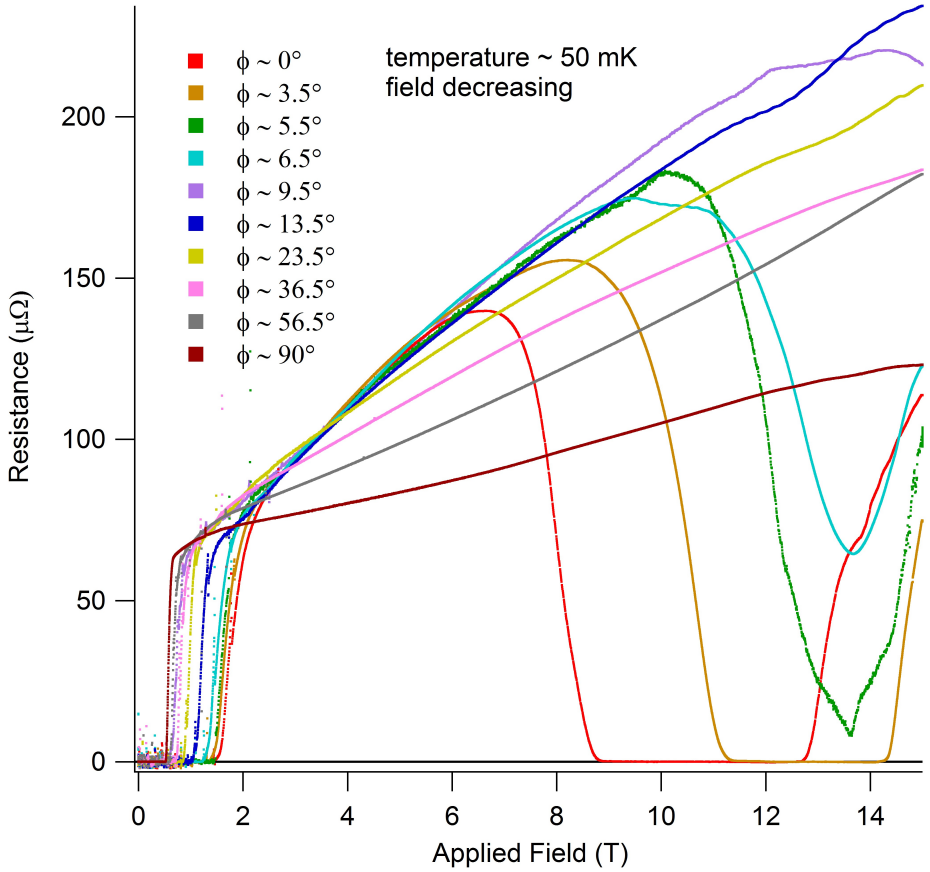

Figure 6.6 The URhGe sample resistance as a function of field, at the fridge base temperature, for a range of rotation angles from 0 to 90°. At small angles superconductivity re-emerges at high field. The high field superconductivity disappears around $\phi \sim 5°$. Quantum oscillations are clearly visable at 13.5° where the magnetoresistance also reaches a maximum, before falling to a minimum at $B \| c$-axis at $\phi \simeq 90°$.

Increasing the temperature dramatically changes the resistivity, first destroying the low-field and then the high-field superconductivity. Figure 6.9 shows the resistance as a function of field at $\phi = 0°$ for various temperatures between fridge base and 1 K.

Just above the high-field superconducting transition temperature, at 450 mK, there are nevertheless signatures of a reduced resistance state around the moment rotation transition field, B_R, in addition to a peak in the resistivity directly at the transition. At 600 mK the influence of nearby superconductivity seems to be gone, leaving only the peak at B_R. The state above the transition field, with the b-axis as easy axis, appears to have generally lower resistance than the state below B_R .

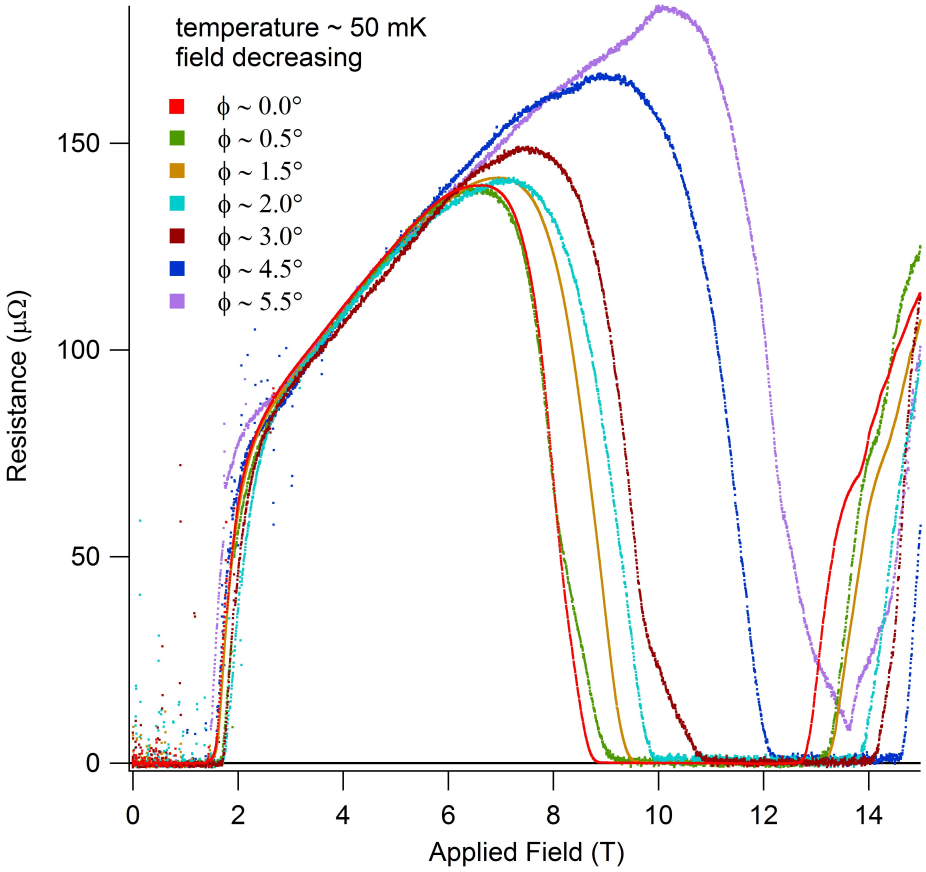

Figure 6.7 The URhGe sample resistance as a function of field, at the fridge base temperature, for a range of rotation angles from 0 to 5.5°. The initial superconducting transition field is weakly anisotropic, showing little variation from just under 2 T, but the re-entrant superconductivity at high field is highly angle dependent. There is additional structure to the data while entering and exiting the high field superconductivity.

As for the previous few figures, the behaviour of the curves while entering and exiting superconductivity is interesting too. For example, the 250 mK curve shows structured variations between 7 and 9 T. More specifically, around 7.5 T there is a slight suppression of the resistance, a feature which can be followed across the range of plots, at increasingly higher field for higher temperature.

At lower temperatures, there is also a repeated kink entering high-field superconductivity, just before the zero-resistance state is reached, and the aforementioned slow variations around 13 to 14 T, possibly due to quantum oscillations and magnetic breakdown.

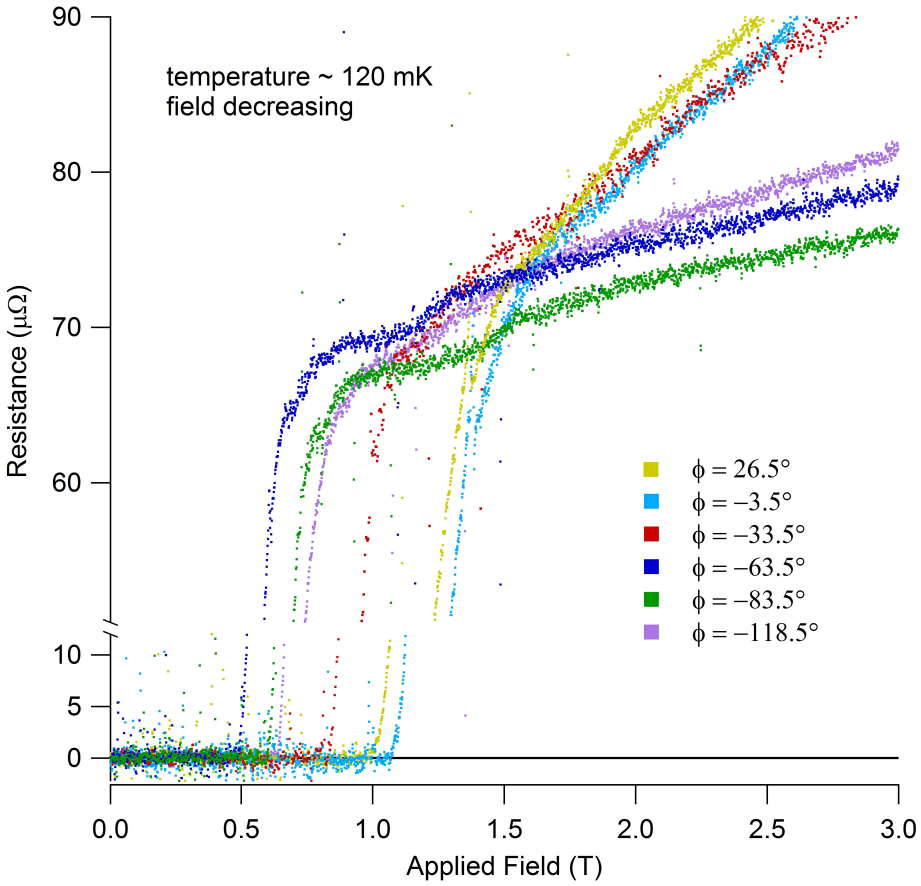

Figure 6.8 The resistance at low field at around 120 mK, showing mostly data from the 'negative' rotation direction, which as expected demonstrates similar behaviour to the usual 'positive' rotation angles. Of particular interest are the $-63.5°$ and $-83.5°$ rotations, which show a two-step exit from superconductivity similar to that observed in the temperature ramp. The same feature is also present at smaller angles, such as in the 26.5° data, though is more difficult to see due to the greater gradient of the resistance with field. Note that the y-axis of this graph has a split range in order to show both the superconducting state and the fine detail in the normal state.

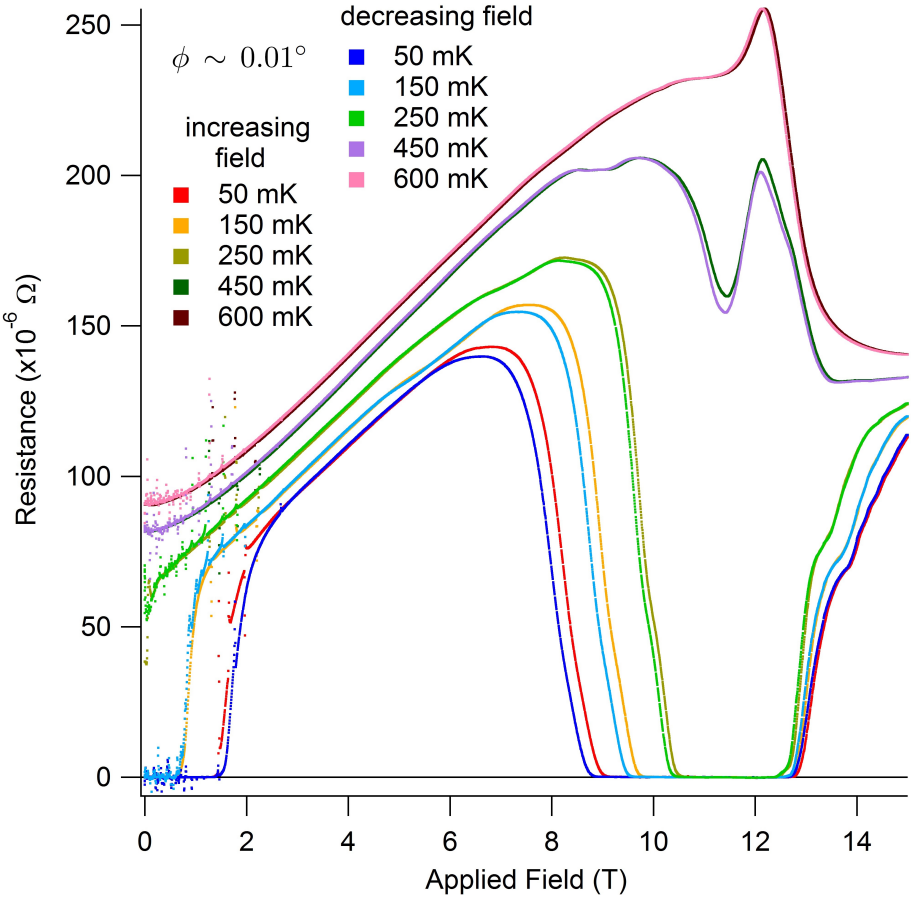

Figure 6.9 The resistance as a function of field at the $\phi = 0°$ position, at a variety of temperatures, showing the evolution of the data from the superconducting to the normal state as temperature is increased. Of specific interest are the number of features in addition to the simple transitions in and out of superconductivity, most notably the peak in the resistance at the moment rotation transition.

6.4 Non-Ohmic Behaviour

It is possible that the extra structure seen around the superconducting transitions is evidence for superconductivity other than that found in the bulk of the sample, such as surface superconductivity or domain wall superconductivity.

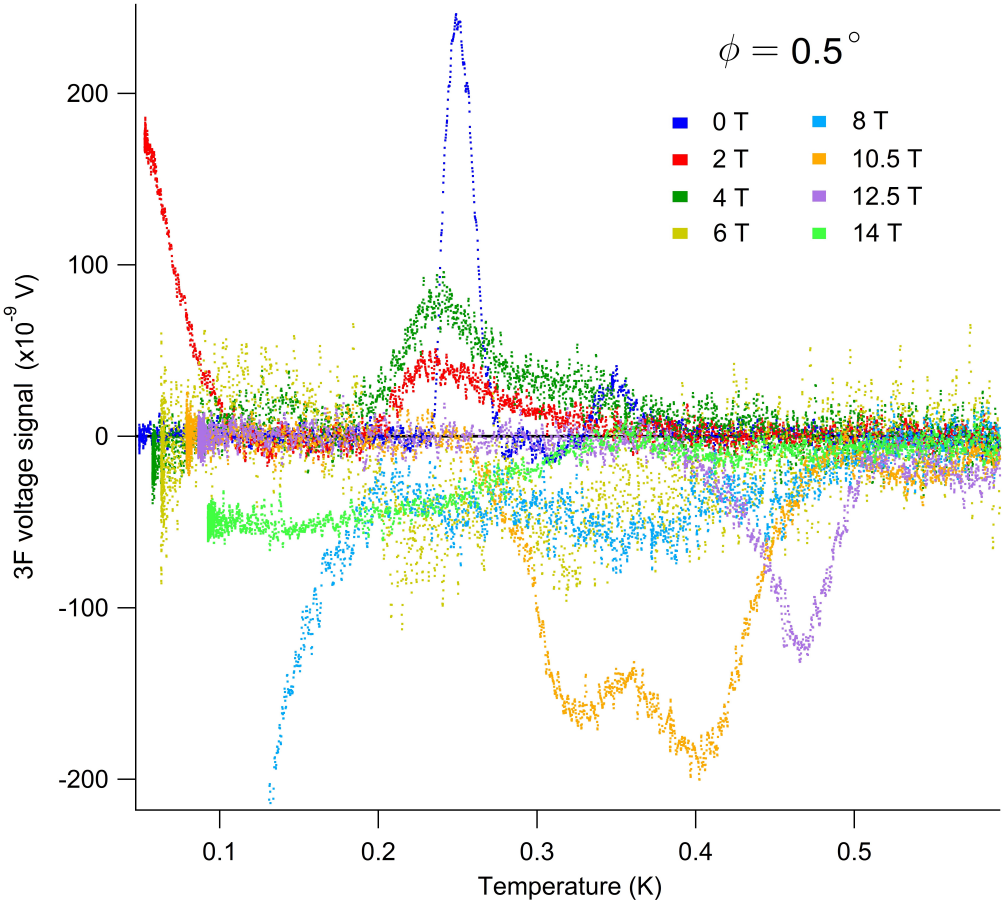

Figure 6.10 The 3F signal measured by the lock-in amplifier as a function of temperature for a variety of fields from 0 to 14 T. For a normal, Ohmic metal the 3F signal should be zero. Non-zero measurements are to be expected at a superconducting transition temperature.

One way that such a superconducting transition could be detected, if it was obscured by the much larger resistivity of the sample bulk, is to look for deviations of the usual linear current-voltage relationship, i.e. deviations from Ohm's law. Any deviations from a linear current-voltage relationship would show up as a departure from a single frequency measurement.

As discussed in section 4.5, the lock-in amplifier usually measures the fundamental harmonic, the voltage signal at the frequency of the applied current. Non-Ohmic

behaviour of this type reveals itself most clearly in the 3F signal, a harmonic at $3\times$ the frequency of the applied current. The 3F signal is normally zero, and although a significant 3F voltage might be expected around the superconducting transition temperatures there should be no 3F signal detected in-between the two regions of superconductivity (around 3 to 7 T) .

Figure 6.10 shows the 3F signal as a function of temperature for URhGe at $\phi = 0°$ at a variety of applied fields. At 0 T there is a large peak at 250 mK, the superconducting transition temperature, as expected. Similarly, at 12.5 T there is a large, negative peak at 450 mK, the highest transition temperature of the high-field superconducting region.

The behaviour of the 10.5 T curve is more interesting. The presence of a non-zero 3F signal is expected at this field, since it lies within the high-field region of bulk superconductivity, but the two peaks observed could be an indication of two different types of superconductivity: the lower temperature peak may indicate the superconducting transition of the bulk and the higher temperature peak may be related to the aforementioned surface or domain wall superconductivity.

The peak observed in the 4 T data is arguably the most intriguing, however, since according to the established phase diagram there is no superconductivity at that field and therefore no detectable transition temperature. The data at 2 T is also unusual: there is a large feature below 0.1 K indicating the transition from bulk superconductivity, but then, similar to the 4 T data, there is also a peak around 250 mK.

More detailed data between 3.5 and 8 T is shown in figure 6.11. At the lowest fields there is a peak at 250 mK, despite the absence of any bulk superconductivity. This peak appears to shift to higher temperature as field increases, moving toward the 450 mK transition temperature of the high-field superconductivity, apparently linking the two superconducting regions.

This might suggest that there is a single superconducting dome on the URhGe temperature-field phase diagram, rather that individual high and low field instances shown in figure 1.7, but that bulk superconductivity is suppressed in the region between the two occurrences. In this scenario the small-volume superconductivity probed by the 3F voltage signal would survive in the region in-between, up to a transition temperature defined by the larger superconducting dome.

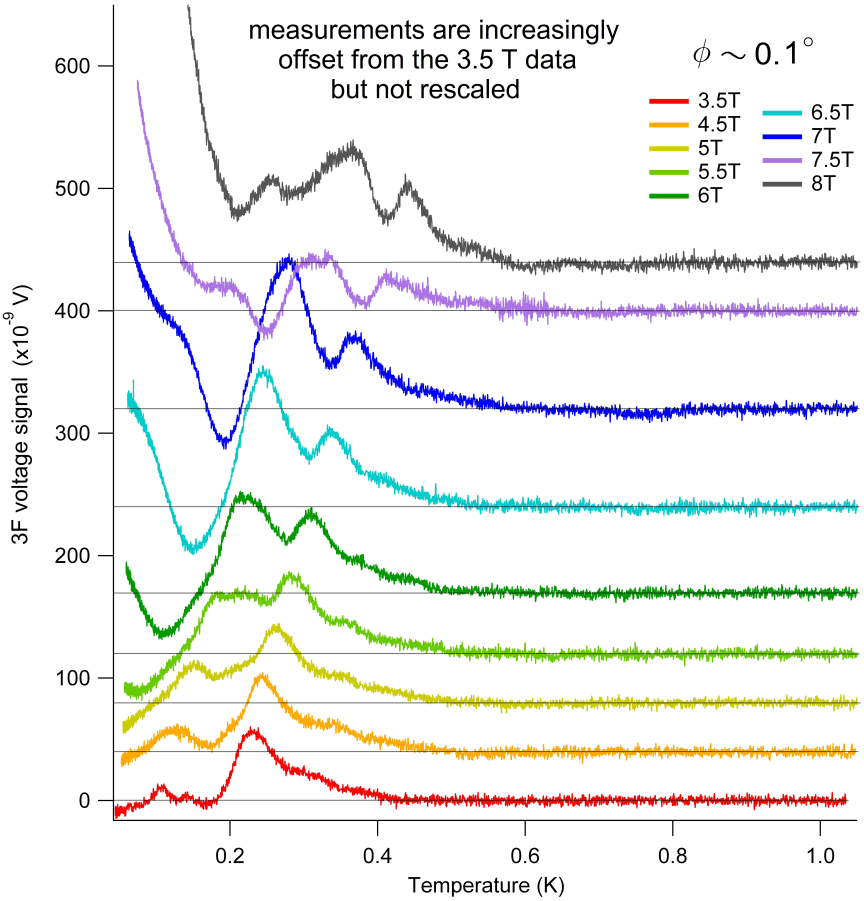

Figure 6.11 The 3F signal measured by the lock-in amplifier as a function of temperature for a variety of fields from 3.5 and 8 T, between the low and high field regions of bulk superconductivity. For a normal, Ohmic metal the 3F signal should be zero. Non-zero measurements are to be expected at a superconducting transition temperature.

Figure 6.11 contains further, puzzling details. An additional second peak emerges at lower temperature, most noticeably around 6.5 to 7 T where it becomes much larger than the higher temperature peak, but then seems to fade away at higher fields. There is no obvious explanation for this feature.

At the lowest temperatures a very large signal is observed at 8 T, presumably due to the influence of the high-field bulk superconductivity, which observation of figure 6.2 shows is indeed present at 8 T and 50 mK. It is however unclear why the feature extends to below 6 T, which should be far from the influence of either bulk superconducting region.

In conclusion, these measurements of the 3F signal provide more questions than answers, and further, more extensive work would be required to make sense of all of the features observed.

6.5 Quantum Oscillations

At fields above about 8 T quantum oscillations can be seen by eye in the resistance. The Shubnikov - de Haas (SdH) oscillations have very small amplitude, as expected for a heavy fermion material, and are only easily seen at the base temperature of the dilution fridge, though of course extend to lower fields and higher temperatures under closer scrutiny and careful data analysis.

SdH oscillations can be seen in some of the measurements presented in figures 6.6 and 6.7. For further analysis, and to make these tiny ripples more obvious, a smooth background curve was fitted to the data and then subtracted to leave just the oscillations. This residual data was then binned, and the averages interpolated to create a smoother wave. When primarily measuring quantum oscillations very slow field ramps were employed, ensuring a high density of data, ideal for binning.

The SdH oscillations are most clearly seen over the range of rotation angles presented in figure 6.12. In order to enhance the visual, the oscillation amplitude in this figure has been multiplied by 10 and the resulting wave superimposed onto the smoothly varying background curve.

At $\phi \simeq 6^\circ$ there is evidently strong influence from the superconducting state, fully entered at slightly lower angles, causing a large drop in resistance around B_R. At $\phi \simeq 8^\circ$ it is unclear if the undulating background resistance is due to another quantum oscillation frequency, a much lower one, or if the variation is also caused by the influence of nearby superconductivity. As previously mentioned, low frequency oscillations can be the result of very small Fermi surface orbits caused by magnetic breakdown.

At higher angles the SdH oscillation amplitude grows, reaching a maximum around $\phi \simeq 16^\circ$. At greater angles the onset of clear oscillations moves to higher fields and for measurements beyond $\phi \simeq 20^\circ$ fields greater than the usual maximum of 15 T must be applied.

SdH oscillations without the background resistance are shown to higher fields in figure 6.13, demonstrating a clear and consistent single frequency and also demonstrating the range of angles over which easily analysed oscillations are observed. At angles greater than $\phi \simeq 28^\circ$, where obvious oscillations begin only above 15 T, it becomes difficult to accurately measure SdH oscillations within the capabilities of the experiment equipment (in terms of base temperature and

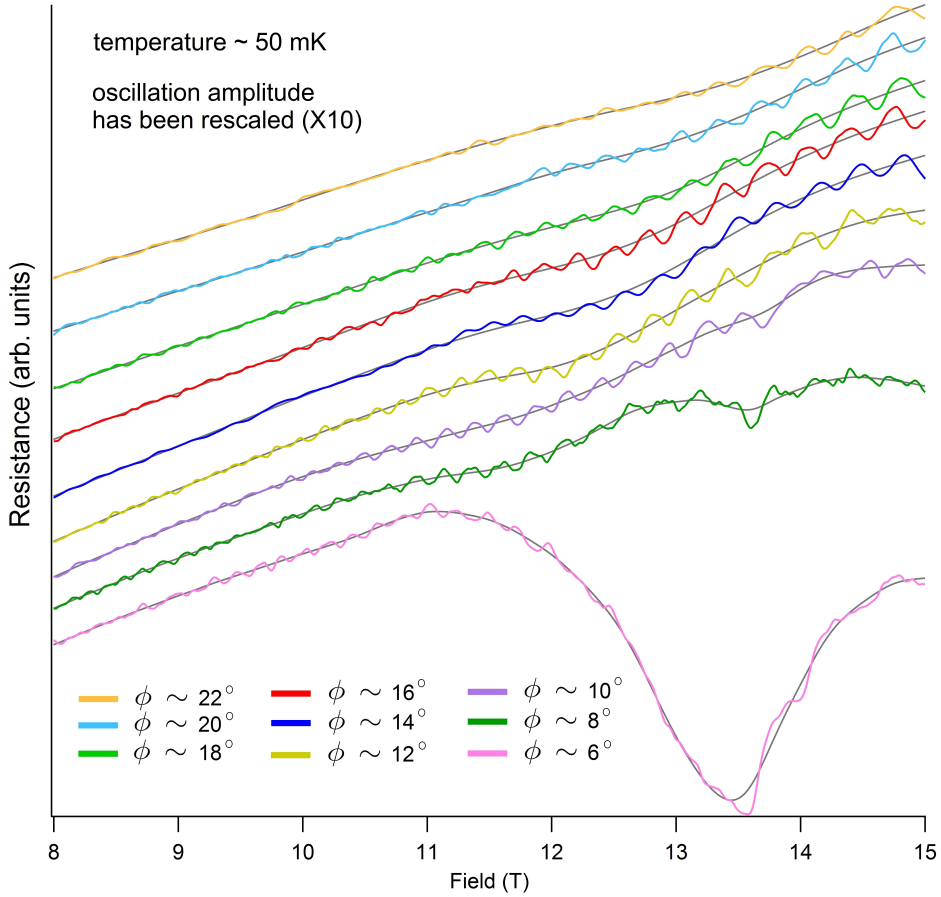

Figure 6.12 The resistance as a function of field, from 8 to 15 T, at the base temperature of the dilution refrigerator (∼50 mK), for a number of rotation angles between 8° and 22°. The quantum oscillations have been extracted from the raw data, fitted by a smoothing average, multiplied by 10, and then superimposed onto the smooth background curve fitted to the original data. The plots have been vertically spaced for clarity but not rescaled.

maximum field).

A notable feature in figure 6.13 is the decrease in amplitude of the oscillations at $\phi \simeq 10^\circ$ at high field, tailing off towards zero beyond about 16.5 T. This phenomenon has been studied in depth by Yellend *et al* in Ref. [48] and will be discussed briefly later in this section.

The Fourier transform of the data presented in figure 6.12, after re-plotting against B^{-1}, is shown in figure 6.14, focused on the single frequency observed at approximately 555 T. This frequency appears to be fairly constant as a function of angle.

Although these 555 T oscillations have been measured in URhGe previously, as

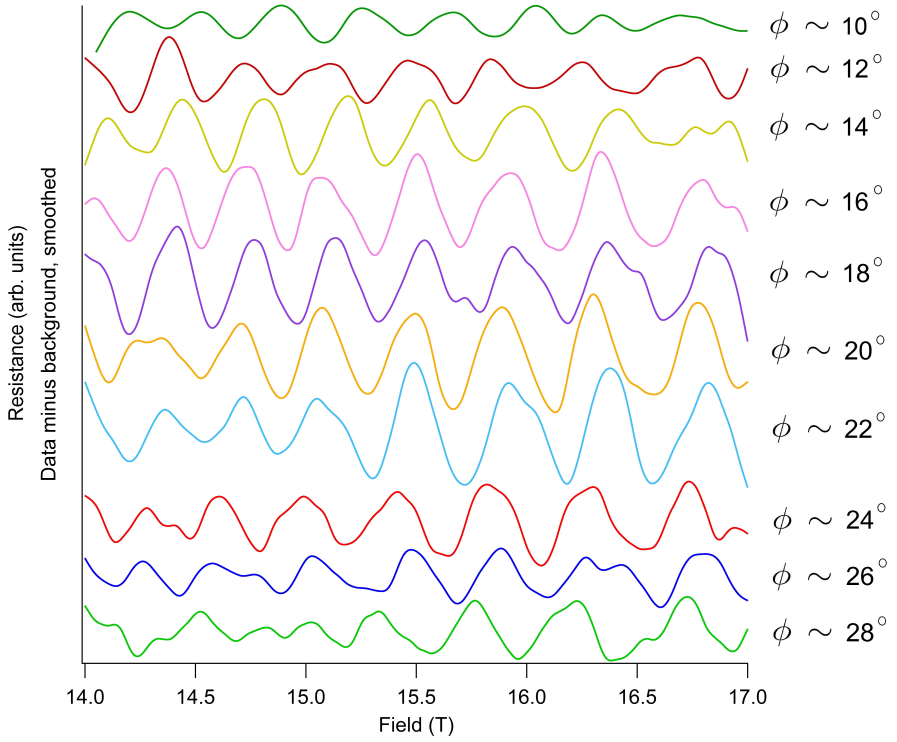

Figure 6.13 Shubnikov-de Haas oscillations between 14 and 17 T at the base temperature of the dilution refrigerator ($\sim$50 mK), for a number of rotation angles between 10° and 28°. A single frequency can be seen, unchanging with angle, which (after plotting against B^{-1}) corresponds to a frequency of 555 T.

presented in Ref. [48], the results of that study were based entirely on a single sample; no other samples measured at the time showed quantum oscillations, presumably due to insufficient purity. Observation of similar SdH oscillations in this project, at the same frequency, provides second-sample verification of the results of Ref. [48] and confirms that the conclusions of that study are not sample specific and can be attributed to the material in general. The SdH oscillations observed in this project are actually clearer than those seen previously, suggesting that the sample is of very high purity.

Rotating to $\phi = 90^\circ$ brings the field parallel to the c-axis and SdH oscillations of different frequencies can be seen, as presented in figure 6.15. There are two main frequencies detectable by eye, a very slow undulation in the resistance accompanied, more noticeably at lower temperatures, by a significantly higher frequency oscillation.

These $B \parallel c$-axis oscillations, while not entirely unobserved in previous studies, have never been characterised well, particularly the temperature dependence of their amplitude, which allows the determination of the effective electron masses.

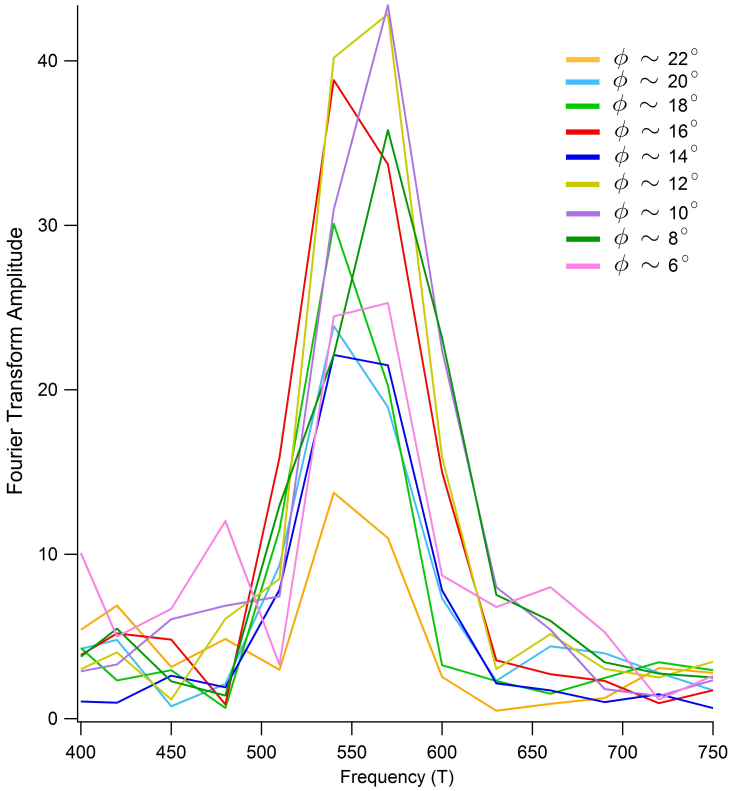

Figure 6.14 The Fourier transform of quantum oscillation data from 10 to 15 T, plotted against B^{-1}, for a number of rotation angles from 6° to 22°. The graph is focused on the frequency 555 T but there are no other oscillation frequencies with significant amplitude over the range 0 to 10,000 T.

Therefore, despite this experiment not being directly related to the main torque magnetometry project, these oscillations were measured extensively, at a number of different temperatures between the fridge base and about 200 mK.

The Fourier transform of this extended dataset reveals peaks at several different frequencies. The most obvious two are at 140 and 1215 T, the low and high frequency oscillations identifiable by eye. The broad peak between them is at 630 T and therefore not an obvious harmonic, unlike the peak at 280 T which is likely a second harmonic of the 140 T frequency. Further analysis of the *c*-axis quantum oscillation dataset is outwith the scope of this thesis, however.

In addition to SdH oscillations in the resistance it was hoped that de Haas - van Alphen (dHvA) oscillations might be observed in the capacitance, as a measure of magnetization. However, the torque magnetometer was primarily designed to measure the large changes in magnetization associated with the moment rotation transition, with a cantilever stiff enough to provide relatively small deflections even at the highest fields (the desirability of which is explained in section 2.5).

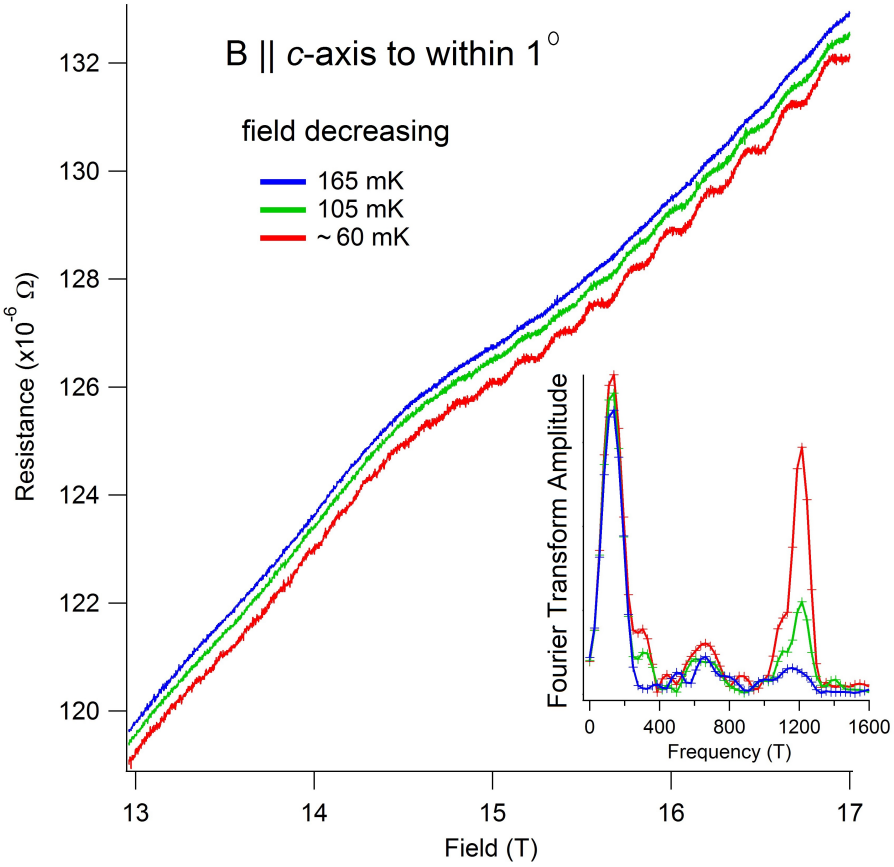

Figure 6.15 **Main:** The resistance as a function of field, for several low temperatures, for the high field range 13 to 17 T. The field is applied parallel to the c-axis. There are two obvious frequencies, one low, one high. The high frequency is very temperature dependent and is barely evident at the highest temperature. **Inset:** The Fourier transform of the same data, plotted against B^{-1}, showing three frequencies, around 100, 700 and 1200 T. The amplitudes of the lower two are relatively unaffected by the temperature over this range, but the amplitude of the higher frequency oscillation decreases dramatically as temperature increases, as expected from the main plot.

The capacitance measurement was therefore unavoidably insensitive to small variations in magnetization, making the detection of dHvA oscillations difficult.

An attempt to look for dHvA oscillations at $\phi \simeq 10°$ is demonstrated in figure 6.16. The residual data after a background subtraction, multiplied by some factor to amplify the effect, is superimposed onto the background capacitance curve in the same manner as in figure 6.12. Unlike in that figure however, where the amplifying factor was $\times 10$, here is is $\times 500$ because of the extremely small amplitude of any possible oscillations compared to the magnitude of the background.

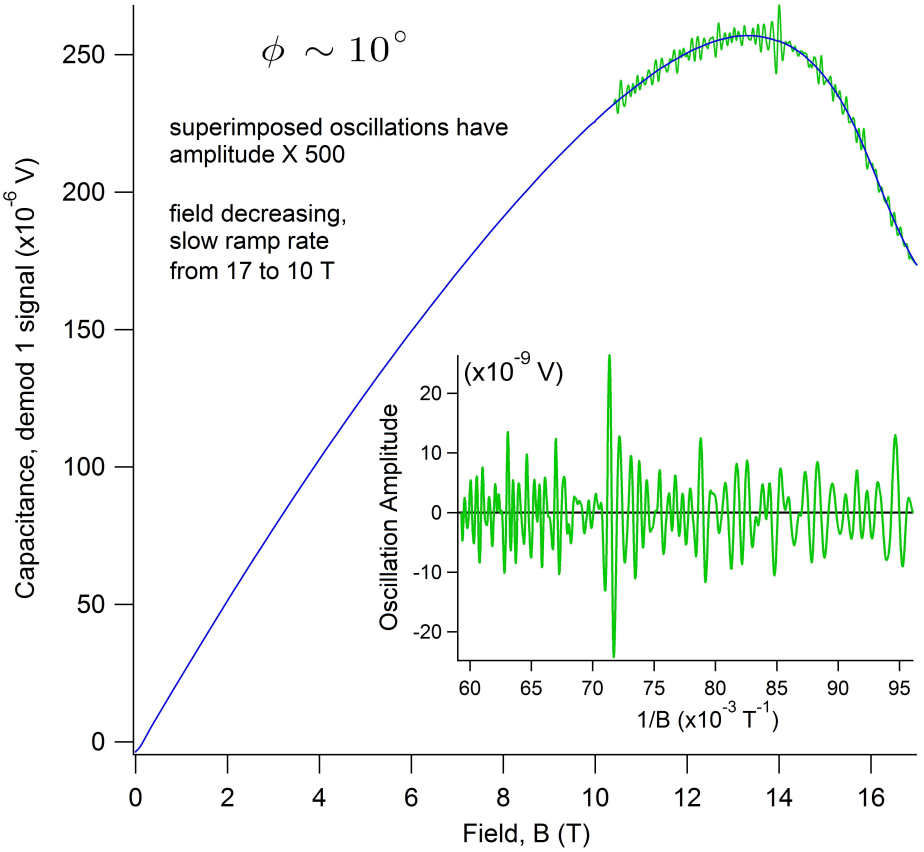

Figure 6.16 **Main:** The capacitance divided by the field, a quantity proportional to the magnetization, plotted as a function of field at roughly 50 mK and a rotation angle of 10°. A substantially slower field ramp rate, ensuring a high data density, was employed from 10 to 17 T. For this graph the residual data, after subtraction of a smooth background curve, has been multiplied by 500 and then superimposed onto the background, which is the plotted curve. **Inset:** The residual data, fitted by a smoothing average and plotted against B^{-1}. There appears to be no periodic variation, suggesting that this may merely be a plot of random experimental noise.

Although dHvA oscillations are should strictly be looked for in the magnetization, for simpler analysis the capacitance, directly proportional to the product of magnetization and field, should suffice. Conversion of the capacitance into some component of the magnetic moment will certainly alter the amplitude of the oscillations but the frequency will be unchanged and there would be no effect on the relative detectability of the oscillations above the noise level of the measurement.

The capacitance data from 10 to 17 T was analysed for some indication of periodic oscillations within the data scatter but no definite dHvA oscillations could be distinguished above the level of experimental noise. The sample platform

temperature was as low as possible, removing all sources of heating (including the thermometer excitation current), waiting at 17 T for 30 minutes, and then measuring while decreasing field to take advantage of the slight demagnetization cooling. The platform was likely around 50 mK at 17 T, decreasing to around 30 mK at 10 T.

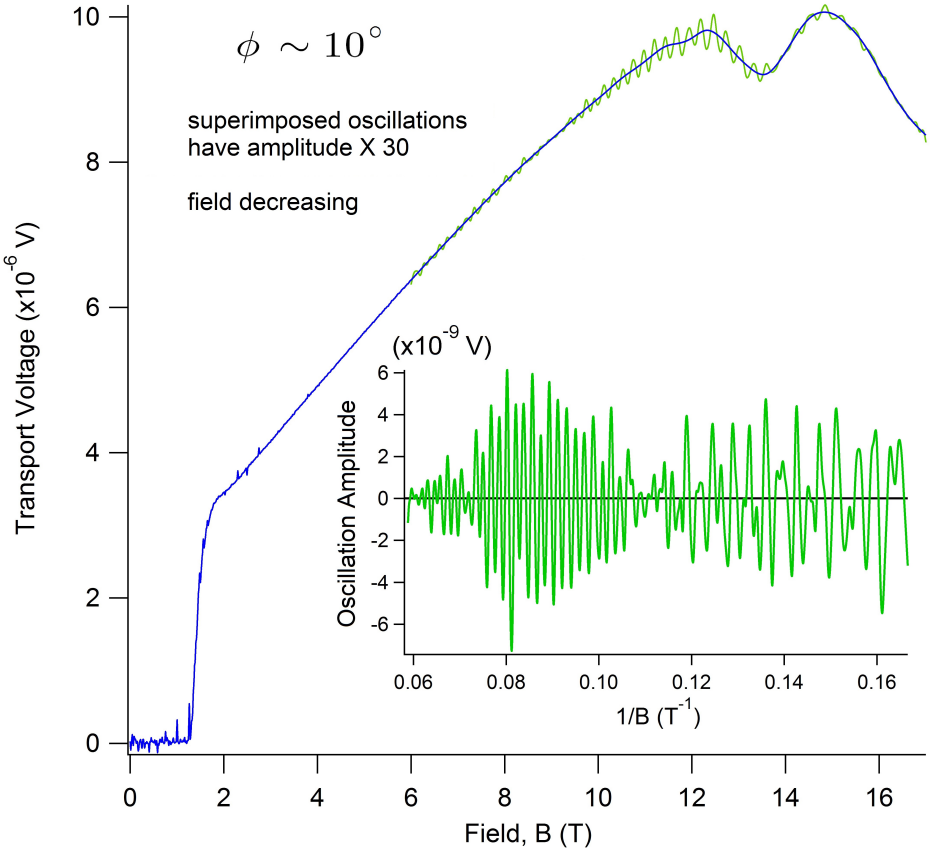

Figure 6.17 **Main:** The transport voltage as a function of field at roughly 50 mK and a rotation angle of 10°. A substantially slower field ramp rate, ensuring a high data density, was employed from 10 to 17 T. For this graph the residual data, after subtraction of a smooth background curve, has been multiplied by 30 and then superimposed onto the background, which is the plotted curve. **Inset:** The residual data, fitted by a smoothing average and plotted against B^{-1}. Clear oscillations are observed below about 0.11 T^{-1}.

Transport data taken simultaneously with the capacitance is shown in figure 6.17. Here the SdH oscillations are smooth and clear, easily analysed down to 6 T, and superimposed on the background with a much smaller amplifying factor of $\times 30$. The data shown in the inset of figure 6.17 is more obviously periodic than the apparently random fluctuations observed in the capacitance. The shape of the background curve is familiar from figures 6.6 and 6.7, which show the raw data and give an indication of the actual size of the oscillations.

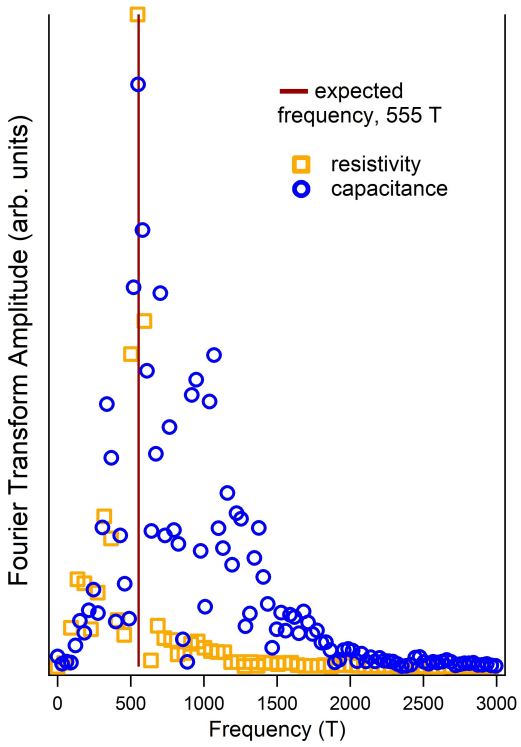

Figure 6.18 The Fourier transform of the magnetization and resistivity data presented in the insets of figures 6.16 and 6.17. The expected frequency of 555 T is marked. The Fourier transform amplitudes of both measurements are peaked at this frequency.

The Fourier transforms of the data shown in the insets of figures 6.16 and 6.17 are shown in figure 6.18, where the expected frequency of 555 T is marked. The resistivity data has a definite peak at this frequency, with very little amplitude at higher frequencies and the low frequency behavior common to Fourier transforms when trying to fit a smoothly varying background to complicated magnetoresistance curves.

The data from the capacitance, by contrast, returns relatively large Fourier transform amplitudes across a wide range of frequencies, from zero up to about 2000 T, suggesting that experimental noise overwhelms any clear quantum oscillations. The result of the Fourier transform is far from uniform, however, and does actually peak around 555 T, indicating that there might be dHvA oscillations right at the limit of detectability. Lower temperatures and/or higher fields would be required to perform any reasonable measurements, at least with the current experimental set-up (potential modifications to the experiment that could allow measurements of dHvA oscillations are discussed in section 7.2.1).

Finally, it is perhaps worth drawing attention to the inset of figure 6.17 and the

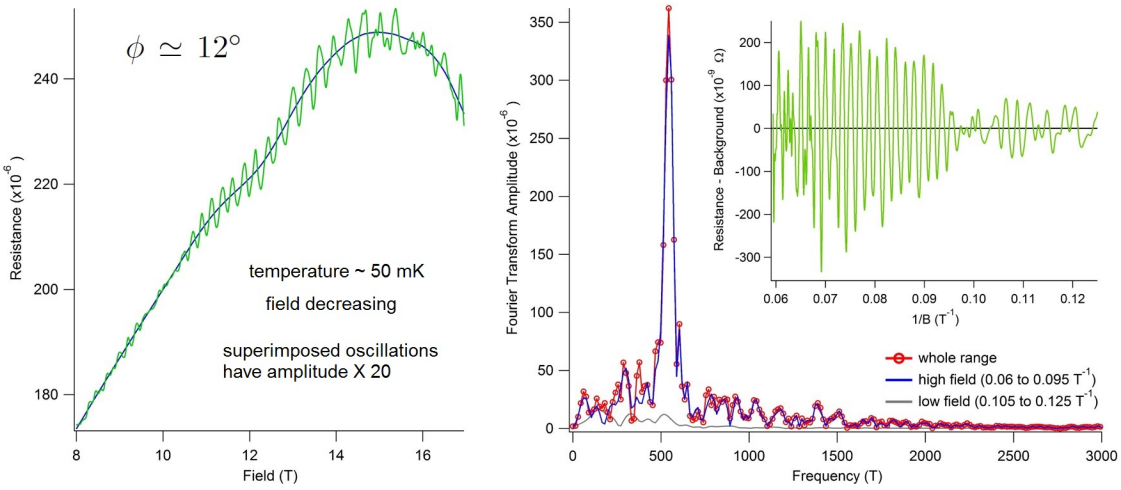

Figure 6.19 **Left:** The resistance as a function of field, from 8 to 17 T, at $\phi \simeq 12°$ and ~ 50 mK. For this graph the residual data, after subtraction of a smooth background curve, has been multiplied by 20 and then superimposed onto the background, which is the plotted curve. **Right:** The Fourier transform of the quantum oscillation data plotted in the inset as a function of B^{-1}. The peak amplitude is at 555 T as expected. Analysing only the data above 10 T results in very little change to the FFT, but analysing the data below 10 T results in a decease of the peak amplitude to almost zero, suggesting that quantum oscillations are not detected in this field range.

varying amplitude that is observed in the oscillations. Specifically, at just over 0.11 T^{-1} there is an apparent zero point, a node-like region, in the oscillations. This corresponds to about 9 T and can be seen in the data in the main figure.

There is also a dramatic decrease in amplitude at high field, above about 14 T (below 0.071 T^{-1}). This is expected, a consequence of the Lifshitz transition described in Ref. [48], concluding that the disappearance of the oscillation frequency is caused by the disappearance of the associated Fermi surface. However, the presence of the node-like region around 9 T suggests beat behaviour as a possible explanation, the effect of two distinct but close frequencies, their separation (which would be about 30 T here) giving the beat frequency.

This idea was explored further using transport measurements at $\phi \simeq 12°$, close to the $\phi \simeq 10°$ rotation but benefiting from a smoother background curve. The quantum oscillations and Fourier transform are shown in figure 6.19. There does indeed appear to be a low field node at this angle too, at a slightly higher field, around 10 T (0.1 T^{-1}).

For deeper analysis, separate Fourier transforms were performed for the range either side of the node at 10 T. The results show that there is an absence of

clear, periodic behaviour in the low-field data, and instead of a beat node 10 T would appear to simply be the field at which high amplitude oscillations suddenly emerge from the background noise of the experiment.

The same analysis was performed, in greater detail, for the $\phi \simeq 10^{\circ}$ quantum oscillations and the conclusions are essentially the same. The decrease in amplitude observed above 14 T in figure 6.17 thus provides support for the Lifshitz transition scenario previously reported.

6.6 Capacitance Measurements

For the majority of rotation angles the capacitance measurements are uninteresting, merely showing a slightly sub-linear increase with field. The torque would give perfectly linear $\Delta C(H)$ if m_{0x} was constant but as field increases the net perpendicular magnetization will decrease due to the gradual rotation of the moment. This decrease is mitigated by the increase in the *magnitude* of the moment, however, and the gradient of capacitance with field is determined by the balance between the two effects.

Empirically, looking at the plots in figure 6.20, it can be seen that, away from the influence of the metamagnetic transition, the rate of increase of the magnitude of the moment is less than the rate of decrease due to its rotation, leading to the sub-linear behaviour observed.

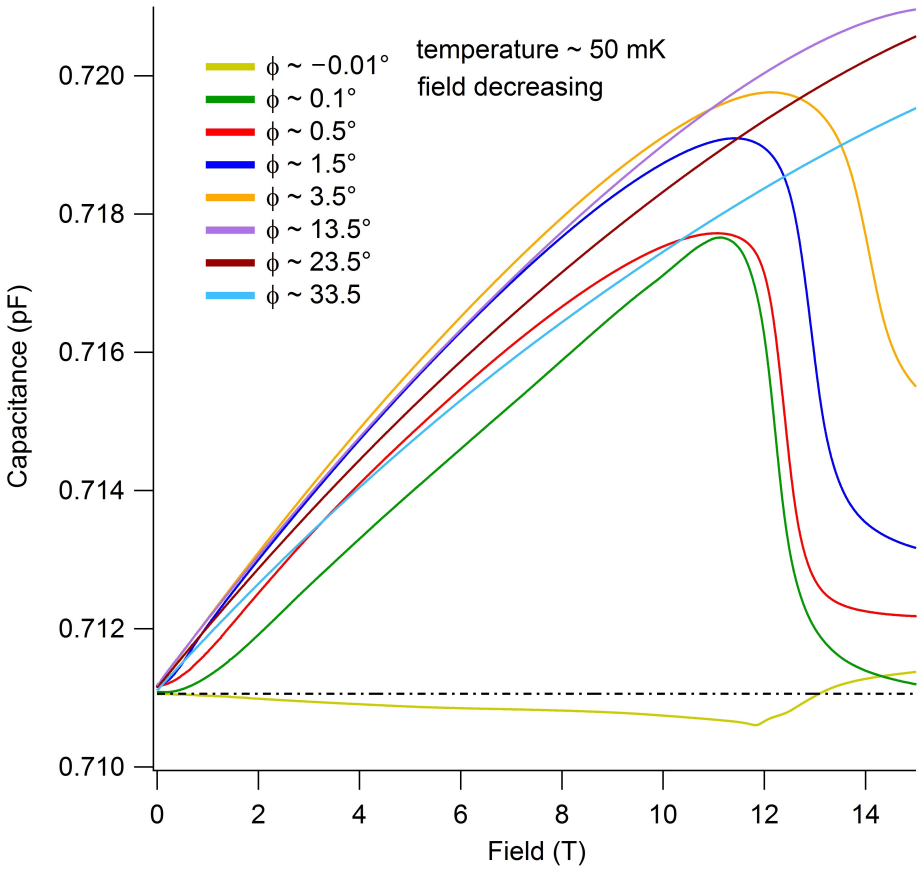

Figure 6.20 The capacitance as a function of field, measured with the AH bridge instrument, for a wide range of rotation angles, at dilution fridge base temperature. The stated angles are correct to within 0.5°, except for the lowest two, which are $0.1° \pm 0.05°$ and $-0.01° \pm 0.01°$.

Rotating to small ϕ and approaching the moment rotation transition, the expected drop in capacitance is observed at high fields, becoming an abrupt fall to $\Delta C = 0$ at $\phi \sim 0.1°$. The data for small angle rotations about this point has already been seen in figure 6.4.

The capacitance appears to have very little dependence on temperature, with no detectable changes between the low temperature superconducting state and the normal state at higher temperature. In contrast to the resistance at $\phi \simeq -0.01°$ shown in figure 6.9, the capacitance at the same rotation angle can be seen in 6.21 and demonstrates only slight variation with temperature.

As temperature increases the magnitude of the ferromagnetic moment decreases slightly due to thermal disorder, thus slightly decreasing the ΔC value, though the changes from base temperature to 600 mK are smaller in magnitude than the magnetic hysteresis. Although the hysteresis is generally small as an absolute value, at this rotation angle it appears large relative to the magnitude of ΔC, which is tiny compared to other measurements at $\phi > 0.1°$.

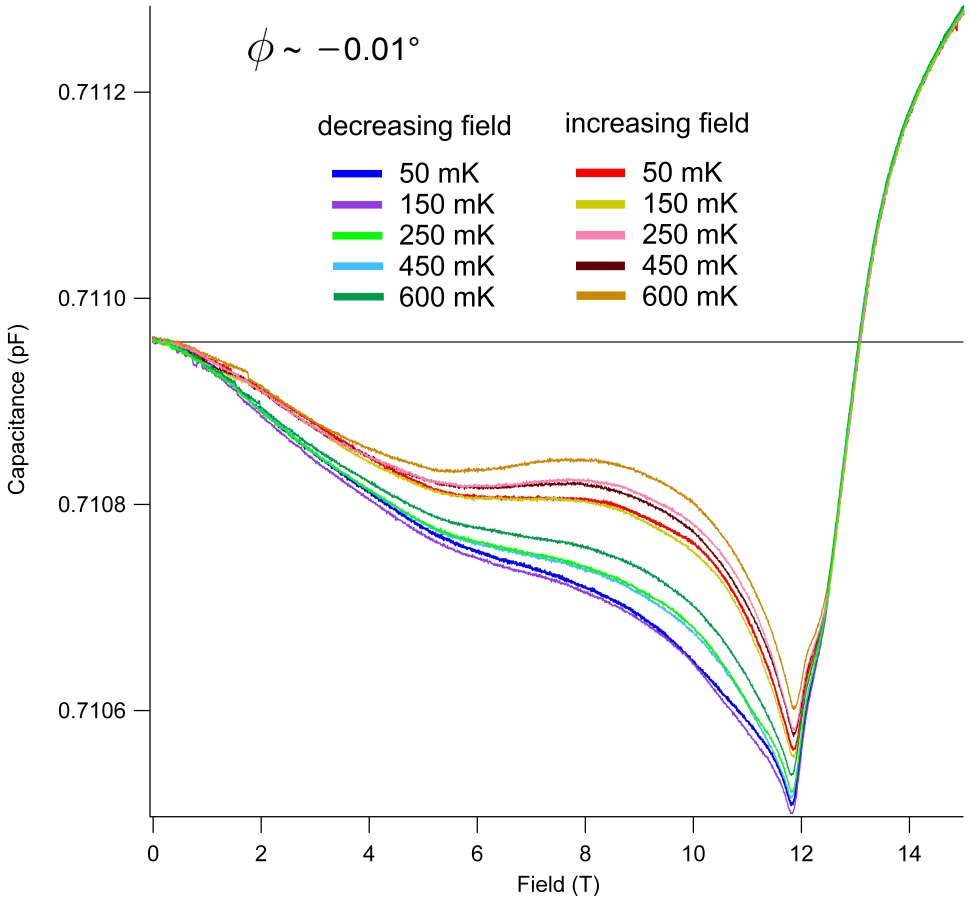

Figure 6.21 The capacitance as a function of field, measured with the AH bridge, for a range of different temperatures at $\phi \simeq -0.01°$. Measurements for both increasing and decreasing field are shown, with the up ramps in 'warm' colours and the down ramps in 'cool' colours to highlight the difference. The temperature variation is much smaller than the magnetic hysteresis.

6.6.1 Field Gradient Magnetometry

The main dataset of this project was collected for field ramps, both up and down, between 0 and 17 T, for several rotation angles within 10° of the $B \parallel b$-axis position. In addition to the main d.c. field an a.c. field modulation was applied, with the magnet system set to 'gradient mode', as described in section 4.3. The field modulation at the sample was tuned to zero as best as possible, using the vector magnet system outlined in figure 4.4, aiming to leave solely the field gradient.

Since the capacitance has little temperature dependence at small angles only two measurement temperatures were included in the main dataset: an easily controllable low temperature of 120 mK, well below the superconducting transition temperature, and a higher temperature of 620 mK, well above any influence of the superconducting state.

As can be seen in figure 6.22, the difference between the capacitance at low and high temperature shrinks as the rotation angle decreases, and for $\phi < 5°$ the two plots are practically indistinguishable, ignoring for now the data at $\phi \simeq 9.5°$, which seems to be something of an anomaly to the trends in this dataset.

The data presented in figure 6.22 is the first demodulation signal from the lock-in amplifier, measuring capacitance by way of the GR bridge instrument, and is related to the magnetization, not the susceptibility, and so is not expected to change behaviour between the superconducting and normal states.

Conversely, the second demodulation signal *could* be related to the susceptibility, in which case it would reveal a strong diamagnetic response within the superconducting state and a large peak in susceptibility at the moment rotation transition. Therefore the second demodulation signal might be expected to be dramatically different between the low and high temperature measurements at small rotation angles, which is indeed the case (see figure 6.25 for example).

This apparent dependence on the susceptibility suggests that the sample is probably not precisely in the modulation field centre, such that there are small a.c. fields present as well as the field gradient. In this case the second demodulation signal is rather more complicated than the expression given in

equation 2.64 for a pure field gradient. A more appropriate expression would be:

$$V_{\text{demod 2}} \propto L \frac{\partial B_z}{\partial z} \left(\frac{1}{2} m_{0x} \cos(\theta) - m_{0z} \sin(\theta) \right) + B_x(x,z) \left(m_{0z} - \frac{\partial m_x}{\partial B_x} B_{0z} \right) - B_z(x,z) \left(m_{0x} + \frac{\partial m_x}{\partial B_z} B_{0z} \right) \quad (6.1)$$

The signal due to $B_x(x,z)$ is likely to be small in comparison with that due to $B_z(x,z)$, not least because the latter is likely to be twice the strength of the former since the axial field gradient is twice as strong as the radial. Considering linear susceptibility for simplicity, the signal from the axial field modulation is roughly proportional to twice m_{0x} because both contributions to the torque sum together, whereas the signal from radial field modulation is roughly proportional to the difference between the two contributions, and if $\partial m_x/\partial B_x \sim \partial m_x/\partial B_z$ then the signal is roughly proportional to $(m_{0z} - m_{0x})$.

At high field any instances of large susceptibility will result in the susceptibility terms dominating the second demodulation signal, where 'large' means $\partial m/\partial B \gg m_0/B_0$ such as at the moment rotation transition. The other terms in equation 6.1, proportional to the magnetic moments, do not scale with the main field and do not spike at the rotation transition, and so will remain relatively small. It should also be noted that B_x and B_z can be both positive or negative depending on how the sample is offset from the field centre, as figure 2.10 shows. Thus the three contributions to the second demodulation signal can sum in various ways.

The alternating field gradient, accompanied by any unintentional field modulation, results in oscillations in the first demodulation signal due to the oscillations of the cantilever. Close observation of figure 6.22 reveals that, because of these oscillations, the lines defining the $\phi \simeq 0°$ plot are significantly thicker than the others, as the 'zoom bubble' on the graph shows. Although similar oscillations are present in the other plots they are too small to see by eye. Very close to $B \parallel b$-axis alignment, however, the oscillation amplitude grows by several orders of magnitude, making the effects clearly observable.

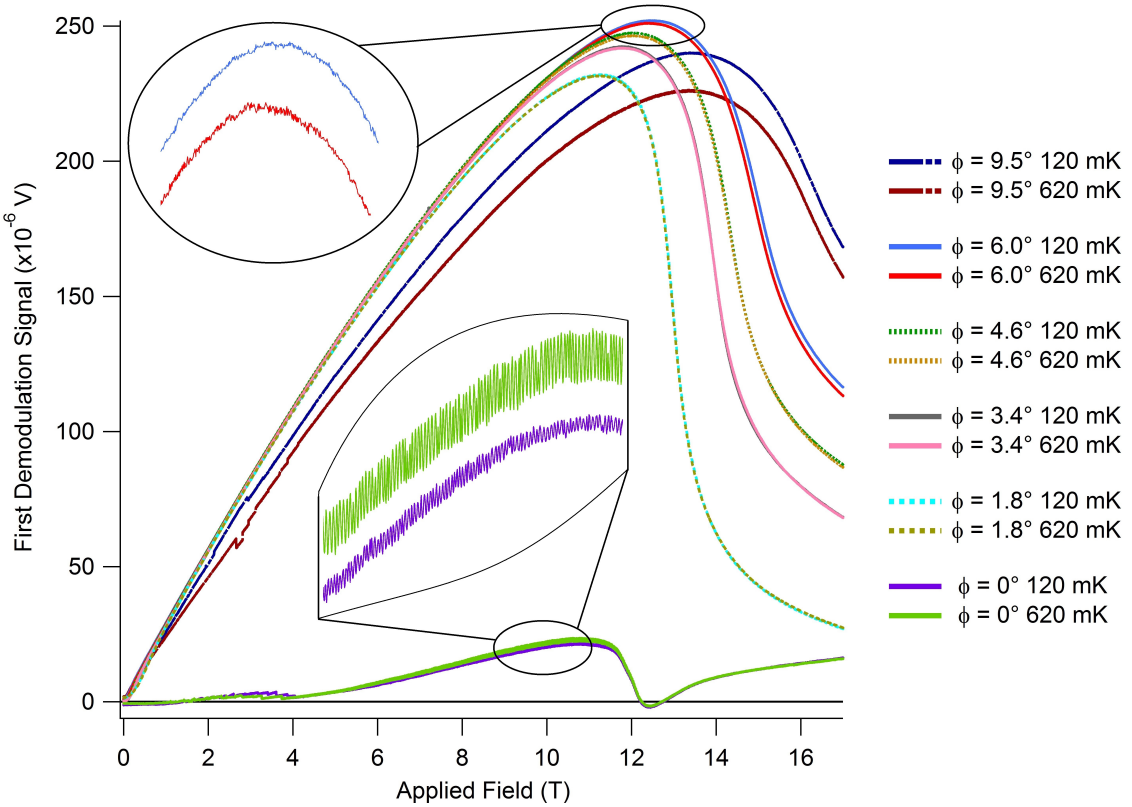

Figure 6.22 The first demodulation signal from the lock-in amplifier, measuring capacitance using the GR bridge instrument, as a function of field for several rotation angles, at 120 and 620 mK. Only the decreasing field measurements are shown, for clarity. There are two 'zoom bubbles' on the graph, showing in greater detail the oscillations due to the a.c. field modulation, which become much larger in amplitude approaching $\phi \sim 0°$.

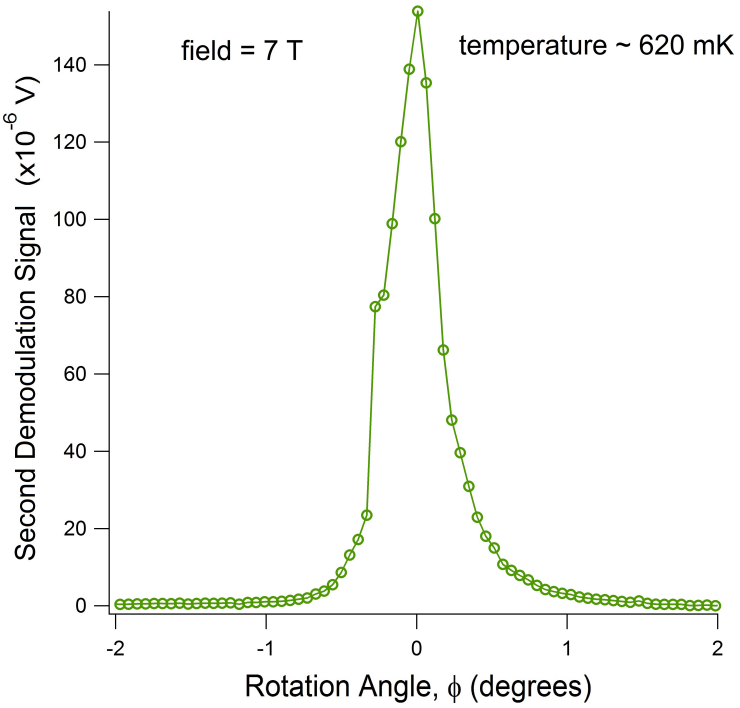

Figure 6.23 The second demodulation signal from the lock-in amplifier, measuring capacitance using the GR bridge instrument, resulting from the gradient mode modulation field, plotted as a function of rotation angle at 7 T and 620 mK, demonstrating the dramatic increase in oscillation amplitude approaching 0°.

The reason for this is that at $\phi \simeq 0°$ the magnetic moments within the domain structure are almost perfectly balanced to give zero net magnetization, which results in the low ΔC values seen, but the susceptibility $\partial m_x/\partial B_x$ is very large because relatively small fields can produce huge changes in net magnetization by resizing the domains. Because of such domain structure effects the $\phi \simeq 0°$ dataset is actually the most difficult to interpret, and it is necessary to rotate a few degrees away from $B \parallel b$-axis alignment to obtain clear results on the vector rotation of the magnetic moment .

To demonstrate how much larger the oscillations in capacitance become approaching the $\phi \simeq 0°$ position the second demodulation signal was measured at a fixed field of 7 T, comfortably distant from B_R, as a function of rotation angle. The results can be seen in figure 6.23, which provides further evidence that the second demodulation signal has a large component proportional to the susceptibility and the field modulation has not been entirely eliminated at the position of the sample.

6.6.2 Measurements at $\phi \simeq 0°$

The full $\phi \simeq 0°$ first demodulation signal dataset is presented in figure 6.24, though at this rotation angle the oscillations detected by the second demodulation can also be seen by eye. There is significant hysteresis this close to $B \parallel b$-axis alignment, as observed earlier in figure 6.21.

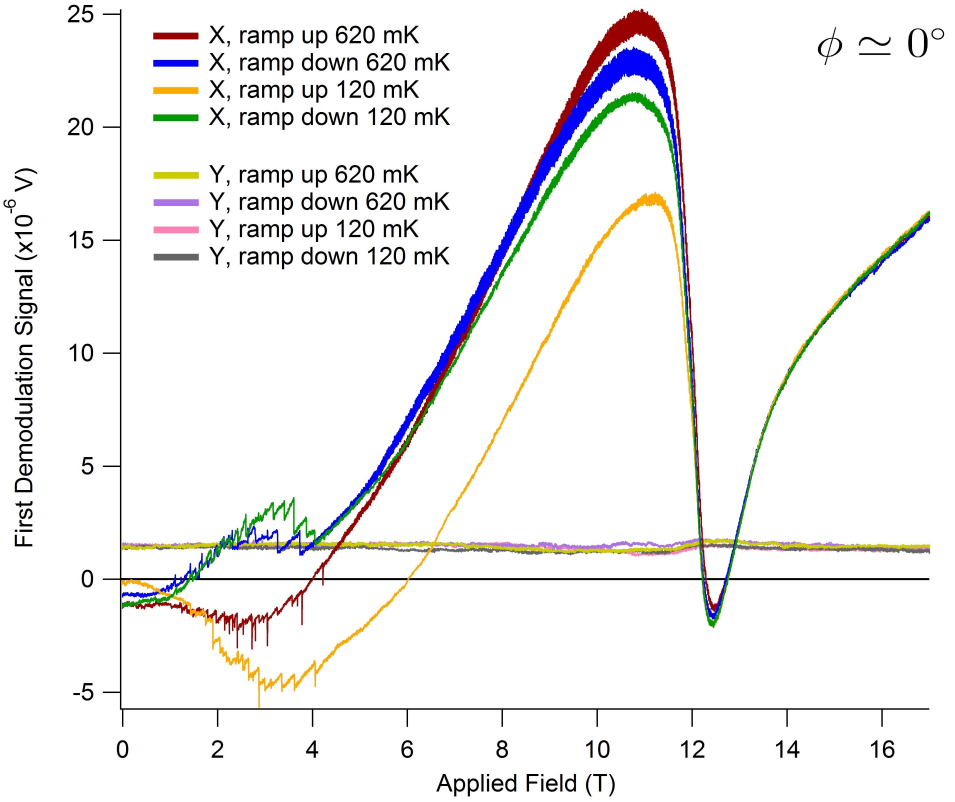

Figure 6.24 The first demodulation signal from the lock-in amplifier, measuring capacitance using the GR bridge instrument, at $\phi \simeq 0°$. Both X and Y components of the low and high temperature measurements, for both increasing and decreasing field, are plotted as a function of field. The Y signal is generally small and constant. The X signal shows the expected moment rotation transition at 12 T, and unexpected hysteresis is observed below 4 T.

In general the magnetic hysteresis is only significant below about $\phi \simeq 1°$ and is therefore not a major a concern for the rest of the dataset outlined by figure 6.22. This conclusion could also be made by observation of figure 6.23, which essentially details the extent to which the domain structure influences the magnetization and susceptibility in a moderately high field.

In regards to magnetic hysteresis, the low-field behaviour observed in figure 6.24 is particularly interesting. Below 4 T there is a sudden increase in hysteresis

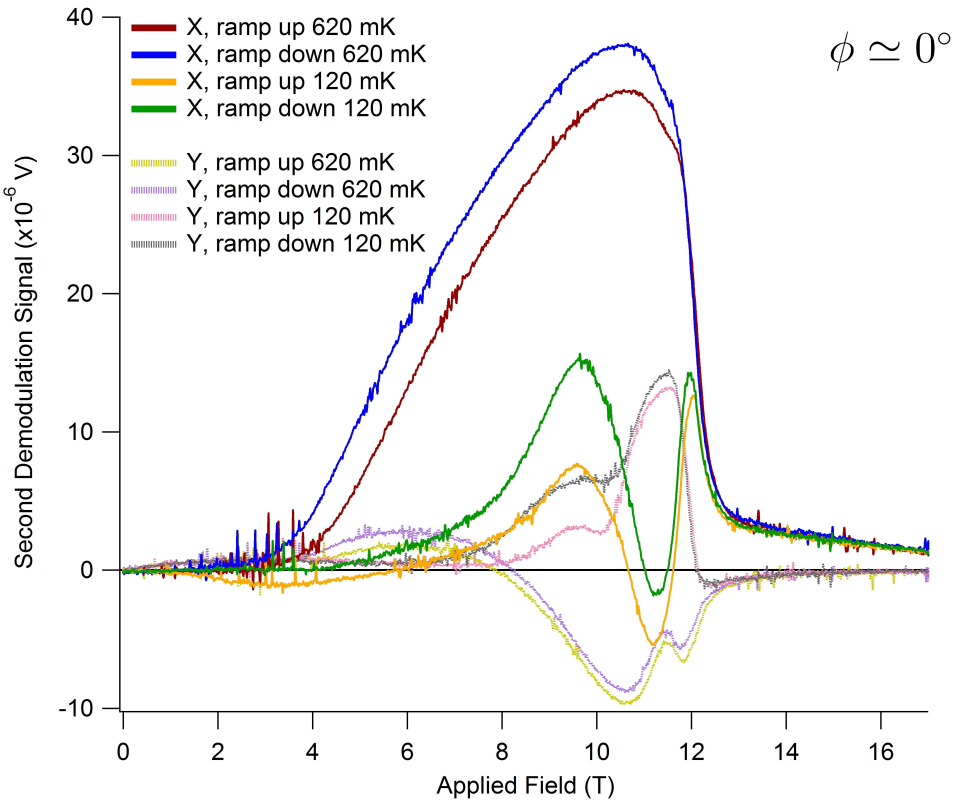

Figure 6.25 The second demodulation signal from the lock-in amplifier, measuring oscillations in capacitance using the GR bridge instrument, at $\phi \simeq 0°$. Both X and Y components of the low and high temperature measurements, for both increasing and decreasing field, are plotted as a function of field. At high temperature the X signal shows the expected moment rotation transition at 12 T and the large magnetic susceptibility below it. At low temperature the diamagnetic response is also present in the superconducting region. The Y signal behavior is complicated, neither small nor constant as might be expected.

and the difference between the up and down field ramps is so dramatic that ΔC becomes negative for the up ramp at 620 mK. At 120 mK the hysteresis is generally larger, such that the up ramp is negative up to 6 T.

There is also an accompanying increase in the roughness of the data below 4 T, which is actually not unusual: the small spikes and jumps in the capacitance data are replicated in resistance measurements and the field-centre thermometer reading for numerous other experiments. Examine the low-field data in figure 6.9 for example.

The presence of such features might not be connected to the unusual hysteresis observed in figure 6.24. However, the onset of both phenomena at 4 T is too coincidental to disregard from the discussion. It is possible that the frequent jumps and data spikes at low-field are due to the rearrangement of the domain

structure and the sudden movements of domain walls as they become unpinned from some impurity potential. In this case the unusually large hysteresis at low-field may indicate a domain restructuring procedure that is completed at 4 T, although it is known (by the fact that the ΔC values at this rotation angle are all very small) that the domain structure itself persists up to the moment rotation transition at high field.

A final observation from figure 6.24 is that the first demodulation signal has a small and constant Y component, which is the expected result of a good capacitance measurement: the Y component represents the conductance and should be unrelated to changes in capacitance, as measured by the X component.

The input to the second demodulation stage of the lock-in amplifier is provided by the X component of the first demodulation signal. This means that the Y component in the second demodulation signal represents oscillations of the cantilever that are 90° out of phase with the field modulation.

The second demodulation signal complimentary to the $B \parallel b$-axis data presented in figure 6.24 is shown in figure 6.25. Unlike those in the first demodulation, the second demodulation Y signals are typically large and show complicated behaviour instead of being constant as expected. This suggests that the magnetic moment is not oscillating entirely in phase with the field modulation.

It follows from the derivation presented in section 2.5.3 that the terms in equation 6.1 proportional to m_{0x} or m_{0z} refer to the amplitude of oscillations in-phase with the field modulation, while the terms proportional to the susceptibility unsurprisingly refer to the amplitude of oscillations in-phase with the response of the magnetic moment to the field modulation. In other words, if the magnetic moment oscillates out-of-phase with the field, then the susceptibility terms in the second demodulation signal will be out-of-phase with the reference signal at the lock-in amplifier, resulting in a significant Y component.

In figure 6.25 the high temperature X signal is large between 4 and 11 T because of the large susceptibility, up to the moment rotation transition at 12 T after which the signal drops a low but finite value, an indication of large m_{0_z} but relatively small susceptibility, as expected. The low temperature data is more difficult to understand because of the added contribution of diamagnetism from the superconductivity. This means that for studies of the moment rotation and determining the individual components of the magnetization the 620 mK data is far more useful.

The data at 120 mK is still very interesting though. The low temperature X signal shows a peak in susceptibility at $B_R \sim 12$ T and the small positive value at high field expected for the rotated moment in the normal state. There is a negative region around 11.5 T, the result of the competition between negative diamagnetism and the positive susceptibility of the rotating moment, which is briefly won by the diamagnetism. At lower fields the superconductivity weakens and then disappears, and positive susceptibility reasserts dominance.

The Y components, which might be expected to be small and constant, are indeed small and constant at very high and low fields, away from the high-field superconductivity and the moment rotation transition. In the middle of the field range, however, the Y signal is as large as the low-temperature X component and reflects some of the same behaviour.

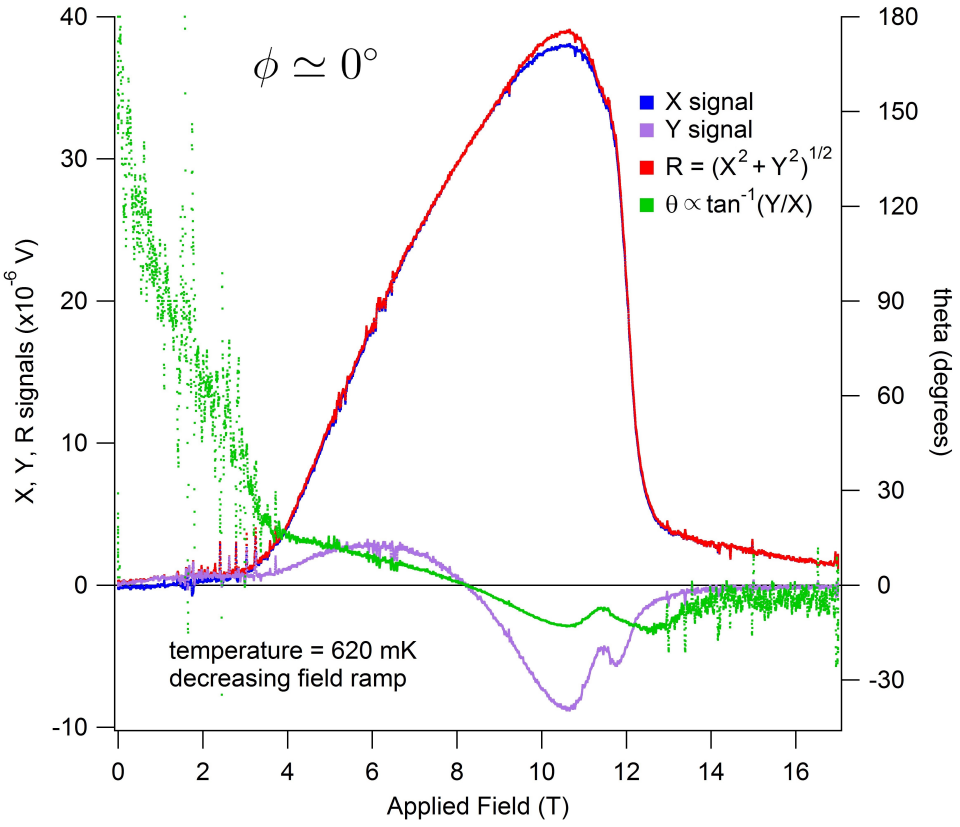

Figure 6.26 The second demodulation signal from the lock-in amplifier, measuring oscillations in capacitance using the GR bridge instrument, at $\phi \simeq 0°$. Both X and Y components of the 620 mK measurement are plotted as a function of field, for decreasing field only. The corresponding phase angle, θ, and total signal amplitude, R, are also plotted. The X and R signals are mostly the same, except around 10 T where the Y signal reaches a maximum. The phase angle varies greatly over the field range.

The Y component would appear to be an genuine expression of cantilever oscillation slightly out of phase with the current applied to the field modulation magnet coils, unlike the artificial phase rotation picked up by the resistance measurement, and simple application of a phase rotation matrix (see section 4.5) cannot reduce this Y signal to a small constant as it does in the case of the resistance.

Figure 6.26 shows the X and Y data for the decreasing field ramp at $\phi \simeq 0°$ and 620 mK. The phase is also shown, clarifying the problem with applying a rotation matrix to the measurement: the phase angle is not constant as a function of field. Hence it is not simply the case that there is a phase lag between, say, the input voltage and the output current to and from the voltage-to-current power amplifiers that drive the magnet coils.

At 0 T the measurement appears to be completely anti-phase with the excitation, meaning that the X signal is simply negative, which can be easily achieved due to the various negative signs in equation 6.1. The phase angle then decreases rapidly, reaching 15° at roughly 4 T, a value of field strength notable from earlier discussion of the first demodulation signal.

At low field the amplitude of the second demodulation signal is relatively small but 4 T marks the abrupt onset of a steep rise. At 4 T the rate of change of the phase angle is also suddenly altered, decreasing much more slowly and crossing zero at 8 T when the Y signal becomes negative. At high field the phase is small and negative, and above B_R is the only field range where the Y signal and the phase behaves as expected.

In summary, the Y signal is sufficiently large that it cannot be ignored, and sufficiently complicated that the measurement cannot be phase-rotated to make it vanish. The pragmatic solution might be to simply consider the full magnitude of the oscillation amplitude, $R = (X^2 + Y^2)^{1/2}$. The calculated R signal is also plotted in figure 6.26. It is essentially the same as the X component except around 10 T where the Y component reaches its maximum.

6.6.3 Measurements up to $\phi \sim 10°$

Moving on to explore the rest of the main dataset, the second demodulation signal at $\phi \simeq 1.8°$ is presented in figure 6.27. The first demodulation data was adequately summarised by figure 6.22 and does not require any further discussion until later, in section 6.7, the most notable feature being the moment rotation transition at roughly 13 T.

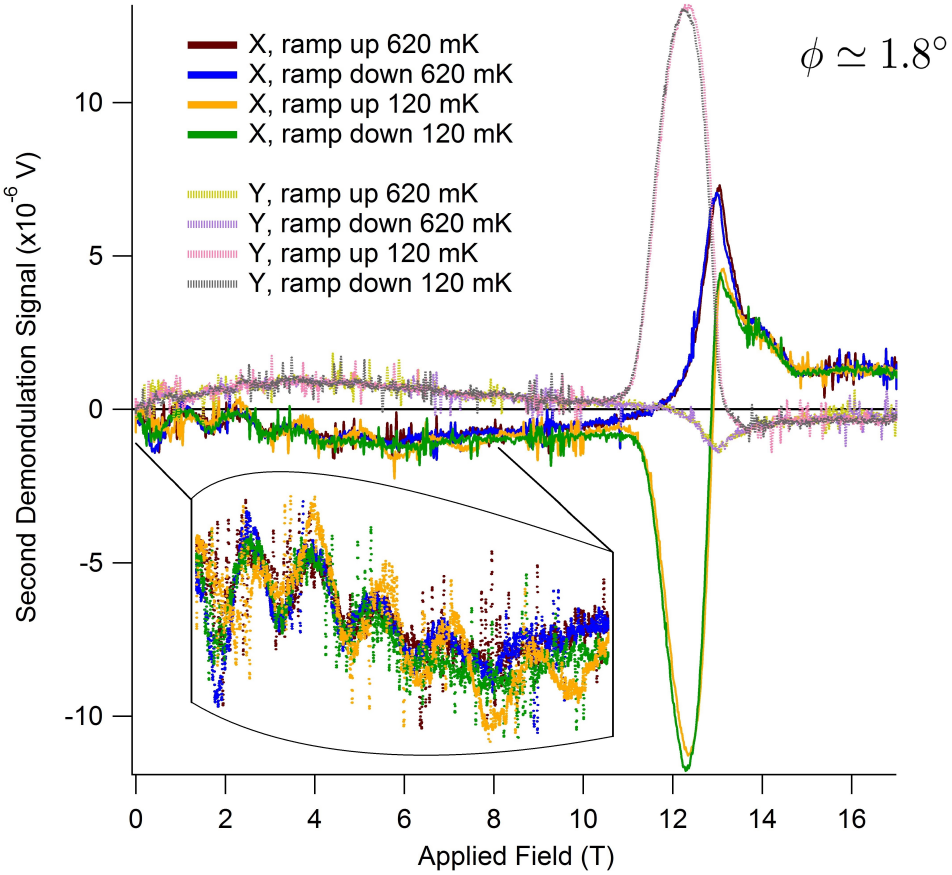

Figure 6.27 The second demodulation signal from the lock-in amplifier, measuring oscillations in capacitance using the GR bridge instrument, at $\phi \simeq 1.8°$. Both X and Y components of the low and high temperature measurements, for both increasing and decreasing field, are plotted as a function of field. There is a sharp peak in the X signal at $B_R \simeq 13$ T, preceded by a large trough at low temperature due to the diamagnetic response of the superconducting state. There is also an unexpected oscillatory nature to the X component at low field, shown in more detail in the 'zoom bubble'.

The behaviour of the second demodulation signal is remarkably different to that at $\phi \simeq 0°$. The huge susceptibility due to the domain structure is gone, leaving a comparatively small and constant X and Y signal across most of the field range, indicative of the gradual rotation of the magnetic moment. The sign for the 620

mK data is also variable, meaning that an R signal analysis as discussed earlier would not strictly be applicable, though an R signal given the sign of X would probably be fine.

At fields below B_R the X component is small and negative, at both high and low temperature. At 13 T the moment rotation transition results in a sharp peak in the X signal, then at high field the signal is positive and approximately constant, as expected. In the high temperature data the peak at B_R simply emerges from the low field behaviour. In the low temperature data the peak at B_R is preceded by a large trough, indicating a strong diamagnetic response. This trough is surprisingly narrow, however, considering that the zero-resistance state is entered at 10 T under these conditions.

Below 10 T the X component is seen to be negative, which is presumably a consequence of the different signs of the three contributions to the signal, as described by equation 6.1. Since the contribution due to B_z is expected to dominate at high field, and the observed peak at the moment rotation is positive while the susceptibility $\partial m_x/\partial B_z$ is negative, B_z is likely to be positive in this formulation. The negative X component at low field is thus explained by the contribution from $-B_z m_{0x}$, though of course there will also be contributions to the signal from the field gradient terms in equation 6.1 and no definite conclusions can be reached from this data alone.

A final observation from figure 6.27 is that there appears to be some kind of oscillatory nature to the voltage signal at low fields. It is difficult to propose a reasonable explanation for this, especially since the period of the oscillations is so large.

Figure 6.28 shows the second demodulation data for $\phi \simeq 3.4°$. At this rotation angle the high and low temperature X signals are essentially the same, the difference between them being much less than the difference between up ramps and down ramps in field, which is inexplicably substantial.

There appears to be no obvious indications of diamagnetism at low temperature in the superconducting region (the zero-resistance state is observed from 11.5 to 14 T), except perhaps in the Y signal, which does show a large peak just below the moment rotation transition. The peak at $B_R \simeq 14$ T is sharp and clear in the X component for both low and high temperature measurements.

The oscillatory behaviour seen before is again observed at low field, though with

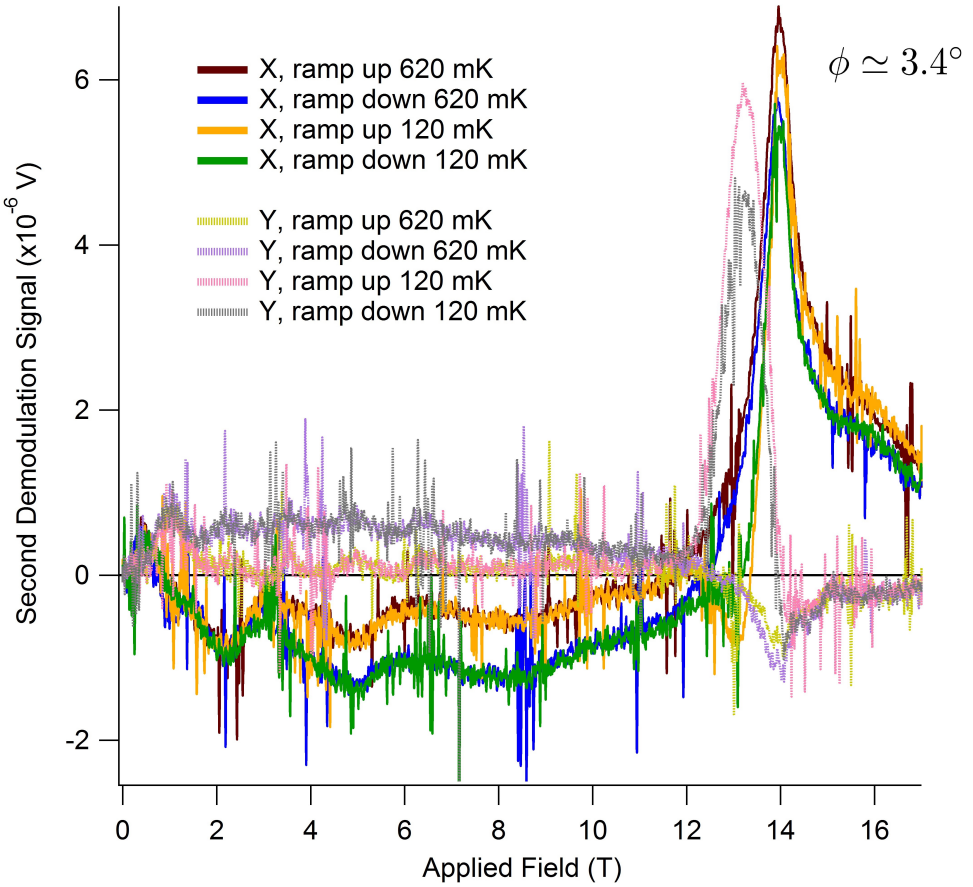

Figure 6.28 The second demodulation signal from the lock-in amplifier, measuring oscillations in capacitance using the GR bridge instrument, at $\phi \simeq 3.4°$. Both X and Y components of the low and high temperature measurements, for both increasing and decreasing field, are plotted as a function of field. There is a clear peak in the X signal at $B_R \simeq 14$ T. Measurements at lower field contain unexpected, large-period oscillations. The only indication of superconductivity is in the low temperature Y component.

longer period than that seen in figure 6.27, and as before there is no obvious explanation for it.

The second demodulation signal data for $\phi \simeq 4.6°$ is shown in figure 6.29, continuing the trend. There is a strong peak at B_R, oscillations of a negative X signal at low field, the Y signal is essentially the inverse and so positive at low field, and it is only in the Y signal that any indication of superconductivity is observed. The substantial hysteresis observed at 3.4° is not present, however.

At $\phi \simeq 6.0°$, figure 6.30, all signs of superconductivity are gone, as was expected by observation of the resistance measurement (figure 6.33). The negative signal at low fields is relatively large, before sweeping up to a positive peak at B_R as

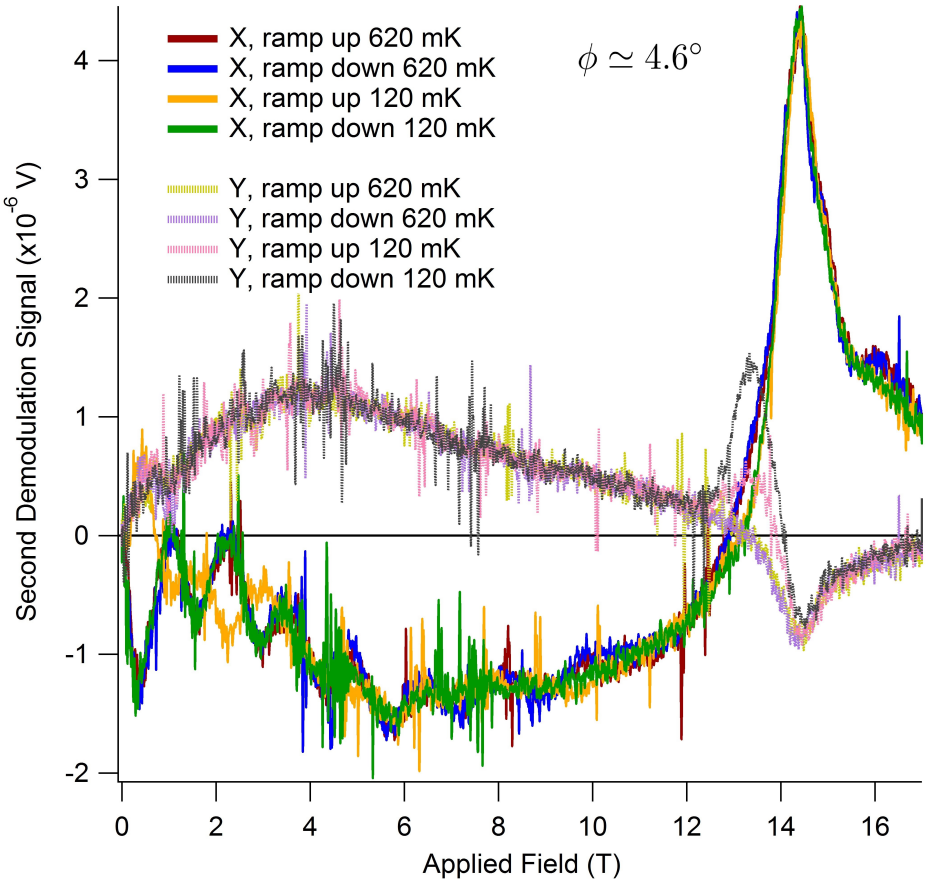

Figure 6.29 The second demodulation signal from the lock-in amplifier, measuring oscillations in capacitance using the GR bridge instrument, at $\phi \simeq 4.6°$. Both X and Y components of the low and high temperature measurements, for both increasing and decreasing field, are plotted as a function of field. Similar to the graphs at other rotation angles, there is a peak at B_R, positive in contrast to the negative X signal at lower fields, and the Y signal appears to be consistently of opposite sign to the X component, except just below B_R at low temperature where there is some indication of the superconducting state.

usual, though the peak is fairly small by comparison.

It is worth nothing here that all of these second demodulation voltages have been adjusted for the second-stage lock-in amplification effects detailed in section 4.5 and are the true signal magnitudes, allowing for comparison across the different rotation angles. At $\phi \simeq 6.0°$ the second demodulation signal ranges from roughly -2 to 3 μV whereas at $\phi \simeq 3.4°$ the main peak reaches to twice that height at about 6 μV, all of which would be dwarfed by the huge signals measured at $\phi \simeq 0.0°$, ranging from -10 to about 40 μV.

Breaking the trend, the behaviour of the second demodulation signal at $\phi \simeq 9.5°$ shown in figure 6.31 is significantly different to the preceding few graphs. The

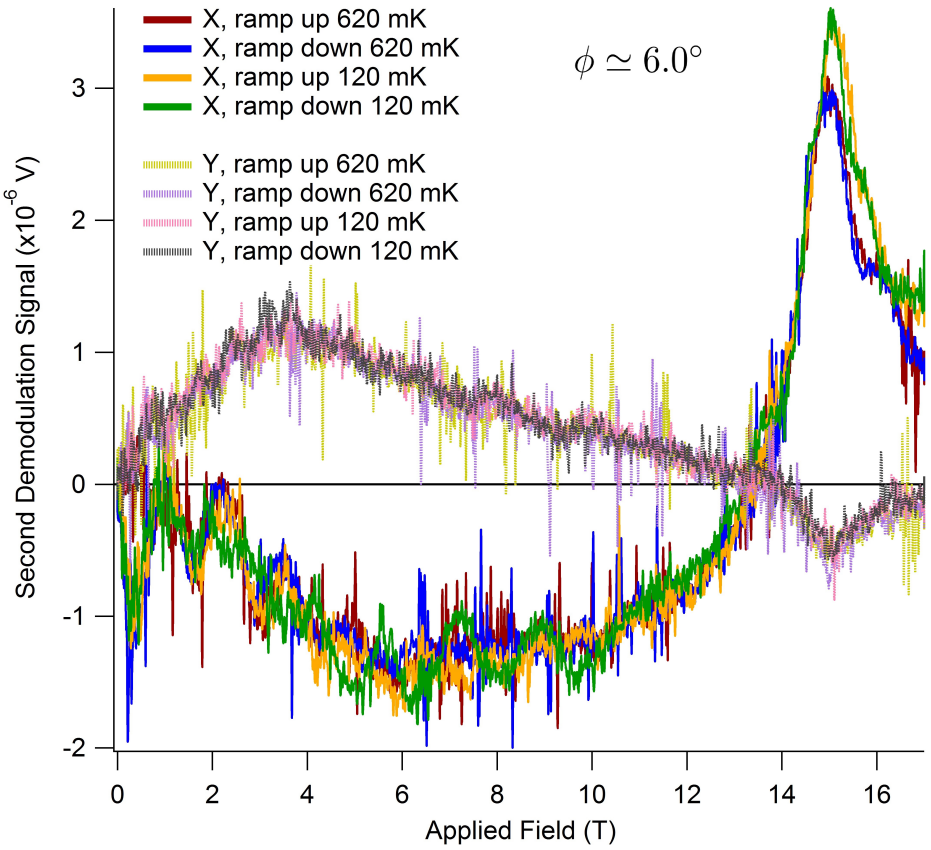

Figure 6.30 The second demodulation signal from the lock-in amplifier, measuring oscillations in capacitance using the GR bridge instrument, at $\phi \simeq 6.0°$. Both X and Y components of the low and high temperature measurements, for both increasing and decreasing field, are plotted as a function of field. Similar to the graphs at other rotation angles, there is a peak at B_R, positive in contrast to the negative X signal at lower fields, and the Y signal appears to be consistently of opposite sign to the X component. There in no evidence of superconductivity at this rotation angle.

first demodulation signal, shown in figure 6.22, is also remarkably different to the data at the other rotation angles: the signal is smaller than expected and there is a surprisingly large difference between the low and high temperature measurements.

In figure 6.31 the X and Y signals at 620 mK are both large for the majority of the field range and have opposite sign, but the X component is positive in contrast to the negative signals observed previously. Also, due to a change in lock-in amplifier sensitivity settings, the tandem demodulation amplification factor here was only $\times 50$ instead of the usual $\times 100$, so the signal is actually twice the size it seems in comparison to the previous second demodulation signal graphs.

There is no definite peak related to the moment rotation transition, though at this rotation angle the quantum critical end point (QCEP) of the metamagnetic transition has been passed (see figure 1.10), leaving only a crossover centred on a field strength that may be beyond the maximum 17 T accessible in this experiment. However, a simple linear extrapolation (figure 6.32) suggests that at $\phi \simeq 9.5°$ the crossover region might just be accessible.

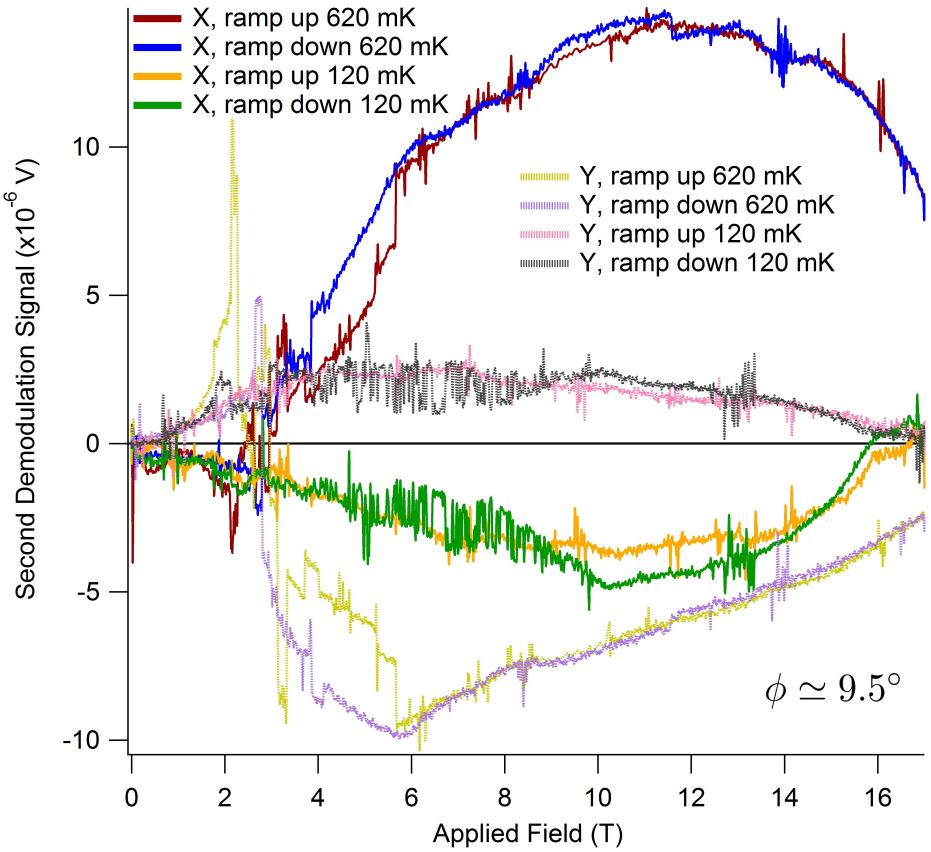

Figure 6.31 The second demodulation signal from the lock-in amplifier, measuring oscillations in capacitance using the GR bridge instrument, at $\phi \simeq 9.5°$. Both X and Y components of the low and high temperature measurements, for both increasing and decreasing field, are plotted as a function of field. The high temperature X signal is large and positive across most of the field range, dropping at high field, possibly due to the influence of the moment rotation crossover expected to be around 16.5 T. The low temperature X signal, by contrast, is negative across most of the field range.

The low temperature behaviour, which in the absence of any superconductivity should be much the same as the higher temperature data, is instead remarkably different to the 620 mK curves. It is of opposite sign, except above about 16 T where there is a sign change, possibly related to the metamagnetic crossover. The remarkably different behaviour of the low and high temperature measurements

at $\phi \simeq 9.5°$ is yet another aspect of this dataset that is difficult to explain. The anomalous behaviour could be related to passing the QCEP, however the critical point is hit around $\phi \simeq 5°$ so the previous graph in figure 6.30 should also be showcasing data from beyond the QCEP and it looks little different from the plots at lower angle.

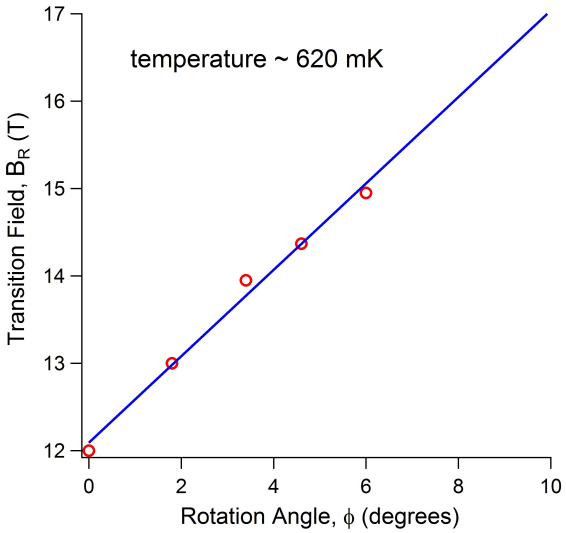

Figure 6.32 The critical field for the magnetic moment rotation transition, B_R, as a function of rotation angle ϕ for the angles encountered in the main torque magnetometry dataset, with the exception of $\phi \simeq 9.5°$ for which there is no obvious indication of a transition or crossover. The position of the transition was taken as the position of the peak in the second demodulation signal for the 620 mK decreasing field measurements. A linear fit, extrapolated to 17 T, the maximum field available in this project, would suggest a crossover around 16.5 T at $\phi \simeq 9.5°$.

6.6.4 Corresponding Resistance Measurements

The transport voltage measured simultaneously with the capacitance is presented, for the main dataset, in figure 6.33. The X signal is shown, after the necessary lock-in amplifier signal rotation to ensure zero resistance within the superconducting state and a small and constant Y signal, as described in section 4.5.

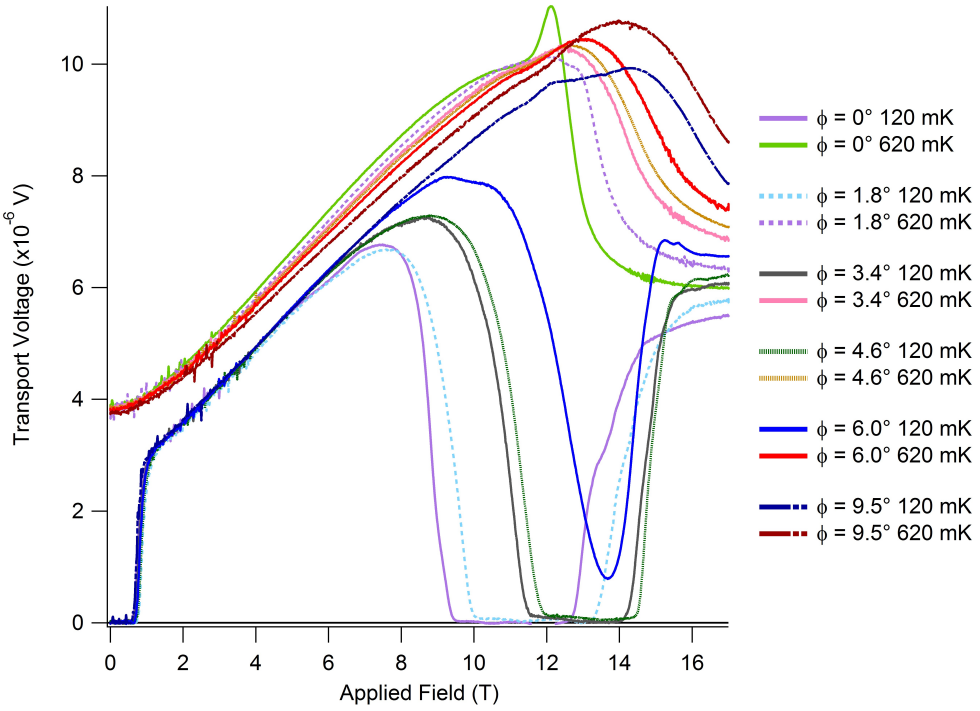

Figure 6.33 The resistance as a function of field for the rotation angles comprising the main dataset of the torque magnetometry project, for decreasing field measurements at 120 mK and 620 mK. The low temperature data is particularly useful since it indicates the extent of the zero-resistance state of the high-field superconductivity.

For the record, in this instance the experimental set-up involved the use of a balancing, floating transformer to generate the measurement current, which was roughly 200 μA. The reason for this change (from the usual 350 μA applied directly by the lock-in amplifier signal generator) was the presence of an unintentional short to ground in the circuit, which can be rectified by floating the entire circuit.

The key advantage of measuring the transport properties of the sample simultaneously with the magnetic properties is the ability to very accurately compare the observed superconducting critical fields while the sample is under the exact same

conditions (temperature, field, rotation angle, etc.). Specifically, the transition to a zero resistance state can be contrasted with the transition to the negative susceptibility of a diamagnetic state, as measured by the second demodulation signal from the capacitance bridge.

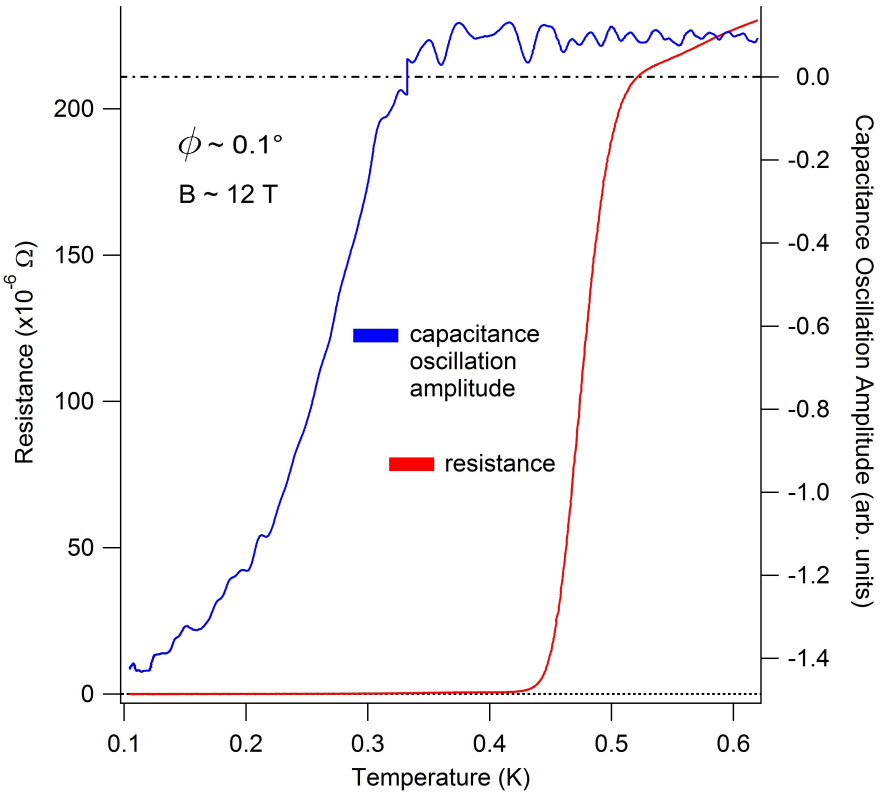

Figure 6.34 The sample resistance, and the second demodulation signal from the capacitance bridge, as a function of temperature at $\phi \sim 0.1°$ and 12 T. The oscillations in capacitance are caused by a transverse field modulation of about 6 G. The transition to a zero-resistance state occurs roughly 100 mK higher than the temperature at which the oscillations in capacitance become out-of-phase with the field modulation, i.e. a diamagnetic response, indicative of bulk superconductivity. Diamagnetism is then strengthened as temperature is decreased further.

In figure 6.34 the sample resistance and the second demodulation signal from the capacitance bridge are plotted as a function of temperature at $\phi \sim 0.1°$ and 12 T, where the superconducting transition temperature should be around 450 mK. Here the oscillations in capacitance are caused by a transverse field modulation, as described by equation 2.63. No longitudinal modulation has been applied and there are no significant field gradients.

For the transverse field modulation measurements the Y component is generally smaller than the X and consistently has the same sign. In figure 6.34 the total magnitude of the oscillations, the second demodulation R signal, has been plotted,

though the sign of X has been preserved, reversed, and then applied to the R data such that it has the same sign as the susceptibility.

In this case R is proportional to $(B_{0z}\,\partial m_x/\partial B_x - m_{0z})$. It is large and negative at low temperature but decreases gradually as temperature rises, crossing zero around 330 mK, and is small, positive and roughly constant above about 370 mK. In the normal state neither the magnetization nor the susceptibility is expected to change much with temperature over the small range below 1 K, and so the roughly constant value observed at higher temperatures would be the expected behaviour if $\sim$350 mK was indicative of the superconducting transition temperature.

If the assumption is made that any dramatic changes in $(B_{0z}\,\partial m_x/\partial B_x - m_{0z})$ over the temperature range are due to the susceptibility rather than the magnetization, which seems reasonable considering that the latter definitely does not change sign, then the point at which the R signal becomes negative could be considered as the onset of diamagnetism, with the diamagnetic response strengthening as temperature is lowered further.

Observation of 6.34 suggests that the point at which the sample becomes diamagnetic is about 100 mK lower than the point at which the resistance becomes zero, which is very interesting. Often the temperature at which a type II superconductor becomes resistive is slightly lower than the bulk transition to the normal state, due to the melting of the vortex lattice and the resulting flux-flow resistivity, however the diamagnetic response should be a probe of bulk superconductivity so it is unusual that the zero-resistance state persists to higher temperatures than the diamagnetic state.

Figure 6.35 shows a graph of the high-field superconducting transition temperature across the range 10 to 13.5 T. At these two end points the transition in the capacitance oscillation amplitude is too unclear to provide reliable data points, the variation in susceptibility being too small to resolve a definite change in sign and behaviour, but 10 and 13.5 T could essentially be considered as the bounds of the superconducting region as defined by the diamagnetic state.

The superconducting region defined by the zero-resistance state also ends abruptly at 13.5 T, though at the lower end continues down to 8 T, as seen in figure 6.9 or in the phase diagram presented in figure 1.7. The limited-range phase diagram plotted in figure 6.35 shows that the transition to diamagnetism occurs at consistently lower temperature than the transition in resistivity, which was taken as the point of 50% normal state resistance.

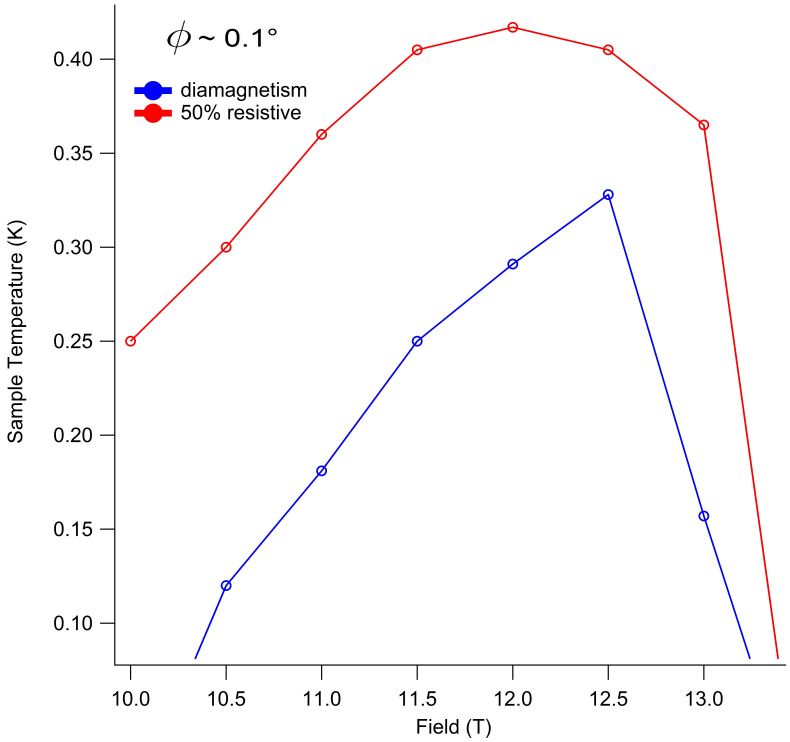

Figure 6.35 The superconducting transition temperatures, determined by the zero-resistance state and the presence of diamagnetism, plotted as a function of field at $\phi \sim 0.1°$. The position of the transition in resistance was taken as the temperature at which the resistance reaches 50% of the normal state value. There is a consistent and significant difference between the two, with the departure from the diamagnetic state generally occurring $\sim$100 mK before the departure from the zero-resistance state.

6.7 Decomposed Magnetization

The second demodulation signal does not display the expected behavior for a pure field gradient and it seems highly likely that there is also field modulation present, which although very small does produce significant torque oscillations, especially at fields where the susceptibility becomes very large. In this case it is unfortunately not possible to determined the parallel-to-field component of the magnetization without more information, namely the transverse susceptibility $\partial m_x/\partial B_x$ as a function of B_{0z}.

Even if this information was known, subtraction of all the additional terms from equation 6.1 to leave just m_{0z} is unlikely to result in accurate, low noise data because there are just too many different variables involved. For example, measurements with purposeful transverse and longitudinal field modulation can be performed, but their contributions to equation 6.1 would need to be rescaled according to the magnitude of the unintentional modulation fields present in the field gradient data, which is very uncertain. Of course if that information *was* known for certain then the modulation fields could simply be adjusted more accurately to leave just the field gradient.

Nevertheless, an attempt to subtract the field modulation data from the field gradient result is shown in figure 6.36. The data presented in figure 6.30 is duplicated and accompanied by a subsequent measurement where the magnet system has merely been switched from gradient to modulation mode, keeping the transverse field modulation the same. The data from this measurement has then been halved, which rescales the peaks in both datasets to roughly the same size, the logic being that the peak is due to the susceptibility terms and therefore does not involve the field gradient contribution.

There does indeed seem to be a difference between the two rescaled curves at high field, where the field gradient signal is expected to be at a maximum, but plotting the difference as a function of field results in a very noisy graph without much meaningful structure. Attempts to calculate the magnetic moment m_{0z} from the resulting data are not particularly fruitful.

An alternate approach is to simply improve the elimination of modulation fields at the sample. Instead of using the pick-up coils to probe the position of the field centre, the signal from the torque oscillations can be used to investigate the effect

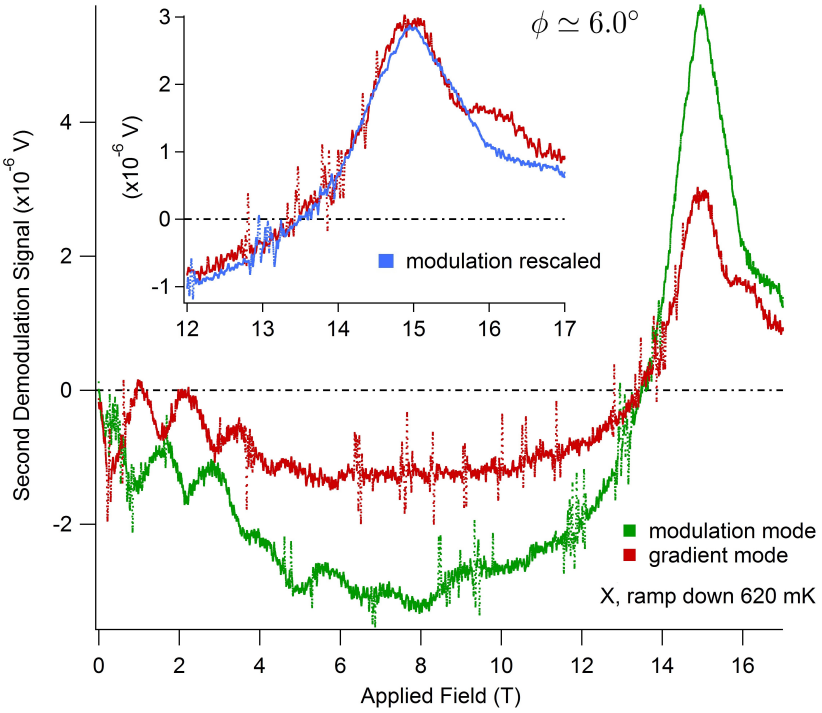

Figure 6.36 The second demodulation signal as a function of field at 620 mK. **Main:** Measurements in modulation and gradient mode, where both have the same transverse field modulation applied. In field gradient mode an apparently unsuccessful attempt has been made to eliminate any field modulation at the sample, resulting in a peak at the moment rotation transition at approximately 15 T. **Inset:** The modulation mode data has been halved such that the peak high is roughly the same as in the gradient mode data. The difference between the curves is possibly entirely due to the effects of the field gradient.

of changing the balance of the field strengths generated by the different magnet coils.

In much the same way as resistance measurements of a sample can be used to measure the temperature of the sample directly, instead of measuring the temperature of a separate thermometer mounted some small distance away, the measurement data from the sample could possibly be used to tune the modulation fields to zero directly at the sample, instead of tuning the fields at the pick-up coils a small distance away.

The effect of varying the relative currents in the field gradient mode magnet coils is shown in figure 6.37. At this point in time the additional pick-up coils surrounding the sample were not present so the angle sensors were used to probe the field modulation (using some basic geometry to account for the fact that they were rotated $\sim 37°$ relative to the field). The sample was rotated a couple of

degrees from $B \| b$-axis alignment to avoid the domain structure effects.

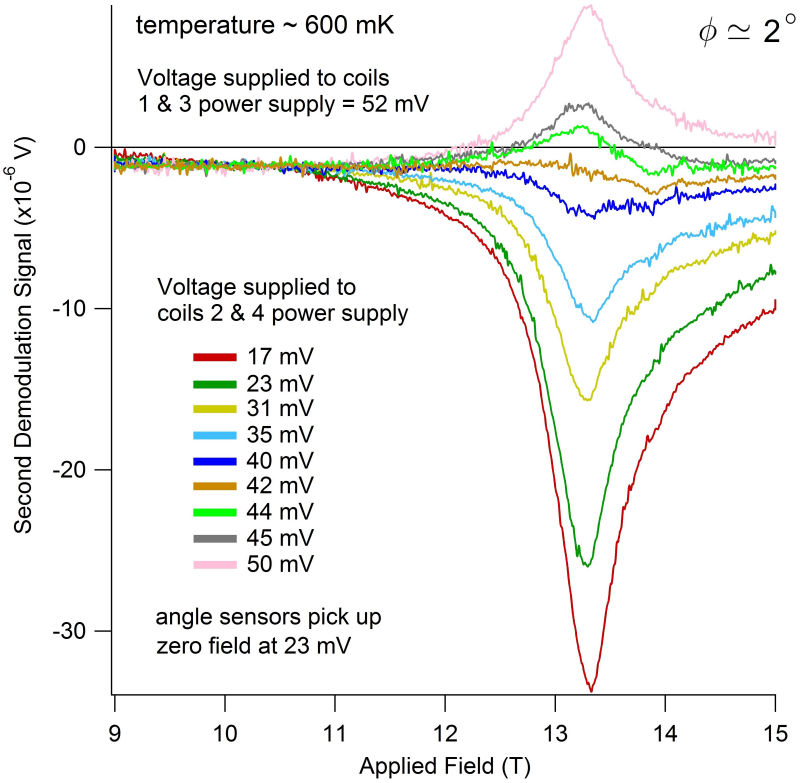

Figure 6.37 The second demodulation signal as a function of field from 9 to 15 T for various different ratios of the current supplied to the field modulation magnet coils operating in gradient mode. The current in coils 1 & 3 was fixed at 52 mV $\rightarrow$ 0.62 A and the current in coils 2 & 4 was as indicated by the legend (1 V $\rightarrow$ 12 A). Zero field modulation was picked up by the angle sensors at 23 mV input to the coils 2 & 4 power supply. The rotation angle was $\phi \sim 2^\circ$. The expected signal at 15 T for a pure field gradient was around 8 μV. The temperature was roughly 600 mK, ensuring that the sample was in the normal (rather than superconducting) state.

The angle sensors registered zero pick-up when slightly less than half of the current supplied to coils 1 & 3 was supplied to coils 2 & 4, which (reassuringly) is about the same ratio used in the final experimental set-up described in section 4.3. The angle sensors were mounted a significant distance away from the sample, however, so this was not expected to eliminate the field modulation at the sample position. The value $\sim$23 mV does serve as a useful guide though.

Also useful is the expected magnitude of the signal at high field. From figure 1.9 the magnetization around 15 T is $\sim 0.5\,\mu_B$/f.u. which for the field gradient applied here (about 0.05 Tm^{-1}) should result in a second demodulation signal of around 8 μV from the magnetic force in the absence of any torques from field modulations. Hence the 23 mV plot is actually not far off the expected response

at 15 T.

The unexpected feature is the large negative peak at the moment rotation transition due to the high susceptibility, which only enters the measurement if there is non-zero field modulation. Tuning away the peak also diminishes the signal, such that at 42 mV supplied to the coils 2 & 4 power supply the peak has essentially vanished but the signal is basically small and constant across the field range, and not at all reflective of the parallel-to-field component of the magnetization.

Sticking with 23 mV supplied to the coils 2 & 4 power supply, a transverse field modulation was then applied at various strengths and polarities but appeared to have little impact on the peak, other than increasing or reducing the height slightly. At full power (limited by system heating), producing a field of about 1.2 mT, the supposedly corrective transverse modulation only reduced the peak height by a small fraction.

Calculations show that 1.2 mT should be more than enough to correct for any unintentional transverse field modulation so it seems likely that the peak is caused by the longitudinal modulation, however no combination of different longitudinal fields (from different currents in coils 2 & 4) and transverse fields appeared to produced the expected results for a pure field gradient setup.

In conclusion, abandoning the second demodulation results for now, only the component of magnetization perpendicular to the field could be determined. The final results, from the main first demodulation signal dataset, are shown in figure 6.38. Potential advancements in the experimental set-up that could allow full completion of the project by measuring the other component of magnetization are discussed in section 7.2.1.

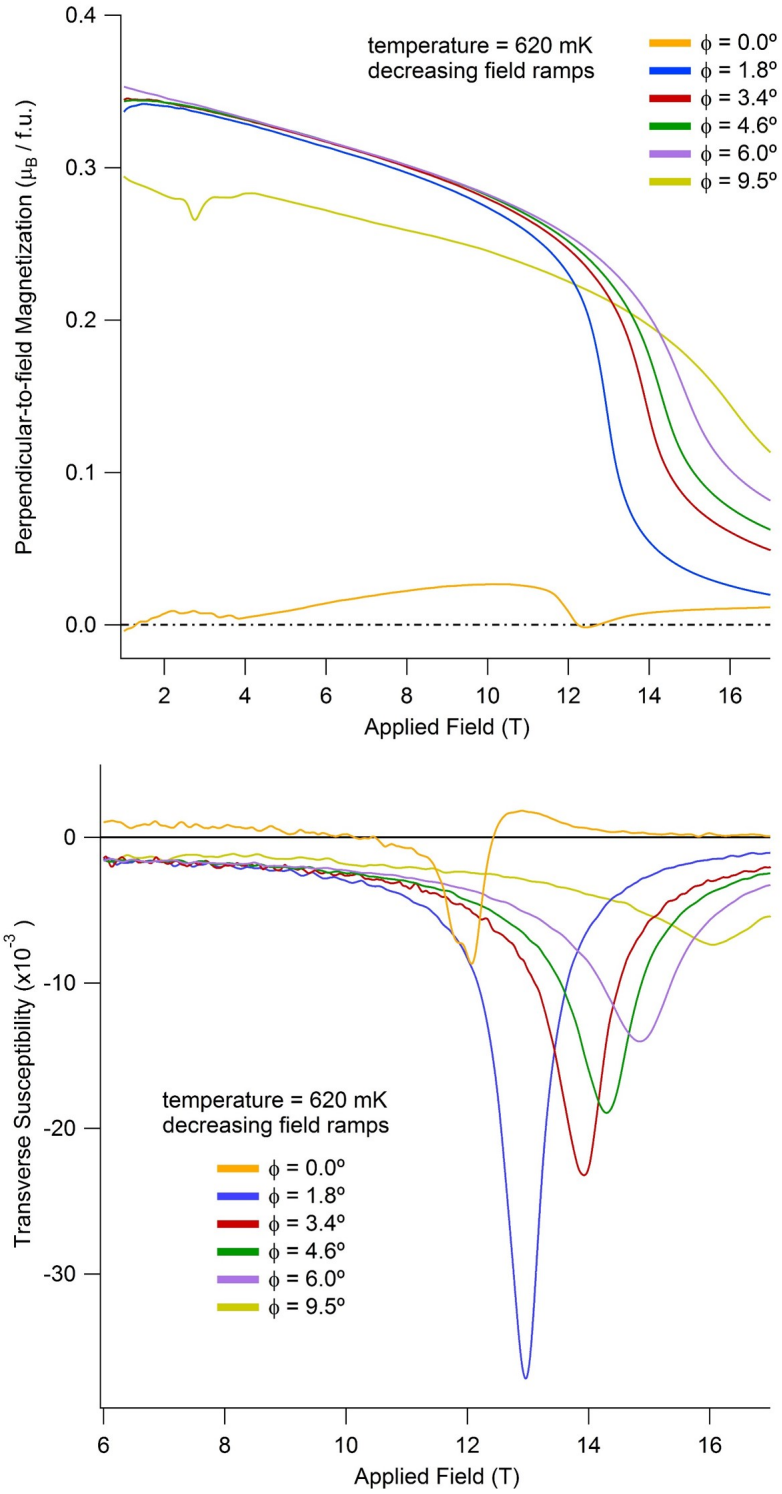

Figure 6.38 **Top:** The component of magnetization perpendicular to the field, as a function of field, for various rotation angles, showing the sudden decrease expected at the moment rotation transition, which moves to higher field as the rotation angle increases. **Bottom:** The derivative of the plots above, thus showing the transverse susceptibility $\partial B_x/\partial B_z$, which peaks at the moment rotation transition.

Chapter 7

Conclusions

A sensible place to start with the conclusion of the UGe_2 Hall effect project is a comparison with the published results presented in Ref. [35], which is a full investigation of the Hall effect in UGe_2 at ambient pressure. The authors find a large increase in n, essentially the simple inverse of the ordinary Hall coefficient, upon cooling from the FM1 state through T_X to the FM2 phase, from a high-temperature FM1 value around 0.2 holes/f.u. to a base-temperature FM2 value around 1.6 holes/f.u.

Although this published study is not directly comparable to that covered in this thesis, due to the different direction of applied magnetic field, it does nevertheless provide a useful reference point, especially since the investigation outlined in this thesis was performed on a single sample. The corresponding result is summarised by figure 5.33, showing a similar jump in the Hall coefficient upon cooling, at low pressure, from FM1 to FM2, from roughly 0.2 holes/f.u. to a base-temperature 1.2 holes/f.u. respectively. As such the two studies do agree fairly well, despite the difficulties encountered in untangling the ordinary and anomalous contributions to the Hall effect at higher pressure where magnetization data is sparse.

New results to highlight from figure 5.33 are that the jump in Hall coefficient from FM1 to FM2 follows the T_X line in the P-T phase diagram almost perfectly, and that there is then an entirely different, but equally abrupt, change in Hall coefficient crossing the critical pressure where T_X reaches absolute zero.

Crossing the critical pressure at low temperature, at about 10 K for example, sees a change from the low-pressure FM1 value of about 0.2 holes/f.u to a high-

pressure FM1 value of roughly 0.2 electrons/f.u. Crossing at base temperature, from the FM2 phase ($\sim$ 1.2 holes/f.u.) to the high-pressure FM1 state, thus shows an even more dramatic change, with the same sign reversal (positive n to negative; hole to electrons) accompanied by a drop of an order of magnitude.

Hence the major conclusion of the UGe_2 study is that the FM1 phases either side of the critical pressure would appear to be fundamentally different, as far as the Fermi surfaces are concerned at least, despite having similar magnetization. Also, although the Hall coefficient changes by an order of magnitude from FM1 to FM2 as a function of temperature, crossing the phase transition as a function of pressure sees a sign reversal as well as a similar jump in magnitude.

In conclusion, there are significant and substantial changes to the Fermi surfaces in the region of the P-T phase diagram surrounding the first-order quantum critical point in UGe_2, which are highly likely to provide the magnetic fluctuations responsible for the emergence of p-wave superconductivity. Further work is however required in order to determine exactly what those changes in the Fermi surfaces are.

A similar conclusion can be made for the URhGe project. The main objective, to determine both the parallel- and perpendicular-to-field components of magnetization as a function of field crossing the first-order quantum critical point, was essentially found to be impossible with the current experimental set-up precisely because of the large magnetic fluctuations that were expected in the critical region of the phase diagram.

The sharply peaked magnetic susceptibilities at the critical point that made the modulated torque magnetometry technique difficult to apply, since there were too many different, substantial contributions to the measurements in the critical region, is effectively the very phenomena that is expected to be responsible for the emergence of superconductivity.

As such, the fact that such strongly peaked susceptibilities were encountered is, in itself, even in the absence of the ability to properly measure and quantify them, evidence for the scenario that high susceptibility and magnetic fluctuations provide the mechanism for superconducting electron pairing. Similar to the Hall effect project, further work is required in order to determine exactly what those magnetic fluctuations are (specifically, which are stronger, the longitudinal or the transverse).

The main achievement of the torque magnetometry project described in this thesis was therefore the development of the technique itself, which as yet does not appear in any scientific literature in the full, complicated, multi-component form discussed in chapters 2, 4 and 6. Indeed the description of the technique provided in this thesis, though apparently straightforward when all aspects of it are laid out coherently and together in its entirety, is the final product of many experimental iterations resulting in incremental improvements to the methodology, occurring over the course of several years, and even the little, seemingly trivial details should not be overlooked by any reader interested in performing similar experiments.

The use of the passive capacitance bridge and lock-in amplifier double demodulation techniques, in combination with the set-up of three pairs of modulating magnets, in perpendicular orientations, for simultaneous magnetization, differential susceptibility and resistivity measurements at 50 mK up to 17 T, of such a tiny sample of a 3d ferromagnet, for a study across a wide range of rotation angles with 0.01° resolution, is a novel experimental technique, unique in its flexibility, complexity, accuracy and precision.

Finally, although the main objectives for both the UGe_2 and the URhGe projects were not fully accomplished (both being somewhat ambitious for the timescales involved), a large amount of useful data and incidental results were gathered during the pursuit of the main aims, and a number of other interesting observations can be made about the two materials. These are listed in full in the following two sections: detailed, technical summaries of the key findings for each project.

7.1 Detailed UGe_2 Hall Resistivity Conclusions

The combination of resistivity measurements and the Hall effect provides various methods of determining critical points T_C, T_X and H_X, allowing the phase diagram of UGe_2 to be plotted with high accuracy and precision. Manganin wire measurements also ensure that a reliable value of pressure is associated with each critical point; the temperature dependence of the pressure within the piston-cylinder cell was determined and found not to vary significantly over the low temperature measurement range.

The crossover at T_X was found to be very broad at low pressure. The critical region narrows approaching P_X and as the crossover becomes a phase transition the features in the resistivity associated with T_X become sharp. The phase line from the critical end point of the transition at roughly 7 K to the first-order quantum critical point at 0 K was found to be almost vertical, providing support for the shape of the phase transition plane sketched in figure 1.6.

The feature in the temperature derivative of the resistivity associated with T_C changes form as pressure increases, from a peak at the lowest pressures to a trough at the highest, possibly due to the change from second to first order and passing the tricritical point at approximately 14 kbar.

The Hall resistivity was found to be generally negative around 2 K but it swiftly becomes positive as temperature increases and peaks around T_C, suggesting that ρ_{xy} becomes dominated by the anomalous Hall effect. The AHE in UGe_2 appears to have significant contributions proportional to both ρ_{xx} and ρ_{xx}^2, and since the longitudinal resistivity grows rapidly with temperature the anomalous Hall resistivity increases even more steeply than the resistivity, leading to the AHE dominating at temperatures above about 10 to 15 K.

The gradient of the Hall resistivity with field is negative across most of the measured phase diagram, with the exception of the low temperature FM1 region above P_X where it is mostly positive, or at least a much smaller negative than elsewhere. Increasing temperature toward T_C sees a huge increase in $\widetilde{R}_0 = \partial\rho_{xy}/\partial T$ and it becomes large and positive in the PM state, such that on the same scale $\widetilde{R}_0$ at low temperature looks to be almost zero. The small size of the Hall effect in the FM state around T_X is partly responsible for the difficulty in obtaining good measurements (low signal-to-noise) but might be expected if

UGe_2 is a compensated material.

An interesting feature in the $\widetilde{R}_0$ measurements is that there is an abrupt change crossing P_X around 10 K, which is significantly above the determined values of T_X immediately below P_X (and at those pressures the definition of T_X is sharp). Hence there appears to be a dramatic change in the Hall coefficient, a change in sign as well as magnitude, moving between what is traditionally characterised as the same FM1 phase either side of the P_X line, although $\widetilde{R}_0$ is not strictly the Hall coefficient so this can only be considered as a preliminary result.

At 2 K both ρ_{xx} and ρ_{xy} are observed to have mostly linear field dependence. The the Hall resistivity at 2 K seems to be dominated by the ordinary Hall effect, as evidenced by a straight-line intercept of roughly zero, and the magnetoresistivity evidently does not follow the usual field-squared dependence seen in simpler metals. Fitting the ordinary and anomalous contributions to the Hall resistivity measurement produces reasonably accurate results, despite the somewhat noisy data, as seen in figure 5.19.

The value of the ordinary Hall coefficient provided by the fit is negative as expected from measurements of $\widetilde{R}_0$, and the anomalous Hall coefficients R_{a_1} and R_{a_2} are found to have similar magnitudes, such that neither dominates the expression and allows the other term to be disregarded. R_{a_1} is positive, while R_{a_2} is negative, therefore the earlier conclusion that the the Hall resistivity becomes large and positive at higher temperature due to the AHE implies that the R_{a_1} term *must* grow to far exceed the R_{a_2} term as temperature increases.

Regarding the magnetoresistivity results, a simple conclusion is that the more strongly polarised state is charactertised by a reduced resistivity, both for the FM2 phase below T_X and P_X and for the field-induced FM2 state at high pressure.

The 2 K results show a significant change in the ordinary Hall coefficient crossing P_X, from a relatively constant negative value across the FM2 phase to a much smaller, yet still negative, value above P_X. This is consistent with the $\widetilde{R}_0$ measurements at 2 K; it is not until slightly higher temperatures that positive values above P_X are observed. Regarding the anomalous Hall coefficients, R_{a_1} appears to increase slightly with pressure but R_{a_2} shows little change, although it is difficult to draw significant conclusions due to the uncertainties on the data points.

At higher temperature R_0 proves to be slightly different to $\widetilde{R}_0$. An effectively

constant value of R_0 is measured across the entire FM2 phase, right up to the transition temperature; above T_X there is an steep drop to a much larger negative values. Similar to $\widetilde{R}_0$ positive values of R_0 are observed immediately above P_X at around 10 K, confirming the conclusion that there is a major change in the ordinary Hall coefficient crossing the critical pressure between what is supposedly the same FM1 either side. Unfortunately the data becomes too noisy at low temperature at higher pressures to judge whether or not these positive values persist throughout the FM1 phase below 10 K.

Inverting the ordinary Hall coefficient and calculating the single-band carrier concentration makes the changes crossing T_X and P_X easier to see. Figure 5.33 is essentially one of the main conclusions of the Hall effect project. There is a clear and consistent change in n from roughly 1 electron per uranium in the FM2 phase to about 0.1 to 0.2 electrons per uranium in the FM1 phase, with the exception of immediately above P_X at low temperature where n relates to roughly 0.3 holes. Evidently there is considerable, and presumably consequential, variation in R_0 in the vicinity of both the CEP and the QCP.

Abrupt changes in the ordinary Hall coefficient can be related to Fermi surface reconstruction, such as a Lifshitz transition, or sudden changes in the relative conductivities of different bands at the Fermi level, perhaps related to changes in magnetism though the breakdown of Kondo screening. A possible scenario might include both: a small pocket of Fermi surface shrinks to nothing at a Lifshitz transition at P_X, which though small contains a large proportion of the conduction electrons involved in Kondo screening, meaning that when the Fermi surface disappears the hybridisation between these electrons and the local moments is destroyed, leaving the moments unscreened and resulting in enhanced magnetization, as in the strongly polarised FM2 state.

The Lifshitz transition and the freeing of conduction electrons from screening and hybridisation would probably alter the balance of conductivities on the remaining conduction bands, which can by itself result in big changes to the Hall coefficient, although the expression presented in equation 2.19 is complicated and it is difficult to speculate in advance whether the combination of Fermi surface reconstruction, Kondo breakdown, and any associated changes in band conductivities would increase, decrease or change the sign of the Hall coefficient.

Leaving speculation aside for now, a definite conclusion is that there are significant, and remarkably different, changes in the ordinary Hall coefficient crossing

T_X and crossing P_X, and such abrupt variations in the vicinity of the QCP likely produces the kind of critical fluctuations between incompatible magnetic ground states that leads to novel phase formation such as superconductivity.

In order to progress further in understanding the changes surrounding the QCP it would be useful to have information about the conductivities and carrier concentrations of the different bands crossing the Fermi level. This would be the ultimate goal of the Hall effect project. Attempts to extract such information from the experiment are discussed in section 2.3, which essentially concludes that for a multiband material obtaining such results from simple resistivity measurements is challenging. An attempt at fitting the data to a simple two-band model is made in this thesis but the results cannot be considered reliable.

However, a useful conclusion is that at 2 K UGe_2 is found to be between the limits of the 'high' and 'low' field regimes for the Hall effect, with the critical value of $\omega_c\tau = 1$ estimated at 10 T. As temperature increases UGe_2 moves further toward the the low field limit for measurements made up to a maximum of 9 T, as they are in this project, thus simplifying the analysis of the ordinary Hall coefficient, but then approaching T_X the magnetoresistance becomes negative and the standard formulae for the Hall effect and the magnetoresistivity are no longer applicable. Multi-band fitting is likely possible with more sophisticated models and formulae, though this may require more quantitatively accurate measurements of the magnetoresistivity and probably all components of the resistivity tensor.

The anomalous Hall effect also shows dramatic changes at the FM1-FM2 transition. Though roughly equal in magnitude below T_X, the R_{a1} term (proportional to ρ_{xx}) becomes much larger than the R_{a2} term (proportional to ρ_{xx}^2) at temperatures above the transition, suggesting a predominantly skew-scattering contribution to the AHE. At low temperature the side-jump and/or intrinsic mechanisms of the AHE make the larger contribution. Typical quantum critical 'cone-like' behaviour is seen in the two terms of the AHE above the QCP, where both contributions are observed to increase most rapidly with temperature at the critical pressure.

7.2 Detailed URhGe Torque Magnetometry Conclusions

The primary sample used for the study was confirmed to be high purity (implying a large mean free path, as desired for ferromagnetic superconductivity), with a determined RRR of about 100 and superconductivity observed at both low and high field, with transition temperatures peaked at 250 mK and 450 mK respectively.

A dip in the resistance (of the order 10%) was observed before entering the superconducting state at 0 T, over a range ~ 100 mK higher than the 250 mK transition temperature. This could be evidence of sample inhomogeneity, and a small region of the sample with higher than average purity having a higher T_{SC}, but even in very pure specimens a transition temperature much above 250 mK has never been reported in the literature. Instead this could be evidence of another type of superconductivity, domain wall or surface, with a higher transition temperature than the bulk.

A similar step in the resistance is observed when exiting the low-field superconducting state by application of field, more prominently for rotation angles near $B \parallel c$-axis alignment, also around 10% of the normal state resistance in size. Again, this might be evidence of a superconducting state with a significantly higher critical field than the bulk, such as domain wall superconductivity, although this would require the domain structure to still be present at fields of 1 T applied in the easy axis direction, which seems very unlikely.

Near $B \parallel b$-axis alignment clear transitions in both the capacitance and resistance are observed at high field, in finely detailed, low-noise measurement data. The zero resistance state is observed over a wide range of field, between 8 and 13 T at the base temperature of the dilution refrigerator, which suggests that the sample is well thermalised to the rotator platform.

A sharp minimum in the magnitude of $\Delta C/\Delta B$ is observed for perfect $B \perp c$-axis alignment, implying a huge reduction in the net magnetic moment in the easy axis direction due to domain cancellation of the sample magnetization, suggesting that the domain structure in this case extends to high field. The zero-crossing in ΔC at fields below B_R can be used to achieve remarkable precision in the alignment of the sample relative to the field (to within 0.01°, limited only by

the practical capabilities of the rotator), however it should be remembered that $B \perp c$-axis alignment does not result in perfect $B \parallel b$-axis alignment.

The Laue diffraction results reveal a 1.4° mis-alignment of the a axis (and thus the b-c plane) after mounting the sample on the cantilever, a tilting of the b-c plane which may either be corrected or exacerbated slightly depending on the mechanical orientation of the dilution fridge unit within the cryostat and magnet system. Assuming a worst case scenario of a 5° tilt this means that, due to the radial symmetry of the field, although it is possible to perfectly align $B \perp c$-axis it is never possible to align $B \parallel b$-axis, merely the vertical projection of that axis. In this example, the parallel-to-field magnetization would then be $M_z = M_b \cos(5°)$.

Very close to $B \perp c$-axis alignment substantial hysteresis is observed in the capacitance measurement up to B_R, supporting the hypothesis that the domain structure survives to high field. At the moment rotation transition ΔC drops to zero and then changes sign, becoming negative for fields immediately above B_R, which can be easily explained by the aforementioned b-c plane tilting and the change in easy axis from c to b at the transition. Increasing field should then rotate the moment away from the b-axis to further align with the field, reducing the negative ΔC to zero.

This is evidently (figure 6.5) not the case: there is a second change in sign at higher field and then ΔC continues to increase, which is very difficult to explain. Even changing the initial sign of $\Delta C/\Delta B$ has no effect on the region of positive ΔC above about 13 T, which in this thesis remains an unresolved mystery.

The zero-resistance state associated with the high-field superconductivity disappears at $\phi \sim 5°$ at 120 mK, and is the probable position of the QCEP, although a drop in resistance at the crossover related to the moment rotation transition is observed up to $\phi \sim 9°$. A reduced resistance is generally expected near a superconducting transition, especially if the sample is inhomogeneous and the transition is substantially broadened, but the extension of some small amount of superconducting pairing up to $\phi \sim 9°$ would suggest that the pairing mechanism is particularly robust. This is perhaps surprising considering that the transverse (to field) susceptibility presented in figure 6.38 shows that magnetic fluctuations at B_R decrease rapidly with rotation angle, though of course the unmeasured longitudinal fluctuations might have a shallower angle dependence.

It is also known from direct measurements of the susceptibility within the high-field superconducting phase that the zero-resistance state persists to higher

temperatures and fields than the diamagnetic response, so evidence of decreased resistance persisting to much higher rotation angles than bulk superconductivity is reasonably consistent.

At higher temperatures a definite peak is seen at B_R, followed by a state of lower resistance, which is slightly unusual since resistance generally increases with field and there is no reason to suspect that the polarised paramagnetic state above B_R would have a lower scattering rate than the ferromagnetic state at lower field. The same behaviour is reported in [49] however, investigating the difference between longitudinal or transverse magnetoresistance for $B \parallel b$-axis. There is little difference in the resistivity either side of B_R in the longitudinal case but for current applied in the c-axis direction the data looks almost exactly the same as in figure 6.9, where the lower resistance above B_R is (unsurprisingly) attributed to the moment rotation. Specifically, the current changes from being roughly parallel to the magnetization at low field to being transverse to both the magnetization and the field above B_R, which results in significantly reduced resistivity.

There are non-Ohmic components to the resistivity with complicated structure across an extensive range of the URhGe phase diagram. A generally accepted theory is that the two regions of superconductivity in URhGe are instances of the same phenomenon and that in the field range between them it is simply the case that the applied field is greater than the upper critical field, which then peaks around the moment rotation transition, leading to the re-emergence of the superconducting phase.[9] This is supported by evidence of a peak in the Sommerfeld coefficient, presumably related to a greatly enhanced effective mass, and thus a peak in the upper critical field.

This implies that superconductivity could potentially exist between the low and high field regions if the critical field was raised or if the effects of the applied field were somehow suppressed. The latter is a possibility explored by these measurements of non-Ohmic behavior, the presence of which suggests the existence of restricted-volume superconductivity such at that found at domain walls (as discussed in section 4.5). An externally applied field can be cancelled out, or at least reduced, within the small region of a domain wall by the large internal fields due to ferromagnetism and the locally changing orientation of the spin-alignment.

Such a reduction in the external field may allow some form of superconductivity

to survive between the two regions of bulk superconductivity, leading to the features observed in the 3F voltage signal. This possibility only arises because of the persistence of a strong ferromagnetic domain structure up to very high fields when the easy axis is precisely oriented perpendicular to the applied field, as detailed by figure 6.23, and so a careful angle study of the 3F voltage would provide supporting evidence for the idea. All of the structure in the data presented in figure 6.11 is very difficult to explain without more information though.

Quantum oscillation (Shubnikov-de Haas) measurements confirm the existence of a 555 T frequency around $\phi \sim 10^\circ$ in a second sample, other than the one used in [48], and also provide some supporting evidence for the purported Lifshitz transition. There were also some very low frequency oscillations observed in the data, possibly due to magnetic breakdown if not a very small pocket of Fermi surface, but these would require a larger range of field to investigate properly. Shubnikov - de Haas oscillations were also measured for $B \parallel c$-axis and three main frequencies were detected, the established 100 T and 1200 T frequencies and a previously unseen one at 700 T. Quantum oscillations in the capacitance, essentially de Haas - van Alphen oscillations, may have been detected right at the experimental limit of signal-to-noise, also at a frequency of 555 T at $\phi \sim 10^\circ$.

The main goal of the project, to simultaneously determine both parallel- and perpendicular-to-field components of the magnetization and susceptibility, was not successfully completed within the time-frame of this PhD research. The field gradient magnetometry experiment proved too sensitive to unintentional field modulation and attempts to eliminate these fields were ultimately unsuccessful. However, a vast amount of interesting data was collected during the attempted measurements, and the following observations can be made.

- The susceptibility is generally huge at $\phi \sim 0^\circ$ because of the persistent domain structure, and for useful data on the vector components of the magnetization a rotation of one or two degrees away from $B \parallel b$-axis alignment is necessary.

- There is a peak in the second demodulation signal at B_R due to the transverse susceptibility, which is positive, but the signal at lower field is generally negative. This is difficult to interpret because of the complexity of the formula that describes the measurement, however the negative peak just below B_R at low temperature is due to the diamagnetic response of the superconducting state. This peak is surprisingly narrow considering

how broad the range of superconductivity is when measured by the zero-resistance state.

- This difference between the presence of diamagnetism and zero-resistance is explored further in figure 6.35, showing a sizable difference between the two and suggesting that there might be some form of superconductivity that persists to higher temperatures and fields than the bulk state.

- There are unexpected, low frequency, large amplitude oscillations in the second demodulation signal at low field. There is little temperature dependence to the signal and so the oscillations are unlikely due to slow variations in temperature. They are a feature of the data that is very difficult to find an explanation for, however they are consistently present, appearing in multiple measurements under various different conditions.

- It does not appear practical to measure separately various different components of the magnetic moment and the susceptibility, transverse and longitudinal, for different directions of field modulation, and then attempt to subtract these quantities from a field gradient magnetometry measurement complicated by unintended field modulation to leave just the gradient signal. Instead the measurement should be improved to eliminate the complications.

- It also does not appear practical to use the measurement data itself to attempt to probe the magnetic environment of the sample and tune the applied fields to eliminate the undesired modulation.

- The peak in the second demodulation signal at B_R rapidly decreases in size rotating away from $B \parallel b$-axis alignment, as does the strength of the associated superconductivity, reinforcing the link between high susceptibility, magnetic fluctuations and the emergence of superconductivity. The peak in the second demodulation signal shows that not only is the moment rotating rapidly with increasing field at B_R, but also that tiny oscillations in field can produce large oscillations in magnetization, that the system is truly susceptible to the large magnetic fluctuations desirable for unconventional electron pairing in ferromagnetic superconductivity.

- Unfortunately the experiments in this project were not able to distinguish whether longitudinal or transverse fluctuations were predominantly responsible for the superconducting pairing mechanism, but the following section

provides some ideas for future improvements to the experimental setup that should allow the necessary measurements to be performed to reach a conclusion on the topic.

7.2.1 Extensions and Improvements

One of the difficulties encountered in analysing the torque data was the slight tilting of the b-c plane such that $B \perp c$-axis alignment did not also mean $B \perp c$-axis alignment, there was always some small component of the a-axis involved. This did not matter too much, since the a-axis is magnetically hard, but it did make the capacitance results rather confusing, specifically regarding the high field behaviour of plots such as those found in figure 6.5. An obvious solution would be more exact mounting and the careful alignment of the dilution refrigerator probe relative to the cryostat magnet, but this is difficult to achieve in practice.

A more interesting solution would be to produce a T-shaped cantilever, with a thin neck, capable of twisting as well as bending. This would allow two components of the torque to be measured simultaneously, using two base plates and analysing the relative changes in capacitance. In this way the a-axis contribution could be measured and the effects of the b-c plane tilting quantified. It would however add complexity to an already complicated experiment.

It would be useful to perform the experiment with a variety of different cantilevers in order to learn more about the calibration factors, which as discussed in section 4.4 are not determined well from the estimated properties and measured dimensions of the cantilever.

It would also be useful to perform the experiment with a variety of samples, to see if any of the results are sample specific, such as the features observed in the resistivity entering and exiting the superconducting states, which may be due to some form of sample inhomogeneity.

Performing experiments with a range of samples of different RRR allows the effects of sample purity to be investigated too, although "more samples, more fields, more temperatures, more orientations" is always an easy thing to say when listing extensions to a study.

However, measuring at a few extra rotation angles between the $\phi \sim 6.0^\circ$ and $\phi \sim 9.5^\circ$ datasets would be necessary in order to see how the data evolves

between them and determine whether there is a trend or if the $\phi \sim 9.5°$ dataset is an anomaly due to some error in the experiment at that particular angle. Measurements over this range would also allow more accurate determination of the position of the QCEP.

Adding compensation coils to the cantilever for a null-deflection experiment could allow proper measurements of de Haas - van Alphen oscillations in the capacitance. In a null-deflection set-up the compensation coil produces a magnetic moment that opposes, and exactly cancels, the magnetic moment of the sample. In this case the cantilever remains stationary for the duration of the field ramp and the key measurement is the amount of current required by the compensation coil in order to keep ΔC zero. Since the cantilever is stationary the gap between the lever and base plate can be very small and the lever can be very soft, and therefore much more sensitive to small changes in magnetization such as quantum oscillations.

The implementation of this set-up is complicated in URhGe by the rotation of the magnetic moment. To counter this, two perpendicularly oriented coils would be required and the vector product of the moments they produce balanced against the moment of the sample as it rotates. The feedback system required to keep ΔC zero is a bit more complex in this case, and another drawback is the weight placed on the cantilever by two coils, especially because the purpose of the null-deflection set-up is to then use a much softer lever.

A bonus of the null-deflection set-up might be that the coils on the cantilever, very close to the sample, could be co-opted as pick-up coils to probe the field modulation environment at the sample and guide it closer to the field centre for the field gradient magnetometry experiment. This is admittedly unlikely to work, since the compensation coils would be very small so the pick-up voltage might not be very easy to measure.

A more reasonable solution to the field centre problem would be to add sensors (pick-up coils, or possible Hall sensors) in the area surrounding the sample at precisely known distances from the sample in precisely known directions. In this way the data from a collection of sensors can be compared to the field profiles expected from the calculations presented in figure 2.10, and the modulation fields adjusted appropriately to centre the field at the sample.

Another improvement for the Faraday magnetometry experiment would be to use stronger field gradients, which would involve the use of stronger transverse field

modulation, which ideally means replacing the copper wire magnet coils created during this project with superconducting wire magnet coils. The issues with this idea are covered in section 4.3.1, and a more realistic solution to the overheating of the copper coils is to perhaps find a way of immersing them in the helium bath, outside of the IVC.

Finally, two obvious extensions to the project are: 1) Further investigation into the 3F voltage signals and the non-Ohmic behaviour potentially related to domain wall superconductivity, and 2) Further investigation into the differences between the zero-resistance state and the diamagnetic state, since the experimental set-up used in this project is very well equipped to simultaneously measure susceptibility, magnetization and resistance to high accuracy and in very fine detail. It is generally remarkable that the susceptibility from field modulation of about 1 G can be measured on top of an applied field of 170,000 G.

Appendix A

UGe_2 Critical Points

Run Code	Pressure at 300 K (kbar)	Pressure at 30 K (kbar)	Method 1 T_C (K)	Method 2a T_C (K)	Method 2b T_C (K)	Method 3 T_C (K)	Taken as T_C (K)
A	0	0	52.3	52.3	53.2	52.3	52.8
B	7.5	7.8	43.4	42.3	43.1	42.5	42.7
C	8.3	9.0	42.6	40.9	41.7	40.6	41.3
D	9.3	10.3	39.1	38.6	39.6	40.8	39.1
E	9.7	10.8	38.0	37.2	38.2	37.7	37.7
F	10.1	11.0	36.6	36.2	37.0	36.5	36.6
G	10.7	11.7	35.4	34.8	35.8	35.8	35.3
H	11.0	12.0	34.1	33.6	34.6	34.2	34.1
I	11.5	12.4	32.9	32.0	32.8	32.3	32.4
J	11.8	12.8	31.5	30.9	31.7	30.2	31.3
K	12.1	13.3	30.2	29.5	30.6	---	30.1
L	12.6	13.6	---	27.5	28.9	---	28.2
M	13.0	14.3	---	24.5	26	---	25.3

Figure A.1 Estimates of the Curie temperature as determined by the various methods outlined in section 5.1, for each experimental run. The weighted average taken as the final result is highlighted in red.

Run Code	Pressure at 30 K (kbar)	Method 1 T_X (K)	Method C T_X (K)	Literature T_X (K)	Method A/B H_X (K)	Literature H_X (K)
A	0	---	---	---	---	---
B	7.8	23.8	19.5	16.80	---	---
C	9.0	20.0	16.5	15.3	---	---
D	10.3	16.8	14.0	13.2	---	---
E	10.8	14.4	11.8	11.4	---	---
F	11.0	11.6	10.1	9.9	---	---
G	11.7	9.6	8.5	8.5	---	---
H	12.0	7.6	6.7	7.5	---	---
I	12.4	---	---	6.3	---	---
J	12.8	---	---	---	1.25	---
K	13.3	---	---	---	1.75	0.2
L	13.6	---	---	---	3	0.85
M	14.3	---	---	---	4	1.8

Figure A.2 Estimated values of T_X and H_X as determined by the various methods outlined in section 5.2, for each experimental run. The literature values corresponding to the calculated Curie temperatures shown in red in figure A.1, sourced from [18], are also listed. The T_X values plotted on the phase diagram shown in figure 5.14 are highlighted in red.

Appendix B

The Force on a Magnetized Material

The main contenders for the force on a magnetized body residing within a field gradient are the correct:

$$\vec{F} = \left(\vec{m} \cdot \vec{\nabla}\right)\vec{B} \tag{B.1}$$

or the similar, though ultimately incorrect, expression:

$$\vec{F} = \vec{\nabla}\left(\vec{m} \cdot \vec{B}\right) \tag{B.2}$$

The confusion arises quite naturally from the definition of the potential energy of a magnetic dipole in a field, which is $U = -\vec{m} \cdot \vec{B}$. Taking the usual definition of force as negative the gradient of the potential energy leads to $\vec{F} = -\nabla(U)$ and the expression given in equation B.2. This is the formula stated in chapter 6.1 of Ref. [92] as the force on "a perfect dipole of infinitesimal size" or an "infinitesimal loop" of current-carrying wire, although Ref. [92] goes on to say that, regarding $U = -\vec{m} \cdot \vec{B}$, "the energy required to keep the current flowing [in the infinitesimal loop] is a different problem."

This terminology is of course for the "Ampère model" of a magnetic dipole as a tiny current loop, rather than the "Gilbert model" of a magnetic dipole as a pair of separated monopoles. The difference is discussed in Ref. [92] and also covered in Ref. [136] in relation to magnetic forces. The situation is perhaps clearer in electrostatics, where monopoles actually physically exist and distinctions between

dipole models are unnecessary.

The analogous situation in electrostatics is a dielectric material in electric field $\vec{E}$ with polarisation $\vec{P}$, equal to the dipole moment $\vec{p}$ per unit volume. In the case of a single dipole $\vec{F} = \vec{\nabla}(\vec{p} \cdot E)$ and $\vec{F} = (\vec{p} \cdot \vec{\nabla})\vec{E}$ are fully equivalent, although this is generally not the case for the magnetic analog.

Regarding electrostatics, Ref. [92] notes that "it is safer to stick with $\vec{F} = (\vec{p} \cdot \vec{\nabla})\vec{E}$ [since for] materials in which the dipole moment is itself a function of position, the $\vec{F} = \vec{\nabla}(\vec{p} \cdot E)$ expression would imply (incorrectly) that $\vec{p}$ *too* is to be differentiated."

The somewhat subtle difference between the two expressions arises from consideration of the energy of the dielectric system as a whole, including the electric field. Rather than considering the potential energy of a single dipole, consider instead the work done in displacing a polarised material some infinitesimal distance within an electric field, provided by some battery power source. In this case "the *battery also does work* as the dielectric moves"[92] if the electric field is held constant by the fixed potential of the battery.

Going back to magnetostatics, the work done by the magnet to maintain a constant field whilst moving a magnetized body within a field gradient is $B \cdot \delta m$ for the resulting infinitesimal change in magnetic moment δm. Relating this work to a force (on the magnetized body), $F = -B \cdot (\delta m / \delta x)$ for some infinitesimal displacement δx, or in more general notation, $\vec{F} = -\vec{B} \cdot \vec{\nabla}(m)$.

The total force on the body, essentially seeking to minimise not just the internal energy of the body but the total free energy of the system as a whole, is thus given by:

$$\begin{aligned} \vec{F} &= -\nabla(U) - \vec{B} \cdot \vec{\nabla}(m) \\ &= \vec{\nabla}\big(\vec{m} \cdot \vec{B}\big) - \vec{B} \cdot \vec{\nabla}(m) \\ &= \big(\vec{m} \cdot \vec{\nabla}\big)\vec{B} + \vec{B} \cdot \vec{\nabla}(m) - \vec{B} \cdot \vec{\nabla}(m) \\ &= \big(\vec{m} \cdot \vec{\nabla}\big)\vec{B} \end{aligned} \tag{B.3}$$

This is essentially an expression of Lenz's law, that "nature abhors a change in flux" and there will be a force from the magnet to oppose any changes in the magnetization. Phrased another way, for the magnet to maintain a constant field, by way of a constant current in the solenoid, the magnet power source

must provide additional energy to overcome the E.M.F. induced by the moving magnetic magnetic material.

It should be noted that this is technically a treatment for electrostatics applied by analog to the magnetic dipole case, but such analysis is fairly standard, covered in detail in Ref. [137] as well as in Ref. [92], and should be robust.

Dealing with the magnetization of a ferromagnet from the outset, where the magnetic moment is provided by electron spin, it could also be argued that is is not actually possible to establish a microscopic gradient within an individual magnetic moment. In this treatment of discrete spins, the total force on the sample is given by the sum of the forces on each individual moment, forces related to a field gradient acting upon a uniform magnetic moment. In other words *for each individual moment*: $\nabla(m_i) = 0$ and $\vec{F_i} = \vec{\nabla}(\vec{m_i} \cdot \vec{B}) = (\vec{m_i} \cdot \vec{\nabla})\vec{B}$.

Put another way, although the total ferromagnetic moment may be increased by the magnetized body moving in some particular direction, thus minimising the energy $-\vec{m} \cdot \vec{B}$, in a discrete, microscopic treatment there is no way for each individual moment to 'know' of this potential energy saving and therefore there can be no force from the $(\vec{B} \cdot \vec{\nabla})\vec{m}$ term.

This can be confusing since, for a material with finite susceptibility, there is evidently a *macroscopic* gradient to the magnetic moment, resulting from the response of the magnetization to the field gradient. In this case the $\vec{m}$ in equation B.1 refers to the average magnetic moment of the sample.

In conclusion, even starting from B.2 and failing to take into account the work done by the magnet and the additional force appearing in B.3, the formula should immediately reduce down to equation B.1 anyway, ultimately (and perhaps fortuitously) reaching the correct expression.

For example, both Ref. [97] and Ref. [101] state equation B.2 as the full formula for the magnetic force on a magnetized body, before reducing the expression down to equation B.1. To clarify, this 'simplification' is somewhat misleading, since it is not due to some special circumstance, such as uniform sample magnetization, but instead due to the fact that equation B.1 is actually the more naturally correct expression. By contrast, other published literature on the subject does indeed state outright that equation B.1 is the force on a magnetized body; Ref. [95] quoting the work of Ref. [138] is a good example.

In the special case of a field gradient applied in a single direction only, usually denoted the z direction, equation B.1 can then be simplified to $F_z = m \cdot \partial B/\partial z$, which is the most common form of the expression, the starting point in Ref. [98] or Ref. [96] for example. As Ref. [95] mentions in a footnote however, "it is impossible to have only $\partial B/\partial z \neq 0$ " and satisfy Maxwell's equations, as discussed in section 2.5.3 of the main thesis text.

It might not be immediately apparent why such lengthy discussion and careful deliberation on the differences between equation B.1 and equation B.2 is necessary. Hopefully a specific example will make it obvious.

In section 2.5.3 of the main thesis text, the 'second demodulation signal' resulting from oscillations of the torque due to the alternating field gradient is given as:

$$V_{\text{demod 2}} \propto L\cos(\theta)\, m_{0x}\, \frac{\partial B_x}{\partial x} - L\sin(\theta)\, m_{0z}\, \frac{\partial B_z}{\partial z} \tag{B.4}$$

Had this expression been derived from equation B.2, including the magnetic moment within the spatial derivative, the result would be:

$$\begin{aligned} V_{\text{demod 2}} \propto\ & L\cos(\theta)\,(m_{0x} + \frac{\partial m_z}{\partial B_x} B_{0z})\,\frac{\partial B_x}{\partial x} \\ & - L\sin(\theta)\,(m_{0z} + \frac{\partial m_z}{\partial B_z} B_{0z})\,\frac{\partial B_z}{\partial z} \end{aligned} \tag{B.5}$$

where the susceptibility enters the expression via $\partial m/\partial x \simeq (\partial m/\partial B)(\partial B/\partial x)$.

In this case, supposing $\theta \sim 90°$ to simplify matters, leaving only the second term, the second demodulation signal is related to the derivative of $m_{0z}B_{0z}$ as follows.

$$\frac{V_{\text{demod 2}}}{(L\sin\theta)\,(\partial B_z/\partial z)} \propto -(m_{0z} + \frac{\partial m_z}{\partial B_z} B_{0z}) = -\frac{d}{dB_{0z}}(m_{0z}B_{0z}) \tag{B.6}$$

The parallel-to-field component of the magnetic moment, m_{0z}, could then be found by integration of the measurement data. Explicitly:

$$m_{0z} \propto \frac{1}{B_{0z}} \int_0^{B_{0z}} \frac{-V_{\text{demod 2}}}{(L\sin\theta)\,(\partial B_z/\partial z)}\, dB_{0z} \tag{B.7}$$

Although, as concluded earlier, this approach is ultimately incorrect, stemming from the use of equation B.2 instead of equation B.1, it seems worth highlighting

due to the nature of the experimental data presented in this thesis. The results for the second demodulaion signal presented in section 6.6 do appear to be more related to the susceptibility than the magnetization, and integrating the data does appear to produce something that looks very much like the parallel-to-field component of the magnetization.

Hence the results initially seemed to support the analysis derived from equation B.2, which was mistakenly applied earlier in the project. The mistake was uncovered by both more careful consideration of the theory, leading to the discussion presented in this appendix, and the realisation of other ways in which the data could look more like the susceptibility than the magnetization, as discussed in section 6.6 of the main thesis text.

In summary, though usually a banal mistake without consequence, in complex situations where the magnetization is not uniform and the susceptibility far from linear there can be major consequences from taking equation B.2 as the magnetic force instead of the correct formula, which is equation B.1.

Appendix C

Unsuccessful Magnetoresistance Fitting

An example of attempting to fit the measured magnetoresistance at 10.3 kbar and 2 K is shown in figure C.1 on the following page. The poor results demonstrate that the standard two-band formula, specifically equation 2.27, cannot accurately describe the data and more sophisticated formulae will be required, as discussed in section 2.3.

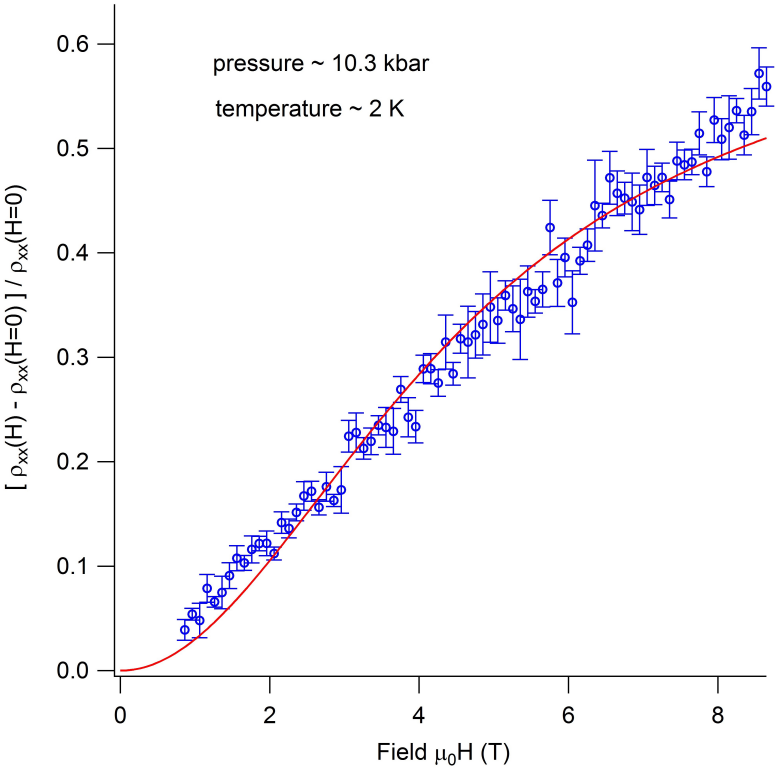

Figure C.1 An example of attmpting to fit the magnetoresistance to the two-band model described by equation 2.28. The $\omega_c\tau = 1$ point implied by the fit, which is obviously invalid, occurs mid-way though the field range, transitioning from the low field limit, where 2.28 is defined and the magnetoresistace is supposedly quadratic, to the high field limit, where the magneotresistance supposedly begins to saturate. The actual data appears to be simply linear, however, with neither quadratic field dependence at low field nor saturation of the magnetoresistance at high field. The conclusion therefore is that the model is incorrect and cannot accurately describe the experimental evidence. More sophisticated models that can give rise to linear magnetoresistance will be required.

Bibliography

[1] S. Julian. Pairing with spin fluctuations. *Physics*, **5**(17), (2012).

[2] A. D. Huxley, E. Ressouche, B. Grenier, D. Aoki, J. Flouquet, and C. Pfleiderer. The co-existence of superconductivity and ferromagnetism in actinide compounds. *Journal of Physics: Condensed Matter*, **15**:1945–1955, (2003).

[3] A. Shick and W. Pickett. Magnetism, Spin-Orbit Coupling, and Superconducting Pairing in UGe_2 . *Physical Review Letters*, **86**(2):300–303, (2001).

[4] T. Terashima, T. Matsumoto, C. Terakura, S. Uji, N. Kimura, M. Endo, T. Komatsubara, H. Aoki, and K. Maezawa. Magnetic phase diagram and the pressure and field dependence of the Fermi surface in UGe_2. *Physical Review B*, **65**(17), (2002).

[5] R. Settai, Y. Haga, M. Nakashima, S. Ikeda, T. Okubo, S. Araki, Y. Onuki. A change of the Fermi surface in UGe_2 across the critical pressure. *Journal of Physics: Condensed Matter*, **14**:29–36, (2002).

[6] V. Taufour, A. Villaume, D. Aoki, G. Knebel, J. Flouquet. Magnetic field evolution of critical end point in UGe_2. *Journal of Physics: Conference Series*, **273**(012017), (2011).

[7] F. Lévy, I. Sheikin, B. Grenier, and A. D. Huxley. Magnetic field-induced superconductivity in the ferromagnet URhGe. *Science*, **309**:1343–1346, (2005).

[8] D. Aoki, A. Huxley, E. Ressouche, I. Sheikin, J. Flouquet, J.P. Brison, and C. Paulsen. Superconductivity in two itinerant uranium ferromagnets: UGe_2 and URhGe. *Journal of Physics and Chemistry of Solids*, **63**(6–8):1179–1182, (2002).

[9] F. Lévy, I. Sheikin, and A. Huxley. Acute enhancement of the upper critical field for superconductivity approaching a quantum critical point in URhGe. *Nature Physics*, **3**(7):460–463, (2007).

[10] S. B. Dugdale. Probing the fermi surface by positron annihilation and compton scattering. *Low Temp. Phys.*, **40**(328), (2014).

[11] I. Lifshitz and M. Kaganov. Some problems of the electron theory of metals. *Soviet Physics Uspekhi*, **2**(6):831–855, 1960.

[12] A. L. Cornelius, J. S. Schilling, D. Mandrus, and J. D. Thompson. Anomalous hydrostatic pressure dependence of the Curie temperature of the Kondo-lattice compound YbNiSn to 38 GPA. *Physical Review B*, **52**(22):699–702, (1995).

[13] S. Nair, S. Wirth, S. Friedemann, F, Steglich, Q. Si, and A. J. Schofield. Hall effect in heavy-fermion metals. *Advances in Physics*, **61**(00):2–83, (2012).

[14] N. Nagaosa, J. Sinova, S. Onoda, A. H. MacDonald, N. P. Ong. Anomalous Hall effect. *Reviews of Modern Physics*, **82**(2):1539–1592, (2010).

[15] J. R. Hook and H. E. Hall. *Solid State Physics*. John Wiley & Sons Ltd., (2001). Second Edition.

[16] N. W. Ashcroft and N.D. Mermin. *Solid State Physics*. Brooks/Cole, (1976).

[17] L. H. Dmowski and E. Litwin-Staszewska. The variation of the pressure coefficient of Manganin sensors at low temperatures. *Measurement Science and Technology*, **10**:343–347, (1999).

[18] C. Pfleiderer and A. D. Huxley. Pressure dependence of the magnetization in the ferromagnetic superconductor UGe_2. *Physical Review Letters*, **89**(14), (2002).

[19] N. Tateiwa, T. C. Kobayashi, K. Hanazono, K. Amaya, Y. Haga, R. Settai and Y. Onuki. Pressure-induced superconductivity in a ferromagnet UGe_2. *Journal of Physics: Condensed Matter*, **13**:17–23, (2001).

[20] H. Kotegawa, V. Taufour, D. Aoki, G. Knebel, and J. Flouquet. Evolution toward Quantum Critical End Point in UGe_2. *Journal of the Physical Society of Japan*, **80**(083703), (2011).

[21] A. Huxley, I. Sheikin, E. Ressouche, N. Kernavanois, D. Braithwaite, R. Calemczuk, and J. Flouquet. UGe_2: A ferromagnetic spin-triplet superconductor. *Physical Review B*, **63**(144519), (2001).

[22] G. Oomi, T. Kagayama, Y. Onuki. Critical electron scattering in UGe_2 near the magnetic phase transition induced by pressure. *Journal of alloys and compounds*, **273**:482–485, (1998).

[23] S. S. Saxena, P. Agawal, K. Ahilan, F. M. Grosche, R. K. W. Haselwimmer, M. J. Steiner, E. Pugh, I. R. Walker, S. R. Julian, P. Monthoux, G. G. Lonzarich, A. Huxley, I. Sheikin, D. Braithwaite, and J. Flouquet. Superconductivity on the border of itinerant-electron ferromagnetism in UGe_2. *Nature*, **406**:587–592, (2000).

[24] E. D. Bauer, R. P. Dickey, V. S. Zapf, and M. B. Maple . Coexistence of superconductivity and ferromagnetism in polycrystalline UGe_2. *Journal of Physics:*, **13**, (2001).

[25] N. Tateiwa, K. Hanazono, T. C. Kobayashi, K. Amaya, T. Inoue, K. Kindo, Y. Koike, N. Metoki, Y. Haga, R. Settai, Y. Onuki. Magnetic properties of a pressure-induced superconductor UGe_2. *Journal of the Physical Society of Japan*, **70**:2876–2879, (2001).

[26] S. Wantanabe and K. Miyake. Coupled CDW and SDW fluctuations as an origin of anomalous properties of ferromagnetic superconductor UGe_2. *Journal of the Physical Society of Japan*, **71**:2489–2499, (2002).

[27] D. Fay and J. Appel. Coexistence of p-state superconductivity and itinerant ferromagnetism. *Physical Review B*, **22**(7):3173–3182, (1980).

[28] A. B. Pippard. *Magnetoresistance in Metals*. Cambridge University Press, (1989). Paperback Reissue (2009).

[29] H. Yamagami and A. Hasegawa. Fermi surface of the ferromagnetic heavy-electron compound UGe_2. *Physica B: Physics of Condensed Matter*, **186-188**:182–184, (1993).

[30] Y. Onuki, S. Yun, I. Ukon, I. Umehara, K. Satoh, I. Sakamoto, M. Hunt, P. Messon, P. Probst, N. Springrod. High Field Magnetoresistance and de Haas-van Alphen Effect in UGe_2. *Journal of the Physical Society of Japan*, **60**(7), (1991).

[31] T. Terashima, T. Matsumoto, C. Terakura, S. Uji, N. Kimura, M. Endo, T. Komatsubara, and H. Aoki. Evolution of Quasiparticle Properties in UGe_2 with Hydrostatic Pressure Studied via the de Haas-van Alphen Effect. *Physical Review Letters*, **87**(16), (2001).

[32] Y. Haga, M. Nakashima, R. Settai, S. Ikeda, T. Okubo, S. Araki. A change of the Fermi surface across the metamagnetic transition under pressure in UGe_2. *Journal of Physics: Condensed Matter*, **14**(14), (2002).

[33] T. C. Kobayashi, K. Hanazono, N. Tateiwa, K. Amaya, Y. Haga, R. Settai, and Y. Onuki. Pressure-induced superconductivity in a ferromagnet, UGe_2: resistivity measurements in a magnetic field. *Journal of Physics: Condensed Matter*, **14**:10779–10782, (2002).

[34] T. Nishioka, G. Motoyama, S. Nakamura, H. Kadoya, and N. K. Sato. Unusual nature of ferromagnetism coexisting with superconductivity in UGe_2. *Physical Review Letters*, **88**(23), (2002).

[35] V. H. Tran, S. Paschen, R. Troć, M. Baenitz, and F. Steglich. Hall effect in the ferromagnet UGe_2. *Physical Review B*, **69**(195314), (2004).

[36] V. Taufour, D. Aoki, G. Knebel, and J. Flouquet. Tricritical point and wing structure in the itinerant ferromagnet UGe_2. *Physical Review Letters*, **105**(217201), (1996).

[37] R. Troć, Z. Gajek, and A. Pikul. Dualism of the $5f$ electrons of the ferromagnetic superconductor UGe_2 as seen in magnetic, transport, and specific-heat data. *Physical Review B*, **86**(224403), (2012).

[38] M. Kepa, D. A. Sokolov, M. Böhm, and A. D. Huxley. Magnetic excitations in the ferromagnetic superconductor UGe_2 under pressure. *Journal of Physics: Conference Series*, **568**(4), (2014).

[39] S. Sakarya, P. C. M. Gubbens, A. Yaouanc, P. Dalmas de Réotier, D. Andreica, A. Amato, U. Zimmermann, N. H. van Dijk, E. Brück, Y. Huang, and T. Gortenmulder. Positive muon spin rotation and relaxation measurements on the ferromagnetic superconductor UGe_2 at ambient and high pressure. *Physical Review B*, **81**(2), (2010).

[40] K. Prokeš, T. Tahara, and Y. Echizen. Electronic properties of a URhGe single crystal. *Physica B*, **311**:220–232, (2002).

[41] F. Hardy, A. Huxley, J. Flouquet, C. Pfleiderer. (P, T) phase diagram of the ferromagnetic superconductor URhGe. *Physica B*, 359–361:1111–1113, (2005).

[42] D. Aoki, A. Huxley, E. Ressouche, D. Braithwaite, J. Flouquet, J-P. Brison, E. Lhotel, and C. Paulsen. Coexistence of superconductivity and ferromagnetism in URhGe. *Nature*, **413**:613–616, (2001).

[43] N. T. Huy, A. Gasparini, D. E. de Nijs, Y. Huang, J. C. P. Klaasse, T. Gortenmulder, A. de Visser, A. Hamann, T. Görlach, and H. v. Löhneysen. Superconductivity on the border of weak itinerant ferromagnetism in UCoGe. *Physical Review Letters*, **99**(6):3–6, (2007).

[44] F. Hardy and A. D. Huxley. p-Wave superconductivity in the ferromagnetic superconductor URhGe. *Physical Review Letters*, **94**(247006), (2005).

[45] V. Mineev. Reentrant superconductivity in URhGe. *Physical Review B*, **91**(1), (2015).

[46] F. Lévy, I. Sheikin, B. Grenier, C. Marcenat, and A. Huxley. Coexistence and interplay of superconductivity and ferromagnetism in URhGe. *Journal of physics. Condensed matter*, **21**(16), (2009).

[47] F. Hardy, D. Aoki, C. Meingast, P. Schwiess, P. Burger, H. v. L'ohneysen, and J. Flouquet. Transverse and longitudinal magnetic-field responses in the Ising ferromagnets URhGe, UCoGe, and UGe_2. *Physical Review B*, **83**(19):3–6, (2011).

[48] E. A. Yelland, J. M. Barraclough, W.Wang, K. V. Kamenev, and A. D. Huxley. High-field superconductivity at an electronic topological transition in URhGe. *Nature Physics*, **7**:890–894, (2011).

[49] D. Aoki, G. Knebel, and J. Flouquet. Fermi Surface Instabilities in Ferromagnetic Superconductor URhGe. *Journal of the Physical Society of Japan*, **83**(094719), (2014).

[50] A. D. Huxley. Ferromagnetic superconductors. *Physica C: Superconductivity and its Applications*, **514**:368–377, (2015).

[51] C. M. Hurd. *The Hall Effect In Metals And Alloys*. Plenum Press, 1st edition edition, (1972).

[52] J. M. Ziman. *Principles of the Theory of Solids*. Cambridge University Press, (1972). Second Edition.

[53] R. H. McKenzie, J. S. Qualls, S. Y. Han, and J. S. Brooks. Violation of Kohlers rule by the magnetoresistance of a quasi-two-dimensional organic metal. *Physical Review B*, **57**(19), (1998).

[54] C. Kittel. *Introduction to Solid State Physics*. John Wiley & Sons, Inc., (1966). Third Edition.

[55] H. v. Löhneysen, A. Rosch, M. Vojta, and P. W$'$olfle. Fermi-liquid instabilities at magnetic quantum phase transitions. *Reviews of Modern Physics*, **79**:1015–1075, (2007).

[56] I. M. Lifshitz. Anomalies of electron characteristics of a metal in the high pressure region. *Soviet Physics JEPT*, **11**(5):1130–1135, (1958).

[57] M. Bercx and F.F. Assaad. Metamagnetism and lifshitz transitions in models for heavy fermions. *Physical Review B*, **86**(7):075108, (2012).

[58] C. Liu, T. Kondo, R. M. Fernandes, A. D. Palczewski, E. D. Mun, N. Ni, A. N. Thaler, A. Bostwick, E. Rotenberg, J. Schmalian, S. L. Budko, P. C. Canfield, and A. Kaminski. Evidence for a Lifshitz transition in electron-doped iron arsenic superconductors at the onset of superconductivity. *Nature Physics*, **6**:419–423, (2010).

[59] J. Abbott, O. Ergeneman, M. Kummer, A. Hirt, and B. Nelson. Modeling magnetic torque and force for controlled manipulation of soft-magnetic bodies. *IEEE Transactions on Robotics*, **23**(6):1247–1252, (2007).

[60] A. N. Dobrynin, T. R. Gao, N. M. Dempsey, and D. Givord. Experimental determination of the magnetization dependent part of the demagnetizing field in hard magnetic materials. *Applied Physics Letters*, **97**(192506), (2010).

[61] G. Zheng, M. Pardavi-Horvath, X. Huang, B. Keszei, and J. Vandlik. Experimental determination of an effective demagnetization factor for nonellipsoidal geometries. *Journal of Applied Physics*, **79**(8), (1996).

[62] D. X. Chen, E. Pardo, and A. Sanchez. Demagnetizing factors for rectangular prisms. *IEEE Transactions On Magnetics*, **41**(6), (2005).

[63] J. A. Osborn. Demagnetizing factors of the general ellipsoid. *Physical Review*, **67**(11), (1945).

[64] B. D. Cullity. *Introduction to magnetic materials*. Addison-Wesley, (1972). Appendix 6.

[65] P. M. C. Rourke, A. F. Bangura, C. Proust, J. Levallois, N. Doiron-Leyraud, D. LeBoeuf, L. Taillefer, S. Adachi, M. L. Sutherland, and N. E. Hussey. Fermi-surface reconstruction and two-carrier model for the Hall effect in $YBa_2Cu_4O_8$. *Physical Review B*, **82**(2), (2010).

[66] R. E. Peierls. *Quantum Theory of Solids*. Oxford University Press, (1955). (Oxford Classics 2001 Edition).

[67] E. Fawcett and W. Reed. Effects of Compensation on the Galvanomagnetic Properties of Nonmagnetic and Ferromagnetic Metals. *Physical Review*, **131**(6), (1963).

[68] N. A. Sinitsyn. Semiclassical theories of the anomalous Hall effect. *Journal of Physics: Condensed Matter*, **20**(023201), (2008).

[69] P. Bruno. *Handbook of Magnetism and Advanced Magnetic Materials*, volume The Berry Phase in Magnetism and the Anomalous Hall Effect. John Wiley & Sons, Ltd., (2007). p.540-558.

[70] A. Crépieux and P. Bruno. Theory of the anomalous Hall effect from the Kubo formula and the Dirac equation. *Physical Review B*, **64**(014416), (2001).

[71] S. Onoda, N. Sugimoto, and N. Nagaosa. Intrinsic versus extrinsic anomalous Hall effect in ferromagnets. *Physical Review Letters*, **97**(12):1–4, (2006).

[72] F. Haldane. Berry curvature on the fermi surface: Anomalous hall effect as a topological fermi-liquid property. *Physical Review Letters*, **93**(20):1–4, (2004).

[73] Y. Shiomi, Y. Onose, and Y. Tokura. Effect of scattering on intrinsic anomalous Hall effect investigated by Lorenz ratio. *Physical Review B*, **81**(054414), (2010).

[74] Z. Fang, N. Nagaosa, K. S. Takahashi, A. Asamitsu, R. Mathieu, T. Ogasawara, H. Yamada, M. Kawasaki, Y. Tokura, and K. Terakura. The Anomalous Hall Effect and Magnetic Monopoles in Momentum Space. *Science*, **302**(5642):92–95, (2003).

[75] P. Středa. Anomalous Hall conductivity: Local orbitals approach. *Physical Review B*, **82**(045115), (2010).

[76] E. Hall. XVIII. On the "Rotational Coefficient" in nickel and cobalt. *Phil. Mag.*, **12**(157), (1881).

[77] R. Karplus, J. M. Luttinger. Hall effect in ferromagnetics. *Physical Review*, **95**(5):1154–1160, (1954).

[78] J. Smit. The Spontaneous Hall Effect in Ferromagnetics II. *Physica*, **24**:39–51, (1958).

[79] L. Berger. Side-jump Mechanism for the Hall Effect of Ferromagnets. *Physical Review B*, **2**(11):4559–4566, (1970).

[80] J. Kondo. Anomalous hall effect and magnetoresistance of ferromagnetic metals. *Progress of Theoretical Physics*, **27**(4):772–792, (1962).

[81] M. Berry. Quantal phase factors accompanying adiabatic changes. *Proc. R. Soc. Lond. A*, **392**(1802), (1984).

[82] N. Nagaosa. Anomalous Hall Effect – A New Perspective. *Journal of the Physical Society of Japan*, **75**(4), (2006).

[83] N. A. Sinitsyn, Q. Niu, J. Sinova, and K. Nomura. Disorder effects in the anomalous Hall effect induced by Berry curvature. *Physical Review B*, **72**(45346), (2005).

[84] X. Wang, D. Vanderbilt, J. R. Yates, and I. Souza. Fermi-surface calculation of the anomalous Hall conductivity. *Physical Review B*, **76**(19):1–11, (2007).

[85] P. Mitra, N. Kumar, and N. Samarth. Localization and the anomalous Hall effect in a dirty metallic ferromagnet. *Physical Review B*, **82**(035205), (2010).

[86] Y. Yang. Anomalous hall effect in heavy electron materials. *Physical Review B*, **87**(045102), (2013).

[87] P. Sacramento, V. R. Vieira, and V. Dugaev. Anomalous hall effect in superconductors with spin-orbit interaction. *Physical Review B*, **85**(014518), (2012).

[88] C. Kittel. *Introduction to Solid State Physcs.* John Wiley & Sons, Inc., (1966). Fourth Edition.

[89] L. Onsager. Interpretation of the van Alphen, de Haas effect. *Phil. Mag.*, **43**(344), (1952).

[90] D. Shoenberg. De Haas-van Alphen effect and electronic structure of metals. *Proc. Phys. Soc. (London)*, **79**, (1962).

[91] D. Shoenberg. *Magnetic oscillations in metals*. Cambridge University Press, (1984). Reissue (2009).

[92] D. Griffiths. *Introduction to Electrodynamics*. Prentice-Hall, Inc., (1999). (Third Edition).

[93] T. Beléndez, C. Neipp, and A. Beléndez. Large and small deflections of a cantilever beam. *European Journal of Physics*, **23**:371–379, (2002).

[94] O. H. Chung. Null-Deflection Magnetometer for Anisotropy Studies of Layered Superconductors. *Journal of the Korean Physical Society*, **32**(5):758–761, (1997).

[95] J. Cape and R. Young. Canted helmholtz coils for constant-gradient Faraday balance magnetometry. *Review of Scientific Instruments*, **42**(7):1061–1063, (1971).

[96] R. T. Lewis. A Faraday type magnetometer with an adjustable field independent gradient. *Review of Scientific Instruments*, **42**(1):31–34, (1971).

[97] J. Brooks, M. J. Naughton, Y. P. Ma, P. M. Chaikin, and R. V. Chamberlin. Small sample magnetometers for simultaneous magnetic and resistive measurements at low temperatures and high magnetic fields. *Review of Scientific Instruments*, **58**(1):117–121, (1987).

[98] D. Zhang, C. Probst, and K. Andres. A novel and sensitive Faraday-type magnetometer for the field range from 0 to 12 T. *Review of Scientific Instruments*, **68**(10), (1997).

[99] K. O'Grady, V. Lewis, and D. Dickson. Alternating gradient force magnetometry: Applications and extension to low temperatures. *Journal of Applied Physics*, **73**(10):5608–5613, (1993).

[100] L. Thomas, A. Rahmani, P. Renaudin, A. Wack. High-sensitivity in-plane vector magnetometry using the alternating gradient force method. *Journal of Applied Physics*, **93**(10):7062–7064, (2003).

[101] D. Slobinsky, R. A. Borzi, A. P. MacKenzie, S. A. Grigera. Fast sweep-rate plastic Faraday force magnetometer with simultaneous sample temperature measurement. *Review of Scientific Instruments*, **83**(12):1–6, (2012).

[102] A. J. Leggett. *Quantum Liquids*. Oxford University Press, (2006).

[103] J. F. Annett. *Superconductivity, Superfluids and Condensates*. Oxford University Press, (2004).

[104] M. Tinkham. *Introduction to Superconductivity*. Dover Publications, Inc., 1996. (Second Edition).

[105] J. Bardeen, L. N. Cooper, and J. R. Schrieffer. Theory of Superconductivity. *Physical Review*, **108**(5):1175–1204, (1957).

[106] D. R. Tilley and J. Tilley. *Superfluidity and Superconductivity.* IOP Publishing Ltd., (1990). Chapter 11: High-T_c superconductors.

[107] D. Aoki and J. Flouquet. Superconductivity and ferromagnetic quantum criticality in uranium compounds. *Journal of the Physical Society of Japan*, **83**(6):1–9, (2014).

[108] P. Monthoux, D. Pines and G. G. Lonzarich. Superconductivity without phonons. *Nature*, **450**:1177–1183, (2007).

[109] A. J. Millis, S. Sachdev, and C. M. Varma. Inelastic scattering and pair breaking in anisotropic and isotropic superconductors. *Physical Review B*, **37**(10):2975–4986, (1988).

[110] N. Mathur. Magnetically mediated superconductivity in heavy fermion compounds. *Nature*, **394**(6688):39–43, (1998).

[111] S. Paschen, T. Lühmann, S. Wirth, P. Gegenwart, O. Trovarelli, C. Geibel, F. Steglich, P. Coleman, and Q. Si. Hall-effect evolution across a heavy-fermion quantum critical point. *Nature*, **432**:881–885, (2004).

[112] S. Ernst, S. Kirchner, C. Krellner, C. Geibel, G. Zwicknagl, F. Steglich, and S. Wirth. Emerging local Kondo screening and spatial coherence in the heavy-fermion metal $YbRh_2Si_2$. *Nature*, **474**:362–366, (2011).

[113] S. Friedemann, N. Oeschler, S. Writh, C. Krellner, C. Geibel, F. Steglich, S. Paschen, S. Kirchner, and Q. Si. Discontinuous Hall coefficient at the quantum critical point in $YbRh_2Si_2$. *Journal of Physics: Condensed Matter*, **23**(094216), (2011).

[114] T. R. Kirkpatrick and D. Belitz. Universal low-temperature tricritical point in metallic ferromagnets and ferrimagnets. *Physical Review B*, **85**(13), (2012).

[115] T. R. Kirkpatrick, D. Belitz, T. Vojta, and R. Narayanan. Strong Enhancement of Superconducting T_c in Ferromagnetic Phases. *Physical Review Letters*, **87**(12), (2001).

[116] A. D. Huxley, S. J. C. Yates, F. Lévy, and I. Sheikin. Odd-parity superconductivity and the ferromagnetic quantum critical point. *Journal of the Physical Society of Japan*, (2007).

[117] K. Yokogawa. Solidification of high-pressure medium Daphne 7373. *Japanese Journal of Applied Physics*, **46**(6A):3636–3639, (2007).

[118] L. J. van der Pauw. A method of measuring the resistivity and Hall coefficient on lamellae of arbitrary shape. *Philips Technical Review*, **20**(8):220–224, (1958).

[119] Yu. G. Kataev, L. G. Lavrent'eva and I. P. Porrebnyak. Experimental comparison of four-point methods for measuring the Hall effect and the electrical conductivity. *Fizika*, **12**(2):20–25, (1969).

[120] R. Chwang, B. J. Smith and C. R. Crowell. Contact size effects on the van der Pauw method for resisitivity and Hall coefficient measurement. *Solid-State Electronics*, **17**:1272–1227, (1974).

[121] H. C. Montgomery. Method for measuring electrical resisitivity of anisotropic materials. *Journal of Applied Physics*, **42**(7):2971–2975, (1971).

[122] W. L. V. Price. Extension of van der Pauw's theorem for measuring specific resistivity in discs of arbitrary shape to anisotropic media. *Journal of Physics D: Applied Physics*, **5**:1127–1132, (1972).

[123] J. D. Wasscher. Note on four-point resistivity measurements on anisotropic conductors. *Philips Research Reports*, **16**:301–306, (1961).

[124] V. E. Oleinikov and N. N. Polyakov. Concurrent measurements on conductivity and Hall coefficient tensor components of anisotropic semiconductor films. *Russian Physics Journal*, 43(6), (2000).

[125] N. N. Polyakov. Transverse conduction voltage in the study of anisotropic semiconductor crystals and films. *Fizika*, **3**:34–40, (1993).

[126] P. V. Frolov and N. N. Polyakov. On measurement of the Hall coefficient of anisotropic semiconductor single crystals and films. *Russian Physics Journal*, **43**(7), (2000).

[127] V. N. Bogomolov and V. P. Zhuze. Some modern methods of measuring the Hall effect. *Poroshkovaya Metallurgiya*, **6**(12):89–95, (1962).

[128] B. F. Logan, S. O. Rice, and R. F. Wick. Series for Computing Current Flow in a Rectangular Block. *Journal of Applied Physics*, **42**(7), (1971).

[129] B. L. Brandt, D. W. Liu, and L. G. Rubin. Low temperature thermometry in high magnetic fields. VII. Cernox^{TM} sensors to 32 T. *Review of Scientific Instruments*, **70**(1):104–110, (1999).

[130] A. Jayaraman. Ultrahigh pressures. *Review of Scientific Instruments*, **57**(6):1013–1031, (1986).

[131] O. E. Andersson and B. Sundqvist. Low temperature calibration of Manganin pressure gauges. *Review of Scientific Instruments*, **68**(2), (1997).

[132] L. H. Adams, R. W. Goranson, and R. E. Gibson. Construction and properties of the Manganin resistance pressure gauge. *Review of Scientific Instruments*, **8**:230–235, (1937).

[133] Yu. A. Atanov and E. M. Ivanova. High-pressure measurements with Manganin pressure gauges. *Izmeritel'naya Tekhnika*, **2**:247–250, (1971).

[134] J. D. Thompson. Low-temperature pressure variation in a self-clamping pressure cell. *Review of Scientific Instruments*, **55**(2), (1984).

[135] T. Combier. Ferromagnetic quantum criticality studied by hall effect measurements in UCoAl. *Journal of the Physical Society of Japan*, **82**(10), (2005).

[136] T. Boyer. The force on a magnetic dipole. *American Journal of Physics*, **56**(8), (1988).

[137] J. D. Jackson. *Classical Electrodynamics*. John Wiley and Sons, (1999). (Third Edition).

[138] W. F. Brown. Electric and magnetic forces: A direct calculation. i. *American Journal of Physics*, **19**(290), (1951).